

The significance of the Cretaceous Kluane Schist in the Mesozoic Assembly of the North American Cordillera.

by

William. F. McKenzie

M. Earth Sci., University of Oxford, 2018

B.A. (Geology), University of Oxford, 2017

Thesis Submitted in Partial Fulfillment of the
Requirements for the Degree of
Doctor of Philosophy

in the
Department of Earth Sciences
Faculty of Science

© William. F. McKenzie 2023
SIMON FRASER UNIVERSITY
Summer 2023

Copyright in this work is held by the author. Please ensure that any reproduction or re-use is done in accordance with the relevant national copyright legislation.

Declaration of Committee

Name: William F. McKenzie

Degree: Doctor of Philosophy

Title: The Significance of the Cretaceous Kluane Schist in the Mesozoic Assembly of the North American Cordillera

Committee: **Chair: Andy Calvert**
Professor, Earth Sciences

H. Daniel Gibson
Co-supervisor
Professor, Earth Sciences

Brendan Dyck
Co-supervisor
Assistant Professor, Earth, Environment and Geographical Sciences
University of British Columbia - Okanagan

Maurice Colpron
Committee Member
Head, Bedrock Geology
Yukon Geological Survey

Reid Staples
Examiner
Lecturer, Earth Sciences

Luke Beranek
External Examiner
Associate Professor, Earth Sciences Memorial
University of Newfoundland

Abstract

The Cordillera of western North America is an archetypal accretionary orogen. During the Mesozoic, two significant periods of terrane accretion are recognised within the Canadian-Alaska (“Northern”) Cordillera: 1) the accretion of the Intermontane terranes to the western Laurentian margin from ca. 200 to ca. 180 Ma and, (2) the subsequent accretion of the Insular terranes to the Intermontane terranes, possibly as early as ca. 174 Ma and as late as ca. 70 Ma. Information regarding the precise timing and tectonic drivers of this Mesozoic accretionary history is held within a series of inverted Jura-Cretaceous basins exposed at the interface between the pericratonic Intermontane and exotic Insular terranes. Of these inverted basins, the Kluane Schist, southwest Yukon, represents one of the largest and most continuous exposures.

The Kluane Schist consists of metamorphosed and deformed low-Al pelites that were deposited during the very latest stages of Insular terrane accretion. Detrital zircon geochronology reveals a Late Cretaceous maximum depositional age for the Kluane Schist and Hafnium-isotope geochemistry provides strong provenance ties to Triassic–Cretaceous zircon sources currently exposed within the southern Yukon Tanana terrane. Detailed petrography, petrological modelling, and *in-situ* monazite petrochronology demonstrate the metamorphism of the Kluane Schist occurred during the override of the Yukon-Tanana terrane between ca. 70–55 Ma. This metamorphic evolution, combined with its continentally-dipping, Buchan-style inverted metamorphic sequence and tops-to-the-southwest shear structures are consistent with the Kluane Schist representing the uppermost part of a contractional forearc to an arc built upon the Yukon-Tanana terrane. This geodynamic setting for the Kluane Schist is most compatible with models of Insular terrane accretion that involve east-dipping subduction below a westward migrating North American continent during the Mesozoic.

Keywords: Jura-Cretaceous basins; North American Cordillera; Insular terrane accretion; Phase equilibria modelling; Petrochronology; Detrital zircon geochronology

Acknowledgements

First and foremost, I would like to thank both my supervisors, Brendan Dyck & Dan Gibson, for their guidance, advice, and encouragement throughout the duration of my project. Your mentorship has undoubtedly lead me to mature as a scientist and provided me with expertise and confidence to give any problem that I may encounter in my future career a good ol' college try! I am also extremely grateful to Maurice Colpron at the Yukon Geological Survey for being such a generous host on my trips up to Whitehorse and always providing insightful and inspiring discussions on Cordilleran geology. Maurice and the Yukon Geological Survey are also thanked for all their support during my field seasons up north, without which the successful fieldwork completed within this project would not have been possible.

I am also extremely grateful to all of those outside of my supervisory committee that have gone above and beyond to make this project a success. Thanks to my co-authors Matt Steele-MacInnis and Kyle Larson for their expertise, discussion, and feedback that helped hone some of the work completed by this thesis into submittable publications. Steve Israel is thanked for all his insightful discussions into the Kluane Schist and accompaniment and guidance during fieldwork. Thanks also to all of those at the Yukon Geological Survey, in particular Tyler Ambrose and David Moynihan, for their help, support, and advice during my work up in Yukon. Sudip Shrestha and Mark Button are thanked for their assistance with microprobe and monazite analyses. Thanks also to Josh Davies, Morgann Perrot, and Corey Wall for the collection and processing of detrital zircon U-Pb and Hf-isotope data which I was unable to do myself during the pandemic. A big thank you also to Alex Rea and Raj Aulakh for their assistance during fieldwork in often unpredictable and trying Yukon conditions. I would also like to thank all those at SFU who provided help and support beyond my project. Thanks to Matt Plotnikoff and Elilan Ganesaths for all their technical and fieldwork assistance and to Lorena Munoz, Tarja Väisänen, and Alyssa Hamilton-Messenger for their help with everything administrative.

Finally, a massive thank you to all my family and friends. To all the new friendships I have made throughout my time and travels in Canada, you guys have really made this a truly special experience! To my friends back in the UK, thanks for your

continuous encouragement and always being around for a beer despite the eight-hour time difference! Thank you to my parents for your unwavering support and belief that I could actually pull this off, and instilling me with the confidence to make the move out to Canada in the first place. Lastly, to Sarah, thanks for your abiding love and inspiration, I couldn't have done this without you!

Table of Contents

Declaration of Committee	ii
Abstract.....	iii
Acknowledgements	iv
Table of Contents.....	vi
List of Tables.....	ix
List of Figures.....	x
List of Acronyms.....	xxi
Preface/Image.....	xxii
Chapter 1. Introduction to thesis.....	1
1.1. Thesis scope and geological context.....	1
1.2. Thesis objectives	6
1.3. Thesis structure and statement of contribution	7
1.4. References.....	8
Chapter 2. Geology of Southwest Yukon.....	13
2.1. Cordilleran-scale terrane groups.....	13
2.1.1. Intermontane terranes: the Yukon-Tanana terrane.....	13
2.1.2. Insular terranes: Alexander and Wrangellia.....	16
2.2. Terrane-intervening strata	17
2.2.1. Bear Creek assemblage.....	17
2.2.2. The Dezadeash Formation.....	18
2.2.3. Blanchard River assemblage.....	19
2.2.4. The Kluane Basin.....	21
2.3. References.....	30
Chapter 3. Tectono-metamorphic evolution of the Cretaceous Kluane Schist, Southwest Yukon	39
Abstract.....	39
3.1. Introduction.....	40
3.2. Geological Context	43
3.3. Methods	46
3.3.1. Analytical methods	46
3.4. Results	50
3.4.1. Petrology and field relationships across the Kluane Schist.....	50
3.4.2. Whole rock and mineral chemistry.....	64
3.4.3. Garnet-hosted fluid inclusion composition and graphite crystallinity	69
3.5. Metamorphic sequence and pressure-temperature conditions.....	72
3.5.1. Mineral reactions.....	72
3.5.2. Petrological modelling and quantified <i>P–T</i> conditions of metamorphism	80
3.6. Discussion.....	87
3.6.1. Comparison with previous studies.....	87

3.6.2.	Tectonic evolution of the Kluane Schist	90
3.6.3.	Tectonic significance of the Kluane Schist within Southwest Yukon	93
3.7.	Conclusions	94
3.8.	References	95

Chapter 4. A record of Late Cretaceous to early Paleogene Insular terrane accretion within the Northern Cordillera; insights from monazite petrochronology across the Kluane Schist, southwest Yukon 108

Abstract.....	108
4.1. Introduction.....	109
4.2. Geological setting	111
4.3. Methods	115
4.3.1. Analytical methods	115
4.4. Results	120
4.4.1. Petrology of Samples	120
4.4.2. Monazite microstructure and chemistry	123
4.4.3. Monazite petrochronology	126
4.4.4. Petrological modelling	131
4.5. Discussion	133
4.5.1. Linking monazite age and petrologic zone.....	133
4.5.2. The influence of the Ruby Range batholith.....	139
4.5.3. <i>P-T-t</i> evolution of the Kluane Schist	141
4.5.4. Implications for Insular terrane accretion	142
4.6. Conclusions.....	145
4.7. References.....	146

Chapter 5. Insights into the timing and style of Cretaceous Insular terrane accretion from detrital zircon geochronology across the Kluane Schist, southwest Yukon..... 159

Abstract.....	159
5.1. Introduction.....	160
5.2. Geological Setting	163
5.2.1. Intermontane terranes: the Yukon-Tanana terrane.....	163
5.2.2. Insular terranes: Alexander and Wrangellia terranes.....	166
5.2.3. Terrane-intervening strata: Jura-Cretaceous basins.....	167
5.3. Methods	172
5.3.1. Zircon Uranium-Lead (U-Pb) geochronology and Hafnium-isotope geochemistry by LA-MC-ICP-MS	172
5.3.2. Zircon U-Pb dating by Chemical Abrasion-Thermal Ionization Mass Spectrometry (CA-TIMS).....	176
5.3.3. Data Presentation and Statistical Tests	177
5.4. Results	179
5.4.1. Detrital zircon U-Pb geochronology and Hafnium-isotope geochemistry	179
5.4.2. CA-TIMS U-Pb geochronology	184

5.5.	Discussion	186
5.5.1.	Evidence for partial zircon recrystallization	186
5.5.2.	Provenance of the Kluane Schist	187
5.5.3.	Maximum depositional age (MDA) for the Kluane Schist	194
5.5.4.	Correlative rock packages within the North American Cordillera and geodynamic setting of the Kluane Schist	198
5.5.5.	Implications for Insular terrane accretion	202
5.6.	Conclusions	210
5.7.	Acknowledgements	210
5.8.	References	211
Chapter 6.	Conclusions	236
6.1.1.	Re-evaluating the metamorphic and deformational evolution of the Kluane Schist	237
6.1.2.	Constructing a <i>P-T-t-D</i> path for the Kluane Schist using <i>in-situ</i> monazite petrochronology	238
6.1.3.	Unravelling the timing and original geodynamic setting of Kluane Schist deposition	239
6.1.4.	Potential correlations between the Kluane Schist and other Jura-Cretaceous basins within the Northern Cordillera	240
6.2.	Summary of tectonic model and insight into the timing, style, and tectonic nature of Insular terrane accretion within the northern Cordillera	243
6.3.	Potential future research avenues	247
6.4.	References	250
Appendix A:	Supporting information for Chapter 3.	256
Appendix B:	Supporting information for Chapter 4.	262
Appendix C:	Supporting information for Chapter 5.	273
Appendix D:	Supplementary data file.	279
Appendix E:	Supplementary data file.	280
Appendix F:	Supplementary data file.	281
Appendix G:	Supplementary data file.	282
Appendix H:	Supplementary data file.	283
Appendix I:	Supplementary data file.	284
Appendix J:	Supplementary data file.	285
Appendix K:	Supplementary data file.	286

List of Tables

Table 3.1.	Summary of the <i>P-T</i> estimates completed across the Kluane Schist (see Fig. 3.2 for sample locations). Av <i>P</i> = average pressure estimate; GPMB = garnet–plagioclase–muscovite–biotite barometer estimate; GBAQ = garnet–biotite–Al–silicate–quartz barometer estimate; grt–bt = garnet–biotite thermometer estimate. “Not completed” indicates where obtaining at <i>P-T</i> estimate was not appropriate (see main text for detailed reasons why). 83
Table 4.1.	Summary of the relationship between monazite grain structure, trace element chemistry and age with structural level and metamorphic grade across the Kluane Schist. All ages presented are lower intercept ages (see Fig. 4.6) unless denoted * where a single ²³⁸ U/ ²⁰⁶ Pb age (²⁰⁷ Pb corrected) is presented. Individual domains are labelled with numbers and coloured for their relative Y content; dark greys refer to relative depletions in Y while lighter greys relative Y enrichments. 128

List of Figures

- Figure 1.1. The location of the study area within the terrane collage of the Northern Cordillera (modified from Colpron & Nelson, 2011). Other Jura-Cretaceous basinal assemblages that are also situated at the interface between the Insular and Intermontane terranes are highlighted and labelled. Note the terrane colours used in this map; these remain consistent throughout the remainder of the thesis.2
- Figure 1.2. Current models pertaining to Insular terrane accretion within the Northern Cordillera (modified after: Pavlis *et al.*, 2019; Sigloch & Mihalynuk, 2020); a-b) “Andean models” as described in the main text; a) Andean model variant with dual east-dipping subduction zones (e.g., Box *et al.*, 2019; Trop *et al.*, 2020; Waldien *et al.*, 2021b); b) Andean model variant envisaging Jura-Cretaceous basins as post-accretionary pull-apart depocenters and entrapped forearc assemblages (e.g., Gehrels & Saleeby 1987; McClelland *et al.* 1992; van der Heyden 1992; Monger *et al.*, 1994; Kapp & Gehrels, 1998; Gehrels *et al.*, 2009); c) “Archipelago models” as described in the main text with an extensive Jura-Cretaceous ocean that separates the paleo-North American margin from a west-dipping subduction zone along the inboard margin of the Insular terranes (Sigloch & Mihalynuk, 2013; 2017); d-e) Schematic cross-sections of A-A’ in (a) and B-B’ in (c), respectively.....3
- Figure 2.1. Focused map of the Kluane Schist and its surrounding geology, outlined by the red rectangle in Fig. 1.1 (modified from: Colpron, 2022). The location of samples and key geological features, as described in the text of Chapter 2, are indicated. Representative foliation measurements highlight the major, larger-scale structures preserved across the Kluane Schist. (“m” = mafic body; “c” = carbonate (see main text); KL = Killermun Lake; HJ = Haines Junction). 15
- Figure 2.2. a-b) Sample 20WM42; greenschist-facies, fractured mafic volcanic rocks typical of the Bear Creek assemblage; b) Sample 20WM42 with undeformed pillow structures; c) Sample 20WM41, low-grade argillites typical of the Dezadeash Formation; d) Thin section from locality 18WM13 showing a more mylonitic variety of the Dezadeash Formation found towards its contact with the Blanchard River assemblage; e) Hand sample from 20WM22, a well-foliated, biotite-rich paragneiss typical of the Blanchard River assemblage; f) Hand sample from 20WM23, an Al-rich paragneiss found within the Blanchard River assemblage; note the abundant aluminium-silicate minerals with evidence for coarse sillimanite laths after kyanite. (All sample localities in Fig. 2.1).20
- Figure 2.3. a) Sample 19WM70, greenschist-facies schist in the core of the Kluane Schist; b) Sample 19WM127, a medium-grade, biotite-rich outcrop revealing the dominant, NW-striking, NE-dipping fabric of the Kluane Schist; c) Sample 19WM123, a high-grade paragneiss commonly found within the northern and eastern regions of the Kluane Schist; d) Sample 19WM122, the structurally lowest variety of the Ruby Range batholith, found towards its contact with the Kluane Schist; e) Sample 19WM85; the most common variety of the Ruby Range batholith found within the study

	area, which likely represents its main phase; f) Thin section from locality 18WM08b showing the locally occurring, more alkali-rich variety of the Ruby Range batholith. (All sample localities in Fig. 2.1).26
Figure 2.4.	(<i>overleaf</i>): a-b) Thin sections of samples 18WM09d and 18WM09c respectively; these samples are characteristic of the foliated, carbonate-rich body found to the west of Killermun Lake (c & KL in Fig. 2.1); c) Outcrop view of the ultramafic body found at locality 19WM196 in Fig. 2.1; d-e) Typical appearance of the core and margin regions, respectively, of the ultramafic body found at locality 19WM196; f) Thin section of collected from locality 18WM04 (see Fig. 2.1) showing the mineralogy typical of the undeformed Eocene Hayden Lake suite.....28
Figure 3.1.	a) The location of the study area within the terrane collage of the Northern Canadian and Alaskan Cordillera (modified from Colpron & Nelson, 2011). The Jura-Cretaceous basinal assemblages that are situated between the Insular and Intermontane terranes, which includes the Kluane Schist, are highlighted and labelled. b) Map of the Kluane Basin, outlined by the red rectangle in (a). The distribution of the major lithologies within the Kluane Basin and their relationships to surrounding geological belts is shown (based on Mezger, 1997; Mezger <i>et al.</i> , 2001; Israel <i>et al.</i> , 2015; Vice <i>et al.</i> , 2020; this study).42
Figure 3.2.	Metamorphic assemblage map of northwest Kluane Basin (red rectangle in Figure 3.1b; map based on Israel <i>et al.</i> , 2011b; Colpron & Nelson, 2011; Israel <i>et al.</i> , 2015; this study) outlining the petrological zones defined in this study. Lithologies are the same colour as in Figure 3.1b except where indicated (i.e., “deformed Ruby Range batholith” & “carbonate”). Isograd locations are constrained by assemblage observations from this and previous studies (Mezger <i>et al.</i> , 2001). Petrological zones are highlighted by different shading patterns and indicated by circled numbers. Orange shading represents areas where leucosome is observed in Kluane Schist outcrops. Yellow shading highlights areas where prismatic sillimanite (labelled ‘sil’ on map and sil(p) in key) was observed. The location of young faults was inferred from aeromagnetic surveys (Israel <i>et al.</i> , 2011b). Red stars represent samples taken for XRF analysis and green stars show samples taken for detailed EPMA analysis. Blue numbers refer to analysed samples.45
Figure 3.3.	a) Cross section for lines A-A’ and B-B’ in Figure 3.2 highlighting the relationship between petrologic zone and structural level across the Kluane Schist. Field stations are labelled and highlighted by yellow triangles (In B-B’: v = 110; w = 109; x = 108; y = 106; z: 105/20-40). Average foliation measurements are indicated by short solid lines (Red = D ₁ , black = D ₂). Bracketed and italic sample numbers (e.g., 141) represent measurements and observations that are projected onto the line of section from nearby localities. Observed fabrics and fold geometries (D ₂) are projected into the subsurface. The sense-of-shear recorded by pegmatites (D ₃), where observed, is also indicated. Isograds are directly labelled and indicated by thick solid lines. Photos (b–i) document the typical structures and index minerals characteristic to each petrologic zone and are discussed in detail in the main text.53

- Figure 3.4. Box plot summarising the stability of different minerals with distinct deformation events and petrologic zones across the Kluane Schist. Solid lines show when each mineral is stable, dashed lines represent metastable mineral preservation. Ms = muscovite; cel = celadonite; ab = albite; a/o = andesine/oligoclase; Sillimanite (F) = fibrolitic sillimanite; Sillimanite (P) = prismatic sillimanite; grt(x) = garnet population x (see main text). Graphite stability refers to just that within the matrix, not porphyroblasts.53
- Figure 3.5. Outcrop photos and photomicrographs from zones 1 and 2. a) Muscovite-rich schist, typical of zone 1 towards the centre of the Kluane Schist (07b and 06 in Fig. 3.2). Centimetre-scale dark and light compositional bands (blue and green highlight) reflect original bedding (S₀). Insert shows muscovite–chlorite S₁ fabric overgrown by plagioclase porphyroblasts. b) Photomicrograph of zone 1 schist showing the relationship between fabrics and chlorite–muscovite–titanite assemblage. Note: inclusion trails in plagioclase (yellow dashed lines in insert) are oblique to matrix fabrics. c) Photomicrograph of a lower-grade sample within zone 2; the muscovite–chlorite S₁ fabric is overgrown by plagioclase and the muscovite-rich S_{2a} fabric. S_{2a} wraps zoisite and plagioclase. Calcite is observed as rare inclusions to zoisite. d) Photomicrograph of a higher-grade zone 2 sample. Biotite is associated with a second generation of muscovite ms(2), with both primarily occurring in S_{2a} orientations.55
- Figure 3.6. a) Outcrop photo of a zone 3 schist showing tight F_{2a} folds which are reclined and axial planar to a strong S_{2a} fabric. b) Photomicrograph of plagioclase typical of the lowest-grades units of zone 3. Ca-rich plagioclase cores include zoisite and calcite, overgrow S₁ and are wrapped by S_{2a}. c) Photomicrograph of garnet typical of the lowest-grades units of zone 3. Garnet is coarse, well-faceted and hosts inclusions of calcite, zoisite and S₁ aligned graphite and quartz. d) Photomicrograph of a higher-grade zone 3 schist. Coarse euhedral garnet hosts S₁ aligned inclusions and is partially wrapped by a strong biotite-rich S_{2a} which overprints the relic chlorite–graphite S₁. e) Photomicrograph of a lower-grade zone 5 sample, knotty andalusite poikiloblasts are intergrown with quartz and the S_{2b} fabric and host inclusions of muscovite, biotite and staurolite. Staurolite remains as the dominant porphyroblast within this sample. f) In higher grade zone 5 assemblages fibrolitic sillimanite is associated with biotite-rich fabrics. Note: plagioclase shows distinct tips which are elongate into S_{2b} fabric orientations and host inclusions of andalusite, fibrolitic sillimanite and inclusion-free garnet. Insert shows a relic andalusite porphyroblast wrapped by biotite-rich S_{2b} and replaced by muscovite.58
- Figure 3.7. a) Photomicrograph of sample 19WM245b (245b in Fig. 3.2) highlighting the occurrence of prismatic sillimanite within staurolite-free zone 5 assemblages. Sillimanite tracks the biotite-rich S_{2b} fabric and wraps inclusion-poor garnet. Oriented garnet inclusion trails are highlighted by yellow dashed lines. b) Photomicrograph showing the assemblage common to the lower-grade units of zone 6; cordierite occurs within, and aligned with, the biotite–muscovite–sillimanite S_{2b} fabric. Andalusite and staurolite occur as largely uncorroded porphyroblasts. c) Photomicrograph of a typical zone 6 assemblage. Cordierite replaces

- sillimanite and garnet and is entrained within the S_{2b} gneissic fabric. d) Outcrop photo of polymineralic leucosome lenses apparent within the lower grade regions of zone 7. The aligned lenses of leucosome appear to result from sinistral shearing and foliation collapse. e) Photomicrograph of paleosome domains within a zone 7 gneiss. K-feldspar, cordierite and muscovite overgrow a biotite-rich S_{2b} fabric. Note: two generations of cordierite; $crd_{(1)}$ is aligned with the S_{2b} fabric and hosts sillimanite inclusions while $crd_{(2)}$ overgrows S_{2b} and lacks sillimanite inclusions. f) Photomicrograph of the leucosome within zone 7. Retrograde muscovite overgrew these phases in random orientations. 62
- Figure 3.8. Later stage non-coaxial deformation (D_3) across the Kluane Schist. a) Asymmetric shear folds, F_3 . Red dashed lines highlight the form of F_3 and yellow dashed lines the axial traces with vergence towards the SSW. b) Coarse lensoidal quartz veins within a zone 6 outcrop that provide a top-to-the-SW sense of shear (also see Fig. 3.3a). 63
- Figure 3.9. a) AFM diagram showing the plotting positions of whole rock XRF analyses across the Kluane Schist (red stars, Fig. 3.2). b) Variation in whole rock $Mg/(Mg + Fe)$ (XMg) and $Ca/(Ca + Na)$ (XCa) with petrological zone. c-h) Mineral chemistry v. petrological zone across the Kluane Schist (green stars, Fig. 3.2); in (c and h) we compare mineral chemistry with the bulk composition (red squares) of proximal samples (see Fig. 3.2). In (c, e, f, g) we highlight distinct populations of biotite ($bt_{1/2}$), cordierite ($crd_{1/2}$) and muscovite ($ms_{1/2}$) which are outlined further in the main text. i) plagioclase zonation with petrological zone..... 66
- Figure 3.10. Garnet composition line profile. a) BSE image of a typical of a population (3) inclusion-free garnet mantling a population (2) cloudy core as described in the main text. Yellow spots outline location of probe analyses. b) Rim-to-rim profiles of end-member mole fractions of the garnet shown in (a); end-member mole fractions for a representative fine, inclusion-free garnet typical of zone 5 assemblages (see Fig. 3.6f) are also superimposed with dashed lines. (inc. free grt in pl = inclusion free garnet in plagioclase). 69
- Figure 3.11. a) Fluid and graphite inclusions within garnet from sample 19WM118. b) Images of example fluid inclusions with their Raman spectrum, highlighting carbonic liquid and vapor. Carbonic liquid (L_{CO_2}) occupies the highest proportion at ~80 vol.% with other aqueous liquid (L_{H_2O}) ~15 vol.% and the innermost vapor bubble (V) ~5 vol.%. Comparison between these inclusions highlights the consistency in these ratios we observed during analysis. c) Fluid inclusion isochoric model. Maximum pressure of ~3.7 kbar calculated using an estimated total bulk density of 0.8–0.85 g/cm³ and temperature of 550–600 °C. d) CO_2 – H_2O activity-composition relationships of Aranovich and Newton (1999) combined with our results from Raman spectroscopic analysis provide an estimation of $a_{H_2O} = 0.5$ 70
- Figure 3.12. a-d) AFM plots projected from quartz (qtz), muscovite (ms), albite (ab), anorthite (an), apatite (ap), ilmenite (ilm) and fluid (H_2O) highlighting the key phase relationships resulting in the development of petrological zones 3–6. The pink star represents the average bulk composition of the Kluane Schist (see Fig. 3.9a). Where mineral abbreviations have subscripts these

match the petrological zone from which the analysed mineral composition was recovered. In (a) grt(c) and grt(o) refer to the average garnet core and outer domain compositions from a representative zone 3 garnet respectively. 75

Figure 3.13. Phase diagrams calculated for an average Kluane Schist bulk composition over a select *P-T* area (450–650°C, 2.5–4.5 kbar) using ds5.5, the activity models described in the main text and a variety of *a*H₂O values. Zone 3 assemblages are highlighted in orange, zone 4 in green, zone 5 in blue and zone 6 in purple. A) *a*H₂O = 0.95, b) *a*H₂O = 0.85 c) *a*H₂O = 0.75, d) *a*H₂O = 0.65, e) *a*H₂O = 0.55. Across all diagrams we only observe the prediction of the zone 5 assemblage garnet–andalusite–biotite (+ quartz–plagioclase–ilmenite–H₂O; light blue) below *a*H₂O values of 0.65. f) A best-fit model accounting for observed natural assemblages across the Kluane Schist and their associated *P-T* estimates (see Table 3.1). Yellow dashed line shows range of temperatures returned from graphite crystallinity (see Fig. A1). 82

Figure 3.14. Phase diagram calculated for an average bulk composition of the Kluane Schist using ds5.5 and the activity models described in the main text. Below 500°C *a*H₂O = 0.5, from 500–590°C *a*H₂O = 0.55, from 590–630°C *a*H₂O = 0.95 and above 630°C *a*H₂O = 1 (see Figs. 3.11, 3.13 and main text for discussion). Above the wet solidus (thin red dashed line; red shaded fields) models are run with minimally saturated water contents determined at 4.0 and 2.0 kbar (see Fig. A5 and Chapter 3.3 “*Forward petrological modelling*”). Bold assemblages highlight those best representative of the petrological zones across the Kluane Schist; pink text highlights zone 1 (M₁) and zones 2-7 (M₂) are highlighted in green. Red text refers to a discrepancy between model prediction and thin section observation (additionally, see text on right); these are discussed further in main text. Conventional barometry estimates are outlined by light blue stars. *AvP* estimates are highlighted by green stars. Pink dashed lines refer to temperature estimates from the garnet-biotite thermometer (Holdaway, 2000). All these *P-T* estimates, along with their 1-sigma uncertainties, can be found in Table 3.1. Collectively our results suggest the petrological zones across the Kluane Schist are best represented as a set of nested, clockwise *P-T* loops where peak conditions define a metamorphic field gradient of ~200°C/kbar. 85

Figure 4.1. a) Terrane map of Yukon (after: Colpron & Nelson, 2011). Red box outlines location of the study area shown in b) (KB = Kluane Basin; D.R = Duke River Fault). b) Map showing the distribution of major lithologies within the Kluane Basin of southwest Yukon, other Jura-Cretaceous basins within this region of the Cordillera and their relationship to surrounding geological belts (modified from: Mezger *et al.*, 2001; Israel *et al.*, 2011b; Israel *et al.*, 2015). Within the study area the Intermontane terranes are primarily represented by the Yukon-Tanana terrane. Dashed box outlines approximate location of Figure 4.2. 112

Figure 4.2. Geologic map including petrological zones within the central region of the Kluane Schist (see also Chapter 3). This map represents the red dashed area outlined in Figure 4.1b. All lithologies are the same colour as Figure 4.1b unless indicated (dark pink = foliated variety of the Ruby Range

batholith; Blue = carbonate). Petrological zones are highlighted by different shading and fill patterns and labeled with circled numbers. The mineral assemblage characteristic of each zone is noted in the legend labeled "Petrological zones" (mineral abbreviations after Whitney & Evans, 2010). Field isograds within, and bounding, each petrological zone are shown by dashed lines and labelled with letters (a–l) that correspond to the phases used to define the isograds. Orange shading represents areas where leucosome is observed in Kluane Schist outcrops. Phase maps were made for samples highlighted by red stars, and green stars show the samples selected for monazite trace element analysis and U-Th-Pb petrochronology (full sample descriptions can be found within main text; sample numbers are represented in boxes)..... 114

Figure 4.3.

Advanced Mineral Identification and Characterization System (AMICS) scans highlighting key petrological relationships across the Kluane Schist; the colours used in all AMICS scans are keyed to their respective phases within the legend provided in (a). a) sample 19WM120 is typified by an assemblage containing aluminium silicate and staurolite. Both andalusite and fibrolitic sillimanite occur as rare anhedral phases; plagioclase and metastable staurolite define the dominant porphyroblasts. Insert shows a plain polarized (ppl) photomicrograph; staurolite appears subhedral and prismatic, whereas garnet is corroded and embayed, and fibrolitic sillimanite shows limited development within the biotite-rich fabric. b) Sample 19WM118 (zone 6). Cordierite is present within all zone 6 assemblages at the expense of both sillimanite and garnet (see insert). Also note the inclusion-rich cores and inclusion-free mantles (Grt(m)) typical of garnet within zones 5 & 6. c) Paleosome within sample 19WM240, a stromatic migmatite from the structural base of Zone 7. Coarse and equant cordierite is associated with fibrolitic sillimanite and andalusite (see insert). Inclusion free, peritectic cordierite (p. Crd) and K-feldspar (p.Kfs) overgrew the biotite-rich fabric (see cross-polarized photomicrograph in lower insert). d) schollen-style migmatite from the structural top of zone 7. Paleosome is like that of (c), with leucosome primarily consisting of plagioclase-quartz along with peritectic cordierite (p. Crd in insert). Muscovite and chlorite are considered retrograde phases. 123

Figure 4.4.

Cross section A-A' in Figure 4.2 (No vertical exaggeration). Metamorphic grade increases up structural level. Sample localities are highlighted by yellow triangles and average foliation measurements (S2) projected into the line of section are indicated by short solid lines. Isograds are directly labelled and indicated by thick solid lines. The observed growth and breakdown of distinct garnet populations is indicated by dashed green and blue lines respectively (see main text). Orange dashed line (+L) represents where melt domains were observed (see main text & Fig. 4.2). BSE images above the section show representative monazite with structural level and metamorphic grade. b) A schematic representation of the typical chemical zoning preserved by monazite with structural level and metamorphic grade across the Kluane Schist (see main text and Table 4.1). The average measured monazite [Y], [Sm], and [Gd] from all chemical domains and [Th] from domains 3 and 4 are indicated (see main text)..... 125

- Figure 4.5. Chemical maps of monazite from all analysed samples across the Kluane Schist. For all chemical maps lighter shades of grey represent domains with higher relative concentrations of Y and Th versus domains with darker shades of grey. a-b) Yttrium [Y] maps of grains 11, 14 & 10 from 19WM120 (zone 5); c-d) Yttrium [Y] maps of grains 17, 5 & 7 from 19WM118 (zone 6 base); e-f) Yttrium [Y] maps of grains 1 & 10 from 19WM116 (zone 6 middle); g-h) Yttrium [Y] maps of grains 4 & 3 from 18WM10b (zone 6 top); i) Yttrium [Y] map of grain 12 from 19WM123 (zone 7 base); j) Thorium [Th] map of grain 2 from 19WM123, k) Yttrium [Y] map of grain 2 from 19WM230 (zone 7 top) and l) Thorium [Th] map of grain 2 from 19WM230..... 127
- Figure 4.6. Terra-Wasserburg diagrams showing U-Pb isotope data from *in-situ* monazite analysis across the study area. Ellipses in all plots are provided at 2σ . Data are colour-coded for chemical domain (see main text). Regression lines are anchored on the initial $^{207}\text{Pb}/^{206}\text{Pb}$ ratio determined using the two-stage Pb evolution curve of Stacey & Kramers (1975) and the weighted mean age of all analyses (^{207}Pb corrected). The lower intercept age of each domain present within every sample is provided. The oldest and youngest single age ($^{235}\text{U}/^{206}\text{Pb}$) from each sample is highlighted by a solid ellipse. All ages were calculated, and diagrams created, using the IsoplotR software package (Vermeesch, 2018) for the open, free R platform. 130
- Figure 4.7. Pseudosections for samples 19WM120, 19WM118 and 19WM123, respectively. Coloured fields refer to assemblages characteristic of petrographic zones across the Kluane Schist; orange (zone 3), green (zone 4), light blue (zone 5a), dark blue (zone 5b), purple (zone 6), pink and red (zone 7, paleosome and leucosome, respectively; see Fig. 4.2). All samples are modelled with a varied $a\text{H}_2\text{O}$ as described in the text. Samples experiencing peak conditions below the solidus (19WM120, 19WM118) are modelled assuming H_2O -saturation, and as such phase fields above the H_2O -saturated solidus are left blank. Samples modelled above the solidus (19WM123) assume only the amount of H_2O required to minimally saturate the assemblage in the immediate sub-solidus at 4 kbar. Ti-in-biotite thermometer results are plotted directly on their associated pseudosection and align with the temperatures predicted for each assemblage by our model. Additional P-T estimates (denoted * and presented in Chapter 3) were obtained using the crystallinity of graphite inclusions to garnet, isochor modelling of fluid inclusions in garnet, conventional thermobarometry and the Thermocalc average pressure (AvP) software (see main text & Chapter 3). 133
- Figure 4.8. Summary of the relationships used for petrochronology within this study. Each phase relationship is associated with a relative enrichment or depletion in Yttrium [Y], based primarily on the stability of garnet (e.g., Foster *et al.*, 2002; Gibson *et al.*, 2004); this is reflected by the background colour assigned to each zone. These phase relationships and their effect on monazite growth are discussed in detail in the main text. b) Summary of the P-T conditions experienced by all samples across the Kluane Schist. Polygons refer to the stability field of assemblages characteristic of zones 3–7 (see Figs. 4.2 and 4.7) and are coloured for their inferred relative [Y] content that would be available for reacting

minerals such as monazite (see (a) and Fig. 4.7d). Inset monazite grain sketches highlight the progressive development of observed individual monazite domains along our inferred *P-T* path. c-d) Age distribution plots for (c) 19WM120 (zone 5; structurally low) and (d) 19WM123 (zone 7; structurally high) documenting our inferred domain distinction in terms of absolute [Y] and [Th] with age. In (d) red dashed lines divide analyses from distinct monazite domains 1b, 2, 3, and 4 that are present in sample 19WM123 (see main text and Table 4.1). Diagrams in (d) were generated using the ChrontouR package for the open R platform (Larson, 2020). 136

- Figure 4.9. Terrane map showing the Northern Cordillera of southwest Yukon and south-central Alaska. Jura-Cretaceous basins are overlain and coloured based on their preserved metamorphic histories (Davidson & McPhillips, 2007; Hults *et al.*, 2013; Vice *et al.*, 2020; Waldien *et al.*, 2021a, b; Lowey, 2021; this study). Dextral offset along the Denali fault is considered to have led to the separation of the Kluane Schist-Blanchard River-Dezadeash (DEZ) within southwest Yukon from basins within south-central Alaska, including the Clearwater metasediments (CWS) and Maclaren Schist (Waldien *et al.*, 2021b). The location of the Devil Creek rocks within the Kahiltna Basin of south-central Alaska is also shown (Davidson & McPhillips, 2007). Within this region of the Cordillera, all basins reported to have experienced an episode of high-temperature, low-pressure metamorphism, along with the documented age of this event, are highlighted. See main text for discussion. NMS = Nutzotin Mountains Sequence. 145
- Figure 5.1. Terrane map of the Northern Canadian Cordillera (modified from Colpron & Nelson, 2011), with the location of the study area highlighted in the red dashed box. Jura-Cretaceous basinal assemblages situated at the interface between the Insular and Intermontane terranes are highlighted in dark purple. 161
- Figure 5.2 a) Map of the Kluane Basin and its surrounding geology. Location of detrital zircon samples collected for analysis in this study are highlighted by green stars. The distribution of the major lithologies within the Kluane Basin and their relationships to surrounding geological belts is shown (based on Mezger, 1997; Mezger *et al.*, 2001; Israel *et al.*, 2015; Vice *et al.*, 2020; this study). (carb = carbonate). b) Schematic cross section drawn from southwest to northeast and roughly through the centre of the study area (line of section shown in (a); modified after: Israel *et al.*, 2011a). Our detrital zircon samples are projected along strike onto the line of section to highlight their relative structural position across the Kluane Schist. The major structures bounding and within the Kluane Schist are also shown (see also: Mezger *et al.*, 2001a, b; Israel *et al.*, 2011a, b; Israel & Kim, 2014; Israel *et al.*, 2015; Chapter 3). 166
- Figure 5.3. Stratigraphic chart showing the inferred provenance, depositional ages, lithological characteristics, and metamorphic-deformational constraints for the Jura-Cretaceous basins considered in this study (see also Fig. 5.1). See legend in lower right corner for explanation of symbols and colours. Red bold text indicates inferred basement unit (YT = Yukon-Tanana terrane). Time scale from Walker & Geissman (2022). (Data from: ESB = East Susitna Batholith; Waldien *et al.*, 2021b and references therein; RRB

= Ruby Range batholith; Israel *et al.*, 2011a; Kuskokwim Group: Miller *et al.*, 2007; Bradley *et al.*, 2009; Hults *et al.*, 2013; Koksetna River Sequence: Wallace *et al.*, 1989; Hults *et al.*, 2013; Tordrillo Mountains sequence: Bradley *et al.*, 2009; Wilson *et al.*, 2012; Hults *et al.*, 2013; Yenlo Hills: Hults *et al.*, 2013; Kahiltna Basin: Davidson & McPhillips, 2007; Box *et al.*, 2019; Clearwater metasediments and Maclaren Schist: Waldien *et al.*, 2021a, b; Nutzotin Mountains sequence: Berg *et al.*, 1972; Trop *et al.*, 2002; Manuszak *et al.*, 2007; Hults *et al.*, 2013; Fasulo *et al.*, 2020; Dezadeash Formation: Eisbacher, 1976; Lowey, 2000, 2011, 2019, 2021; Kluane Schist: Israel *et al.*, 2011a; Chapters 3 & 4; Blanchard River assemblage: Vice, 2017; Vice *et al.*, 2020; Gravina Basin: McClelland *et al.*, 1991; Gehrels *et al.*, 1992; Kapp & Gehrels, 1998; Yokelson *et al.*, 2015)..... 172

Figure 5.4. Representative cathodoluminescence (CL) images of detrital zircon grains from (a) 19WM230d, (b) 19WM229, (c) 20WM40, (d) 20WM26 & (e) 20WM25b. The location of the analysis pit and associated age with 2σ uncertainty is shown..... 174

Figure 5.5. Kernel density estimate (KDE) plots of the ages of zircon across the Kluane Schist. (a) 19WM230d, (b) 19WM229, (c) 20WM40, (d) 20WM26, (e) 20WM25b. KDE plots outlined by dashed lines represent plots considering all zircon analyses, whereas KDE plots with solid outlines represent just detrital analyses (see main text sections 5.5.1 and 5.5.2 for full explanation). (f) Cumulative probability function including just detrital grains from all samples. In all plots note change in x-axis at 500 Ma. Precambrian ages are represented by x5 the area of Phanerozoic ages. 181

Figure 5.6. $\epsilon\text{Hf}(t)$ versus age plot across the Kluane Schist; colours as in Figure 5.5. All $\epsilon\text{Hf}(t)$ values are shown with 2σ uncertainties. (a) All Kluane Schist samples combined. Note change in x-axis at 500 Ma. Plots (b-d) show only grains with ages <300 Ma from (b) the northeast Kluane Schist, (c) west Kluane Schist and (d) southeast Kluane Schist (see Fig. 5.2). CHUR = chondritic uniform reservoir. 183

Figure 5.7. The results of Chemical Abrasion-Thermal Ionization Mass Spectrometry (CA-TIMS) completed on a subset of the youngest zircon grains across the Kluane Schist. U-Pb concordia plots summarize both laser-ablation, multi-collector, inductively coupled plasma mass spectrometry (LA-MC-ICP-MS; “(LA)”) and CA-TIMS dates (bold; black outline around the ellipse) when completed on the same grain (2σ uncertainty) (note: ellipse labels also indicate the zircon number for that sample). (a) Samples 19WM230d, 20WM40 and 20WM25b and (b) 19WM229 and 20WM40. Insert grain examples present a direct comparison of the LA-MC-ICP-MS (LA) and CA-TIMS dates, with 2σ uncertainty, returned from each individual grain. CA-TIMS dates are commonly younger than, and in cases statistically separable from, the laser ablation dates from the same grains (see main text, section 5.5.1 for full explanation). 185

Figure 5.8. (a) Contoured $\epsilon\text{Hf}(t)$ data versus age for detrital zircon analyses (all grains < 500 Ma) across the Kluane Schist. Pink dashed line reflects 95th percentile contour. We overlay the age and $\epsilon\text{Hf}(t)$ values of potential Kluane Schist zircon sources (see main text, sections 5.2 and 5.5.2 for

full explanation and data sources). MF = Upper Matanuska Formation; mlK = mid-Late Cretaceous plutons in the southern Talkeetna Mountains; CPC = Coast Plutonic Complex (ca. 100–50 Ma); Yk(p) = Late Cretaceous plutons in Yukon including Casino suite, Prospector Mountain suite, Carmacks Group, Rancheria suite; WH = Whitehorse suite; D = Dawson Range Batholith; Cs = Chisana Formation; Tk = Talkeetna Arc; StE = St. Elias plutonic suite; LL = Long Lake; M = Minto; SR = Simpson Range suite; GL = Grass Lakes suite; YT(F) = Yukon-Tanana (Finlayson) (see also Fig. 5.9). Note where overlays have a hachure pattern $\epsilon\text{Hf}(t)$ values are calculated from whole rock $\epsilon\text{Nd}(t)$ values using the method of Vervoort *et al.*, (2011). Plot developed using the HafniumPlotter routine of Sundell *et al.*, (2019). CHUR = Chondritic Uniform Reservoir. (b) Kernel density estimate (KDE) plots showing all detrital zircon ages across the Kluane Schist (this study) in comparison to all Phanerozoic detrital zircon ages from the Maclaren Schist (Yellow, Waldien *et al.*, 2021a, b) and the Blanchard River assemblage (Blue, Vice, 2017)..... 190

Figure 5.9. Maps highlighting the location of potential sources of Kluane Schist zircon each side of the Denali fault (adapted from: Colpron *et al.*, 2016; Stevens Goddard *et al.*, 2018; Fasulo *et al.*, 2020; all ages reported are zircon U-Pb). Note the omission of ~75 km between panels (a) and (b). Underlying terrane maps are not labelled but coloured the same as in Fig. 5.1 (i.e., after: Colpron & Nelson, 2011). (a) Potential sources in south-central Alaska and (b) in Yukon(see also Fig. 5.6). In both maps Jura-Cretaceous basins are highlighted and patterned for their dominant provenance (see Fig. 5.3 and main text section 5.5.2 for explanation and references). DC = Devil Creek area of Davidson & McPhillips (2007). 192

Figure 5.10. Maximum depositional age (MDA) constraints across the Kluane Schist. (a) Kernel Density Estimate plots showing the distribution and amount of detrital and recrystallized (rc.) zircon within each of our Kluane samples. We compare these against established geological constraints within the Kluane Basin (Israel *et al.*, 2011a, b; Chapter 4). Combined, we used these KDE plots to determine the youngest graphical peak age (YPP; see main text, section 5.5.3 and Table H5). b) Comparison of the MDA estimates returned from YPP, YSP, YGC2s, YGC1s, and MLA methods and sample location across the Kluane Schist (see also Table H5). The timing of metamorphic monazite growth in the Kluane Schist is also indicated (see chapter 4). c) U/Th ratios of all detrital and recrystallized zircon with age across the Kluane Schist see also Table H7)..... 197

Figure 5.11. Comparison of potentially correlative Jura-Cretaceous rock packages within the Northern Cordillera (see Fig. 5.9). (a-b) Multidimensional scaling (MDS) plots of U-Pb age spectra from individual samples across the Kluane Schist (this study), Maclaren Schist (Waldien *et al.*, 2021a, b), Blanchard River assemblage (Vice, 2017), Clearwater metasediments (Waldien *et al.*, 2021a) and Dezadeash Formation (Lowey, 2019); (a) comparison of the Kluane Schist with the Blanchard River assemblage and Maclaren Schist, and (b) comparison of the Kluane Schist with the Dezadeash Formation and Clearwater metasediments. c) Pressure-age graph summarising equivalent depositional, metamorphic, and geochronological datasets extracted from continentally derived Jura-Cretaceous metasedimentary units within the Northern Cordillera (see

main text section 5.5.4 for full explanation). DC = Devil Creek rocks (see Fig. 5.9; Davidson & McPhillips, 2007); BR = Blanchard River assemblage (Vice, 2017; Vice *et al.*, 2020); KS = Kluane Schist (this study; Chapter 4); MS = Maclaren Schist (Davidson & McPhillips, 2007; Waldien *et al.*, 2021a, b). ESB = East Susitna Batholith (Nokleberg, 2015); RRB = Ruby Range batholith (Israel *et al.*, 2011a, b).200

Figure 5.12. Tectonic model accounting for the accretion of the Insular terranes to the paleo-western margin of North America, centered around the current location of the Alaska-Yukon border. Specific events defining the time periods outlined in the model (t1 to t5) are discussed in detail in the main text, section 5.5.5. Based on geologic evidence recovered from Jura-Cretaceous basinal assemblages we prefer a model involving a second east-dipping subduction zone below the paleo-western margin of North America during the latest Mesozoic (c.f., Hulst *et al.*, 2013; Box *et al.*, 2019; Trop *et al.*, 2020; Waldien *et al.*, 2021b). However, note that such a subduction zone is not a fundamental requirement for our model when considering the current uncertainties regarding the nature of the crust separating the Insular and Intermontane terranes during the Mesozoic (see main text, section 5.5.5 for discussion). (INS = Insular terranes; IMS = Intermontane terranes; SFZ = Shakwak fault zone; VCSZ = Valdez Creek Shear Zone).203

List of Acronyms

^{235}U	Isotopic notation (e.g., element Uranium with mass 235)
$a\text{H}_2\text{O}$	Water activity
AvP	Average pressure estimate (see Holland & Powell, 1994)
AX	Alexander terrane
BR	Blanchard River assemblage
DEZ	Dezadeash Formation
Dx	Deformation event x
Fx	Fold generation x
Ga	Giga-annum (billion-years-ago)
HJ	Haines Junction
HREE	Heavy Rare Earth Element
IMS	Intermontane terranes
INS	Insular terranes
kbar	Kilobar (pressure)
KS	Kluane Schist
Ma	Mega-annum (million-years-ago)
MREE	Middle Rare Earth Element
Mx	Metamorphic event x
Myr	Millions of years
<i>P-T-t-D</i>	Pressure-Temperature-time-Deformation
RRB	Ruby Range batholith
ST	Stikinia (terrane)
Sx	Fabric generation x
WR	Wrangellia terrane
<i>Xan</i>	Anorthite content (of plagioclase)



A view south across the central Kluane Plateau from the centre of the study area.



A view west across the Shawkak Trench and Kloo Lake from the centre of the study area.

Chapter 1. Introduction to thesis

1.1. Thesis scope and geological context

The Cordillera of western North America represents one of the archetypal accretionary orogens worldwide, being characterized by an amalgamation of distinct crustal blocks referred to as “terrane” (Fig 1.1; e.g., Coney *et al.*, 1980; Cawood *et al.*, 2009). These terranes are often grouped into larger entities which share similar tectonic and/or paleogeographic histories, with examples being the Insular terranes, which includes the Alexander, Wrangellia and Peninsular terranes, and the Intermontane terranes which include the Yukon-Tanana, Stikinia and Quesnellia terranes (Fig. 1.1; e.g., Monger *et al.*, 1982; Colpron & Nelson, 2011). To our current understanding, the progression of terrane accretion within the Canadian and Alaskan Cordillera (herein referred to as the Northern Cordillera) can be broadly subdivided into two events: (1) the initial accretion of the Intermontane terranes to the western Laurentian margin from ca. 200 to ca. 180 Ma and, (2) the subsequent accretion of the Insular terranes to the Intermontane terranes, possibly as early as ca. 174 Ma or as late as ca. 70 Ma (e.g., van der Heyden, 1992; Gehrels, 2001; Dickinson, 2004; Colpron *et al.*, 2007; Gehrels *et al.*, 2009; Beranek & Mortensen, 2011; Monger & Gibson, 2019). The tectonic response to these events is recorded across the width of the Cordillera with terrane accretion, crustal thickening, and the emergence of continental arcs flanked to the east by retroarc foreland basins and fold and thrust belts (e.g., Evenchick *et al.*, 2007). Together these events highlight the emergence of a dynamically linked, bivergent Mesozoic orogen (e.g., Monger and Gibson, 2019).

The progression of Insular terrane accretion remains contentious. Although it is considered to be generally diachronous along-strike of the Cordilleran margin (e.g., Monger, 2014), constraining the precise timing of this accretionary event at individual locations along the 2,000 km long Insular-Intermontane suture has been hampered by its extensive overprinting by multiple phases of mid-Cretaceous to Early Cenozoic deformation, magmatism, and metamorphism (Fig. 1.1; e.g., the Coast Plutonic Complex; Monger *et al.*, 1982; Rubin & Saleeby, 1991; van der Heyden, 1992). A potential window into the tectonic evolution of the Insular-Intermontane suture zone, however, exists within a series of presently segregated and variably metamorphosed Jurassic to Cretaceous (Jura-Cretaceous) sedimentary packages that collectively are considered to have been deposited in a seaway, or series of seaways, separating the Insular and Intermontane terranes (Figs. 1.1 & 1.2; e.g., van der Heyden, 1992;

McClelland *et al.*, 1992; Monger *et al.*, 1994; Hulst *et al.*, 2013; Anderson, 2015; Yokelson *et al.*, 2015; Box *et al.*, 2019; Waldien *et al.*, 2021a, b).

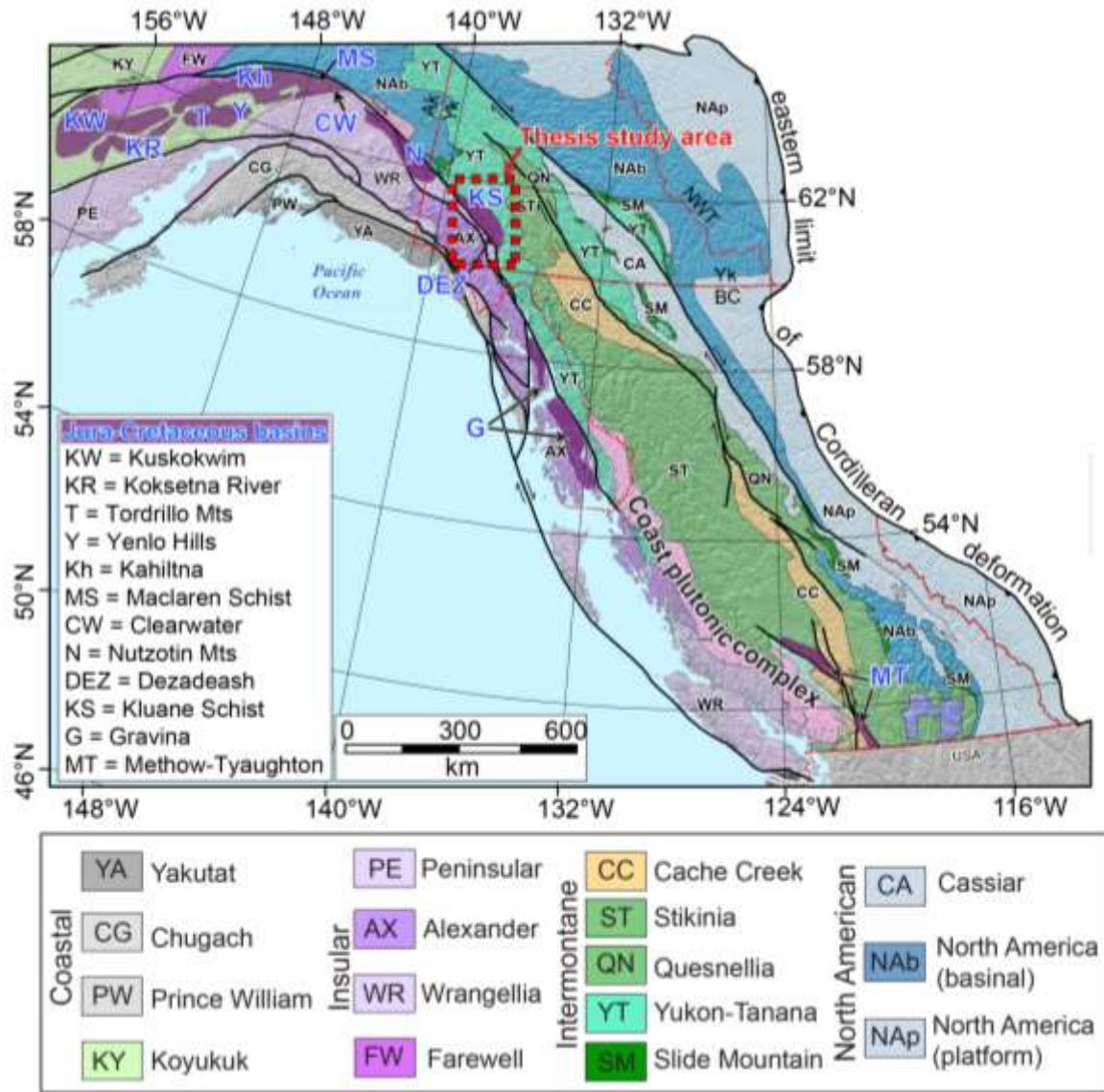


Figure 1.1. The location of the study area within the terrane collage of the Northern Cordillera (modified from Colpron & Nelson, 2011). Other Jura-Cretaceous basinal assemblages that are also situated at the interface between the Insular and Intermontane terranes are highlighted and labelled. Note the terrane colours used in this map; these remain consistent throughout the remainder of the thesis.

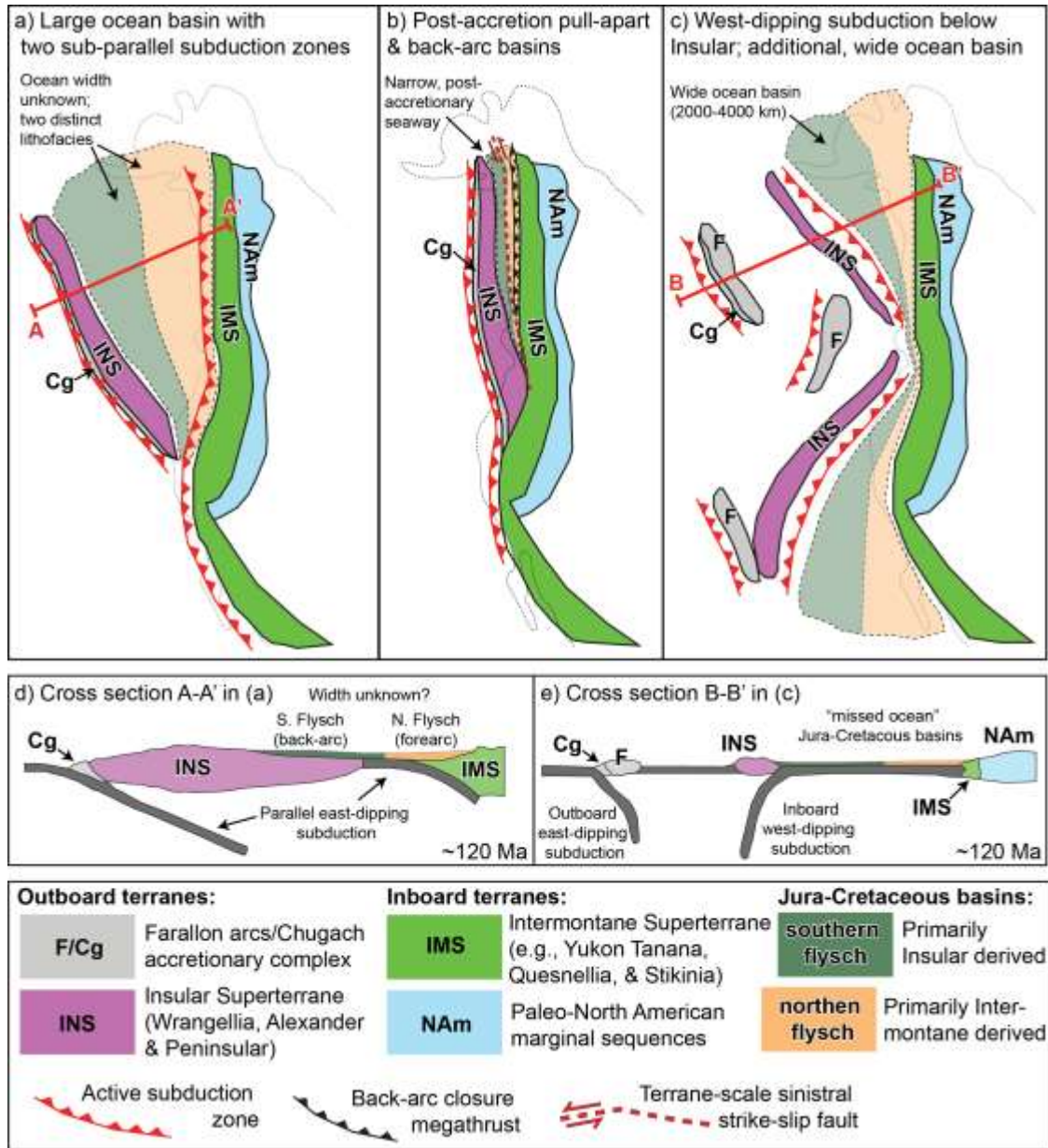


Figure 1.2. Current models pertaining to Insular terrane accretion within the Northern Cordillera (modified after: Pavlis *et al.*, 2019; Sigloch & Mihalynuk, 2020); a-b “Andean models” as described in the main text; a) Andean model variant with dual east-dipping subduction zones (e.g., Box *et al.*, 2019; Trop *et al.*, 2020; Waldien *et al.*, 2021b); b) Andean model variant envisaging Jura-Cretaceous basins as post-accretionary pull-apart depocenters and entrapped forearc assemblages (e.g., Gehrels & Saleeby 1987; McClelland *et al.* 1992; van der Heyden 1992; Monger *et al.*, 1994; Kapp & Gehrels, 1998; Gehrels *et al.*, 2009); c) “Archipelago models” as described in the main text with an extensive Jura-Cretaceous ocean that separates the paleo-North American margin from a west-dipping subduction zone along the inboard margin of the Insular terranes (Sigloch & Mihalynuk, 2013; 2017); d-e) Schematic cross-sections of A-A’ in (a) and B-B’ in (c), respectively.

Recent and past studies agree that these terrane-intervening basins hold vital information relating the timing and tectonic style of Insular terrane accretion within the Northern Cordillera; the collapse of these basins records both metamorphism and deformation associated with Insular terrane accretion while their original geodynamic setting provides insight into the pre-accretionary relationship between the paleo-western margin of North America and the Insular terranes during the Mesozoic (Monger *et al.*, 1982; van der Heyden, 1992; McClelland *et al.*, 1992; Hults *et al.*, 2013; Box *et al.*, 2019; Trop *et al.*, 2020). As such, understanding the development of these basins provides a key test for current models of Insular terrane accretion. However, with the datasets currently available, two principal and diametrically opposed sets of models have emerged that attempt to reconcile the origins and tectonic histories of these Jura-Cretaceous basins with respect to Insular terrane accretion:

- 1) The first set of models are collectively described as “Andean models”. These models envisage prolonged east-dipping subduction beneath the western margin of North America from the Middle Jurassic through to the mid-Late Cretaceous (Fig. 1.2a, b & d; e.g., van der Heyden 1992; McClelland *et al.*, 1992; Monger *et al.*, 1994; Hampton *et al.*, 2010; Hults *et al.*, 2013; Box *et al.*, 2019; Trop *et al.*, 2020). Jura-Cretaceous basin collapse marking the terminal collision of the Insular terranes with the western Cordilleran margin is considered to occur in response to their collective override by a westward migrating North American continent in an upper plate position (Fig. 1.2d; e.g., Monger & Gibson, 2019). Variations to this model include the presence of a second east-dipping subduction zone below the North American margin (Fig. 1.2a; e.g., Hampton *et al.*, 2010; Box *et al.*, 2019; Trop *et al.*, 2020) and the proposition that these younger Jura-Cretaceous basins may represent a series of narrow, post-accretionary pull-apart seaways, back-arc basins or forearc assemblages trapped by lateral arc duplication and strike-slip faulting at the interface between the *previously* accreted Intermontane and Insular terranes (Fig. 1.2b; e.g., Gehrels & Saleeby 1987; McClelland *et al.* 1992; van der Heyden 1992; Monger *et al.*, 1994; Kapp & Gehrels, 1998; Gehrels *et al.*, 2009).
- 2) The second set of models are called the “Archipelago models”. These models suggest the Jura-Cretaceous basins represent an additional, interconnected 2,000–4,000 km wide ocean that once existed between the North American continent and an outboard Insular “archipelago” (Fig. 1.2c & e). This extensive ocean basin is suggested to have closed

progressively from the latest Jurassic through earliest Eocene (ca. 155–50 Ma), driven by west-dipping subduction below the eastern (inboard) margin of the Insular terranes (Fig. 1.2e; Sigloch & Mihalynuk, 2013; 2017). In the Archipelago models, a prolonged, east-dipping subduction zone existed below the western (outboard) margin of the Farallon arcs from the Middle Jurassic. However, east-dipping subduction was absent along the western (outboard) margin of the Insular terranes until at least the latest Cretaceous (Fig. 1.2c & e; Sigloch & Mihalynuk, 2013; 2017).

The disparity in these models largely arises from the disconnect between the datasets and approaches each considers (e.g., Pavlis *et al.*, 2019); Andean models are founded on geological evidence currently preserved within surface exposures of the North American Cordillera, including the age and geochemistry of magmatic arcs, the structural and metamorphic evolution of accretionary complexes, and the occurrence of forearc and back-arc strata (Gehrels & Saleeby 1987; McClelland *et al.* 1992a; van der Heyden 1992; Monger *et al.*, 1994; Kapp & Gehrels, 1998; Gehrels *et al.*, 2009; Hults *et al.*, 2013; Box *et al.*, 2019; Pavlis *et al.*, 2019; Trop *et al.*, 2020), while archipelago models rely more heavily on updated tomographic imaging of the North American mantle, which highlights seismic anomalies that are considered to represent the remanence of the extensive ocean that closed by west-dipping subduction (Sigloch & Mihalynuk, 2013; 2017). The validity of each of these distinct datasets and their ability to accurately describe the style of Insular terrane accretion has been repeatedly questioned by workers within the Cordilleran community (e.g., Monger, 2014; Pavlis *et al.*, 2019; Sigloch & Mihalynuk, 2020; Lowey, 2023). As a result, two fundamental differences arise between either set of models: (1) the location, polarity and age of subduction involved with Insular terrane accretion and (2) the width and geometry of the oceanic basin that once separated the Insular and Intermontane terranes (Fig. 1.2).

The problem I address within this thesis deals with unravelling the original geodynamic setting and metamorphic evolution of the Cretaceous Kluane Schist, the main metasedimentary fill of the terrane intervening Kluane Basin within southwest Yukon (Fig. 1.1). My approach represents ground-truthing and direct testing of the models of Insular terrane accretion outlined above (c.f., Fig. 1.2). I completed geological and structural mapping over three summer seasons (2018-2020), assisted by the Yukon Geological Survey. The primary strategy for the first two seasons was to re-evaluate the tectono-metamorphic evolution of the Kluane Schist and determine its age of metamorphism, a topic which has seen much previous debate (e.g.,

Erdmer & Mortensen, 1993; Mezger *et al.*, 2001a, b; Israel *et al.*, 2011a; Stanley, 2012), while also integrating this with *in-situ* analysis of monazite to determine its pressure-temperature-time-deformation (*P-T-t-D*) evolution. The third field season (2020) was focused on unravelling the original tectonic environment of the Kluane Basin through the selective sampling for detrital zircon across the Kluane Schist. The geological, structural, and metamorphic mapping completed as part of field seasons one and two (2018-2019) provided the basis for the systematic sampling of detrital zircon across the full range of structural levels and metamorphic grades exposed throughout the current geographical extent of the Kluane Schist. The new U-Pb age and Hf-isotope datasets returned from these detrital zircon samples have a bearing on both the provenance and maximum depositional age of the Kluane Schist.

Together these three independent datasets (metamorphic-deformational, monazite petrochronology & detrital zircon) provide insight into the timing and style of deposition, metamorphism, and deformation of the Kluane Schist. Their integration forms the basis to derive a detailed model of Kluane Basin evolution from its initial deposition through metamorphism and inversion to final exhumation, providing a wealth of new information into the tectonic style and timing of Insular terrane accretion within the southwest Yukon region of the North American Cordillera. Comparison of these new datasets with those derived from other Jura-Cretaceous basins of the Northern Cordillera (e.g., Fig. 1.1; Box *et al.*, 2019; Waldien *et al.*, 2021b) provides additional insight into the geometry and width of the Jura-Cretaceous seaway that once separated the Insular and Intermontane terranes, laying out a coherent test for the Cordilleran-scale models currently used to describe Insular terrane accretion (Fig. 1.2).

1.2. Thesis objectives

- 1) Re-evaluation of the relationship between metamorphism and deformation across the Kluane Schist.
- 2) Characterize the *P-T-t-D* history of the Kluane Schist through integrating its metamorphic-deformational evolution with monazite petrochronology.
- 3) Determine the provenance and depositional age of the Kluane Schist protolith.

- 4) Develop a model of Kluane Schist evolution from initial deposition, through inversion and metamorphism to final exhumation.
- 5) Compare the evolution of the Kluane Basin with other Jura-Cretaceous basins of the Northern Cordillera and investigate potential basin correlations and build an 'along-strike' picture for Insular terrane accretion.

1.3. Thesis structure and statement of contribution

Three chapters of this thesis present new data in the form of journal articles that are currently either under review or are formatted for eventual publication. Each of these data chapters builds towards a common goal of providing clarity into the timing and style of Insular terrane accretion within the North American Cordillera, with particular focus on the Cretaceous Kluane Schist within southwest Yukon. As such, this presentation style naturally adds some redundancy and repetition to the introduction, geological context, and references section of each chapter. Further, it is emphasized that although individual chapters include multiple listed authors, the first listed author – Will McKenzie – conducted all fieldwork and sampling, the majority of data collection and processing and was solely responsible for all interpretations, chapter compositions, discussions, and figure drafting. Matthew Steele-MacInnis (University of Alberta) is acknowledged for the collection and processing of the garnet fluid inclusion data presented in Chapter 3. Kyle Larson (University of British Columbia, Okanogan) is acknowledged for the post-analysis processing of monazite U-Th-Pb age and trace element data presented in Chapter 4. Joshua Davis and Morgan Perrot (Université du Québec à Montréal) are acknowledged for the collection of detrital zircon U-Pb age data by both laser-ablation, multi-collector, inductively coupled plasma mass spectrometry (LA-MC-ICP-MS) and Chemical Abrasion-Thermal Ionization Mass Spectrometry (CA-TIMS), and Corey Wall (University of British Columbia, Vancouver) is acknowledged for the collection and initial processing of detrital zircon Hf-isotope data. Both detrital zircon datasets are presented in Chapter 5.

Complementing these three paper-based chapters, three additional chapters (Chapter 1, Introduction; Chapter 2, Geology of the southwest Yukon; Chapter 6, Conclusions) serve to

provide the overall context to the problem addressed by the thesis and outline the fundamental and coherent links between the stand-alone chapters presented.

1.4. References

- Anderson, T.H., 2015. Jurassic (170–150 Ma) basins: the tracks of a continental-scale fault, the Mexico-Alaska megashear, from the Gulf of Mexico to Alaska. *In*: Anderson, T.H., Didenko, A.N., Johnson, C.L., Khanchuk, A.I., MacDonald, J.H. (Eds.), Late Jurassic Margin of Laurasia – A Record of Faulting Accommodating Plate Rotation: Geological Society of America Special Paper 513, p. 107–188. [https://doi.org/10.1130/2015.2513\(03\)](https://doi.org/10.1130/2015.2513(03)).
- Beranek, L.P. and Mortensen, J.K., 2011. The timing and provenance record of the Late Permian Klondike orogeny in northwestern Canada and arc-continent collision along western North America. *Tectonics*, v.30, n.5. <https://doi.org/10.1029/2010TC002849>
- Box, S.E., Karl, S.M., Jones, J.V., Bradley, D.C., Haeussler, P.J. & O’Sullivan, P.B., (2019). Detrital zircon geochronology along a structural transect across the Kahiltna assemblage in the western Alaska Range: Implications for emplacement of the Alexander-Wrangellia-Peninsular terrane against North America. *Geosphere*, v.15, n.6, p.1774-1808. <https://doi.org/10.1130/GES02060.1>
- Cawood, Peter A., Kröner, Alfred, Collins, William J., Kusky, Timothy M., Mooney, Walter D., and Windley, Brian F. (2009) Accretionary orogens through Earth history. *In*: Cawood, P.A., and Kröner, A., (eds.) *Earth Accretionary Systems in Space and Time*. Geological Society, London, Special Publications 318. Geological Society, Bath, UK, p. 1-36. doi: 10.1144/SP318.1
- Colpron, M. and Nelson, J.L., (2011). *A Digital Atlas of terranes for the Northern Cordillera*; British Columbia Ministry of Energy and Mines, BCGS GeoFile 2011-11.
- Colpron, M., Nelson, J.L., & Murphy, D.C. (2007). Northern Cordilleran terranes and their interactions through time. *GSA Today*, v. 17, p. 4–10 <https://doi.org/10.1130/GSAT01704-5A.1>

- Coney, P., Jones, D. & Monger, J. Cordilleran suspect terranes. *Nature*, v.288, p.329–333 (1980). <https://doi.org/10.1038/288329a0>
- Dickinson, W.R., 2004. Evolution of the North American Cordillera. *Annual Review of Earth and Planetary Sciences* 32, pp.13-45.
<https://doi.org/10.1146/annurev.earth.32.101802.120257>
- Erdmer, P. & Mortensen, J.K., 1993. A 1200-km-long Eocene metamorphic-plutonic belt in the northwestern Cordillera: Evidence from southwest Yukon. *Geology*, v.21, n.11, p.1039-1042. [https://doi.org/10.1130/0091-7613\(1993\)021<1039:AKLEMP>2.3.CO;2](https://doi.org/10.1130/0091-7613(1993)021<1039:AKLEMP>2.3.CO;2)
- Evenchick, C.A., McMechan, M.E., McNicoll, V.J., and Carr, S.D., 2007, A synthesis of the Jurassic–Cretaceous tectonic evolution of the central and southeastern Canadian Cordillera: Exploring links across the orogeny, in Sears, J.W., Harms, T.A., and Evenchick, C.A., eds., *Whence the Mountains? Inquiries into the Evolution of Orogenic Systems: A Volume in Honor of Raymond A. Price: Geological Society of America Special Paper 433*, p. 117–145, [https://doi.org/10.1130/2007.2433\(06\)](https://doi.org/10.1130/2007.2433(06)).
- Gehrels, G., Rusmore, M., Woodsworth, G., Crawford, M., Andronicos, C., Hollister, L., Patchett, J., Ducea, M., Butler, R., Klepeis, K. & Davidson, C., (2009). U-Th-Pb geochronology of the Coast Mountains batholith in north-coastal British Columbia: Constraints on age and tectonic evolution. *Geological Society of America Bulletin*, v.121, n. 9-10, p.1341-1361. <https://doi.org/10.1130/B26404.1>
- Gehrels, G.E., 2001. Geology of the Chatham Sound region, southeast Alaska and coastal British Columbia. *Canadian Journal of Earth Sciences*, v.38, n.11, p.1579-1599.
<https://doi.org/10.1139/e01-040>
- Gehrels, G.E. and Saleeby, J.B., 1987. Geologic framework, tectonic evolution, and displacement history of the Alexander terrane. *Tectonics*, v.6, n.2, p.151-173.
<https://doi.org/10.1029/TC006i002p00151>
- Hampton, B.A., Ridgway, K.D., and Gehrels, G.E., 2010, A detrital record of Mesozoic island arc accretion and exhumation in the North American Cordillera: U-Pb geochronology of the Kahiltna basin, southern Alaska: *Tectonics*, v.29, TC4015,
<https://doi.org/10.1029/2009TC002544>

- Hults, C.P., Wilson, F.H., Donelick, R.A. and O'Sullivan, P.B., 2013. Two flysch belts having distinctly different provenance suggest no stratigraphic link between the Wrangellia composite terrane and the paleo-Alaskan margin. *Lithosphere*, v.5, n.6, p.575-594. doi: <https://doi.org/10.1130/L310.1>
- Israel, S., Murphy, D., Bennett, V., Mortensen, J. and Crowley, J., 2011. New insights into the geology and mineral potential of the Coast Belt in southwestern Yukon. In: *Yukon Exploration and Geology 2010*, MacFarlane, K.E., Weston, L.H., and Relf, C. (eds.), Yukon Geological Survey, p. 101-123.
- Kapp, P.A. and Gehrels, G.E., 1998. Detrital zircon constraints on the tectonic evolution of the Gravina belt, southeastern Alaska. *Canadian Journal of Earth Sciences*, v.35, n.3, p.253-268. <https://doi.org/10.1139/e97-114>
- Lowey, G.W., 2023. The good, the bad, and the ugly: Analysis of three arguments in the ongoing debate concerning the polarity of Mesozoic arcs along the western margin of North America. *Geological Society of America Bulletin*, v.135, n. 9-10, p.2591-2600. <https://doi.org/10.1130/B36706.1>
- McClelland, W.C., Gehrels, G.E. & Saleeby, J.B., (1992). Upper Jurassic-Lower Cretaceous basinal strata along the Cordilleran margin: Implications for the accretionary history of the Alexander-Wrangellia-Peninsular terrane. *Tectonics*, v.11, n.4, p.823-835. <https://doi.org/10.1029/92TC00241>
- Mezger, J.E., Chacko, T. & Erdmer, P., (2001b). Metamorphism at a late Mesozoic accretionary margin: a study from the Coast Belt of the North American Cordillera. *Journal of Metamorphic Geology*, v.19, n.2, p.121-137. <https://doi.org/10.1046/j.0263-4929.2000.00300.x>
- Mezger, J.E., Creaser, R.A., Erdmer, P. and Johnston, S.T., 2001a. A Cretaceous back-arc basin in the Coast Belt of the northern Canadian Cordillera: evidence from geochemical and neodymium isotope characteristics of the Kluane metamorphic assemblage, southwest Yukon. *Canadian Journal of Earth Sciences*, v.38, n.1, p.91-103. <https://doi.org/10.1139/e00-076>

- Monger, J.W. & Gibson, H.D., (2019). Mesozoic-Cenozoic deformation in the Canadian Cordillera: The record of a “Continental bulldozer”?. *Tectonophysics*, v.757, p.153-169.
<https://doi.org/10.1016/j.tecto.2018.12.023>
- Monger, J.W., (2014). Logan Medallist 1. Seeking the suture: The Coast-Cascade conundrum. *Geoscience Canada*, v.41, n.4, p.379-398.
<https://doi.org/10.12789/geocanj.2014.41.058>
- Monger, J.W.H., Price, R.A., & Tempelman-Kluit, D.J., (1982), Tectonic accretion and the origin of the two major metamorphic and tectonic welts in the Canadian Cordillera. *Geology*, v.10, n.2, p.70–75. [https://doi.org/10.1130/00917613\(1982\)10<70:TAATOO>2.0.CO](https://doi.org/10.1130/00917613(1982)10<70:TAATOO>2.0.CO)
- Monger, J.W.H., van der Heyden, P., Journeay, J.M., Evenchick, C.A. & Mahoney, J.B., (1994). Jurassic-Cretaceous basins along the Canadian Coast Belt: Their bearing on pre-mid-Cretaceous sinistral displacements. *Geology*, v.22, n.2, p.175-178.
[https://doi.org/10.1130/0091-7613\(1994\)022<0175:JCBATC>2.3.CO;2](https://doi.org/10.1130/0091-7613(1994)022<0175:JCBATC>2.3.CO;2)
- Pavlis, T.L., Amato, J.M., Trop, J.M., Ridgway, K.D., Roeske, S.M. and Gehrels, G.E., 2019. Subduction polarity in ancient arcs: A call to integrate geology and geophysics to decipher the Mesozoic tectonic history of the Northern Cordillera of North America. *GSA Today*, v.29, n.11, p.4-10. <https://doi.org/10.1130/GSATG402A.1>
- Rubin, C.M. and Saleeby, J.B., 1991. The Gravina Sequence: Remnants of a Mid-Mesozoic oceanic arc in southern southeast Alaska. *Journal of Geophysical Research: Solid Earth*, v.96, n.B9, p.14551-14568. <https://doi.org/10.1029/91JB00591>
- Sigloch, K. & Mihalynuk, M.G., (2013). Intra-oceanic subduction shaped the assembly of Cordilleran North America. *Nature*, v.496, n.7443, p.50-56.
<https://doi.org/10.1038/nature12019>
- Sigloch, K. & Mihalynuk, M.G., (2017). Mantle and geological evidence for a Late Jurassic–Cretaceous suture spanning North America. *Geological Society of America Bulletin*, v.129, n.11-12, p.1489-1520. <https://doi.org/10.1130/B31529.1>

- Sigloch, K. and Mihalynuk, M.G., 2020. Comment on GSA Today article by Pavlis et al., 2019: "Subduction polarity in ancient arcs: A call to integrate geology and geophysics to decipher the Mesozoic tectonic history of the northern Cordillera of North America". GSA Today, 30. DOI: 10.1130/GSATG431C.1
- Stanley, B., (2012). Structural geology and geochronology of the Kluane schist, southwestern Yukon Territory. UWSpace. <http://hdl.handle.net/10012/7096> (unpublished Master's thesis, University of Waterloo).
- Trop, J.M., Benowitz, J.A., Koeppe, D.Q., Sunderlin, D., Brueseke, M.E., Layer, P.W. and Fitzgerald, P.G., 2020. Stitch in the ditch: Nutzotin Mountains (Alaska) fluvial strata and a dike record ca. 117–114 Ma accretion of Wrangellia with western North America and initiation of the Totschunda fault. *Geosphere*, v.16, n.1, p.82-110. <https://doi.org/10.1130/GES02127.1>
- van der Heyden, P., 1992. A Middle Jurassic to early Tertiary Andean-Sierran arc model for the Coast belt of British Columbia. *Tectonics*, v.11, n.1, p.82-97. <https://doi.org/10.1029/91TC02183>
- Waldien, T.S., Roeske, S.M. & Benowitz, J.A., (2021b). Tectonic underplating and dismemberment of the Maclaren-Kluane schist records Late Cretaceous terrane accretion polarity and ~480 km of Post-52 Ma dextral displacement on the Denali fault. *Tectonics*, v.40, n.10, e2020TC006677. <https://doi.org/10.1029/2020TC006677>
- Waldien, T.S., Roeske, S.M., Benowitz, J.A., Twelker, E. & Miller, M.S., (2021a). Oligocene-Neogene lithospheric-scale reactivation of Mesozoic terrane accretionary structures in the Alaska Range suture zone, southern Alaska, USA. *Geological Society of America Bulletin*, v.133, n.3-4, p.691-716. <https://doi.org/10.1130/B35665.1>
- Yokelson, I., Gehrels, G.E., Pecha, M., Giesler, D., White, C. and McClelland, W.C., 2015. U-Pb and Hf isotope analysis of detrital zircons from Mesozoic strata of the Gravina belt, southeast Alaska. *Tectonics*, v.34, n.10, p.2052-2066. <https://doi.org/10.1002/2015TC003955>

Chapter 2. Geology of Southwest Yukon

The region considered in this thesis includes the parts of the Dezadeash, Ruby, and Kluane Ranges that surround Haines Junction and lie to the east of Kluane Lake, southwest Yukon (Fig. 2.1). This region represents the locus of exposure for the Triassic through Cretaceous assemblages that are found within the suture zone between the Insular and Intermontane terranes (Fig. 2.1). Exposed rocks include the Late Cretaceous Kluane Schist (Mezger *et al.*, 2001a, b; Israel *et al.*, 2011a, b), the Early Cretaceous Blanchard River assemblage (Vice, 2017; Vice *et al.*, 2020), the Late Jurassic to Early Cretaceous Dezadeash Formation (Lowey, 2007; 2011; 2019), and Late Triassic Bear Creek assemblage (Israel *et al.*, 2015). The Intermontane terranes bound these assemblages to northeast, namely the pericratonic Yukon-Tanana terrane which is primarily composed of pre-late Devonian continental margin deposits, back-arc rocks, and magmatic arcs, while to the southwest these assemblages are truncated by the Denali fault, separating them from rocks of the Insular terranes (Fig. 2.1; e.g., Colpron *et al.*, 2007; Israel *et al.*, 2011a, b). In southwest Yukon, exposure of the Insular terranes includes parts of both the Alexander and Wrangellia terranes, which are characterized by weakly metamorphosed volcanic and volcanoclastic deposits, Late Jurassic arc successions and plutons, Pennsylvanian–Permian batholiths, clastic marine rocks, and carbonate (Fig. 2.1; Colpron *et al.*, 2007; Israel *et al.*, 2014; Beranek *et al.*, 2014, 2017).

2.1. Cordilleran-scale terrane groups

2.1.1. Intermontane terranes: the Yukon-Tanana terrane

The Yukon-Tanana terrane underlies much of central and western Yukon (e.g., Mortensen, 1992). The Yukon-Tanana terrane is considered pericratonic with respect to the North American continent and preserves a long deformational history recording periods of rifting and re-accretion from the early Paleozoic through to Middle Jurassic (e.g., Monger *et al.*, 1982; Colpron *et al.*, 2007; Beranek & Mortensen, 2011; Nelson *et al.*, 2013). Within the area considered in this thesis the Yukon-Tanana terrane is thought to structurally overly all basinal assemblages, including the Kluane Schist, and is comprised of two main units; the Snowcap and Finlayson assemblages (Fig. 2.1; e.g., Israel *et al.*, 2011a).

The Snowcap assemblage forms the basement of much of the Yukon-Tanana terrane within the Northern Cordillera (e.g., Colpron *et al.*, 2006; Piercey & Colpron, 2009). It consists of quartzite, psammite, greenstone, marble, and calc-silicate rocks deposited on the distal western Laurentian margin prior to rifting of Yukon-Tanana terrane away from the continent during the mid-Paleozoic opening of the Slide Mountain Ocean (e.g., Gehrels *et al.*, 1992; Colpron *et al.*, 2006; Piercey & Colpron, 2009). The Devonian to Mississippian volcanic and sedimentary rocks of the Finlayson assemblage lie unconformably above the Snowcap assemblage and are typified by volcanic and sedimentary rocks with arc and back-arc affinity (Colpron *et al.*, 2006; Murphy *et al.*, 2009; Piercey & Colpron, 2009; Israel & Westberg, 2012).

Collectively the Snowcap and Finlayson assemblages, along with the western and northern parts of the Yukon-Tanana terrane, experienced greenschist to amphibolite facies metamorphism and penetrative deformation during the Late Triassic, Early-Middle Jurassic, and Early Cretaceous (e.g., Berman *et al.*, 2007; Staples *et al.*, 2016; Clark, 2017). Within these units, significant magmatic episodes are recorded across southwest Yukon during the Late Devonian–Mississippian (ca. 365–345 Ma; e.g., Grass Lakes and Simpson Range suites; e.g., Nelson *et al.*, 2006), the latest Permian to Early Triassic (ca. 265–250 Ma; e.g., Sulphur Creek suite; e.g., Nelson *et al.*, 2006), Late Triassic to Early Jurassic (ca. 205–175; e.g., Long Lake and Minto suites; Mortensen *et al.*, 1999; Joyce *et al.*, 2015; Colpron *et al.*, 2022), Early to mid-Cretaceous (ca. 115–100 Ma; e.g., Whitehorse suite; e.g., Hart *et al.*, 2006), Late Cretaceous (ca. 80–70 Ma; e.g., Prospector Mountain and Casino suites; Allan *et al.*, 2013; Mortensen *et al.*, 2016), and Paleocene to Early Eocene (ca. 64–57 Ma; e.g., Ruby Range batholith; Israel *et al.*, 2011a). Together these metamorphic and magmatic episodes are suggested to record the initial rifting of the Yukon-Tanana terrane away from the North American margin during the Carboniferous followed by its re-accretion to the North American margin during the Permo-Triassic and the subsequent development of an evolving, west-facing arc build upon the Yukon-Tanana terrane (e.g., Mortensen *et al.*, 1992; Beranek and Mortensen, 2011; Nelson *et al.*, 2013; Colpron *et al.*, 2022).

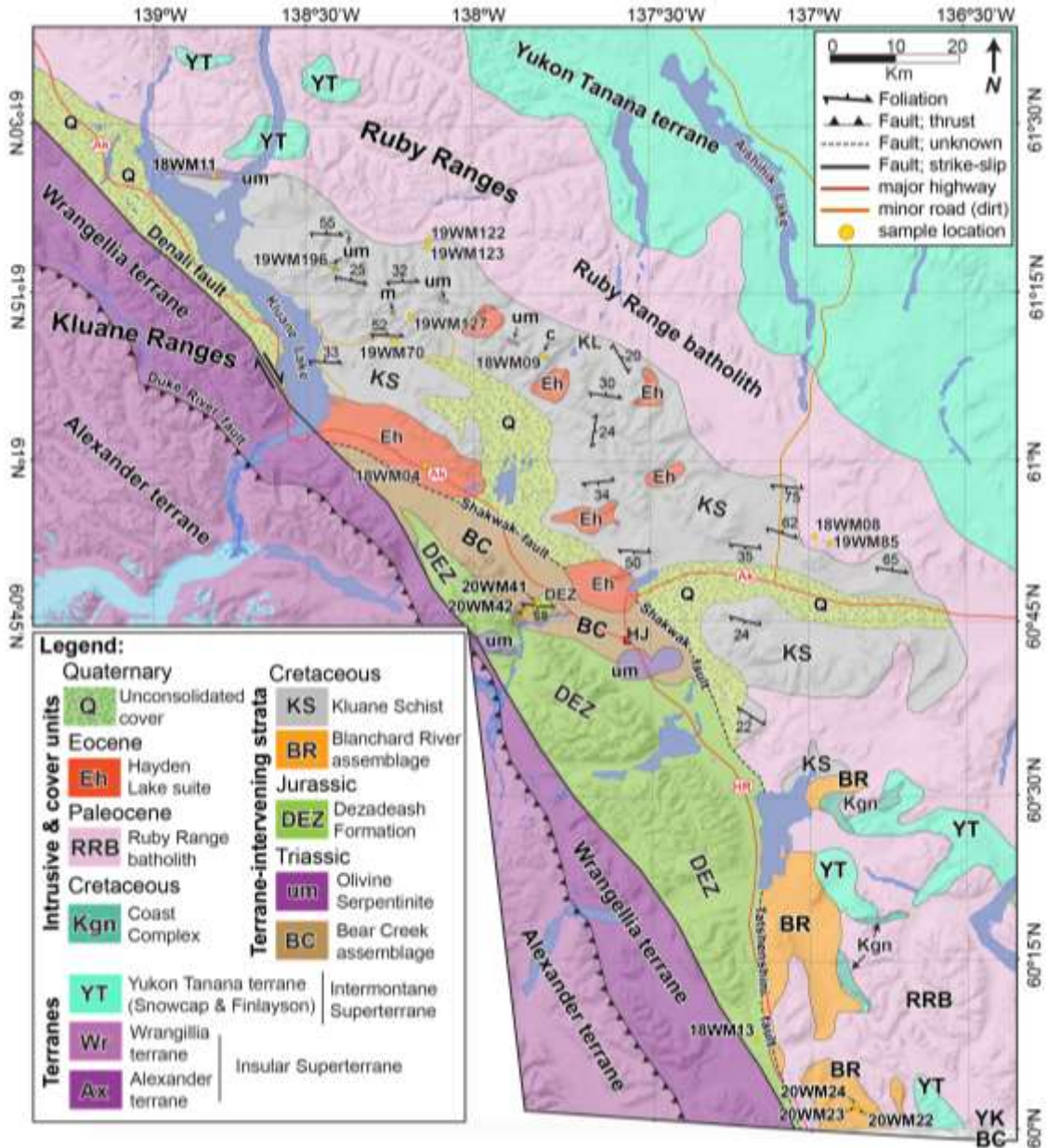


Figure 2.1. Focused map of the Kluane Schist and its surrounding geology, outlined by the red rectangle in Fig. 1.1 (modified from: Colpron, 2022). The location of samples and key geological features, as described in the text of Chapter 2, are indicated. Representative foliation measurements highlight the major, larger-scale structures preserved across the Kluane Schist. (“m” = mafic body; “c” = carbonate (see main text); KL = Killermun Lake; HJ = Haines Junction).

Progressive metamorphism and deformation migrated towards the foreland in the Yukon-Tanana terrane and is considered to record its continued burial as it was accreted to the North American continental margin via a propagating orogenic wedge (Staples *et al.*, 2016). A focused study of Snowcap assemblage rocks near Aishihik Lake, ~50 km northeast of the Kluane Schist (Fig. 2.1), highlights a three-phase deformational and metamorphic history peaking in the amphibolite facies from ca. 200–190 Ma (Clark, 2017). Biotite and muscovite cooling ages record exhumation to upper-crustal conditions by the Early Cretaceous (ca. 126 Ma; Clark, 2017). Within regions farther north of Aishihik Lake, this period of amphibolite facies metamorphism is dated to the Early Cretaceous (ca. 146–118 Ma; Staples *et al.*, 2013), with exhumation recorded during the late Early Cretaceous (ca. 112 Ma; Staples *et al.*, 2013). This progressive exhumation of Yukon-Tanana during the Early Cretaceous is similar with current estimates for the age of sedimentation of the Kluane Schist (ca. 94 Ma; Israel *et al.*, 2011a), providing the potential for an emerging source terrane during Jura-Cretaceous basin development.

2.1.2. Insular terranes: Alexander and Wrangellia

The Insular terranes are considered exotic within the Cordillera, with paleogeographic affinity to Baltican, Siberian and Caledonian realms (e.g., Colpron & Nelson, 2009). Faunal and provenance relationships track the initial transport of the Insular terranes into the paleo-Pacific around the northern margin of Laurentia during the mid-Paleozoic (e.g., Colpron & Nelson, 2009; Beranek *et al.*, 2013). Subsequent southward transport of the Insular terranes is then recorded from the Carboniferous after which they are considered to have evolved within an isolated intra-arc oceanic setting until the Early-Middle Jurassic (e.g., Gehrels *et al.*, 1996; Amato *et al.*, 2009; Colpron & Nelson, 2009, 2011; Nelson *et al.*, 2013).

Alexander and Wrangellia comprise the Insular terranes of southwest Yukon and are separated from the terrane-intervening strata by the Denali fault, a lithosphere-scale fault considered to accommodate ~480 km of dextral offset during the Cenozoic (Fig. 2.1; e.g., Waldien *et al.*, 2021b). As Alexander and Wrangellia likely shared magmatic and deformational histories from at least the Pennsylvanian (e.g., Beranek *et al.*, 2014) and potentially as early as the Late Devonian (Israel *et al.*, 2014), both Alexander and Wrangellia are considered as a

single tectonic entity within the subsequent chapters of this thesis (referred to as the Insular terranes).

The earliest evidence for Insular terrane accretion to the paleo-western margin of North America is observed as Early-Middle Jurassic cross-cutting plutons and overlap sequences within west central British Columbia and southeast Alaska (ca. 180–175 Ma; van der Heyden, 1992; Gehrels, 2001; Gehrels *et al.*, 2009). From this time the Insular terranes remained largely tectonically coupled with the more inboard terranes that made up the western margin of North America at that time, undergoing a diachronous accretion up until their terminal collision in the latest Mesozoic (e.g., van der Heyden, 1992; McClelland *et al.*, 1992; Nelson *et al.*, 2013; Colpron *et al.*, 2015; Sigloch & Mihalynuk, 2013, 2017; Monger, 2014; Box *et al.*, 2019; Trop *et al.*, 2020). Nevertheless, the dynamics and progression of this coupling process along with precise timing and tectonic driver(s) of terrane accretion remain heavily debated, with these forming key questions to be addressed within this thesis.

2.2. Terrane-intervening strata

2.2.1. Bear Creek assemblage

The oldest terrane-intervening unit within the immediate study area is the Late Triassic to Middle Jurassic Bear Creek assemblage (Figs. 2.1, 2.2a, b; ca. 204–162 Ma; Israel *et al.*, 2014; Vice, 2017). To the north the Bear Creek assemblage is separated from the Kluane Schist by the Shakwak fault, an inferred structural feature of unknown kinematics, (Fig. 2.1; e.g., Mezger, 1997; Colpron & Nelson, 2011; Israel *et al.*, 2015) and to the south it is unconformably overlain by the Dezadeash Formation (Fig. 2.1; Israel *et al.*, 2015). Outcrops of the Bear Creek assemblage were visited for one day during the summer of 2020 (20WM42 in Fig. 2.1). Observed outcrops consist of heavily fractured, greenschist facies mafic volcanic rocks with strong serpentinite alteration (Fig. 2.2a). In places, deformed pillow structures were also observed (Fig. 2.2b). Other lithologies within the Bear Creek assemblage not observed during my fieldwork include marine strata including siltstone, sandstone, and mudstone, along with andesitic to basaltic volcano-clastic tuff material (Israel *et al.*, 2015). The metasedimentary units of the Bear Creek produce a unimodal detrital zircon age of ca. 162 Ma (Vice, 2017) and are

considered to conformably overly the volcanic rocks described above, which return a U-Pb zircon age of ca. 204 Ma (Israel *et al.*, 2015).

Regional correlations for the Bear Creek assemblage within the Cordillera remain unclear (Israel *et al.*, 2015). Possible linkages to the Taku terrane of southeast Alaska have been suggested based on their similarities in lithology and structural position (Israel *et al.*, 2015). If correlative, this suggests that the Bear Creek assemblage, as with the Taku terrane, could represent a fragment of the oceanic floor which separated the Insular and Intermontane terranes prior to their accretion (e.g., Gehrels, 2002; Giesler *et al.*, 2016), and thus the basement onto which younger Jura-Cretaceous basinal sediments were deposited.

2.2.2. The Dezadeash Formation

Located to the south and west of Haines Junction, the Dezadeash Formation is separated from Kluane Schist by the Shawkak fault zone and rocks of the Bear Creek assemblage (Fig. 2.1; Israel *et al.*, 2015). Dezadeash outcrops were visited briefly during field seasons in 2018 (18WM13; Figs. 2.1 & 2.2d) and 2020 (20WM41; Figs. 2.1 & 2.2c), revealing a weakly metamorphosed package of fine, sub-greenschist facies argillite that preserves original sedimentary laying, graded bedding, and relic soft sediment deformation (Fig. 2.2c, d). Towards its faulted contact with the Blanchard River assemblage, the Dezadeash Formation can also appear mylonitic (Fig. 2.2d).

Within southwest Yukon, the Dezadeash Formation has been suggested to represent a submarine fan complex, comprising a ~3,000 m thick succession of mass-flow and turbidite deposits interbedded with local carbonate horizons and volcanoclastic rocks (e.g., Eisbacher, 1976; Lowey, 2007). Provenance analysis has indicated its deposition within either a collapsing back-arc basin sourcing from newly uplifted, outboard Insular terranes (McClelland *et al.*, 1992; Lowey, 2007, 2011) or a forearc basin situated on the Wrangellia composite terrane above a west-dipping subduction system (Lowey, 2019). However, possible ties to the inboard intermontane terranes have also been suggested (Mezger *et al.*, 2001a). A Jurassic to Early Cretaceous age for the Dezadeash Formation comes from both detrital zircon ages and fossils (Eisbacher, 1976; Lowey, 2019).

Early work suggested the Dezadeash Formation was a protolith for the higher grade Kluane Schist (Eisbacher, 1976); however, this interpretation has since been dismissed (Mezger *et al.*, 2001a, b; Lowey, 2007; Israel *et al.*, 2011a). Instead, the Dezadeash Formation is considered to have been dextrally offset by the Denali Fault, with correlative units to the southeast of the Denali Fault including the dark argillite, shale, and mass flow conglomerates that make up the Clearwater Mountains Sequence of southcentral Alaska (Fig. 1.1; Waldien *et al.*, 2021a, b), the Nutzotin Sequence along the Alaska-Yukon border (Fig. 1.1; Hults *et al.*, 2013; Box *et al.*, 2019), and parts of the Gravina Belt in southeastern Alaska (Fig 1.1; Kapp & Gehrels, 1998; Hults *et al.*, 2013; Yokelson *et al.*, 2015). Collectively these units are considered to represent a unique flysch belt within the Northern Cordillera, sourced from, and deposited upon, the outboard Insular terranes (Fig. 1.2; e.g., Berg *et al.*, 1972; Hults *et al.*, 2013).

2.2.3. Blanchard River assemblage

The Blanchard River assemblage represents a ~5–6 km thick metasedimentary package of amphibolite facies quartz-biotite schist and paragneiss (Bordet *et al.*, 2015; Vice, 2017; Vice *et al.*, 2020). Originally considered as the southern extension of either the Kluane Schist or Bear Creek assemblage (Fig. 2.1; e.g., Bordet *et al.*, 2015), the Blanchard River assemblage has been recently distinguished from both through detailed mapping, metamorphic analysis, detrital zircon geochronology, and provenance analysis (Vice, 2017; Vice *et al.*, 2020; this study). The Kluhini River thrust marks the upper, eastern boundary of the Blanchard River assemblage where it was overthrust by the Yukon-Tanana terrane. The western boundary is defined by the Tatshenshini shear zone, a southern continuation of the Shakwak fault, which separates the Blanchard River assemblage from rocks of the Dezadeash Formation (Fig. 2.1; Bordet *et al.*, 2015; Vice, 2017; Vice *et al.*, 2020).

The clastic marine protolith of the Blanchard River assemblage is comprised of turbidite sequences of sandstone, mudstone, and siltstone with local sedimentary features including primary bedding, graded bedding, and carbonate lenses (Bordet *et al.*, 2015; Vice, 2017). Provenance studies imply the Blanchard River assemblage was primarily sourced from the inboard Yukon-Tanana terrane; however, minor sourcing from parts of the outboard Insular terranes is also recorded (Vice, 2017). Combined with its Early Cretaceous depositional age (ca. 120–130 Ma; Vice, 2017), the presence of Insular derived zircon within the Blanchard River assemblage suggests proximity between the Insular and Intermontane terranes by this time.



Figure 2.2. a-b) Sample 20WM42; greenschist-facies, fractured mafic volcanic rocks typical of the Bear Creek assemblage; b) Sample 20WM42 with undeformed pillow structures; c) Sample 20WM41, low-grade argillites typical of the Dezadeash Formation; d) Thin section from locality 18WM13 showing a more mylonitic variety of the Dezadeash Formation found towards its contact with the Blanchard River assemblage; e) Hand sample from 20WM22, a well-foliated, biotite-rich paragneiss typical of the Blanchard River assemblage; f) Hand sample from 20WM23, an Al-rich paragneiss found within the Blanchard River assemblage; note the abundant aluminium-silicate minerals with evidence for coarse sillimanite laths after kyanite. (All sample localities in Fig. 2.1).

Typical outcrops of the Blanchard River assemblage are strongly deformed and metamorphosed. Outcrops to the south of Haines Peak were visited during the summer of 2020 (20WM22–24 in Fig. 2.1). Observed lithologies included a well-foliated, biotite-rich paragneiss which preserves an amphibolite facies assemblage consisting of biotite–quartz–plagioclase +/- garnet–kyanite/sillimanite (Fig. 2.2e; 20WM22), an Al-rich paragneiss that hosts abundant aluminium-silicate minerals with evidence for coarse sillimanite laths having replaced kyanite (Fig. 2.2f; 20WM23), and an undeformed leucocratic quartz-rich tonalite (20WM24). This later intrusive unit likely represents an offshoot or early phase of the Ruby Range batholith (e.g., Vice, 2017; Vice *et al.*, 2020). Other units associated with the Blanchard River assemblage that were not observed include a finer grained semi-pelitic paragneiss comprising quartz–biotite–garnet +/- staurolite–kyanite–cordierite–sillimanite and local, coarse grained gabbros that are considered Late Cretaceous in age (Bordet *et al.*, 2015; Vice, 2017; Vice *et al.*, 2020). A distinct, medium- to coarse-grained mylonitic orthogneiss of granodioritic composition occurs locally along the upper contact of the Blanchard River assemblage and interlayered with units of the overlying Yukon-Tanana terrane (“Kgn” in Fig. 2.1.; Bordet *et al.*, 2015; Vice *et al.*, 2020). This unit is often found intruded by granodiorites of the Ruby Range suite providing its inferred Late Cretaceous age, although it could be as old as Permian (Bordet *et al.*, 2015).

Detailed study of the tectono-metamorphic evolution of the Blanchard River assemblage suggests it experienced three distinct metamorphic events; an initial tectonic burial to kyanite-grade conditions (~6.5 kbar, ~650 °C; Vice *et al.*, 2020) from ca. 83–76 Ma, regional exhumation to ~3 kbar between ca. 70–68 Ma and finally a period of intense heating from ca. 63–61 Ma (Vice, 2017; Vice *et al.*, 2020). Collectively, these events are recorded by the overprinting of original higher pressure, kyanite–garnet +/- staurolite mineral assemblages by andalusite–cordierite–spinel (Vice, 2017; Vice *et al.*, 2020). The intense heating recorded between ca. 63–61 Ma, associated with the static recrystallization of cordierite and the growth of sillimanite, is only observed in proximity to the contact of the Paleocene to Eocene Ruby Range batholith where it intrudes the Blanchard River assemblage (e.g., Fig. 2.1; Vice *et al.*, 2020).

2.2.4. The Kluane Basin

The metasedimentary and igneous units that make up the Kluane Basin form the primary focus of this thesis (Fig. 2.1). Outcrop of the Kluane Basin represents the most extensive rock

package exposed within the Intermontane–Insular suture zone of southwest Yukon (Fig. 2.1). As such, the Kluane Basin has been the focus of several previous studies and mapping campaigns (e.g., Erdmer & Mortensen, 1993; Mezger, 1997; Mezger *et al.*, 2001a, b; Israel *et al.*, 2011a, b). However, its metamorphic, age, and structural relationships with surrounding units within southwest Yukon, as well as those farther afield within the Northern Cordillera remain poorly understood (e.g., Israel *et al.*, 2011a). This is particularly apparent when compared with the other Jura-Cretaceous basins within the region, which have all received recent attention and re-evaluation using modern techniques (see above; Blanchard River assemblage, Vice *et al.*, 2020; Dezadeash Formation, Lowey, 2019, 2021; Bear Creek assemblage; Israel *et al.*, 2015).

Current mapping indicates that the Kluane Basin has been thrust over both the Bear Creek assemblage and Dezadeash Formation to the southeast along the Shakwak fault; however, direct observation of this structural relationship is obscured by Quaternary deposits (Fig. 2.1; e.g., Mezger, 1997; Vice, 2017; Israel *et al.*, 2015). Similarly, direct ties between the Kluane Basin and the Insular terranes to the southwest are largely obscured by Cenozoic slip on the Denali fault (e.g., Waldien *et al.*, 2021b), while to the west the bounding structures of the Kluane Basin are concealed under Kluane Lake and Quaternary cover (Fig. 2.1; Israel *et al.*, 2011a, b). To its north and east the Kluane Schist is overlain by rocks of Yukon-Tanana terrane (Israel *et al.*, 2011a), although direct observation of this structural relationship is largely obscured due to its overprinting by the extensive Paleocene-Eocene Ruby Range batholith (Fig. 2.1; Israel *et al.*, 2011a, b).

Structural restorations and metamorphic evaluations have generally led previous workers to agree that the Kluane Schist developed on the upper plate of an east-dipping subduction system (e.g., Mezger, 1997; Mezger *et al.*, 2001; Israel *et al.*, 2011a). Limited geochronology has further suggested the basin remained open until at least the early Late Cretaceous (ca. 94 Ma; Israel *et al.*, 2011a) and was subsequently closed by mid-Late Cretaceous times (ca. 82–72 Ma; Mezger, 1997; Israel *et al.*, 2011a; Stanley, 2012). Nonetheless, there remains significant differences in interpretation regarding the timing of Kluane Basin development and its original geodynamic setting (e.g., Erdmer & Mortensen, 1993; Mezger *et al.*, 2001a, b; Israel *et al.*, 2011a; Canil *et al.*, 2015; Waldien *et al.*, 2021a, b). Early work based on the sedimentary geochemistry of the Kluane Schist, the major metasedimentary fill of the Kluane Basin (Fig. 2.1), suggested its deposition occurred within a back-arc basin correlative with the Dezadeash Formation between Late Jurassic to Early Cretaceous (Mezger *et al.*, 2001a). Whereas detrital

zircon geochronology across the Kluane Schist has indicated the Kluane Basin most likely represents part of a mid-Late Cretaceous forearc assemblage to an arc built on the Yukon-Tanana terrane, with potential correlation to the Maclaren Schist of south-central Alaska (Fig. 1.1; Israel *et al.*, 2011a; Canil *et al.*, 2015; Waldien *et al.*, 2021b).

The Kluane Schist

The main metasedimentary sequence of the Kluane Basin consists of a 160 km long, largely northwest-striking, northeast-dipping belt of graphitic mica-quartz schist and cordierite-bearing paragneiss (Fig. 2.1 and 2.3a-c; Mezger, 1997; Mezger *et al.*, 2001; Israel *et al.*, 2011a, b). Collectively this rock package has been referred to as the Kluane Schist (Tempelman-Kluit, 1974; Eisbacher, 1976; Israel *et al.*, 2011a, b) or the Kluane Metamorphic assemblage (Mezger, 1997; Mezger *et al.*, 2001b). Within this thesis the term Kluane Schist is used to describe both the schistose and paragneiss units exposed within the Kluane Basin (e.g., Fig. 2.3a-c).

The Kluane Schist preserves mineral assemblages ranging from the lower greenschist-facies to the upper amphibolite-/granulite-facies transition (Fig. 2.3a-c; Erdmer & Mortensen, 1993; Mezger, 1997; Mezger *et al.*, 2001b; Israel *et al.*, 2011a). Metamorphic grade shows a general increase from the core of the Kluane Schist, where it is characterized by a graphitic muscovite-chlorite schist (Fig. 2.3a), towards its northern and eastern edges where the Kluane Schist becomes increasingly gneissic and locally migmatitic, preserving centimeter-scale banding defined by darker layers of biotite-cordierite and lighter layers of quartz-feldspar (Fig. 2.3a-c; Mezger, 1997; Mezger *et al.*, 2001b; Israel *et al.*, 2011a). Previous work has documented a complex metamorphic history preserved by the Kluane Schist which includes both regional and contact events (e.g., Erdmer & Mortensen, 1993; Mezger *et al.*, 2001b; Israel *et al.*, 2011a). However, the temporal and spatial extent of these distinct metamorphic events, their relationship to deformation, and the geological processes responsible for their development remain debated (Erdmer & Mortensen, 1993; Mezger *et al.*, 2001b; Israel *et al.*, 2011a; Stanley, 2012).

The age of the Kluane Schist is also poorly constrained. An early Late Cretaceous (ca. 94 Ma) age of Kluane Schist protolith deposition is based on laser ablation inductively coupled plasma mass spectrometry (LA-ICP-MS) U-Pb analysis of two detrital zircon samples (Israel *et al.*, 2011a). Metamorphic ages for the Kluane Schist were determined by analysing rim domains within the same detrital zircon suite, and indicate it experienced at least two metamorphic events at ca. 82 and ca. 70 Ma (Israel *et al.*, 2011a; Stanley, 2012). Zircon dated from a single dyke which crosscuts Kluane Schist foliation constrain major fabric development prior to 71.8–

68.4 Ma (Mezger *et al.*, 2001b; Israel *et al.*, 2011a). Notably, monazite within the same dyke provides a significantly younger age of ca. 55.6 Ma (Israel *et al.*, 2011a). U-Pb isotope dilution-thermal ionization mass spectrometry (ID-TIMS) analyses on monazite and xenotime separates recovered from multiple samples across the Kluane Schist indicate a younger peak metamorphic age of ca. 58–56 Ma (Mortensen & Erdmer, 1992; Erdmer & Mortensen, 1993). Coincidence between those dates and the age of the Ruby Range batholith (ca. 64–57 Ma; Erdmer & Mortensen, 1993; Israel *et al.*, 2011a) have led to suggestion that they may reflect a widespread recrystallisation event related to its intrusion (Mezger, 1997). ^{40}Ar - ^{39}Ar mica dates are inferred to reflect cooling during the final exhumation and uplift of the Kluane Schist between ca. 55–40 Ma (Mortensen & Erdmer, 1992; Mezger, 1997).

Ruby Range batholith

The Ruby Range batholith is a composite pluton that ranges in age from Paleocene to early Eocene (ca. 64–57 Ma; Israel *et al.*, 2011a). Primary exposures of the Ruby Range batholith occur to the north and east of the Kluane Schist where it intrudes across its upper contact with the Yukon-Tanana terrane (Fig. 2.1; Israel *et al.*, 2011a, b). The observed outcrops of the batholith exhibit a range in composition between diorite and granite (Fig. 2.3d, e, f; Israel *et al.*, 2011a, b). Basal exposures of the batholith reveal strongly foliated diorite that typically grades upward into less strongly deformed tonalite (Fig. 2.3d). This foliated texture largely parallels that of the underlying Kluane Schist (2.3c *versus* 2.3d; see also Fig. 2.1 for sample locations). Up-section the Ruby Range batholith generally becomes more felsic, with its most voluminous portion comprising a medium-grained and equigranular quartz–plagioclase–biotite–K-feldspar +/- hornblende granodiorite littered with Kluane Schist xenoliths and mafic enclaves (Fig. 2.3e; Israel *et al.*, 2011a, b). Locally, the batholith can have a more alkali-rich composition, with a medium- to coarse-grained, porphyritic light orange quartz–K-spar–plagioclase–biotite +/- hornblende granite occurring locally throughout the main granodioritic phase of the Ruby Range batholith (Fig. 2.3f). In thin section, phenocrysts of simply twinned orthoclase occur within a groundmass of quartz and plagioclase with rare biotite and hornblende showing limited undulous extinction and irregular grain boundaries (Fig. 2.3f). Where observed, this more alkali-rich phase of the Ruby Range batholith is undeformed and typically shows a sharp, intrusive-like contact with the surrounding alkali-poor phases of the batholith. The uppermost sections of the Ruby Range batholith are reported to be in contact with the overlying Yukon-Tanana terrane (e.g., Fig. 2.1; Israel *et al.*, 2011b), but were not observed during the fieldwork completed as part of this thesis. These uppermost sections are characterized by massive quartz-feldspar

porphyry (Israel *et al.*, 2011a, b). The general coincidence between the crystallisation age of the Ruby Range batholith and syn-deformational metamorphism of the Kluane Schist (e.g., Israel *et al.*, 2011a), along with its sill-like orientation and foliated basal portions suggests the emplacement of the Ruby Range batholith, at least in its earliest phase, was likely syn-tectonic (e.g., Erdmer & Mortensen, 1993; Israel *et al.*, 2011a).

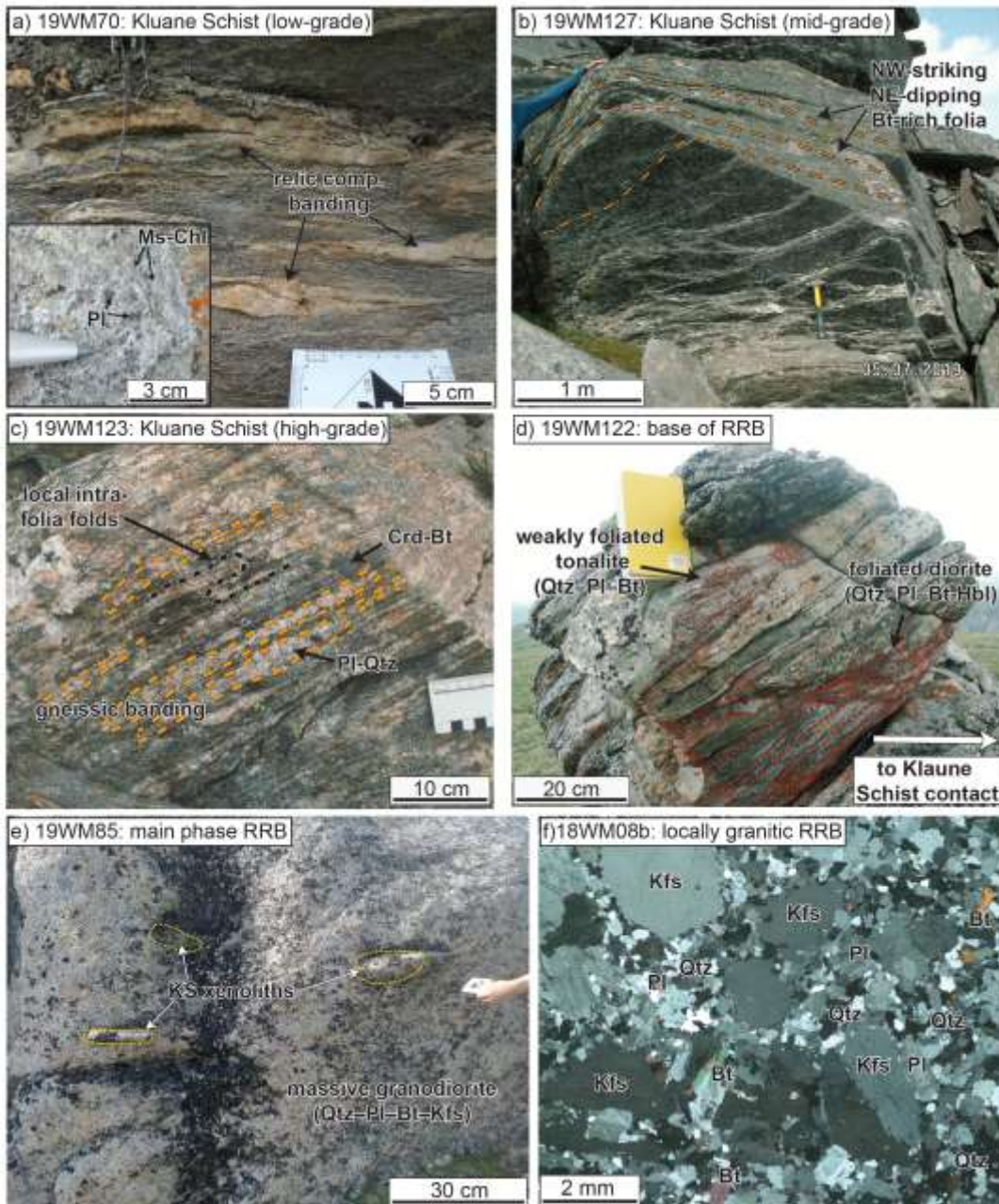


Figure 2.3. a) Sample 19WM70, greenschist-facies schist in the core of the Kluane Schist; b) Sample 19WM127, a medium-grade, biotite-rich outcrop revealing the dominant, NW-striking, NE-dipping fabric of the Kluane Schist; c) Sample 19WM123, a high-grade paragneiss commonly found within the northern and eastern regions of the Kluane Schist; d) Sample 19WM122, the structurally lowest variety of the Ruby Range batholith, found towards its contact with the Kluane Schist; e) Sample 19WM85; the most common variety of the Ruby Range batholith found within the study area, which likely represents its main phase; f) Thin section from locality 18WM08b showing the locally occurring, more alkali-rich variety of the Ruby Range batholith. (All sample localities in Fig. 2.1).

Previous work has speculated about an additional, Late Cretaceous phase to the Ruby Range batholith (Mezger, 1997; Israel *et al.*, 2011a; Stanley, 2012). Four zircon grains recovered from two, cm-scale mafic dykes that crosscut the main foliation of the Kluane Schist provide dates between ca. 77–68 Ma (Mezger, 1997; Israel *et al.*, 2011a; Stanley, 2012). These dykes also host two Late Triassic zircon (ca. 220 Ma) which are interpreted as inherited (Stanley, 2012), and two monazite grains which produce a weighted mean age of ca. 56 Ma (Israel *et al.*, 2011a). The dated Late Cretaceous zircon lack the pristine, euhedral form typical of igneous zircon and show lower Th/U ratios than expected for zircon of igneous origin (<0.5; Hoskin & Black, 2000; Stanley, 2012). This, along with a lack of any Late Cretaceous zircon within more voluminous exposures of the Ruby Range batholith (e.g., Israel *et al.*, 2011a), suggests these Late Cretaceous zircon are most likely inherited from the Kluane Schist. As such, within this thesis the age of the Ruby Range batholith considered to be best constrained to between ca. 64–57 Ma (Israel *et al.*, 2011a).

Carbonate enclaves

A ~150 x 300 m body of light brown to dark green, fine-grained, actinolite–tremolite schist and impure marble interbedded with local mafic and felsic volcanics occurs to the west of Killermun Lake (“18WM09” in Fig. 2.1 & 2.4a, b). A detailed provenance analysis on this outcrop has also not been completed. Due to its similar metamorphic grade and parallel foliation compared with the surrounding Kluane Schist (Fig. 2.4a) it is likely this unit represents a fragment that was incorporated during the deposition of the Kluane Schist protolith. The lack of a clear fault along the contact supports this interpretation. Stanley (2012) noted similarity between this outcrop and the units comprising the overlying Snowcap assemblage of the Yukon-Tanana terrane. It is therefore likely this carbonate-rich enclave represents an olistolith

with affinity to the paleo-western margin of North America (i.e., Yukon-Tanana terrane) that was incorporated with the Kluane Schist protolith during its deposition.

Ultramafic and mafic bodies

Ultramafic bodies are found scattered throughout the Kluane Schist (“um” in Fig. 2.1). These bodies are typically 10’s m to 10 km in scale and show high aspect ratios (Fig. 2.4c). The largest observed occurs at Doghead Point and measures ~15 km in length and ~1km in width (“18WM11” in Fig. 2.1; Mezger, 2000; Canil *et al.*, 2015). These ultramafic bodies appear to be directly interleaved along-strike with the metasediments of the Kluane Schist (e.g., Fig. 2.4c; Mezger, 2000). No contact metamorphism is evident within the surrounding metasediments (Fig. 2.4e). In general, these ultramafic bodies are emerald green to cream coloured and comprise deformed and foliated talc–antigorite–olivine and chlorite–amphibole schists which show fabric development parallel to the Kluane Schist (Fig. 2.4 c-e; Mezger, 2000; Canil *et al.*, 2015). Larger ultramafic bodies can also show distinct core domains which contain metre-scale boulders of massive, largely undeformed, and blocky olivine-rich serpentinite (2.4d; Mezger, 2000). These boulders are typically brecciated with evidence for brittle deformation and slickenlines (2.4d).

Previous studies agree that these ultramafic bodies likely represent syn-depositional olistoliths that were introduced into the Kluane Schist prior to its metamorphism and deformation (Mezger, 2000; Canil *et al.*, 2015). However, the specific origin of these ultramafic bodies is contentious. Their whole-rock geochemical and geochronological characteristics are suggested to tie them to deeper seated ultramafic intrusive bodies currently exposed within arcs of northern Stikinia (Canil *et al.*, 2015). This interpretation infers these deeper-seated bodies were exhumed along crustal-scale faults in the Late Triassic to Jurassic prior to their deposition within the Cretaceous Kluane Schist (Canil *et al.*, 2015). Alternately, oxygen isotope analysis suggests these ultramafic bodies are comparable to ophiolite fragments (Mezger, 2000). As such, Mezger suggests these ultramafic bodies represent fragments of oceanic crust that were subsequently sheared off and interleaved with the Kluane Schist metasediments during basin collapse (Mezger, 2000).

Within the central Kluane Plateau an outcrop of light green to beige porphyritic gabbro shows coarse 5-10 mm clots of milky white plagioclase and abundant cross-cutting clots and veins of radiating, acicular actinolite 20-30 mm in length (“m” in Fig. 2.1). This mafic outcrop lacks significant serpentinization and fabric development. Contact of this body with the

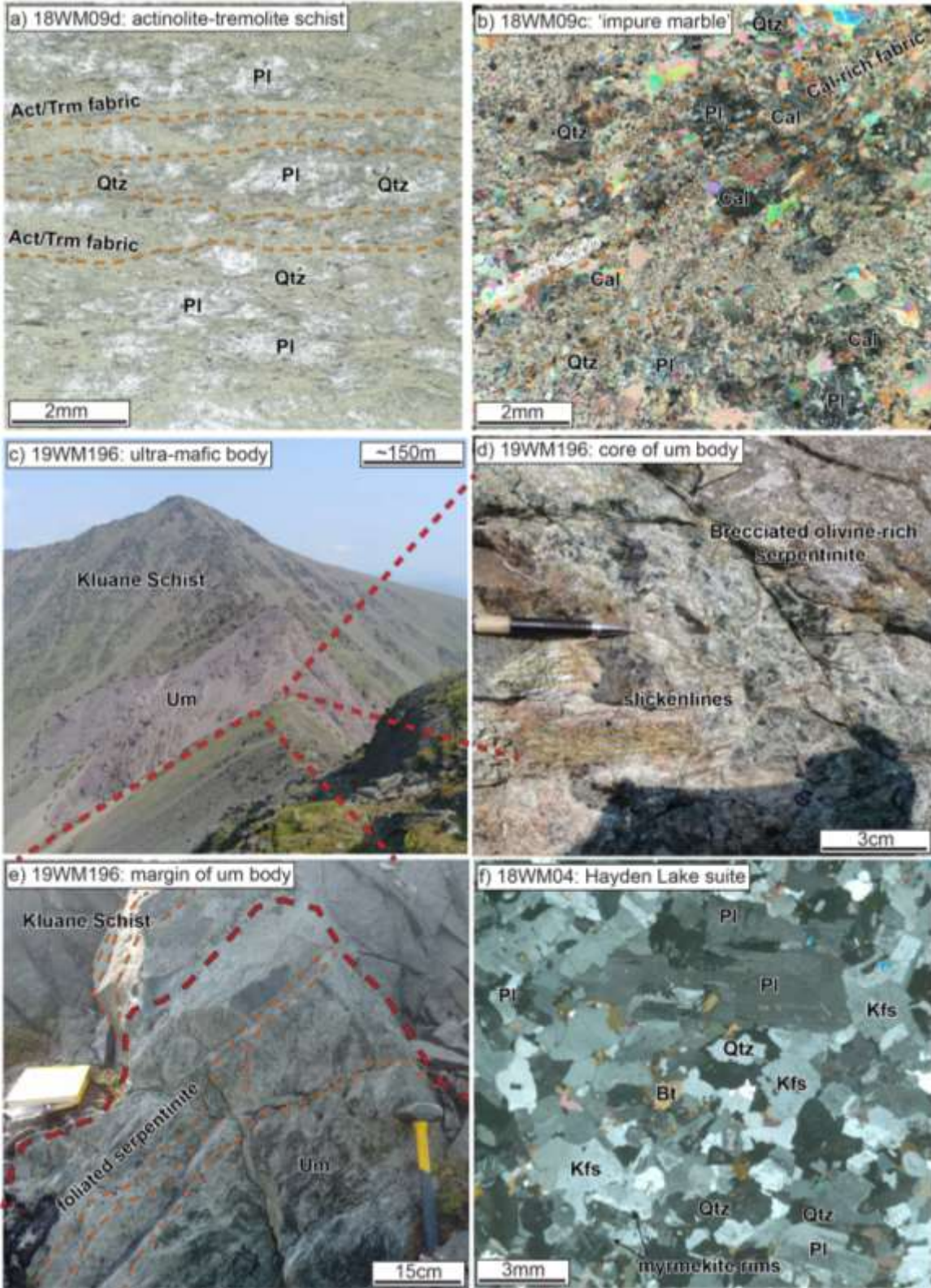
surrounding schist is covered, obscuring evidence for thermal overprinting of the neighbouring schist. The lack of serpentinization and fabric development suggests it may instead be a mafic intrusion that post-dates Kluane Schist deposition and metamorphism.

Hayden Lake suite

The Eocene Hayden Lake suite forms the youngest unit present within the study area (Fig. 2.1; ca. 49 Ma; Israel *et al.*, 2011a). Intrusive bodies of the Hayden Lake suite are typically 5–10 km in diameter and comprise medium- to coarse-grained light to dark grey diorite to granite with local biotite ('Eh' in Fig. 2.1; Israel *et al.*, 2011a). The typical petrology of the Hayden Lake suite includes quartz–plagioclase–K-feldspar +/- biotite–hornblende (Fig. 2.4f). Plagioclase is typically euhedral and shows oscillatory zonation (Fig. 2.4f). Microcline is commonly coarse and euhedral with both feldspar phases often separated by myrmekite rims (Fig. 2.4f). Rare biotite is anhedral often showing alteration to chlorite (Fig. 2.4f). Generally, the Hayden Lake suite remains homogenous throughout the mapped Kluane region. A single small (<1 km) light grey to yellow outcrop with coarse, 2–10 mm abundant gedrite crystals occurs near Garnet Creek.

Rare xenoliths of the Kluane Schist can be found in this intrusive suite. Where biotite is more abundant, the usual salt and pepper appearance of the Hayden Lake suite can show a weak foliation defined by biotite and hornblende. Although rarely seen, this foliation can take on a similar orientation to that preserved within the surrounding Kluane Schist suggesting the intrusion of the Hayden Lake suite, at least in part, occurred late syn-tectonically (e.g., Israel *et al.*, 2011a; Stanley, 2012).

Figure 2.4. (overleaf): a-b) Thin sections of samples 18WM09d and 18WM09c respectively; these samples are characteristic of the foliated, carbonate-rich body found to the west of Killermun Lake (c & KL in Fig. 2.1); c) Outcrop view of the ultramafic body found at locality 19WM196 in Fig. 2.1; d-e) Typical appearance of the core and margin regions, respectively, of the ultramafic body found at locality 19WM196; f) Thin section of collected from locality 18WM04 (see Fig. 2.1) showing the mineralogy typical of the undeformed Eocene Hayden Lake suite.



2.3. References

- Amato, J.M., Toro, J., Miller, E.L., Gehrels, G.E., Farmer, G.L., Gottlieb, E.S. and Till, A.B., 2009. Late Proterozoic–Paleozoic evolution of the Arctic Alaska–Chukotka terrane based on U-Pb igneous and detrital zircon ages: Implications for Neoproterozoic paleogeographic reconstructions. *Geological Society of America Bulletin*, v.121, n.9-10, p.1219-1235. <https://doi.org/10.1130/B26510.1>
- Beranek, L.P. and Mortensen, J.K., 2011. The timing and provenance record of the Late Permian Klondike orogeny in northwestern Canada and arc-continent collision along western North America. *Tectonics*, v.30, n.5. <https://doi.org/10.1029/2010TC002849>
- Beranek, L.P., van Staal, C.R., McClelland, W.C., Israel, S. and Mihalynuk, M.G., 2013. Detrital zircon Hf isotopic compositions indicate a northern Caledonian connection for the Alexander terrane. *Lithosphere*, v.5, n.2, p.163-168. <https://doi.org/10.1130/L255.1>
- Beranek, L.P., van Staal, C.R., McClelland, W.C., Joyce, N. and Israel, S., 2014. Late Paleozoic assembly of the Alexander-Wrangellia-Peninsular composite terrane, Canadian and Alaskan Cordillera. *Geological Society of America Bulletin*, v.126, n.11-12, p.1531-1550. <https://doi.org/10.1130/31066.1>
- Beranek, L. P., W. C. McClelland, C. R. van Staal, S. Israel, and S. M. Gordee, 2017. Late Jurassic flare-up of the Coast Mountains arc system, NW Canada, and dynamic linkages across the northern Cordilleran orogen, *Tectonics*, v.36, n.5, p.877–901. <https://doi.org/10.1002/2016TC004254>
- Beranek, L.P., and Mortensen, J.K., 2011, The timing and provenance record of the late Permian Klondike orogeny in northwestern Canada and arc-continent collision along western North America: *Tectonics*, v. 30, TC5017, <https://doi.org/10.1029/2010TC002849>.
- Berg, H.C., Jones, D.L., and Richter, D.H., 1972, Gravina-Nutzotin Belt; tectonic significance of an upper Mesozoic sedimentary and volcanic sequence in southern and southeastern Alaska, in U.S. Geological Survey, *Geological survey research 1972*, Chapter D: U.S. Geological Survey Professional Paper 800-D, p. D1-D24.

- Berman, R.G., Ryan, J.J., Gordey, S.P. and Villeneuve, M., 2007. Permian to Cretaceous polymetamorphic evolution of the Stewart River region, Yukon-Tanana terrane, Yukon, Canada: P–T evolution linked with in situ SHRIMP monazite geochronology. *Journal of Metamorphic Geology*, v.25, n.7, p.803-827. <https://doi.org/10.1111/j.1525-1314.2007.00729.x>
- Bordet, E., Israel, S. and D. Moynihan, 2015. Geology of the Takhanne River (NTS 115A/2) and Kluhini River (115A/7) map areas, southwest Yukon. In: *Yukon Exploration and Geology 2014*, K.E. MacFarlane, M.G. Nordling and P.J. Sack (eds.), Yukon Geological Survey, p. 1-16.
- Box, S.E., Karl, S.M., Jones, J.V., Bradley, D.C., Haeussler, P.J. & O’Sullivan, P.B., 2019. Detrital zircon geochronology along a structural transect across the Kahiltna assemblage in the western Alaska Range: Implications for emplacement of the Alexander-Wrangellia-Peninsular terrane against North America. *Geosphere*, v.15, n.6, p.1774-1808. <https://doi.org/10.1130/GES02060.1>
- Canil, D., Johnston, S.T., D’Souza, R.J. & Heaman, L.M., (2015). Protolith of ultramafic rocks in the Kluane Schist, Yukon, and implications for arc collisions in the northern Cordillera. *Canadian Journal of Earth Sciences*, v.52, n.7, p. 431-443. <https://doi.org/10.1139/cjes-2014-0138>
- Clark, A. D., Tectono-metamorphic history of mid-crustal rocks at Aishihik Lake, southwest Yukon, [M.S. thesis], Simon Fraser University, Burnaby, BC, 2017.
- Colpron, M. (compiler), 2022. Yukon Bedrock Geology Map. Yukon Geological Survey, Open File 2022-1, 1:1 000 000 scale map and legend.
- Colpron, M. and Nelson, J.L., 2009. A Palaeozoic Northwest Passage: Incursion of Caledonian, Baltican and Siberian terranes into eastern Panthalassa, and the early evolution of the North American Cordillera. *Geological Society, London, Special Publications*, v.318, n.1, p.273-307. <https://doi.org/10.1144/SP318.10>

- Colpron, M., Nelson, J.L. and Murphy, D.C., 2006. A tectonostratigraphic framework for the pericratonic terranes of the northern Canadian Cordillera. Paleozoic evolution and metallogeny of pericratonic terranes at the ancient Pacific margin of North America, Canadian and Alaskan Cordillera: Geological Association of Canada Special Paper, 45, p.1-23.
- Colpron, M., Nelson, J.L., & Murphy, D.C. (2007). Northern Cordilleran terranes and their interactions through time. *GSA Today*, v. 17, p. 4–10 <https://doi.org/10.1130/GSAT01704-5A.1>
- Eisbacher, G.H., (1976). Sedimentology of the Dezadeash flysch and its implications for strike-slip faulting along the Denali fault, Yukon Territory and Alaska. *Canadian Journal of Earth Sciences*, v.13, n.11, p.1495-1513. <https://doi.org/10.1139/e76-157>
- Erdmer, P. & Mortensen, J.K., 1993. A 1200-km-long Eocene metamorphic-plutonic belt in the northwestern Cordillera: Evidence from southwest Yukon. *Geology*, v.21, n.11, p.1039-1042. [https://doi.org/10.1130/0091-7613\(1993\)021<1039:AKLEMP>2.3.CO;2](https://doi.org/10.1130/0091-7613(1993)021<1039:AKLEMP>2.3.CO;2)
- Gehrels, G., Rusmore, M., Woodsworth, G., Crawford, M., Andronicos, C., Hollister, L., Patchett, J., Ducea, M., Butler, R., Klepeis, K. & Davidson, C., 2009. U-Th-Pb geochronology of the Coast Mountains batholith in north-coastal British Columbia: Constraints on age and tectonic evolution. *Geological Society of America Bulletin*, v.121, n.9-10, p.1341-1361. <https://doi.org/10.1130/B26404.1>
- Gehrels, G.E., 2001. Geology of the Chatham Sound region, southeast Alaska and coastal British Columbia. *Canadian Journal of Earth Sciences*, v.38, n.11, p.1579-1599. <https://doi.org/10.1139/e01-040>
- Gehrels, G.E., 2002. Detrital zircon geochronology of the Taku terrane, southeast Alaska. *Canadian Journal of Earth Sciences*, v.39, n.6, p.921-931. <https://doi.org/10.1139/e02-002>
- Gehrels, G.E., Butler, R.F. and Bazard, D.R., 1996. Detrital zircon geochronology of the Alexander terrane, southeastern Alaska. *Geological Society of America Bulletin*, v.108, n.6, p.722-734. [https://doi.org/10.1130/0016-7606\(1996\)108<0722:DZGOTA>2.3.CO;2](https://doi.org/10.1130/0016-7606(1996)108<0722:DZGOTA>2.3.CO;2)

- Gehrels, G.E., McClelland, W.C., Samson, S.D., Patchett, P.J. and Orchard, M.J., 1992. Geology of the western flank of the Coast Mountains between Cape Fanshaw and Taku Inlet, southeastern Alaska. *Tectonics*, v.11, n.3, p.567-585.
<https://doi.org/10.1029/92TC00482>
- Giesler, D., Gehrels, G., Pecha, M., White, C., Yokelson, I. and McClelland, W.C., 2016. U–Pb and Hf isotopic analyses of detrital zircons from the Taku terrane, southeast Alaska. *Canadian Journal of Earth Sciences*, v.53, n.10, p.979-992.
<https://doi.org/10.1139/cjes-2015-0240>
- Hoskin, P.W.O. and Black, L.P., 2000. Metamorphic zircon formation by solid-state recrystallization of protolith igneous zircon. *Journal of Metamorphic Geology*, v.18, n.4, p.423-439. <https://doi.org/10.1046/j.1525-1314.2000.00266.x>
- Hults, C.P., Wilson, F.H., Donelick, R.A. and O'Sullivan, P.B., 2013. Two flysch belts having distinctly different provenance suggest no stratigraphic link between the Wrangellia composite terrane and the paleo-Alaskan margin. *Lithosphere*, v.5, n.6, p.575-594.
doi: <https://doi.org/10.1130/L310.1>
- Israel, S. and Westberg, E., 2012. Geology and mineral potential of the northwestern Aishihik Lake map area, parts of NTS 115H/12 and 13. In: *Yukon Exploration and Geology 2011*, K.E. MacFarlane and P.J. Sack, (eds.), Yukon Geological Survey, p.103-113.
- Israel, S., Beranek, L., Friedman, R.M. and Crowley, J.L., 2014. New ties between the Alexander terrane and Wrangellia and implications for North America Cordilleran evolution. *Lithosphere*, v.6, n.4, p.270-276. <https://doi.org/10.1130/L364.1>
- Israel, S., Cobbett, R., Westberg, E., Stanley, B. & Hayward, N., 2011b. Preliminary bedrock geology of the Ruby Ranges, southwestern Yukon, (Parts of NTS 115G, 115H, 115A and 115B) (1:150 000 scale). Yukon Geological Survey, Open File 2011-2.
- Israel, S., Colpron, M., Cubley, J., Moynihan, D., Murphy, D.C. & Relf, C., (2015). The Bear Creek assemblage: A latest Triassic volcano-sedimentary succession in southwest Yukon. In: *Yukon Exploration and Geology 2014*, K.E. MacFarlane, M.G. Nordling and P.J. Sack (eds.), Yukon Geological Survey, p. 99-112.

- Israel, S., Friend, M. and Borch, A., 2017. Preliminary bedrock geology of the Long Lake and Moraine Lake areas, southwestern Yukon (NTS 115A/15 and 115H/2 and 7). In: Yukon Exploration and Geology 2016, K.E. MacFarlane and L.H. Weston (eds.), Yukon Geological Survey, p. 87-102.
- Israel, S., Murphy, D., Bennett, V., Mortensen, J. and Crowley, J., 2011a. New insights into the geology and mineral potential of the Coast Belt in southwestern Yukon. In: Yukon Exploration and Geology 2010, MacFarlane, K.E., Weston, L.H., and Relf, C. (eds.), Yukon Geological Survey, p. 101-123.
- Kapp, P.A. and Gehrels, G.E., 1998. Detrital zircon constraints on the tectonic evolution of the Gravina belt, southeastern Alaska. *Canadian Journal of Earth Sciences*, v.35, n.3, p.253-268. <https://doi.org/10.1139/e97-114>
- Lowey, G.W., 2007. Lithofacies analysis of the Dezadeash Formation (Jura–Cretaceous), Yukon, Canada: The depositional architecture of a mud/sand-rich turbidite system. *Sedimentary Geology*, v.198, n.3-4, p.273-291. <https://doi.org/10.1016/j.sedgeo.2006.12.011>
- Lowey, G.W., 2011. Volcaniclastic gravity flow deposits in the Dezadeash Formation (Jura-Cretaceous), Yukon, Canada: Implications regarding the tectonomagmatic evolution of the Chitina arc in the northern Cordillera of North America. *Lithos*, v.125, n.1-2, p.86-100. <https://doi.org/10.1016/j.lithos.2011.01.014>
- Lowey, G.W., 2019. Provenance analysis of the Dezadeash Formation (Jurassic–Cretaceous), Yukon, Canada: Implications regarding a linkage between the Wrangellia composite terrane and the western margin of Laurasia. *Canadian Journal of Earth Sciences*, v.56, n.1, p.77-100. <https://doi.org/10.1139/cjes-2017-0244>
- McClelland, W.C., Gehrels, G.E. & Saleeby, J.B., 1992. Upper Jurassic-Lower Cretaceous basinal strata along the Cordilleran margin: Implications for the accretionary history of the Alexander-Wrangellia-Peninsular terrane. *Tectonics*, v.11, n.4, p.823-835. <https://doi.org/10.1029/92TC00241>

- Mezger, J.E., 1997. Tectonometamorphic evolution of the Kluane metamorphic assemblage, southwest Yukon: evidence for Late Cretaceous eastward subduction of oceanic crust underneath North America. Unpublished PhD thesis, University of Alberta, 306 p.
<https://doi.org/10.7939/R3DJ58N76>
- Mezger, J.E., 2000. 'Alpine-type' ultramafic rocks of the Kluane metamorphic assemblage, southwest Yukon: Oceanic crust fragments of a late Mesozoic back-arc basin along the northern Coast Belt. In: Yukon Exploration and Geology 1999, Emond, D.S. and Weston, L.W. (eds.), Exploration and Geological Sciences Division, Yukon Region, Indian and Northern Affairs Canada, p. 127-138.
- Mezger, J.E., Chacko, T. & Erdmer, P., 2001b. Metamorphism at a late Mesozoic accretionary margin: a study from the Coast Belt of the North American Cordillera. *Journal of Metamorphic Geology*, v.19, n.2, p.121-137. <https://doi.org/10.1046/j.0263-4929.2000.00300.x>
- Mezger, J.E., Creaser, R.A., Erdmer, P. and Johnston, S.T., 2001a. A Cretaceous back-arc basin in the Coast Belt of the northern Canadian Cordillera: evidence from geochemical and neodymium isotope characteristics of the Kluane metamorphic assemblage, southwest Yukon. *Canadian Journal of Earth Sciences*, v.38, n.1, p.91-103.
<https://doi.org/10.1139/e00-076>
- Monger, J.W.H., Price, R.A., & Tempelman-Kluit, D.J., (1982), Tectonic accretion and the origin of the two major metamorphic and tectonic belts in the Canadian Cordillera. *Geology*, v.10, n.2, p.70–75. [https://doi.org/10.1130/00917613\(1982\)10<70:TAATOO>2.0.CO](https://doi.org/10.1130/00917613(1982)10<70:TAATOO>2.0.CO)
- Mortensen, J.K. and Erdmer, P., 1992. U-Pb, ^{40}Ar - ^{39}Ar , and K-Ar ages for Metamorphism of the Kluane and Aishihik Assemblages in southwestern Yukon Territory, in Radiogenic age and isotopic studies, Report 6: Geological Survey of Canada Paper n.92-2, p. 135-140.
<https://doi.org/10.4095/134174>
- Mortensen, J.K., 1992. Pre-mid-Mesozoic tectonic evolution of the Yukon-Tanana terrane, Yukon and Alaska. *Tectonics*, v.11, n.4, p.836-853. <https://doi.org/10.1029/91TC01169>

- Murphy, D.C., Mortensen, J.K. and van Staal, C., 2009. 'Windy-McKinley' terrane, western Yukon: new data bearing on its composition, age, correlation and paleotectonic settings. Yukon Exploration and Geology. Edited by LH Weston, LR Blackburn, and LL Lewis. Yukon Geological Survey, p.195-209.
- Nelson, J. L., Colpron, M. & Israel, S. (2013). The cordillera of British Columbia, Yukon, and Alaska. Society of Economic Geology, Special Publication 17. <https://doi.org/10.5382/SP.17.03>
- Piercey, S.J. and Colpron, M., 2009. Composition and provenance of the Snowcap assemblage, basement to the Yukon-Tanana terrane, northern Cordillera: Implications for Cordilleran crustal growth. *Geosphere*, v.5, n.5, p.439-464. <https://doi.org/10.1130/GES00505.1>
- Sigloch, K. & Mihalynuk, M.G., (2013). Intra-oceanic subduction shaped the assembly of Cordilleran North America. *Nature*, v.496, n.7443, p.50-56. <https://doi.org/10.1038/nature12019>
- Sigloch, K. & Mihalynuk, M.G., (2017). Mantle and geological evidence for a Late Jurassic–Cretaceous suture spanning North America. *Geological Society of America Bulletin*, v.129, n.11-12, p.1489-1520. <https://doi.org/10.1130/B31529.1>
- Stanley, B., (2012). Structural geology and geochronology of the Kluane schist, southwestern Yukon Territory. UWSpace. <http://hdl.handle.net/10012/7096> (unpublished Master's thesis, University of Waterloo).
- Staples, R.D., Gibson, H.D., Berman, R.G., Ryan, J.J. and Colpron, M., 2013. A window into the Early to mid-Cretaceous infrastructure of the Yukon-Tanana terrane recorded in multi-stage garnet of west-central Yukon, Canada. *Journal of Metamorphic Geology*, v.31, n.7, p.729-753. <https://doi.org/10.1111/jmg.12042>
- Staples, R.D., Gibson, H.D., Colpron, M. and Ryan, J.J., 2016. An orogenic wedge model for diachronous deformation, metamorphism, and exhumation in the hinterland of the northern Canadian Cordillera. *Lithosphere*, v.8, n.2, p.165-184. <https://doi.org/10.1130/L472.1>

- Tempelman-Kluit, D.J., 1974. Reconnaissance Geology of Aishihik Lake, Snag and Part of Stewart River Map-areas, West Central Yukon (115A, 115F, 115G and 115K), v.73, n.41, Department of Energy, Mines and Resources.
- Trop, J.M., Benowitz, J.A., Koepp, D.Q., Sunderlin, D., Brueseke, M.E., Layer, P.W. and Fitzgerald, P.G., 2020. Stitch in the ditch: Nutzotin Mountains (Alaska) fluvial strata and a dike record ca. 117–114 Ma accretion of Wrangellia with western North America and initiation of the Totschunda fault. *Geosphere*, v.16, n.1, p.82-110.
<https://doi.org/10.1130/GES02127.1>
- van der Heyden, P., 1992. A Middle Jurassic to early Tertiary Andean-Sierran arc model for the Coast belt of British Columbia. *Tectonics*, v.11, n.1, p.82-97.
<https://doi.org/10.1029/91TC02183>
- Vice L., 2017. Late cretaceous to Paleocene evolution of the Blanchard River assemblage, southwest Yukon; implications for Mesozoic accretionary processes in the northwestern Cordillera, [M.S. Thesis], 2017, Burnaby, BC, Simon Fraser University.
- Vice, L., Gibson, H. D. & Israel, S., 2020. Late Cretaceous to Paleocene Tectonometamorphic Evolution of the Blanchard River Assemblage, Southwest Yukon: New Insight into the Terminal Accretion of Insular terranes in the Northern Cordillera. *Lithosphere*, 2020, v.1: 2298288. <https://doi.org/10.2113/2020/2298288>
- Waldien, T.S., Roeske, S.M. & Benowitz, J.A., 2021b. Tectonic underplating and dismemberment of the Maclaren-Kluane schist records Late Cretaceous terrane accretion polarity and ~480 km of Post-52 Ma dextral displacement on the Denali fault. *Tectonics*, v.40, n.10, e2020TC006677. <https://doi.org/10.1029/2020TC006677>
- Waldien, T.S., Roeske, S.M., Benowitz, J.A., Twelker, E. & Miller, M.S., 2021a. Oligocene-Neogene lithospheric-scale reactivation of Mesozoic terrane accretionary structures in the Alaska Range suture zone, southern Alaska, USA. *Geological Society of America Bulletin*, v.133, n.3-4, p.691-716. <https://doi.org/10.1130/B35665.1>

Yokelson, I., Gehrels, G.E., Pecha, M., Giesler, D., White, C. and McClelland, W.C., 2015. U-Pb and Hf isotope analysis of detrital zircons from Mesozoic strata of the Gravina belt, southeast Alaska. *Tectonics*, v.34, n.10, p.2052-2066.
<https://doi.org/10.1002/2015TC003955>

Chapter 3. Tectono-metamorphic evolution of the Cretaceous Kluane Schist, Southwest Yukon

Will McKenzie¹, Brendan Dyck², H. Daniel Gibson¹ & Matthew Steele-MacInnis³

¹ Department of Earth Sciences, Simon Fraser University, Burnaby, BC, Canada

² Department of Earth, Environmental and Geographical Sciences, University of British Columbia, Kelowna, BC, Canada

³ Department of Earth and Atmospheric Sciences, University of Alberta, Edmonton, AB, Canada

Abstract

A wealth of information regarding the Mesozoic evolution of the Northern Canadian and Alaskan Cordillera is held within a series of variably metamorphosed and deformed Jurassic-Cretaceous basins. Located at the interface between the pericratonic Intermontane and exotic Insular terranes, these basins may prove key to understanding the timing and tectonic style of Insular terrane accretion, a topic of longstanding debate. This study unravels the structural and metamorphic evolution of one of these basins, the Kluane Basin, within southwest Yukon.

The Kluane Schist is the primary assemblage of the Kluane Basin. It consists of metamorphosed and deformed low-Al pelites that were intruded by granodioritic plutons of the Paleocene-Eocene Ruby Range batholith. The Kluane Schist preserves a complex metamorphic history that includes both regional and contact events. Previous workers have suggested the variable metamorphic character of the Kluane Schist represents a large thermal aureole related to Ruby Range batholith emplacement. Our work, however, indicates the Kluane Schist can be divided into seven distinct petrologic zones, highlighted by a unique combination of mineral assemblage and structure, that together record a period of regional metamorphism coeval with protracted deformation. Further, we propose the Kluane Schist represents a single lithological package which experienced two distinct phases of deformation, 1) an early greenschist-facies phase that resulted in the development of a bedding-parallel chlorite–muscovite–titanite fabric, preserved by its lowest grade units, and 2) a later amphibolite-facies phase that manifests across higher grade units as the progressive transposition of the earlier chlorite–muscovite fabric into a penetrative biotite-rich schistosity that transitions up-grade into a

segregated gneissic fabric comprised of biotite–cordierite and plagioclase–quartz (+/- sillimanite–K-feldspar–melt).

By integrating the results of detailed petrography and petrological modelling, we demonstrate that the Kluane Schist preserves metamorphic conditions that align with other Buchan-Style terranes worldwide. Our data defines a field gradient across the Kluane Schist ranging from 3.0–3.5 kbar at 375–400 °C to 4–4.5 kbar at 700–750 °C. This record of a coupled Buchan-style metamorphic-deformational evolution and tops-to-the-SW non-coaxial shear structures are consistent with the override of the warm Yukon-Tanana terrane as the principal driver of Kluane Schist metamorphism, rather than intrusion of the Ruby Range batholith.

3.1. Introduction

Within the North American Cordillera, the 3000 km long suture between the more inboard Intermontane terranes and the more outboard and exotic Insular terranes is dotted with numerous Jurassic to Cretaceous (Jura-Cretaceous) basins (Fig. 3.1a; e.g., McClelland *et al.*, 1992; van der Heyden, 1992; Hults *et al.*, 2013; Box *et al.*, 2019). Within western Canada and southern Alaska, these Jura-Cretaceous basins are thought to represent a group of mostly deep-water sediments that once filled a terrane-intervening seaway separating the Insular and Intermontane terranes (McClelland *et al.*, 1992; Gehrels *et al.*, 1992; Monger *et al.*, 1994; Hults *et al.*, 2013; Sigloch & Mihalynuk, 2013, 2017; Box *et al.*, 2019). The metasedimentary units within these basins record a period of mid- to Late Cretaceous deformation and metamorphism associated with the accretion of the Insular terranes to the margin of western North America that included the previously accreted Intermontane terranes (e.g., Hults *et al.*, 2013; Box *et al.*, 2019; Vice *et al.*, 2020; Waldien *et al.*, 2021a). This record of tectonism provides important insight into the nature of this suturing event, which remains contested with regard to its timing and principal tectonic driver (e.g., McClelland *et al.*, 1992; Sigloch & Mihalynuk, 2013, 2017; Monger, 2014; Box *et al.*, 2019).

The Cretaceous Kluane Schist within southwest Yukon represents the relic one of these terrane-intervening basins (Fig. 3.1a; e.g., Mezger, 1997; Israel *et al.*, 2011a). The Kluane Basin is interpreted to have developed in either a back-arc (e.g., Eisbacher, 1976; Lowey, 1992; Mezger *et al.*, 2001) or forearc setting (McClelland *et al.*, 1992; Israel *et al.*, 2011a; Canil *et al.*, 2015; Waldien *et al.*, 2021b), and is dominated by a sequence of largely homogenous pelitic

schists and migmatites collectively referred to as the Kluane Schist (e.g., Tempelman-Kluit, 1974; Eisbacher, 1976) or Kluane Metamorphic Assemblage (Mezger *et al.*, 2001). Previous work has documented a complex metamorphic history within the Kluane Schist, which includes both regional and contact events (e.g., Erdmer & Mortensen, 1993; Mezger *et al.*, 2001). However, the temporal and spatial extent of these metamorphic events, along with the geological processes responsible for their development remains debated (Erdmer & Mortensen, 1993; Mezger *et al.*, 2001; Israel *et al.*, 2011a).

The Kluane Schist preserves mineral assemblages ranging from the lower greenschist to upper amphibolite-facies, which have been suggested to derive either from the juxtaposition of two regionally metamorphosed belts of distinct provenance (Erdmer & Mortensen, 1993), or to be the product of an extensive thermal overprint reflecting a ~5–6 kilometer-wide contact aureole related to emplacement of the Paleocene-Eocene Ruby Range batholith (Mezger *et al.*, 2001). In this study we use petrological, structural, and chemical data along with petrological modelling to unravel the relationship between the distinct mineral assemblages preserved across the Kluane Schist and re-evaluate its tectono-metamorphic history. With these new datasets we also re-examine the potential correlations drawn between the Kluane Schist and other Jura-Cretaceous terrane-intervening assemblages within southwest Yukon (Fig. 3.1b).

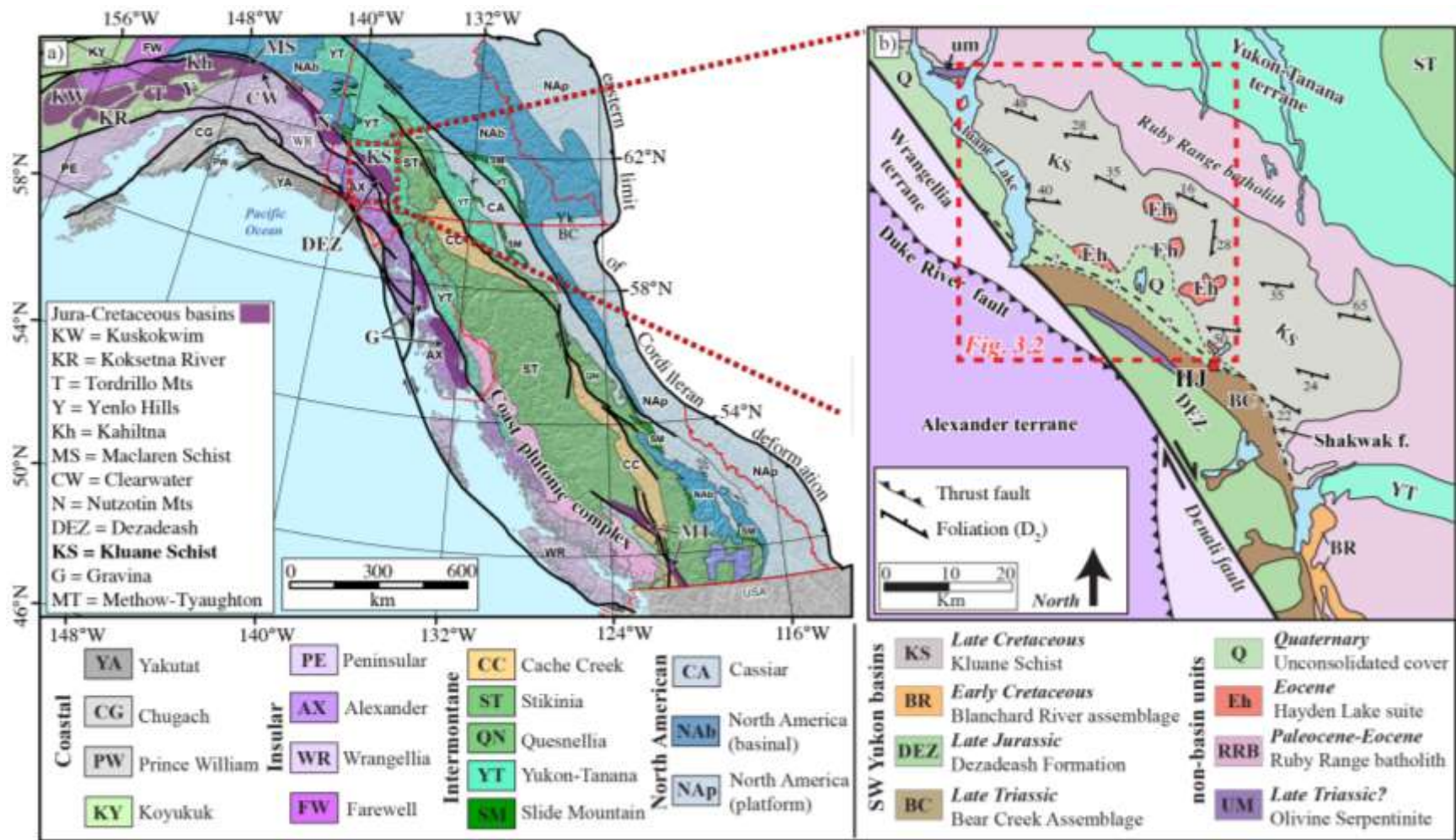


Figure 3.1. a) The location of the study area within the terrane collage of the Northern Canadian and Alaskan Cordillera (modified from Colpron & Nelson, 2011). The Jura-Cretaceous basinal assemblages that are situated between the Insular and Intermontane terranes, which includes the Kluane Schist, are highlighted and labelled. b) Map of the Kluane Basin, outlined by the red rectangle in (a). The distribution of the major lithologies within the Kluane Basin and their relationships to surrounding geological belts is shown (based on Mezger, 1997; Mezger *et al.*, 2001; Israel *et al.*, 2015; Vice *et al.*, 2020; this study).

3.2. Geological Context

The Kluane Schist is the northernmost of four lithological assemblages that lie along the boundary between Yukon-Tanana terrane (assigned as part of the Intermontane terranes; Monger *et al.*, 1982; Colpron *et al.*, 2007) and Alexander and Wrangellia of the Insular terranes within southwest Yukon (Fig. 3.1b; e.g., Mezger *et al.*, 2001; Israel *et al.*, 2011a, b; Israel *et al.*, 2015; Vice *et al.*, 2020). From north to south the other three lithological assemblages include the Late Triassic Bear Creek assemblage, a volcano-sedimentary succession with potential linkage to the Alexander or Taku terranes (Israel *et al.*, 2015) and two Jura-Cretaceous basal assemblages; the Late Jurassic Dezadeash Formation, derived primarily from the outboard Insular terranes (e.g., Lowey, 2018) and the Early Cretaceous Blanchard River assemblage, which crops out along the southern edge of the Kluane Schist and is considered to be largely derived from the inboard Intermontane terranes (Fig. 3.1b; Vice, 2017; Vice *et al.*, 2020). To the southeast, the Shakhak fault, an inferred structural feature of unknown kinematics, separates the Kluane Schist from rocks of the Bear Creek assemblage and Dezadeash Formation (Fig. 3.1b; e.g., Mezger, 1997; Colpron & Nelson, 2011; Israel *et al.*, 2015). To the southwest the Kluane Schist is truncated by the Denali fault, separating it from rocks of the Insular terranes (Fig. 3.1b). The northern and eastern contact of the Kluane Schist with overlying Yukon-Tanana terrane rocks is obscured by the intrusion of the extensive Paleocene-Eocene Ruby Range batholith, a composite plutonic body grading from moderately foliated quartz-diorites at its base to massive quartz-feldspar porphyry up-section (Fig. 3.1b; Israel *et al.*, 2011a, b).

The Kluane Schist is exposed as a 160 km long, largely northwest-striking belt of graphitic mica-quartz schist and cordierite bearing paragneiss (Fig. 3.1b; e.g., Mezger *et al.*, 2001; Israel *et al.*, 2011a, b). Metamorphic grade increases away from the core of the Kluane Basin, where the Kluane Schist is characterized by a graphitic muscovite-rich schist, towards its northern and eastern edges where the Kluane Schist becomes increasingly gneissic and locally migmatitic, preserving centimetre-scale banding defined by darker layers of biotite–cordierite and lighter layers of quartz–feldspar (Figs. 2 and 3; Mezger *et al.*, 2001; Israel *et al.*, 2011a). Previous petrological modelling has suggested this metamorphic character is the result of two distinct metamorphic episodes (Mezger *et al.*, 2001): (1) an initial medium-*T*, medium-*P* event (peak; ~7 kbar, 510°C) that developed mineral assemblages up to garnet-grade synchronous with deformation and (2) a high-*T*, low-*P* event (~3.5–4.5 kbar, 530–720°C) evidenced by the static growth of a staurolite–aluminium-silicate–cordierite sequence within higher-grade amphibolite

facies schists and gneisses (Mezger *et al.*, 2001). Mapped isograds relating to this second event run-parallel to, and document an increase in metamorphic grade towards, the Ruby Range batholith (see Fig. 3.2 in Mezger *et al.*, 2001). Together with evidence for the annealing of previously developed microstructure, this second event has been suggested to document an extensive, 5–6 km wide contact aureole to the Ruby Range batholith (Erdmer, 1991; Mezger *et al.*, 2001). Recent studies, however, have reported more complex structural relationships between the highest-grade units of the Kluane Schist (e.g., Israel *et al.*, 2011a) with moderate to strong deformational fabrics preserved at the base of the Ruby Range batholith suggesting it was initially emplaced syn-tectonically, rather than as a static intrusion (Murphy *et al.*, 2009; Israel *et al.*, 2011a, b).

The age of the Kluane Schist is poorly constrained. Current estimates based on two detrital zircon samples suggest a Late Cretaceous (ca. 94 Ma) maximum depositional age (MDA) for the Kluane Schist protolith (Israel *et al.*, 2011a). The age of metamorphism for the Kluane Schist was constrained by dating zircon rim domains from the same detrital zircon suite, indicating there were at least two metamorphic events at ca. 82 and ca. 70 Ma (Israel *et al.*, 2011a; Stanley, 2012). Zircon dated from a single dike which crosscuts Kluane Schist foliation constrains major fabric development prior to ca. 72–68 Ma (Mezger *et al.*, 2001; Israel *et al.*, 2011a). However, monazite within the same dike provides a significantly younger age of 55.6 ± 0.6 Ma (Israel *et al.*, 2011a), suggesting the dated zircon were potentially inherited from the Kluane Schist host rock.

Other units of the Kluane Basin include volumetrically minor and discontinuous bodies of ultramafic talc-schists that are interleaved with Kluane Schist metasediments (“um” in Figs. 1b and 2). The origin of these ultramafic bodies is contentious; they are either interpreted as dismembered fragments of oceanic crust (Mezger, 2000) or imbricated parts of deep-seated arc-related cumulates exhumed into the Kluane Schist along shear zones in northwest Stikinia presently found ~270 km to the southeast (Canil *et al.*, 2015). Rare, foliated and metamorphosed carbonate bodies have been interpreted to represent olistoliths of Yukon-Tanana terrane affinity (“carbonate” in Fig. 3.2; Stanley, 2012). However, a detailed provenance analysis is yet to be completed. Hornblende normative diorite to quartz diorite intrusions of the Eocene Hayden Lake suite are the youngest lithology within the study area (e.g., Israel *et al.*, 2011a, b; Stanley, 2012). These kilometer-scale intrusions are massive and largely undeformed (“Eh” in Fig. 3.2; Israel *et al.*, 2011b).

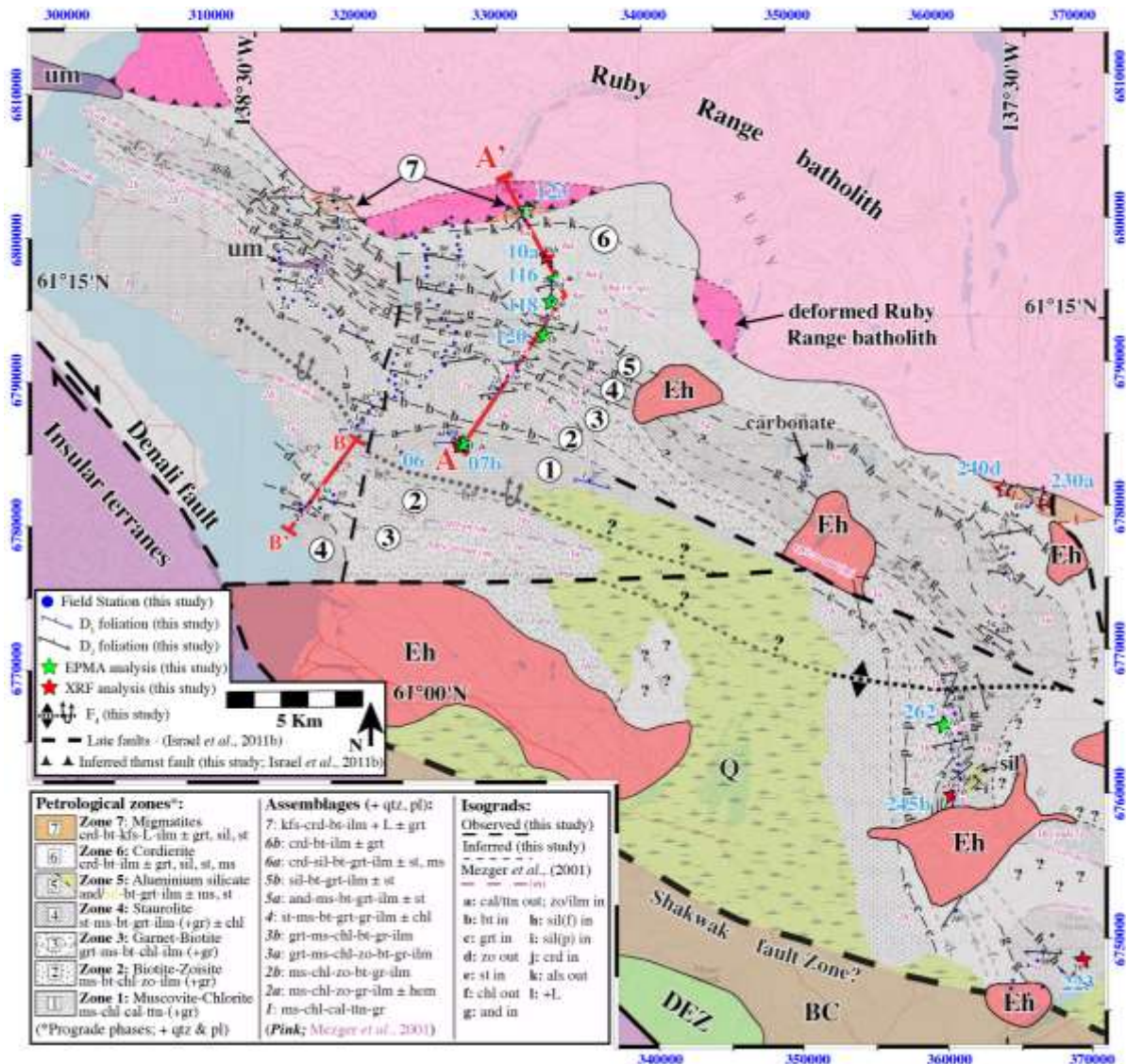


Figure 3.2. Metamorphic assemblage map of northwest Kluane Basin (red rectangle in Figure 3.1b; map based on Israel *et al.*, 2011b; Colpron & Nelson, 2011; Israel *et al.*, 2015; this study) outlining the petrological zones defined in this study. Lithologies are the same colour as in Figure 3.1b except where indicated (i.e., “deformed Ruby Range batholith” & “carbonate”). Isograd locations are constrained by assemblage observations from this and previous studies (Mezger *et al.*, 2001). Petrological zones are highlighted by different shading patterns and indicated by circled numbers. Orange shading represents areas where leucosome is observed in Kluane Schist outcrops. Yellow shading highlights areas where prismatic sillimanite (labelled ‘sil’ on map and sil(p) in key) was observed. The location of young faults was inferred from aeromagnetic surveys (Israel *et al.*, 2011b). Red stars represent samples taken for XRF analysis and green stars show samples taken for detailed EPMA analysis. Blue numbers refer to analysed samples.

Within southwest Yukon the Blanchard River assemblage (Fig. 3.1b) represents a similar belt of Jura-Cretaceous metapelitic rocks to the Kluane Schist, with both units suggested to share a similar metamorphic evolution (Mezger *et al.*, 2001; Vice *et al.*, 2020). However, despite their proximal location (Fig. 3.1b) and similar lithology these units consistently show discrepancy in their preserved mineral assemblage and structure (Mezger *et al.*, 2001; Vice *et al.*, 2020). The Blanchard River assemblage documents similar high-pressure conditions (~6.5 kbar, 635–650°C) to that suggested for the Kluane Schist (~7 kbar, 510°C; e.g., Mezger *et al.*, 2001), although its mineral assemblages typically contain kyanite, while its lower-pressure assemblages (~3 kbar) are considered syn-deformational and are clearly shown to overprint previous higher-pressure metamorphism (Vice *et al.*, 2020). Such high-pressure phases (e.g., kyanite) and the distinct syn-deformational overprinting relationships seen across the Blanchard River assemblage have not previously been reported across the Kluane Schist (c.f., Mezger *et al.*, 2001 & Vice *et al.*, 2020). Equally, within the Blanchard River assemblage the thermal effect of the Ruby Range batholith is observed as a third, distinct metamorphic event that is restricted to the assemblages directly adjacent to the igneous contact (Vice *et al.*, 2020). These inconsistencies further highlight the need to re-evaluate the metamorphic evolution of the Kluane Schist in order to assess a potential correlation between the two units.

3.3. Methods

3.3.1. Analytical methods

Whole rock and mineral chemistry

Six samples were analysed by X-Ray fluorescence spectroscopy (XRF) to determine the variability in bulk composition across the Kluane Schist. XRF analysis was completed by Bureau Veritas Commodities Canada Ltd, in Vancouver, British Columbia and included eleven major oxides (SiO₂, Al₂O₃, TiO₂, Fe₂O₃, MgO, CaO, MnO, Na₂O, K₂O, P₂O₅ and Cr₂O₃) along with seven trace elements (Ba, Ni, Sr, Zr, Y, Nb, Sc). Selected samples come from a variety of localities and metamorphic grades across the Kluane Schist (red stars, Fig. 3.2). All bulk rock compositional data can be found in the supplemental Table D1.

Mineral chemical analyses were completed on six samples across the Kluane Schist (green stars, Fig. 3.2) using wavelength-dispersive X-ray spectroscopy (WDS) on a CAMECA

SX-5 Field Emission Electron Probe Micro-Analyser (EPMA) at the University British Columbia, Okanagan. We analysed seven major assemblage minerals (chlorite, muscovite, biotite, garnet, staurolite, plagioclase and cordierite). The standards used for calibration were garnet spessartine for Si and Mn, titanite for Ti, garnet almandine for Al and Fe, wollastonite for Ca, albite for Na, diopside for Mg, orthoclase for K, apatite for P, fluorite for F and synthetic KCl for Cl. WDS quantification of Si, Al and F used the LTAP crystal; Ti, Ca, K, P and Cl used the LPET crystal; Fe and Mn used the LLIF crystal; and Na and Mg used the TAP crystal. A 20 keV acceleration voltage and 20 nA beam current was used to maximize analytical resolution and minimize sample damage. We analysed several spot locations across each porphyroblastic phase (garnet, staurolite, plagioclase, cordierite, and coarse biotite) to assess any chemical variations within individual grain. All mineral compositional data can be found in the supplemental Tables E1–E7.

Raman spectroscopy

To quantify evolution of water activity ($a_{\text{H}_2\text{O}}$) during metamorphism we conducted petrographic and Raman spectroscopic analysis of fluid and graphite inclusions in garnet within sample 19WM118 (118 in Fig. 3.2). A doubly polished thin section was used for analysis. Petrography of inclusions was done using an Olympus BX53 microscope and a 100x long working distance objective lens. Raman spectroscopy was done using a Horiba LabRam HR Evolution Raman microscope at the University of Alberta. For Raman excitation, we used a 532 nm (green) laser focused through a 100x long working distance objective and using a confocal pinhole aperture of 50 μm . A grating of 1800 grooves/mm was utilized for high spectral resolution. The nominal laser power was 100 mW at the source, but a neutral density filter in the incident beam path was applied to reduce the power to 25 %. This was to avoid laser damage to the host garnet. Raman spectra were collected using 3 accumulations of 30 s each over the spectral range from 1000 to 4000 cm^{-1} to encompass the Raman bands of CO_2 , graphite and H_2O (Frezzotti *et al.*, 2012).

The density of CO_2 in fluid inclusions was estimated by applying a modified version of the Raman CO_2 densimeter of Lamadrid *et al.* (2017). Specifically, Lamadrid *et al.* (2017) showed that the densimeter calibration needs to be adapted to each laboratory by analysis of suitable standards; our analyses used synthetic $\text{H}_2\text{O}-\text{CO}_2$ fluid inclusions to adjust the calibration curve accordingly. For density calculations, the software package PeakFit was used to extract the peak positions of the CO_2 Fermi diad, using a Gaussian-Lorentzian peak shape

and a linear baseline. Bulk composition, density and isochore of the fluid inclusions were estimated using the approach and equations outlined by Steele-MacInnis (2018).

Temperature was estimated based on the crystallinity of graphite mineral inclusions within garnet of sample 19WM118 according to the calibration equation of Beyssac *et al.* (2002). Again, Raman peaks for the D- and G-bands of carbonaceous inclusions were fitted quantitatively using the PeakFit software, Gaussian-Lorentzian peak shapes and a linear baseline (Fig. A1).

Forward petrological modelling

All phase diagrams were calculated using the petrological modelling software Theriak-Domino (de Capitani & Brown, 1987; de Capitani & Petrakakis, 2010). Modelling was completed within the chemical system MnNCKFMASHO (MnO–Na₂O–CaO–K₂O–FeO–MgO–Al₂O₃–SiO₂–H₂O–TiO₂–O₂). We tested three combinations of datasets and activity-composition models: (1) ds6.2 of Holland & Powell (2011) coupled with the metapelite HPx-eos of White *et al.*, (2014), (2) the modified SPaC14 dataset of Spear & Cheney (1989) and activity models as described in Pattison & Debuhr (2015) and (3) ds5.5 of Holland & Powell (1998), with activity models for plagioclase (Holland & Powell, 2003; ternary feldspar, Cbar 1 field); biotite, garnet and melt, (White *et al.* 2007); white mica (Coggon & Holland 2002; margarite omitted); ilmenite (White *et al.* 2000); orthopyroxene, (White *et al.* 2002); and staurolite, chlorite, cordierite and H₂O, (Holland & Powell 1998). Clinozoisite and zoisite are modelled as pure end-member phases within our ferric-free chemical system.

Of these three modelling combinations none fully satisfies all our observed natural mineral relationships across the Kluane Schist (Figs. A2–4). In particular, the cordierite-free andalusite–biotite–garnet +/- muscovite (+ plagioclase–quartz) assemblage (assemblage 5a in Fig. 3.2) is not produced by any modelling combination. Potential reasons and solutions to this are discussed in detail in Chapter 3.5. Aside from the absence of assemblage 5a, models run with ds5.5 provide a better prediction of our observed mineral assemblages, and importantly, the order of observed paragenesis across the Kluane Schist than either ds6.2 or SpaC14 (c.f., Figs. A2–4). Models run with the more recent ds6.2 do not produce the biotite-free, zoisite-bearing assemblages observed within the lower-grade units of the Kluane Schist (assemblage 2a in Figs. 3.2 and A4) or the sillimanite-free cordierite bearing assemblages typical of higher-grade units (assemblage 6b in Figs. 3.2 and A4). Models run with the SPaC14 dataset predict zoisite-

bearing mineral assemblages down temperature of chlorite–muscovite–titanite, the opposite to that observed across the Kluane Schist (Figs. 3.2, 3.3 and A3) while the occurrence of garnet downgrade of staurolite is predicted at significantly higher pressures than that suggested by either ds5.5 or ds6.2 (Figs. A2–4). Models run with the SPaC14 dataset also fail to produce the sillimanite-free cordierite bearing assemblages typical of the higher-grade units of the Kluane Schist (assemblage 6b in Figs. 3.2 and A3). As such we choose ds5.5 for our final models. Recent studies have highlighted similar results when comparing modelling results to observed metapelitic assemblages (e.g., Waters, 2019; Dyck *et al.*, 2020), especially when considering a ferric-free system and cordierite-bearing equilibria (Pattison & Goldsmith, 2022).

Additionally, we incorporate the results from garnet fluid inclusion analysis to produce a phase diagram that accounts for variable $a_{\text{H}_2\text{O}}$ with metamorphic grade. This is discussed in detail in Chapter 3.5. Finally, our model considers excess free H_2O at sub-solidus conditions and only the amount of H_2O required to minimally saturate the assemblage in the immediate sub-solidus in the supra-solidus domain (c.f., Dyck *et al.*, 2020; Pattison & Goldsmith, 2022). In order to account for the decrease in melt H_2O content with decreased pressure (e.g., Brown *et al.*, 1995) we also separate out the supra-solidus domain into two regions (1.5–3.5 kbar and 3.5–5.5 kbar), with each modelled independently with its associated minimally saturated H_2O composition (2.7 mol H_2O at 2 kbar for the 1.5–3.5 kbar domain and 3.0 mol H_2O at 4 kbar for the 3.5–5.5 kbar domain; c.f., Pattison & Goldsmith, 2022; T - XH_2O diagrams in Fig. A5). Our resulting phase diagram stitches these supra- and sub-solidus regions at their common wet solidus.

Thermobarometry

To complement our forward petrological modelling and provide further constraint on the metamorphic conditions experienced by the Kluane Schist, we calculated the peak conditions experienced by four samples across the Kluane Schist using thermobarometry (19WM262, 19WM120, 19WM118, 19WM123; sample locations on Fig. 3.2). Peak pressure conditions were estimated by applying multi-equilibria thermobarometry using the AvP function within the *Thermocalc* software package (version tc345 with ds5.5, Holland & Powell, 1994). Mineral end-member activities were calculated using *AX* (Holland & Powell, 2009) to remain consistent with our chosen activity models for forward petrological modelling. A particular advantage to this approach is the ability to define $a_{\text{H}_2\text{O}}$ for calculation which has been shown to greatly improve the accuracy of results (e.g., Holland & Powell, 2008; Waters, 2019). As such, AvP calculations

were completed with $a\text{H}_2\text{O}$ values in line with the results from our Raman spectroscopy, graphite crystallinity and constraints provided by our forward phase equilibrium modelling.

Conventional barometry calculations were completed using the garnet–muscovite–biotite–plagioclase barometer (Wu, 2015) and the garnet–biotite–aluminium-silicate–quartz barometer (Wu, 2017). For graphite-free samples temperatures were also calculated using the garnet–biotite thermometer (Holdaway, 2000). Conventional thermometry was not applied to graphite-bearing samples due to the large imprecision in thermometer equilibria when $a\text{H}_2\text{O}$ cannot be assumed = 1 (e.g., Waters, 2019). Across all conventional thermobarometry calculations we set $X\text{Fe}^{3+} = \text{Fe}^{3+}/\text{Fe}_{\text{total}}$ as 0.11 for biotite (e.g., Forshaw & Pattinson, 2021), and assumed a negligible Fe^{3+} component to garnet (e.g., Dyar *et al.*, 2002; Forshaw & Pattinson, 2021).

3.4. Results

3.4.1. Petrology and field relationships across the Kluane Schist

The overall structure of the Kluane Schist is dominated by a largely northwest-striking, northeast-dipping schistosity which shows limited variation across its current exposure (Figs. 3.1b and 3.2). Within the central region of the basin this schistosity can be observed to locally dip south, defining an antiform that plunges shallowly towards the east and deflects mineral isograds (Fig. 3.2; c.f., Mezger *et al.*, 2001). Combined with the general increase in metamorphic grade moving from its core towards the north and east (Fig. 3.2), the Kluane Schist defines an inverted, hot-side-up metamorphic field gradient towards its contact with the Ruby Range batholith (Fig. 3.2; e.g., Muller, 1967; Erdmer & Mortensen, 1993; Mezger *et al.*, 2001; Israel *et al.*, 2011a, b). A normal metamorphic field gradient is also observed to reach at least staurolite-grade along the southeastern edge of Kluane Lake (Figs. 3.2 and 3.3). The symmetry of mineral assemblages about the core of the Kluane Schist recorded in this and previous studies potentially reflects an extension of the overturned southern limb of the east plunging antiform observed to the west (Fig. 3.2; e.g., Mezger, 1997). Combined, our detailed petrography and fieldwork, using over 300 field localities and 65 thin sections, suggests that the evolution of major structures observed across the Kluane Schist is intrinsically linked to the mineral assemblages preserved. As such, we divide the Kluane Schist into seven unique

petrological zones which consist of units with a distinct combination of mineral assemblage, microstructure, and outcrop style (Figs. 3.2 and 3.3).

Fabrics preserved in the Kluane Schist

The structures observed across the petrologic zones within the Kluane Schist are consistent with two distinct phases of deformation (Figs. 3.2–3.4). The first of these, D_1 , is best preserved within the lowest-grade units of the Kluane Schist in the form of a bedding parallel chlorite–muscovite–titanite–calcite foliation, S_1 (Figs. 3.3i and 3.5a-b). Striking west and dipping moderately to the north, S_1 is the lowest-grade fabric observed across the Kluane Schist (Fig. 3.3a). To north and south, this foliation is progressively transposed by a second phase of deformation, D_2 , into a penetrative, regional S_2 foliation (Figs. 3.2 and 3.3a). The progressive transposition of S_1 is recorded across the Kluane Schist by: 1) initial crenulation of S_1 to form an oblique S_{2a} fabric that commonly defines an axial planar cleavage to symmetrical F_{2a} folds (Figs. 3.3h, and 3.5b), and 2) the progressive reorientation of S_{2a} into a pervasive WNW-striking, NNE-dipping biotite-rich foliation, S_{2b} (Fig. 3.3f). S_{2b} is commonly accompanied by symmetrical, rootless and isoclinal F_{2b} folds (Fig. 3.3f). Within the highest-grade units of the Kluane Schist, biotite-rich S_{2b} folia are progressively coarsened and segregated to form a cm-scale gneissic banding (Fig. 3.3b).

D_{1-2} generally records a period of coaxial flattening deformation dominated by S-tectonites defined by S_{1-2a} fabrics and planar S_{2b} folia (Figs. 3.3 and 3.4). At low metamorphic grade, units show symmetric pinch and swell structures (Fig. 3.3i), while medium-grade units show symmetric F_{2a} and F_{2b} folds (Fig. 3.3f, h) along with the symmetrical wrapping of the matrix around porphyroblasts of index minerals that contain straight inclusion trails (Fig. 3.3g). These observations all imply the predominance of pure shear and flattening during early Kluane Schist deformation (e.g., Spry, 1974; Law, 1986; Mukherjee, 2017). At higher metamorphic grades poikiloblasts exhibit rotated inclusion trails and are commonly asymmetrically wrapped by the matrix foliation (Fig. 3.3e). This is attributed to a greater influence of simple shear during higher-grade metamorphism and later-stage Kluane Schist deformation (Figs. 3.3 and 3.4; e.g., Zwart, 1962; Brown *et al.*, 1995; Mezger, 2010). In general, our observations consistently document greenschist- to granulite-facies metamorphism coeval with evolving deformation (Figs. 3.3 and 3.4). The annealing and coarsening of mineral assemblages and the overgrowth of the S_{2b} gneissic fabric is observed within the structurally highest units of the Kluane Schist, approaching the contact with the overlying Ruby Range batholith (Fig. 3.3).

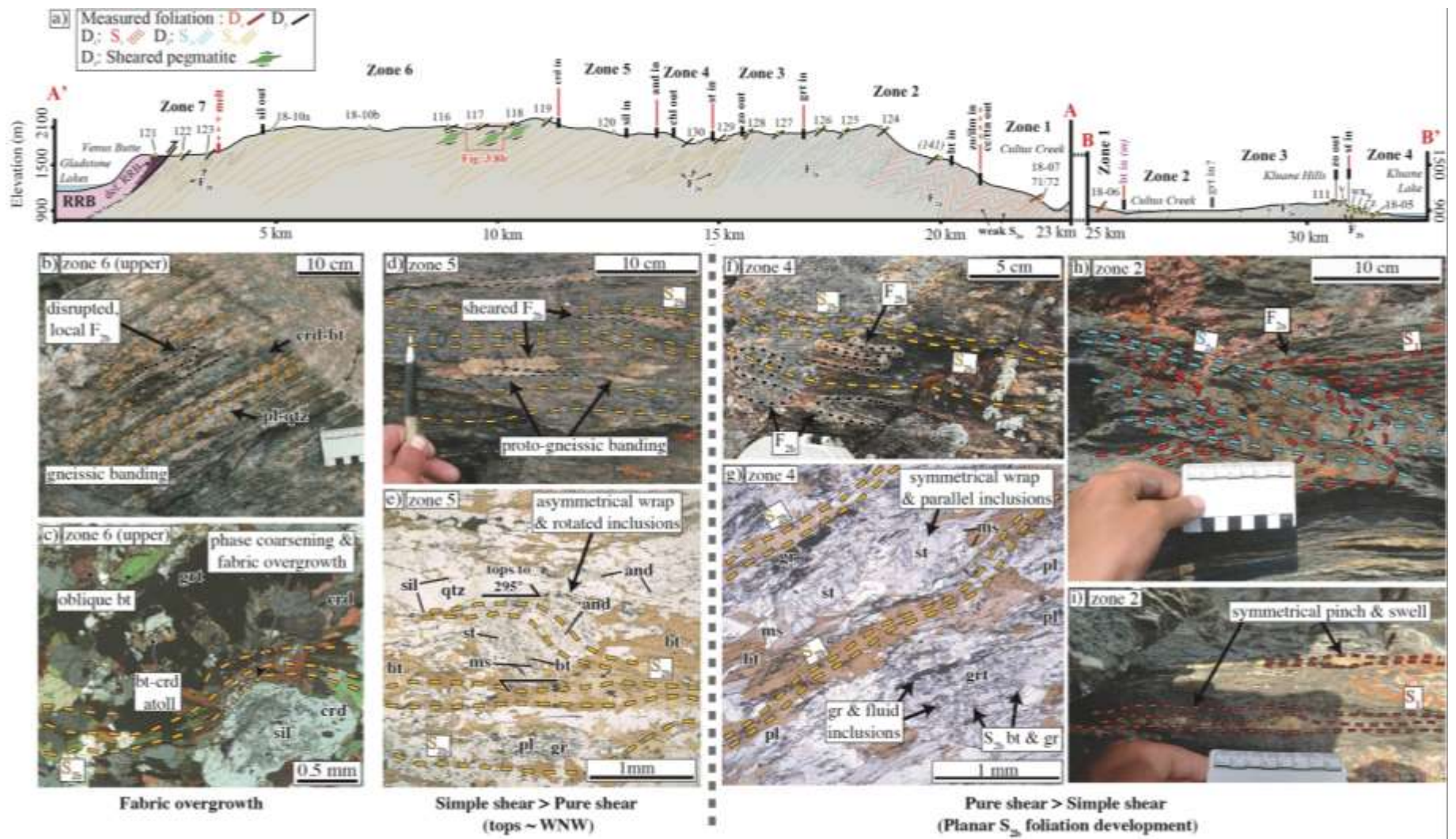


Figure 3.3. a) Cross section for lines A-A' and B-B' in Figure 3.2 highlighting the relationship between petrologic zone and structural level across the Kluane Schist. Field stations are labelled and highlighted by yellow triangles (In B-B': v = 110; w = 109; x = 108; y = 106; z: 105/20-40). Average foliation measurements are indicated by short solid lines (Red = D₁, black = D₂). Bracketed and italic sample numbers (e.g., *141*) represent measurements and observations that are projected onto the line of section from nearby localities. Observed fabrics and fold geometries (D₂) are projected into the subsurface. The sense-of-shear recorded by pegmatites (D₃), where observed, is also indicated. Isograds are directly labelled and indicated by thick solid lines. Photos (b–i) document the typical structures and index minerals characteristic to each petrologic zone and are discussed in detail in the main text.

Deformation phase:	D ₁ (zone 1)	Early D ₂ (zone 1 - 3)	Mid-D ₂ (zone 4)	Late-mid D ₂ (zone 5 - 6)	Late D ₂ Pre-D ₃ (zone 6 - 7)	Regional 'overprints'		
Mineral growth:						D ₁	D ₂	
Quartz	—	—	—	—	—	<i>tops to the SW/SSW shearing & L-tectonite development</i>	—	
Titanite	—	—	—	—	—		—	
Chlorite	—	—	—	—	—		—	—
Calcite	—	—	—	—	—		—	—
Zoosite	—	—	—	—	—		—	—
Muscovite (ms)	—	—	—	—	—		—	—
Muscovite (cel)	—	—	—	—	—		—	—
Plagioclase (ab)	—	—	—	—	—		—	—
Plagioclase (a/o)	—	—	—	—	—		—	—
Biotite	—	—	—	—	—		—	—
Garnet ₂₀	—	grt ₂₀	grt ₁₀	—	—		—	—
Garnet ₁₀	—	—	—	grt ₁₀	grt ₁₀		—	—
Staurolite	—	—	—	—	—		—	—
Andalusite	—	—	—	—	—		—	—
Sillimanite (F)	—	—	—	—	—		—	—
Sillimanite (P)	—	—	—	—	—		—	—
Ilmenite	—	—	—	—	—		—	—
Hematite	—	—	—	—	—		—	—
Cordierite ₀₁	—	—	—	—	—		—	—
Cordierite ₀₂	—	—	—	—	—		—	—
K-Feldspar	—	—	—	—	—	—	—	
Leucosome	—	—	—	—	—	—	—	
Graphite (matrix)	—	—	—	—	—	—	—	
Fabrics & Structures developed:	S ₁	F _{2a} - S _{2a} (pure shear)	F _{2b} - S _{2b} - L ₂ (pure shear)	Simple shear of F _{2b} & S _{2b}	S _{2b} coarsening & overgrowth	F ₃ - L ₃ (simple shear)	F ₄	

Figure 3.4. Box plot summarising the stability of different minerals with distinct deformation events and petrologic zones across the Kluane Schist. Solid lines show when each mineral is stable, dashed lines represent metastable mineral preservation. Ms = muscovite; cel = celadonite; ab = albite; a/o = andesine/oligoclase; Sillimanite (F) = fibrolitic sillimanite; Sillimanite (P) = prismatic sillimanite; grt(x) = garnet population x (see main text). Graphite stability refers to just that within the matrix, not porphyroblasts.

Petrological Zones of the Kluane Schist

Zone 1: chlorite–muscovite schist. The lowest grade units of the Kluane Schist are found at its structurally lowest levels (Fig. 3.3). Zone 1 units are lustrous and silver-blue in appearance (Fig. 3.5a insert). Compositional banding (S_0) is readily observed in outcrop and defined by distinct carbonaceous, quartz-rich and mica-rich layers (Fig. 3.5a). The more aluminous mica-rich domains contain plagioclase porphyroblasts along with muscovite and chlorite (Fig. 3.5a insert). Millimetre-scale quartz banding is often seen parallel to compositional banding.

Zone 1 schists consist of a mineral assemblage containing chlorite–muscovite–plagioclase–quartz +/- titanite–calcite (Fig. 3.5b). Muscovite–chlorite–titanite–calcite defines S_1 , which is overgrown by plagioclase with inclusions of titanite, quartz, chlorite, muscovite, and graphite (Fig. 3.5b). S_1 fabrics are locally crenulated into a muscovite-rich S_{2a} (Fig. 3.5b). Plagioclase is wrapped by S_{2a} and often preserves inclusion trails oblique to both S_1 and S_{2a} (Fig. 3.5b). Centimetre-scale, close to tight F_{2a} folds are locally observed within outcrop. S_1 foliations are more strongly crenulated within the hinge zones of these F_{2a} folds (Fig. 3.3h).

Zone 2: biotite-zoisite schist. Moving away from the core of the Kluane Schist, metamorphic grade increases with structural level (Figs. 3.2 and 3.3). Zone 2 rocks are a darker blue colour and less lustrous than in zone 1 (Fig. 3.3h). Quartz bands appear coarser and locally recrystallized (Fig. 3.3h). S_0 is difficult to make out in outcrop due to a more pervasive overprinting by tight and reclined F_{2a} folds (Fig. 3.3h). S_1 represents the dominant planar fabric within zone 2 and is defined by an assemblage of chlorite–muscovite–quartz–plagioclase–graphite +/- ilmenite–biotite–zoisite (Fig. 3.5 c, d). The assemblage of zone 2 lacks titanite and shows a reduction in calcite abundance compared with zone 1 (Fig. 3.5 c, d). Muscovite shows an increased abundance in zone 2 while chlorite abundance is reduced compared with zone 1 (Fig. 3.5c, d). S_{2a} fabrics are strongly developed within F_{2a} fold hinges and comprise biotite–zoisite–muscovite–ilmenite–graphite +/- chlorite–hematite (Fig. 3.5d). Graphite is more abundant in zoisite bearing lithologies. Biotite is seen upgrade of zoisite and is associated with the strong development of S_{2a} fabrics (Fig. 3.5d). Biotite abundance steadily increases moving upgrade across zone 2, while chlorite and muscovite decrease in abundance. S_{2a} fabrics are strengthened with increased structural level and metamorphic grade and are commonly observed to crosscut chlorite-rich S_1 fabrics within the highest-grade units of zone 2 (Fig. 3.5d). Plagioclase porphyroblasts preserve rotated S_1 inclusion trails and are wrapped by the S_{2a} fabric (Fig. 3.5c).

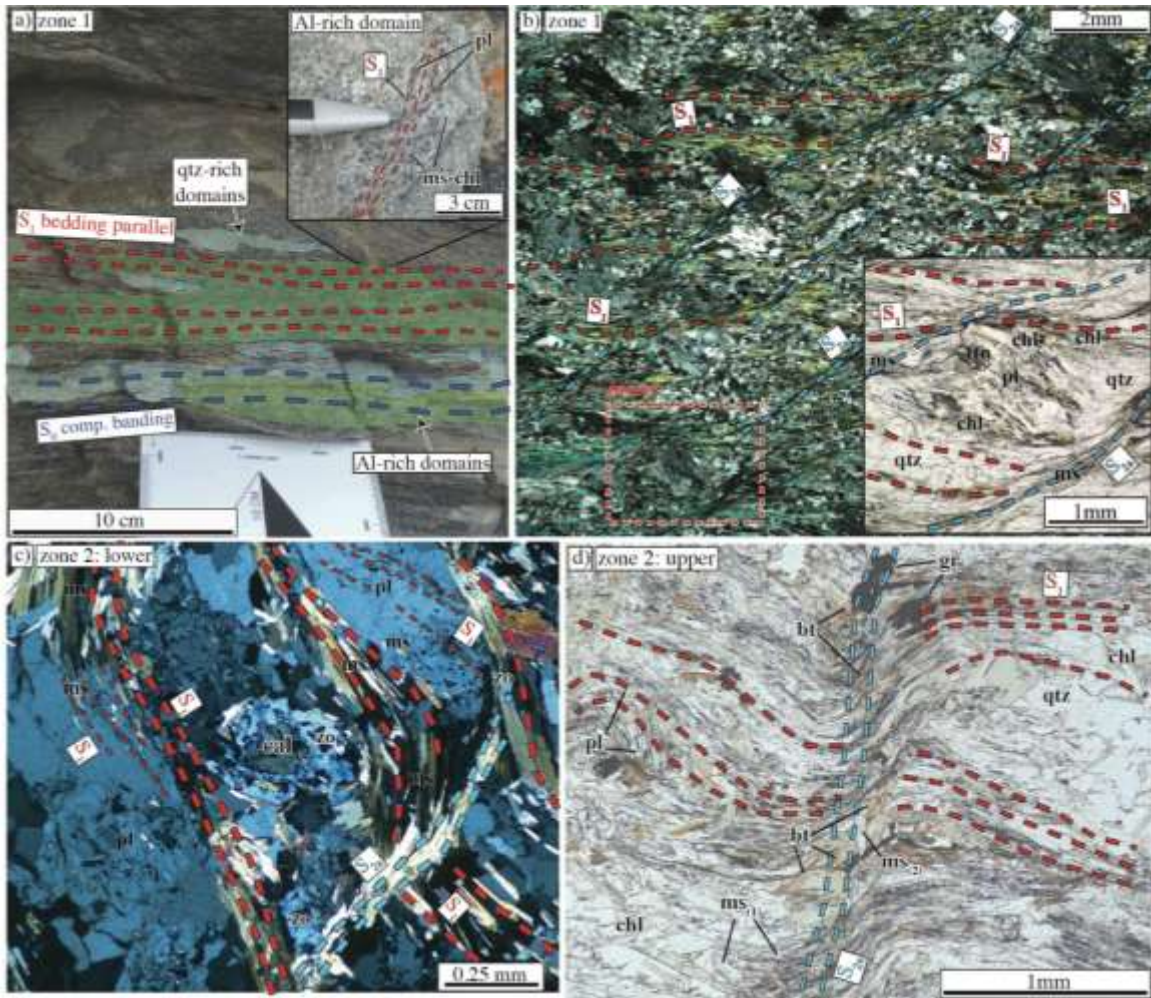


Figure 3.5. Outcrop photos and photomicrographs from zones 1 and 2. a) Muscovite-rich schist, typical of zone 1 towards the centre of the Kluane Schist (07b and 06 in Fig. 3.2). Centimetre-scale dark and light compositional bands (blue and green highlight) reflect original bedding (S_0). Insert shows muscovite–chlorite S_1 fabric overgrown by plagioclase porphyroblasts. b) Photomicrograph of zone 1 schist showing the relationship between fabrics and chlorite–muscovite–titanite assemblage. Note: inclusion trails in plagioclase (yellow dashed lines in insert) are oblique to matrix fabrics. c) Photomicrograph of a lower-grade sample within zone 2; the muscovite–chlorite S_1 fabric is overgrown by plagioclase and the muscovite-rich S_{2a} fabric. S_{2a} wraps zoisite and plagioclase. Calcite is observed as rare inclusions to zoisite. d) Photomicrograph of a higher-grade zone 2 sample. Biotite is associated with a second generation of muscovite $ms(2)$, with both primarily occurring in S_{2a} orientations.

Zone 3: garnet-biotite schist. Continuing up structural section from zone 2, the Kluane Schist is distinctly darker in colour, losing the blue hue common to the lower-grade units (Fig. 3.6a). All traces of S_0 are lost in zone 3 outcrops (Fig. 3.6a). Quartz banding is regularly spaced and is parallel to S_{2a} (Fig. 3.6a). Reclined F_{2a} folds are tightened and often dismembered moving up-section within zone 3 (Fig. 3.6a). Although these folds are tighter and almost isoclinal in places, F_{2a} can still be readily identified within a given outcrop and their symmetrical geometry can be traced at the metre-scale (Fig. 3.6a).

The typical mineral assemblage of zone 3 consists of biotite–plagioclase–muscovite–garnet–chlorite–quartz–ilmenite +/- zoisite–calcite (Fig. 3.6b, c, d). Both garnet and plagioclase host inclusions of zoisite and calcite within the lowest grade regions of zone 3 (Figs. 3.6b, c and A6). At these lower grades, garnet shows macroscopically rational crystal face development with its radial, hexagonal growth pattern outlined by matrix graphite and inclusions of quartz and zoisite (Fig. 3.6b). Zoisite is lost from the assemblage a short distance up-grade of the first appearance of garnet (Fig. 3.6c *versus* 3.6d). Within these zoisite-free assemblages garnet remains coarse, albeit less euhedral, and is partially wrapped by S_{2a} (Fig. 3.6d). At these higher grades garnet hosts inclusions of S_1 quartz, biotite, graphite, and calcite (Fig. 3.6d). Plagioclase is abundant throughout zone 3 assemblages, typically hosting chlorite, graphite and biotite inclusion trails that align with relic S_1 fabrics (Fig. 3.6d). Plagioclase also commonly has distinctly inclusion free rim domains which show partial wrapping by the S_{2a} fabric (Fig. 3.6b, d). Chlorite and muscovite show a decreased abundance compared with zones 1 and 2 and are largely restricted to S_1 orientations (Fig. 3.6d). The more dominant S_{2a} foliation is primarily defined by biotite (Fig. 3.6d). This microstructural-mineral relationship is progressively reinforced with increased metamorphic grade across zone 3 (Fig. 3.6b, c, d).

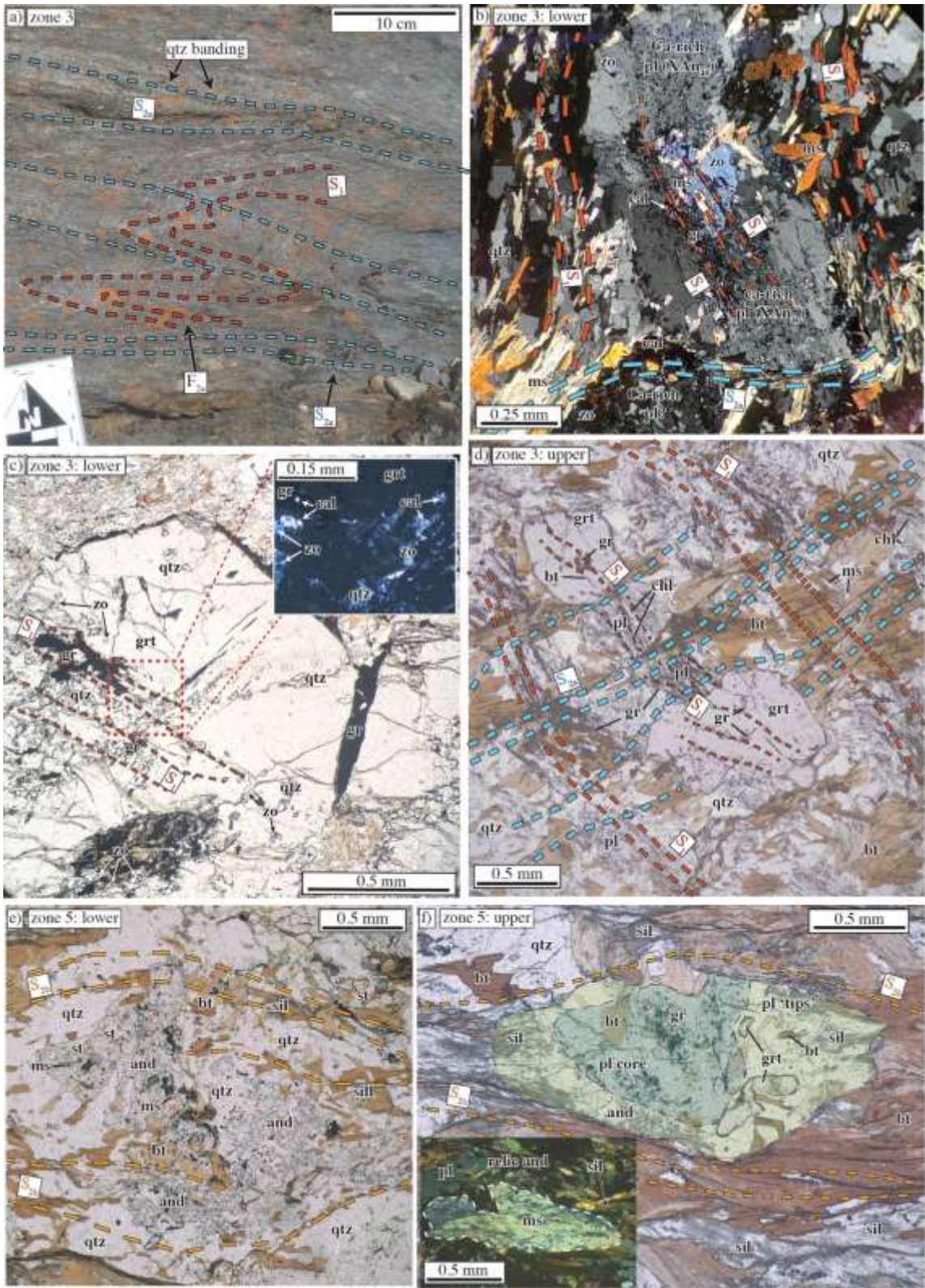


Figure 3.6. a) Outcrop photo of a zone 3 schist showing tight F_{2a} folds which are reclined and axial planar to a strong S_{2a} fabric. b) Photomicrograph of plagioclase typical of the lowest-grades units of zone 3. Ca-rich plagioclase cores include zoisite and calcite, overgrow S_1 and are wrapped by S_{2a} . c) Photomicrograph of garnet typical of the lowest-grades units of zone 3. Garnet is coarse, well-faceted and hosts inclusions of calcite, zoisite and S_1 aligned graphite and quartz. d) Photomicrograph of a higher-grade zone 3 schist. Coarse euhedral garnet hosts S_1 aligned inclusions and is partially wrapped by a strong biotite-rich S_{2a} which overprints the relic chlorite-graphite S_1 . e) Photomicrograph of a lower-grade zone 5 sample, knotty andalusite poikiloblasts are intergrown with quartz and the S_{2b} fabric and host inclusions of muscovite, biotite and staurolite. Staurolite remains as the dominant porphyroblast within this sample. f) In higher grade zone 5 assemblages fibrolitic sillimanite is associated with biotite-rich fabrics. Note: plagioclase shows distinct tips which are elongate into S_{2b} fabric orientations and host inclusions of andalusite, fibrolitic sillimanite and inclusion-free garnet. Insert shows a relic andalusite porphyroblast wrapped by biotite-rich S_{2b} and replaced by muscovite.

Zone 4: staurolite schist. Structurally above zone 3, the staurolite-bearing mineral assemblages that define zone 4 are observed (Figs. 3.2 and 3.3). Rocks of zone 4 are dark in colour and S_{0-1} , S_{2a} and F_{2a} are no longer observed in outcrop (Fig. 3.3f). Instead, outcrops are dominated by S_{2b} and isoclinal F_{2b} intra-folia folds (Fig. 3.3f). Quartz banding is penetrative and regularly spaced, paralleling S_{2b} (Fig. 3.3f).

The assemblage typical of zone 4 rocks consists of staurolite-biotite-muscovite-plagioclase-quartz-ilmenite +/- garnet-chlorite (Fig. 3.3g). There is a reduced abundance of muscovite and chlorite as compared with zones 1-3. Staurolite and plagioclase form the major porphyroblasts within zone 4. Staurolite exhibits a prismatic habit, elongate parallel to, and wrapped by the biotite S_{2b} foliation (Fig. 3.3g). Plagioclase porphyroblasts are wrapped by S_{2b} and contain inclusion trails of graphite and biotite that are oblique to S_{2b} . Garnet occurs locally in aluminous domains and has a cloudy appearance due to abundant graphite and fluid inclusions (Fig. 3.3g). Garnet rims show an embayed texture and are locally infilled by quartz, biotite, muscovite and occasionally plagioclase (Fig. 3.3g). Garnet is wrapped by S_{2b} fabrics and shows inclusions of quartz and S_{2b} -oriented biotite and graphite (Fig. 3.3g). This relationship suggests garnet grew syn-kinematically during S_{2b} development.

Zone 5: andalusite/sillimanite schist. Continuing up structural section, outcrops within zone 5 are dark in colour and dominated by a biotite-rich S_{2b} schistosity along with a centimetre-scale penetrative quartz banding (Fig. 3.3d). This penetrative quartz-rich banding can be seen

to have developed through the shearing out of rootless F_{2b} fold limbs into the foliation plane (Fig. 3.3d). This transposition of F_{2b} folds within zone 5 lithologies marks the initial development of the distinct gneissic banding common to units within zones 6 and 7. Upgrade across zone 5, the occurrence of F_{2b} folds decreases as the Kluane Schist is progressively dominated by a coarse and regularly spaced gneissic band (Fig. 3.3b, d).

Directly upgrade of zone 4, the rocks of zone 5 consist of the assemblage andalusite–plagioclase–biotite–garnet–ilmenite +/- muscovite–staurolite–sillimanite (Fig. 3.6e). Andalusite first appears as knotty anhedral porphyroblasts that in are locally intergrown with the S_{2b} fabric and quartz (Fig. 3.6e). Graphite is largely lost from the matrix of zone 5 lithologies, only observed as inclusions within coarser porphyroblasts (Fig. 3.6e). Staurolite occurs as relic porphyroblasts within zone 5 with their direct replacement by andalusite evidenced by local staurolite relics remaining preserved as inclusions within andalusite poikiloblasts (Figs. 3.3e and 3.6e). Andalusite poikiloblasts also host biotite, muscovite, and quartz inclusions (Figs. 3.3e and 3.6e). Most andalusite grains are wrapped by S_{2b} fabrics and appear elongate and aligned with S_{2b} . In some domains andalusite has curved biotite inclusions trails, suggesting it grew syn-kinematically during clockwise non-coaxial shear (Fig. 3.3e). Prismatic plagioclase also shows elongation parallel to the S_{2b} fabric within zone 5 (Fig. 3.6f). Plagioclase cores host a variety of inclusion orientations like that seen in zone 4. In contrast, the tips of prismatic plagioclase are distinctly graphite free and locally show inclusions of fine biotite, andalusite and fibrolitic sillimanite with S_{2b} orientations (Fig. 3.6f). Garnet is also observed within zone 5 assemblages. Garnet is euhedral and shows distinctly inclusion-free outer domains, mantled on the cloudy, fluid inclusion-rich cores common to zone 4 (Fig. 3.7c). Finer, inclusion-free garnet is also observed included within graphite free plagioclase domains (Fig. 3.6f). Muscovite is less abundant compared with zone 4, and is observed within S_{2b} fabrics and included within andalusite porphyroblasts (Figs. 3.3e and 3.6e).

Higher-grade units within zone 5 show an increased abundance of fibrolitic sillimanite where it generally occurs associated with biotite-rich S_{2b} fabrics (Fig. 3.6f). The abundance of fibrolitic sillimanite within zone 5 assemblages coincides with the replacement of relic andalusite porphyroblasts with muscovite and the growth of prismatic plagioclase tips (Fig. 3.6f, insert). Locally within higher grade regions of zone 5, prismatic sillimanite occurs along with fibrolitic sillimanite (Figs. 3.2 and 3.7a). Andalusite and staurolite are absent from these units. Prismatic sillimanite occurs parallel to S_{2b} , wrapping both garnet and plagioclase (Fig. 3.7a). Within these units, clear inclusion-poor garnet porphyroblasts are wrapped by S_{2b} fabrics.

Garnet cores host inclusion of quartz, biotite and rare graphite that run oblique to the S_{2b} fabric, while garnet rims are distinct and inclusion-free (Fig. 3.7a).

Zone 6: cordierite gneiss. Farther up structural section, zone 6 outcrops are dominated by a coarse, centimetre-scale penetrative gneissic banding and often take on a faint orange colour (Fig. 3.3b). Cordierite abundance increases rapidly within zone 6, occurring primarily within darker, biotite-rich bands, while lighter bands consist of quartz and plagioclase (Fig. 3.7c). This change in petrology and structure has led previous workers to suggest these gneissic units may be of different affinity to the Kluane Schist (Erdmer, 1991; Mortensen and Erdmer, 1993; Israel *et al.*, 2011a, b). However, rare relic F_{2b} folds can be found that, although are typically dismembered, show a similar geometry to those downgrade (Fig. 3.3a, b). Within the highest-grade regions of zone 6, gneissic banding remains penetrative, but is coarser and the contrast between light and dark bands is undulous and irregular (Fig. 3.3b).

The structurally lowest lithologies of zone 6 consist of an assemblage including cordierite–biotite–quartz–plagioclase–muscovite–ilmenite +/- garnet–andalusite–sillimanite–staurolite (Fig. 3.7b). Abundant elongate cordierite is associated with the biotite–muscovite S_{2b} fabric and can be seen wrapping local poikiloblasts of andalusite and staurolite, which show limited evidence of corrosion (Fig. 3.7b). Andalusite poikiloblasts generally lack the muscovite inclusions observed within zone 5 (Fig. 3.7b). Upgrade within zone 6 prograde muscovite is also lost from the S_{2b} fabric (Fig. 3.7c). The euhedral, graphite free garnet crystals typical of zone 5 also show strong corrosion and embayment by cordierite within these higher-grade gneisses (Fig. 3.7c). Fibrolitic sillimanite occurs towards the base of zone 6 and shows a general decrease in abundance moving structurally upward with a corresponding increase in cordierite (Figs. 3.7b *versus* 3.7c *versus* 3.3c). The majority of plagioclase porphyroblasts show alignment with the S_{2b} fabric and host inclusions of biotite, quartz, and graphite, but never cordierite (Fig. 3.7c). Instead, cordierite can be seen to wrap both plagioclase and garnet (Fig. 3.7c). Within the highest-grade units of zone 6, cordierite is coarse and euhedral, often overgrowing bundles of fibrolitic sillimanite and S_{2b} fabrics (Fig. 3.3c). Fibrolitic sillimanite-free biotite shows coarsening and growth semi-oblique to the S_{2b} fabric and local garnet shows atolls of biotite and cordierite (Fig. 3.3c). Both cordierite and biotite retain a general orientation sub-parallel with S_{2b} fabrics (Fig. 3.3c).

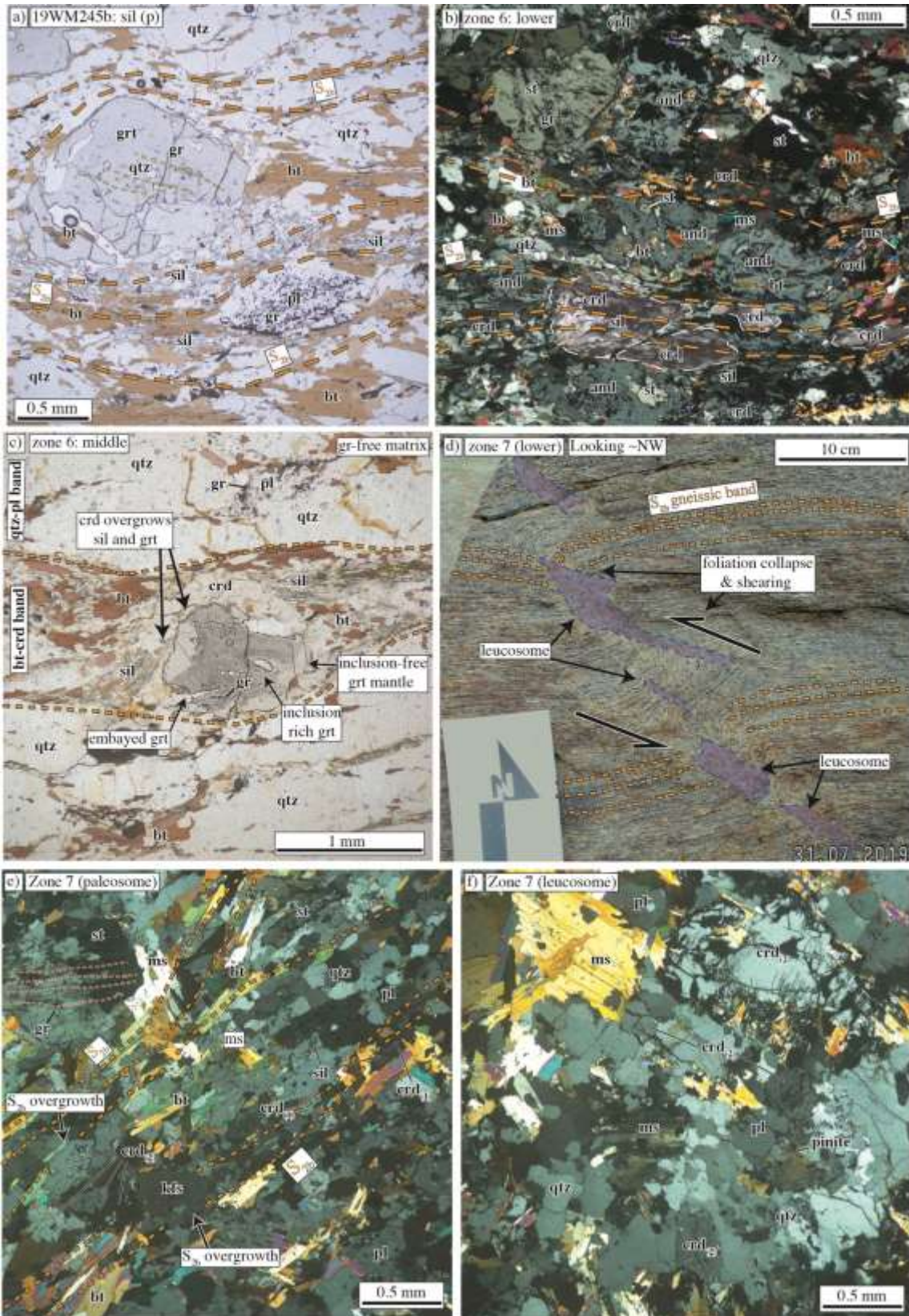


Figure 3.7. a) Photomicrograph of sample 19WM245b (245b in Fig. 3.2) highlighting the occurrence of prismatic sillimanite within staurolite-free zone 5 assemblages. Sillimanite tracks the biotite-rich S_{2b} fabric and wraps inclusion-poor garnet. Oriented garnet inclusion trails are highlighted by yellow dashed lines. b) Photomicrograph showing the assemblage common to the lower-grade units of zone 6; cordierite occurs within, and aligned with, the biotite–muscovite–sillimanite S_{2b} fabric. Andalusite and staurolite occur as largely uncorroded porphyroblasts. c) Photomicrograph of a typical zone 6 assemblage. Cordierite replaces sillimanite and garnet and is entrained within the S_{2b} gneissic fabric. d) Outcrop photo of polymineralic leucosome lenses apparent within the lower grade regions of zone 7. The aligned lenses of leucosome appear to result from sinistral shearing and foliation collapse. e) Photomicrograph of paleosome domains within a zone 7 gneiss. K-feldspar, cordierite and muscovite overgrow a biotite-rich S_{2b} fabric. Note: two generations of cordierite; $crd_{(1)}$ is aligned with the S_{2b} fabric and hosts sillimanite inclusions while $crd_{(2)}$ overgrows S_{2b} and lacks sillimanite inclusions. f) Photomicrograph of the leucosome within zone 7. Retrograde muscovite overgrew these phases in random orientations.

Zone 7: migmatite. Polymineralic plagioclase–quartz–cordierite leucosome appears to be locally developed within isolated northern regions of the Kluane Schist (Figs. 3.2 and 3.7f). Plagioclase and cordierite are euhedral and equant, and do not have a particular shape preferred orientation (Fig. 3.7f). Quartz is coarse and irregular in shape showing undulous extinction and apparent quartz–plagioclase–plagioclase dihedral angles $<45^\circ$ (Fig. 3.7f). Spongy and randomly orientated muscovite and chlorite are interpreted as retrograde phases (Fig. 3.7f). Towards the southern edge of zone 7 (Figs. 3.2 and 3.3) stromatic migmatites occur (Fig. 3.7d), while towards the north and in contact with the Ruby Range batholith zone 7 contains schollen-style migmatites (Mehnert, 1968). Locally, in areas which have undergone foliation collapse or folding, leucosome within stromatic migmatites can take on a star or web appearance (Fig. 3.7d). Consistent tops-to-the-SSW orientation among these structures suggests melt migration into several sinistral shear bands (Fig. 3.7d; e.g., Brown *et al.*, 1995).

Paleosomes within zone 7 are typically a faint orange colour and consists of quartz–biotite–cordierite–plagioclase +/- K-feldspar–garnet–fibrolite (Fig. 3.7d, e). A regularly spaced, centimetre-scale gneissic banding is present and is similar to that observed within zone 6 (Fig. 3.7d, e). F_{2b} folding is not readily observed within outcrop. Rare, corroded staurolite are present and preserve aligned graphite inclusion trails like those seen in zone 4 (Fig. 3.7e). Garnet is anhedral and corroded, preserving atolls of muscovite, chlorite, and cordierite. Fibrolitic sillimanite shows a marked decrease in abundance, only locally occurring as inclusions within

coarse cordierite (Fig. 3.7e). Local K-feldspar is associated with biotite-rich domains and appears to overgrow biotite S_{2b} fabrics (Fig. 3.7e). Cordierite shows two distinct populations within migmatic units; one roughly aligned with S_{2b} fabrics, which hosts sillimanite inclusions ($crd_{(1)}$) and a second which shows an irregular shape, overgrows S_{2b} and lacks sillimanite inclusions ($crd_{(2)}$; Fig. 3.7e).

Late deformation features

The rocks of the Kluane Basin experienced two additional deformation events prior to final exhumation (Fig. 3.4). These events, D_3 and D_4 , had a limited effect on the preserved mineral assemblage but act to modify the original orientation of the fabrics and petrologic zones developed during D_{1-2} .

D_3 occurred during a period of non-coaxial strain and is associated with the development of a mineral alignment lineation which trends NE–SW. In the sense-of-shear plane viewed parallel to the mineral alignment lineation, asymmetrical shear folds, F_3 , verge SSW to SW, and asymmetrical boudinaged quartz pegmatites provide a tops-to-the-SW sense of shear (Fig. 3.8). Both structures overprint previously developed S_2 fabrics and suggest a period of SSW-to SW-directed shear during D_3 (Fig. 3.8).

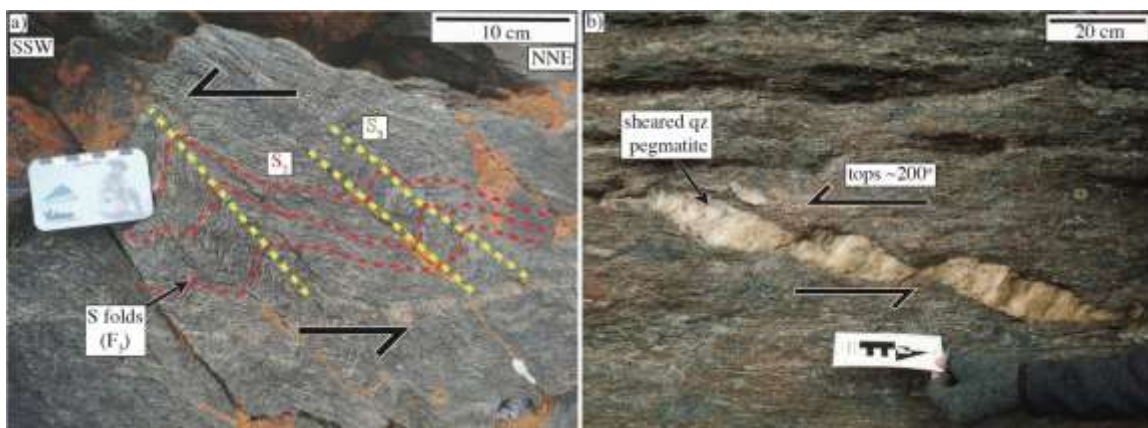


Figure 3.8. Later stage non-coaxial deformation (D_3) across the Kluane Schist. a) Asymmetric shear folds, F_3 . Red dashed lines highlight the form of F_3 and yellow dashed lines the axial traces with vergence towards the SSW. b) Coarse lensoidal quartz veins within a zone 6 outcrop that provide a tops-to-the-SW sense of shear (also see Fig. 3.3a).

D₄ is associated with the development of open buckle folds that are 10s m to km in wavelength and trend E-W with a moderate plunge in both directions (Fig. 3.2). These folds overprint all earlier fabrics (D₁₋₃) and are interpreted to have significantly post-dated their development, as suggested by their more brittle nature. D₄ likely led to the development of the east-plunging antiform which is observed to deflect our mapped mineral isograds and petrological zones within the central and southwestern regions of the Kluane Schist (Fig. 3.2).

3.4.2. Whole rock and mineral chemistry

The range of whole rock compositions from the Kluane Schist are summarized in Figure 3.9a, b. Trends in mineral composition as a function of petrologic zone are shown in Figure 3.9c–h. Figure 3.9i plots the zonation preserved by representative plagioclase crystals from zones 1 and 3–7. All raw whole rock and mineral chemistry data can be found in Tables D1 and E1-E6.

Whole rock chemistry

Whole rock compositions plot within a tight cluster in AFM space with limited apparent grade-dependent variation (Fig. 3.9a). Differences in Si, Na, and Ca for all samples are accounted for by projection from quartz and feldspar (Fig. 3.9a). An additional projection from apatite and ilmenite is applied to all whole rock compositions except for 18WM06 (“06” in Fig. 3.9a), where we project from titanite, rather than ilmenite, based on the observed mineral assemblage (c.f., Figs. 3.4 and 3.5b). Whole rock A' values [molar (Al-3K-Na-2Ca)/2] (Spear, 1993) range from 0.005–0.027, with difference in A' value showing no relation to metamorphic grade (Fig. 3.9a and Table D1). A' values of the Kluane Schist are typical of low-Al pelites, plotting below the garnet-chlorite tie line in AFM space (Fig. 3.9a; e.g., Thompson, 1957; Spear, 1993). We also observe a limited variability of 0.36–0.39 in whole rock [Mg/(Mg+Fe)] across the Kluane Schist (Fig. 3.9b and Table D1). Whole rock [Ca/(Ca+Na)] shows a larger variability between 0.13–0.34, however, when one muscovite schist sample is removed (“06” of zone 1), this difference is reduced to 0.28–0.34 (Fig. 3.9b and Table D1). The general lack of variation in the whole rock chemistry with changes in the mineral assemblage preserved suggests the distribution of our petrological zones across the Kluane Schist is not primarily controlled by bulk composition (c.f., Fig. 3.2).

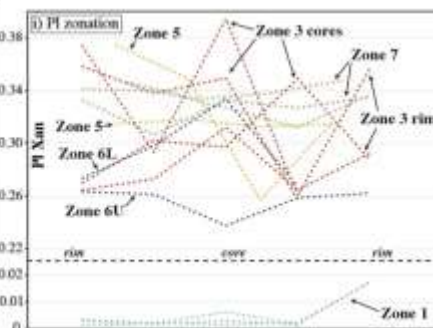
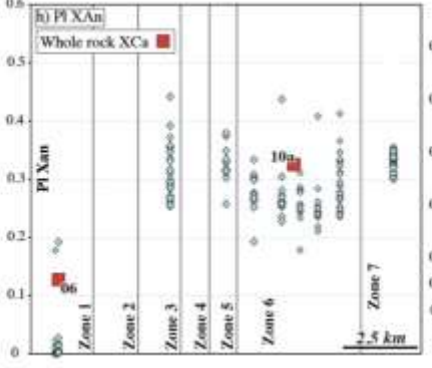
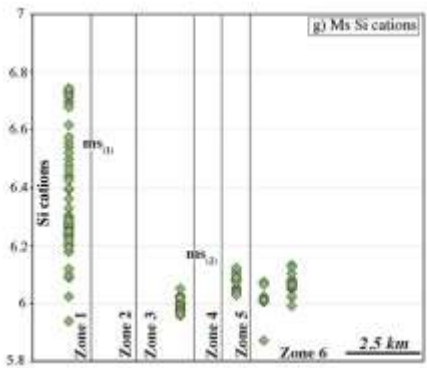
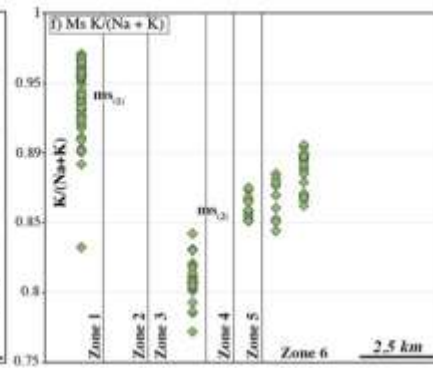
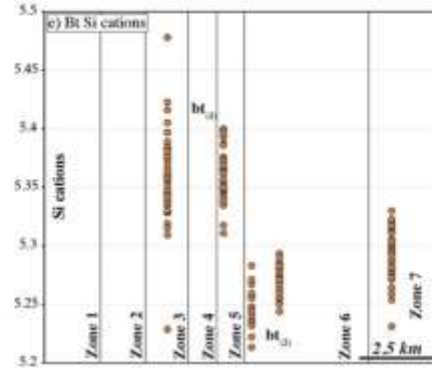
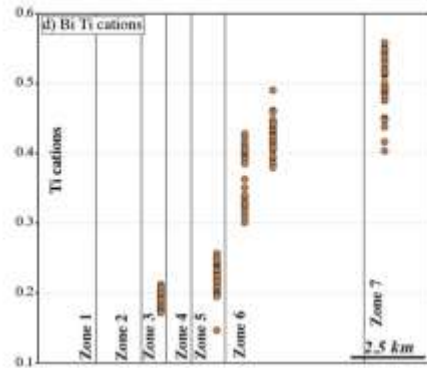
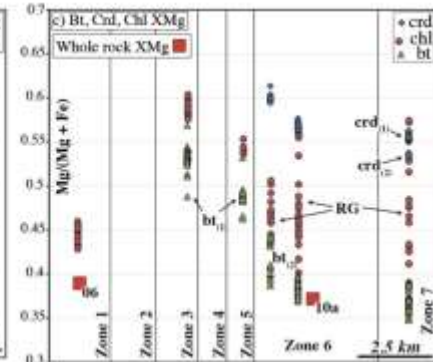
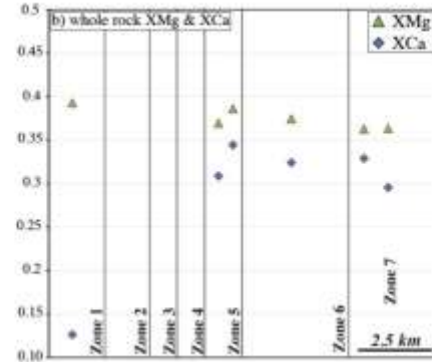
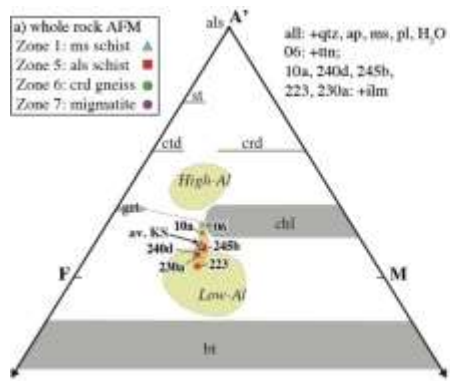


Figure 3.9. a) AFM diagram showing the plotting positions of whole rock XRF analyses across the Kluane Schist (red stars, Fig. 3.2). b) Variation in whole rock Mg/(Mg + Fe) (XMg) and Ca/(Ca + Na) (XCa) with petrological zone. c-h) Mineral chemistry v. petrological zone across the Kluane Schist (green stars, Fig. 3.2); in (c and h) we compare mineral chemistry with the bulk composition (red squares) of proximal samples (see Fig. 3.2). In (c, e, f, g) we highlight distinct populations of biotite (bt_{1/2}), cordierite (crd_{1/2}) and muscovite (ms_{1/2}) which are outlined further in the main text. i) plagioclase zonation with petrological zone.

Biotite, chlorite, and cordierite

Biotite, chlorite, and cordierite largely co-vary with a trend of decreasing Mg/(Mg + Fe) with increasing metamorphic grade between zones 3–7 (Fig. 3.9c). In contrast, chlorite within zone 1 shows the lowest average Mg/(Mg + Fe) across the Kluane Schist (Fig. 3.9c). The more widely spread Mg/(Mg + Fe) values obtained from chlorite within zones 6–7 (Fig. 3.9c) come from a secondary population which overgrows prograde fabrics. Cordierite shows two populations within zone 7 with distinct Mg/(Mg + Fe) values; these correlate with the two cordierite populations observed in thin section (Fig. 3.9c; i.e., crd₍₁₎ and crd₍₂₎ in Fig. 3.7e). Overall, the trends we observe in biotite, chlorite and cordierite Mg/(Mg + Fe) appear independent of whole-rock bulk composition (c.f., Fig. 3.9a, b, c). Additionally, biotite shows an increase in Ti across all petrological zones (Fig. 3.9d) with two distinct populations (bt₍₁₎ and bt₍₂₎) highlighted by a variation in Si cations between zones 5 and 6 (Fig. 3.9e). No systematic chemical zonation is observed across single mineral grains of biotite, chlorite, or cordierite (Tables E3–6).

Muscovite

Muscovite K/(Na + K) varies between 0.76–0.97 showing a decrease from an average of 0.94 in zone 1 to 0.81 in zone 3 (Fig. 3.9f). Zone 1 muscovite has the highest average K/(Na + K) across the Kluane Schist (Fig. 3.9f). From zone 3, muscovite K/(Na + K) increases with metamorphic grade from 0.81 in zone 3 to 0.87 in zone 6 where prograde muscovite is lost from the assemblage (Fig. 3.9f). The Tschermak content of muscovite, measured in this study as Si cations per 22-oxygen formula unit, shows significant spread in zone 1 with values ranging between 5.79–6.74 (average: 6.37; Fig. 3.9g). Upgrade muscovite shows a more restricted range of Tschermak contents between 5.87–6.13 with no significant variation with grade (Fig. 3.9g).

Plagioclase

Plagioclase compositions (X_{an}) range widely across the Kluane Schist (Fig. 3.9h). There is a significant increase in anorthite content moving between zone 1 and 3; plagioclase from zone 1 is almost entirely albitic ($X_{an} < 0.02$) while zones 3–7 exhibit a spread of compositions between oligoclase and andesine (Fig. 3.9h). This variation shows correlation with an increase in whole rock X_{an} (cf. Fig. 3.9b). Across zone 3–6 there is a general decrease in X_{an} and an overall reduction in the range of plagioclase compositions returned from each sample, except for the upper portion of zone 6 near the transition to zone 7 (Fig. 3.9h). Between zones 6–7 there is a slight increase in plagioclase X_{an} (Fig. 3.9h). Plagioclase zonation (in terms of X_{an}) is limited within zone 1 albite (Fig. 3.9i). Zone 3 plagioclase typically preserves more anorthite rich cores ($X_{an} \sim 0.31\text{--}0.39$) than rims ($X_{an} \sim 0.26\text{--}0.37$) (Fig. 3.9i). Within zones 5 and 6 plagioclase shows more variable zonation patterns with grains showing both normal and reverse zonation to no zonation at all (Fig. 3.9i). Zone 7 plagioclase generally lacks significant chemical variation (Fig. 3.9h, i).

Garnet

The Kluane Schist hosts four distinct populations of garnet. Each of these garnet populations has a unique chemistry outlined below. Full garnet chemical profiles can be found in Table E8.

(1) Coarse, euhedral graphite-rich garnet is common to zone 3 assemblages (e.g., Fig. 3.6c, d). Population (1) garnet cores are characterized by high-grossular (0.20 molar fraction) and spessartine contents (~ 0.16). Both grossular and spessartine then show steady decrease towards population (1) garnet rims (~ 0.05 , ~ 0.1 , respectively; Table E8). $Mg/(Mg + Fe)$ values generally show a steady increase from ~ 0.12 within garnet cores to ~ 0.16 at garnet rims (Table E8). A sharp increase in spessartine and decrease in $Mg/(Mg + Fe)$ is observed within $\sim 140\text{--}150\ \mu\text{m}$ of garnet rims (Table E8). The absence of other porphyroblasts within the analysed sample along with garnet preserving a generally euhedral texture (Fig. 3.6c, d) suggests this zonation pattern largely reflects growth rather than resorption (e.g., Pattison & Tinkham, 2009). The sharp increase in spessartine observed within garnet rims may reflect the consumption of ilmenite during garnet growth (e.g., Pattison & Tinkham, 2009). However, as ilmenite occurs within the matrix and we do not observe the associated Mg-enrichment suggested to accompany ilmenite breakdown, we instead interpret garnet rim chemistry to represent limited resorption (Table E8; e.g., Conolly & Cesare, 1993; Kohn & Spear, 2000; Pattison & Tinkham, 2009)

(2) Cloudy, embayed, and corroded garnet which is rich in fluid inclusions and associated with zone 4 staurolite bearing assemblages (e.g., Fig. 3.3g). Compositional profiles across cloudy population (2) garnet are highly variable (Table E8). Population (2) garnet typically preserves spessartine-rich, grossular-poor cores (Table E8). Core to rim Mg/(Mg + Fe) values for population (2) garnets are also highly asymmetrical and show an inconsistent variation between crystals (Table E8). All analysed crystals consistently record a sharp increase in spessartine content towards their rim coupled with a decrease in Mg/(Mg + Fe) that likely reflect a period of garnet resorption (Table E8; e.g., Kohn & Spear, 2000; Pattison & Tinkham, 2009). We interpret this resorption to reflect a period of garnet consumption during the growth of the Mg-rich staurolite that typifies both zone 4 and 5 assemblages across the Kluane Schist (e.g., Fig. 3.3g and Table E5; Dempster *et al.*, 2017).

(3) Inclusion free garnet which occurs mantled on cloudy garnet cores in zones 5–6 and as individual grains within zone 5 (e.g., Fig. 3.6f and 3.7c). Population (3) garnet appears in common association with zone 5-6 aluminium silicate bearing assemblages (Fig. 3.6f). Within these higher-grade assemblages both garnet populations (2 & 3) show more uniform chemical profiles compared with garnet downgrade (Fig. 3.10 and Table E8). However, we do observe a consistent change in garnet chemistry when traversing from inclusion-rich garnet cores to inclusion-free mantles (Fig. 3.10). There is a consistent decrease in grossular from 0.06 to 0.04 molar fraction and increase in almandine molar fraction from 0.72 to 0.74, which occurs over a narrow interval (<40 μm) where inclusion-free garnet was analysed adjacent to cloudy garnet (Fig. 3.10). The smaller, inclusion-free garnet grains within zones 5 and 6 (e.g., Fig. 3.6f) have similar chemistry to that of inclusion-free regions of larger garnet and are thus assigned to population (3) (dashed lines in Fig. 3.10). Towards the edge of these inclusion-free domains, within ~80–130 μm of garnet rims, increased spessartine and decreased Mg/(Mg + Fe) likely records a degree of garnet resorption (Fig. 3.10; Kohn & Spear, 2000; Pattison & Tinkham, 2009). This most likely occurs in response to cordierite growth as suggested by the association of our analysed garnet, cordierite, and sillimanite (Figs. 3.7c and 3.10).

(4) Corroded garnet within zones 6–7 which is often embayed by, and shows atolls of cordierite and biotite (e.g., Fig. 3.3c and 3.7c). Garnet population (4) lacks the systematic variation in chemistry with inclusion pattern as seen in zones 5–6 (Table E8). Uniform grossular and spessartine profiles are seen across all garnets from zone 7 (Table E8). Strong variation in garnet composition in proximity to cordierite atolls suggests exchange of cations and re-

equilibration with the surrounding rock matrix was the key driver for the chemical profiles preserved by zone 7 garnet (Table E8).

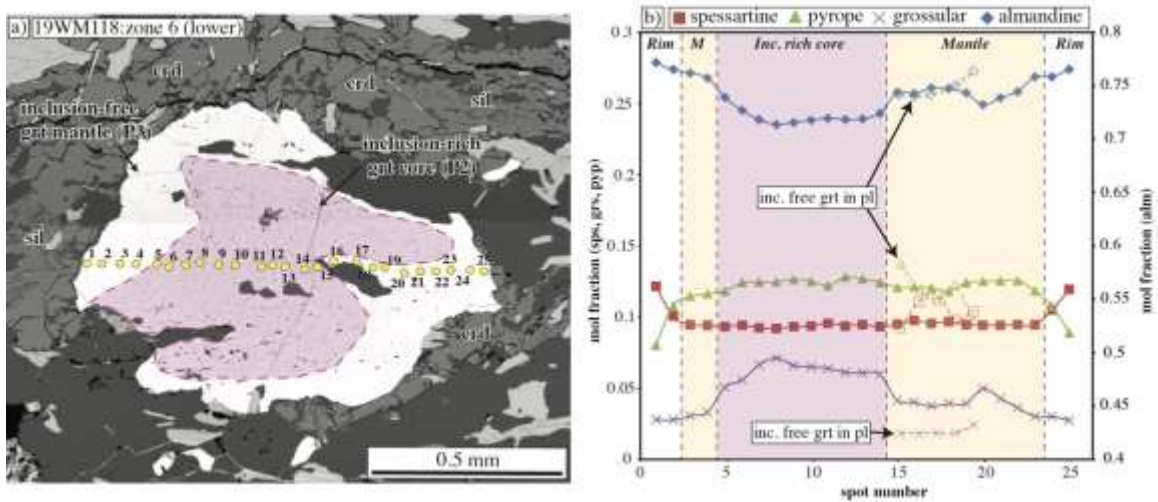


Figure 3.10. Garnet composition line profile. a) BSE image of a typical of a population (3) inclusion-free garnet mantling a population (2) cloudy core as described in the main text. Yellow spots outline location of probe analyses. b) Rim-to-rim profiles of end-member mole fractions of the garnet shown in (a); end-member mole fractions for a representative fine, inclusion-free garnet typical of zone 5 assemblages (see Fig. 3.6f) are also superimposed with dashed lines. (inc. free grt in pl = inclusion free garnet in plagioclase).

3.4.3. Garnet-hosted fluid inclusion composition and graphite crystallinity

Raman spectroscopy was completed on garnet-hosted fluid inclusions to provide an estimation of the a_{H_2O} during the metamorphism of the Kluane Schist, and thus improve the validity of our thermodynamic modelling (e.g., Bader *et al.*, 2014). Raman spectroscopy was completed on garnet-hosted fluid inclusions. Raman spectroscopy was also completed on garnet-hosted graphite mineral inclusions to provide an independent temperature estimate for Kluane Schist metamorphism.

Both fluid and graphite mineral inclusions are hosted exclusively in the inclusion-rich core of the analyzed garnet (population (2), sample 19WM118) which is enveloped in an inclusion-free rim (population (3); Fig. 3.11a). Graphite is absent from the rock matrix. This distribution suggests that the analyzed inclusions are primary in origin and were trapped during the early stages of garnet growth.

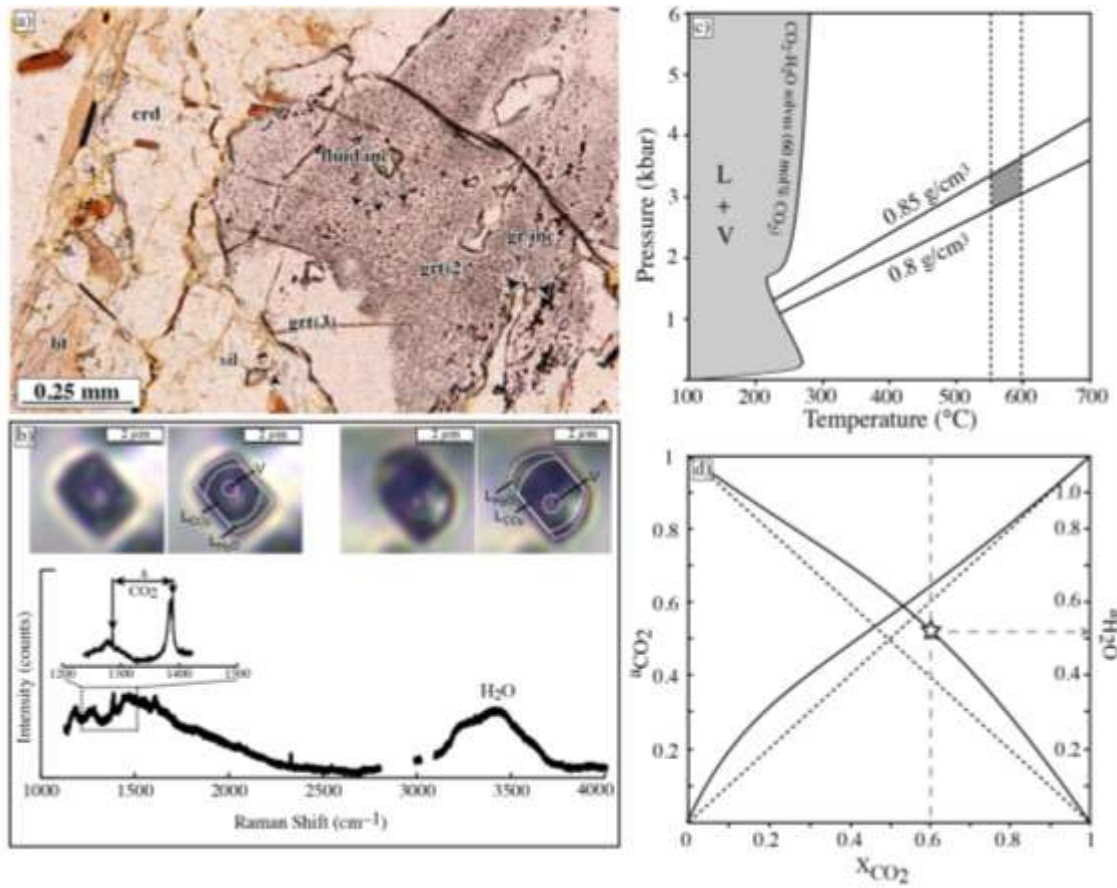


Figure 3.11. a) Fluid and graphite inclusions within garnet from sample 19WM118. b) Images of example fluid inclusions with their Raman spectrum, highlighting carbonic liquid and vapor. Carbonic liquid (L_{CO_2}) occupies the highest proportion at ~80 vol.% with other aqueous liquid (L_{H_2O}) ~15 vol.% and the innermost vapor bubble (V) ~5 vol.%. Comparison between these inclusions highlights the consistency in these ratios we observed during analysis. c) Fluid inclusion isochoric model. Maximum pressure of ~3.7 kbar calculated using an estimated total bulk density of 0.8–0.85 g/cm³ and temperature of 550–600 °C. d) CO₂–H₂O activity-composition relationships of Aranovich and Newton (1999) combined with our results from Raman spectroscopic analysis provide an estimation of $a_{H_2O} = 0.5$.

Visual estimation of the volumetric phase ratios in the fluid inclusions was challenging owing to the relatively high refractive index of garnet and the small inclusion size, which rendered many of the inclusions too dark to clearly observe the phase assemblage. However, in some inclusions the three-phase assemblage of aqueous liquid, carbonic liquid and vapor was identifiable by observing the motion of the vapor bubble, which “rattled” inside the carbonic liquid portion (Fig. 3.11b). In all such inclusions, the carbonic liquid fraction occupies the highest proportion of the inclusion volume at ~80 vol.%, whereas the outer aqueous liquid occupies ~15

vol.% and the innermost vapor bubble occupies ~5 vol.% (Fig. 3.11b). These estimated volume fractions were consistent between all analyzed inclusions, suggesting that the inclusions are unmodified and preserve the composition and density of the trapped fluid.

Raman spectroscopic analysis of the fluid inclusions showed that the OH-stretching band of H₂O is essentially the same as pure H₂O (Fig. 3.11b; Sun *et al.*, 2010), which indicates very low to negligible salinity of the aqueous liquid. In addition to the Raman peaks of the Fermi diad of CO₂ fluid, we also observe relatively strong Raman peaks at ~1276 and 1384 cm⁻¹ indicative of molecular CO₂ dissolved in the aqueous fluid (Fig. 3.11b; Frezzotti *et al.*, 2012). The Fermi diad itself overlaps somewhat with these latter peaks, and repeat analyses showed variable peak splitting (Δ) ranging from ~103 to 104.2 cm⁻¹, indicating carbonic fluid densities of both vapor (~0.2 g/cm³) and liquid CO₂ (~0.7 g/cm³), consistent with our visual observations (Fig. 3.11b). It should be noted that the vapor bubble generally moved around too rapidly to allow for targeted analysis of either liquid or vapor CO₂ independently, so each analysis likely sampled both fluids simultaneously. Nevertheless, by incorporating the visually estimated relative volume fractions of carbonic liquid and vapor, we were able to estimate the overall CO₂ density of ~0.68 g/cm³, a bulk composition of 60 mol.% CO₂ + 40 mol.% H₂O, and a total bulk density of 0.80-0.85 g/cm³.

We conducted isochoric modeling of the fluid inclusions based on the above constraints and using an estimated temperature range of 550-600 °C (Fig. 3.11c; solvus curve for an H₂O-CO₂ fluid of 60 mol.% CO₂ is reproduced from Connolly & Bodnar, 1983). Projection of the relevant fluid isochores to this temperature range yields a maximum pressure estimate of ~3.7 kbar at 600 °C (Fig. 3.11c).

The activities of H₂O and CO₂ were estimated based on the above constraints, as well as using the data of Aranovich and Newton (1999). An activity of H₂O of ~0.5 was obtained for an H₂O-CO₂ fluid of 60 mol.% CO₂ at 600 °C and 4 kbar (Fig. 3.11d). We acknowledge that such low water activities are unlikely to be related to the presence of graphite alone (Connolly & Cesare, 1993), particularly during the mineral dehydration associated with progressive garnet growth (Pattison, 2006). However, we highlight that garnet across the Kluane Schist typically hosts mineral inclusions of calcite (Figs. 3.6c and A6), suggesting the presence of calcite and/or a carbonate-rich fluid during early garnet growth. Recent Raman spectroscopy of garnet fluid inclusions associated with the presence of a carbonate-rich fluid produce $a_{\text{H}_2\text{O}}$ values in line with our own (0.1–0.65; Bader *et al.*, 2014).

Our Raman spectroscopic results of graphite mineral inclusions consistently show a strong, pronounced G band and only a weak to nearly absent D1 band (Fig. A1), indicative of relatively high temperature graphite (Beysac et al. 2002). Based on the relative integrated intensities of the two latter Raman bands and using the calibration equation provided by Beysac et al. 2002, we obtain temperature estimates ranging from 500 to 630 °C (Fig. A1).

3.5. Metamorphic sequence and pressure-temperature conditions

3.5.1. Mineral reactions

The limited variation in Kluane Schist bulk chemistry indicates the differences in mineral assemblage and chemistry are largely the result of changing metamorphic conditions. In the following chapter we document the sequence of reactions pertaining to these changing conditions that resulted in our observed paragenesis across the Kluane Schist.

Zone 1: development of bedding parallel fabrics (S₁)

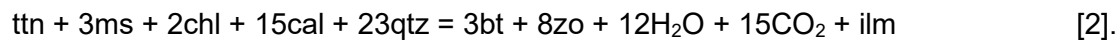
The S₁ bedding parallel fabrics comprise chlorite–muscovite–titanite–calcite (Fig. 3.5b). Initial albitic porphyroblasts, which overgrow S₁, are likely stabilized by the less calcic whole rock compositions typical of zone 1 (Fig. 3.9b). As the albite porphyroblasts analysed in zone 1 lack calcium-enrichment towards their rims (Fig. 3.9i) and are primarily associated with S₁ oriented muscovite, titanite, and chlorite (e.g., Figs. 3.5b), they likely grew while both calcite and titanite remained stable within the assemblage. As such, these albite porphyroblasts along with their associated S₁ fabric document initial Kluane Schist metamorphism at conditions around prehnite-pumpellyite to greenschist transition, where albite is considered to form during the breakdown of zeolite-facies clays (e.g., Bishop, 1972; Coombs *et al.*, 1976; Utada, 2001; metamorphic mineral abbreviations from “The Canadian Minerologist list of symbols for rock- and ore-forming minerals” updated December 30, 2019 and accessed from:

<https://www.mineralogicalassociation.ca/wordpress/wp-content/uploads/2020/01/symbols.pdf>)

Zeolite-facies clays = ab + H₂O [1].

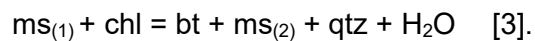
Zone 2a: Zoisite-in and initial biotite growth

Zoisite is associated with graphite-rich domains, calcite and titanite (Fig. 3.5c). Zoisite is typically aligned with the S_{2a} fabric and is observed to directly replace calcite within the lower-grade regions of zone 2 (Fig. 3.5c). Calcite and titanite are lost from the assemblage just upgrade of zone 1 (Figs. 3.4 and 3.5c, d). Ilmenite and rare hematite are present. At slightly higher grades biotite enters the assemblage and holds a similar microstructural position to zoisite (Fig. 3.5d). The appearance of biotite is associated with a reduction in chlorite abundance (Fig. 3.5b *versus* 3.d). Combined these observations suggest zoisite growth and initial biotite production via:



Zone 2b: Continued growth of biotite

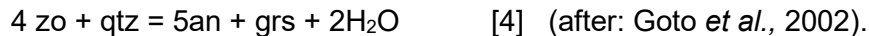
Towards the higher-grade regions of zone 2 progressive biotite growth is most likely supported by the tschermaks exchange associated with the recrystallisation of S₁-oriented chlorite and muscovite (e.g., Figs. 3.5d and 3.9f, g; Ernst, 1963; Ramsay, 1973; Pattison, 1987):



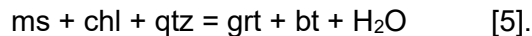
Equation [3] accounts for the second population of S_{2a} oriented muscovite wrapping zoisite and the distinct change in muscovite chemistry between zones 1 and 3 (i.e., ms₍₁₎ and ms₍₂₎; Figs. 3.5d and 9f, g).

Zone 3: garnet-in

The lowest grade assemblage within zone 3 comprises coarse, euhedral garnet which hosts inclusions of zoisite, graphite, calcite and S_1 aligned quartz (Fig. 3.6c). Plagioclase shows a similar microstructural character, with their cores containing inclusions of calcite, zoisite and S_1 aligned muscovite and chlorite (Fig. 3.6b). Both garnet and plagioclase show partial wrapping by the S_{2a} fabric (Fig. 3.6b, d). Within these lower-grade zone 3 assemblages zoisite shows a decreased abundance in the matrix compared with zone 2. The similar textures preserved by zone 3 garnet and plagioclase, their similar microstructural position, and shared Ca-rich core chemistry (e.g., Figs. 3.5 b, c, d, 3.9i and Table E8) suggests they likely developed coevally at the expense of zoisite (i.e., [4]; c.f., Goto *et al.*, 2002). Upgrade within zone 3, zoisite is rapidly lost from the assemblage (e.g., Fig. 3.6c *versus* 3.6d) and garnet preserves progressive growth zonation moving to less grossular-rich and more Mg/(Mg + Fe) rich chemistries (Table E8). These higher-grade zone 3 assemblages also show a marked decrease in chlorite and muscovite (e.g., Fig. 3.6d). Combined these observations suggest the continued growth of garnet likely occurred at the expense of both chlorite and muscovite:



And



In AFM space, the increase in chlorite Mg/(Mg + Fe) between zone 1 to zone 3 mirrors the core to rim evolution of garnet compositions (Figs. 3.9c, 3.12a and Table E8). This serves to destabilise chlorite with respect to the Kluane Schist bulk composition and promote the growth of garnet and biotite (Fig. 3.12a; i.e., [5] as the bulk compositions now lie closer to the garnet-biotite tie line). Partial wrapping of garnet by biotite-rich S_{2a} fabrics (e.g., Fig. 3.6d) further implies the production of biotite coeval with this period of garnet growth (c.f., S_1 vs. S_{2a} in Fig. 3.6d).

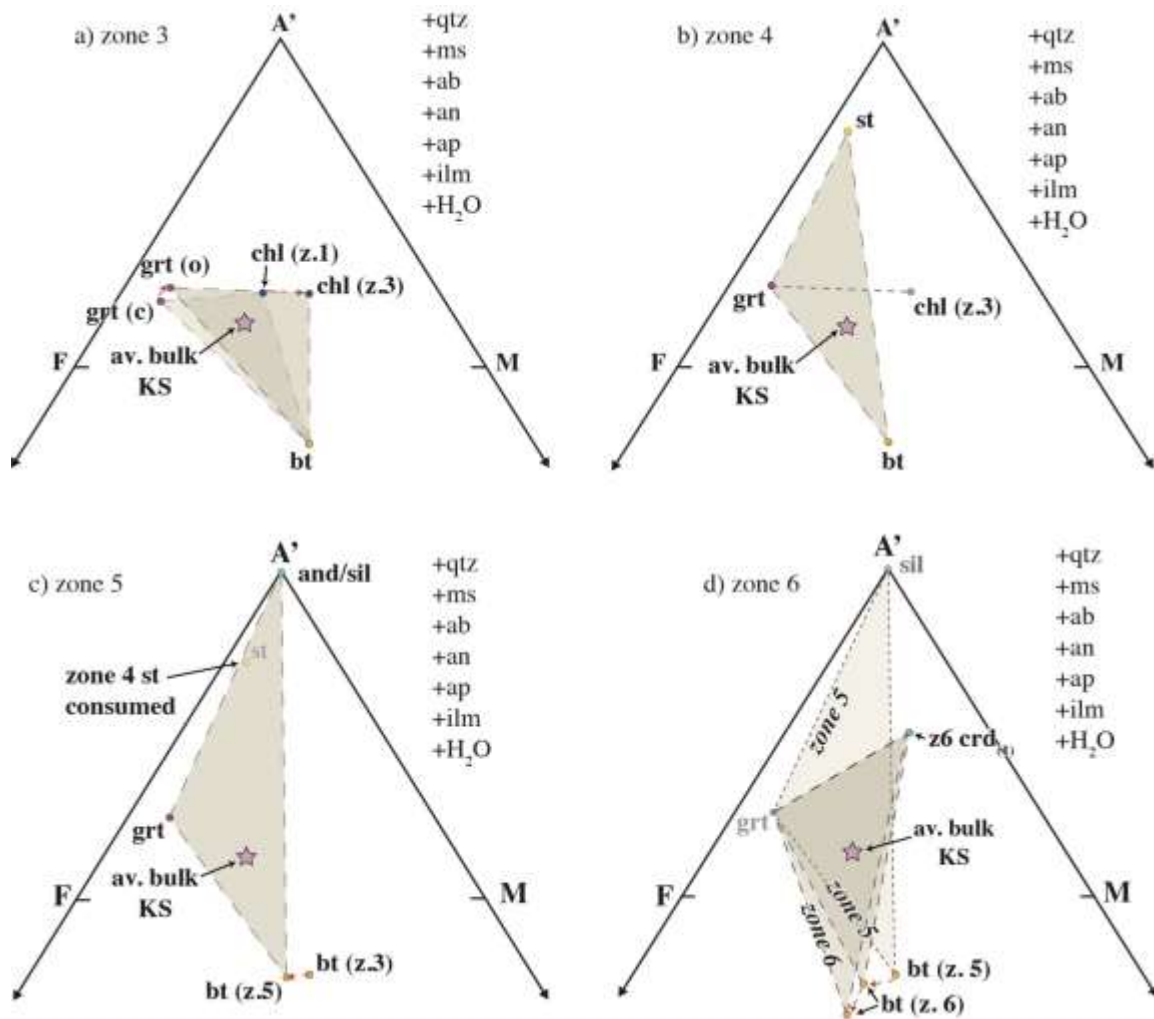


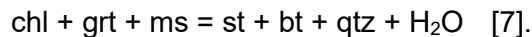
Figure 3.12. a-d) AFM plots projected from quartz (qtz), muscovite (ms), albite (ab), anorthite (an), apatite (ap), ilmenite (ilm) and fluid (H_2O) highlighting the key phase relationships resulting in the development of petrological zones 3–6. The pink star represents the average bulk composition of the Kluane Schist (see Fig. 3.9a). Where mineral abbreviations have subscripts these match the petrological zone from which the analysed mineral composition was recovered. In (a) grt(c) and grt(o) refer to the average garnet core and outer domain compositions from a representative zone 3 garnet respectively.

Zone 4: staurolite-in

Chlorite abundance is significantly reduced immediately upgrade of the first appearance of staurolite (c.f., Figs. 3.4 and 3.3g). This implies initial staurolite production at the expense of chlorite:



However, as chlorite abundance is limited within zone 4 and staurolite is typically observed as abundant, coarse, and euhedral porphyroblasts (e.g., Fig. 3.3g), it is unlikely that reaction [6] accounts for total staurolite production across the Kluane Schist. Instead, the common association between staurolite and the cloudy, embayed and corroded garnets typical of zone 4 suggests their involvement in the production of staurolite (Fig. 3.3g; e.g., Dempster *et al.*, 2017). Garnet rims within these staurolite bearing assemblages (population (2) above) typically preserve evidence for resorption coupled with a sharp decrease in Mg/(Mg + Fe) (Table S9). This is consistent with their consumption during the growth of the Mg-rich staurolite typical of the Kluane Schist:

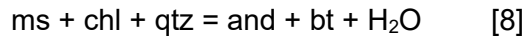


This reaction is expressed as a tie line flip in AFM space (Figs. 3.12b) and is consistent with the development of the biotite-rich S_{2b} fabrics typical of zone 4 (Fig. 3.3g).

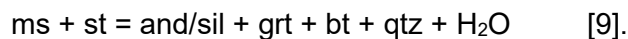
Zone 5: aluminosilicate-in

Within the lower grade regions of zone 5, knotty anhedral porphyroblasts of andalusite are locally intergrown with the S_{2b} fabric and quartz (Fig. 3.6e). Andalusite hosts inclusions of staurolite, biotite and muscovite (Fig. 3.3e and 3.6e). Within these lower-grade zone 5 rocks, staurolite persists as the major porphyroblast and the S_{2b} fabric shows a decrease in muscovite

compared with zone 4 (Fig. 3.6e). Chlorite is absent from the prograde assemblage (Fig. 3.6e). These observations point to initial andalusite growth via:



Further andalusite growth within higher-grade zone 5 samples is observed to occur directly at the expense of the zone 4 assemblage staurolite–biotite–muscovite–quartz (e.g., Fig. 3.3e). The resulting assemblage lacks the staurolite porphyroblasts seen downgrade. Instead staurolite occurs included within andalusite along with biotite, quartz, and rare muscovite (Fig. 3.3e). Population (3) inclusion-free garnet is also observed both as mantles to cloudy population (2) garnet and as finer, individual crystals (Fig. 3.6f). These distinct, low Ca-garnets (e.g., Fig. 3.10) are typically associated with graphite-free plagioclase, andalusite and sillimanite (Fig. 3.6f). Combined these observations imply continued aluminum silicate growth at the expense of staurolite and muscovite (Fig. 3.12c):



Reaction [9] likely superseded [8] when the limited chlorite was exhausted from the lowest grade rocks of zone 5. However, the persistence of relic staurolite throughout zone 5 suggests underlying kinetic controls may also play a role (e.g., Pattison & Tinkham, 2009).

Upgrade within zone 5, fibrolitic sillimanite appears in more biotite-rich and less muscovite-rich S_{2b} fabrics, plagioclase grew graphite-free tips, and andalusite is replaced by muscovite (e.g., Fig. 3.6f). The direct replacement of andalusite by fibrolitic sillimanite and inclusion of population (3) garnet in plagioclase, both suggest fibrolitic sillimanite growth post-dates [9] (Fig. 3.6f). Fibrolitic sillimanite growth likely occurs through a combination of three distinct reactions, accounting for its close association with the biotite-rich S_{2b} fabric (c.f., Carmichael, 1969):

a) $\text{and} + \text{qtz} = \text{ms}$ [10],

b) $\text{bt} = \text{ab}$ [11],

c) $\text{ms} + \text{ab} = \text{sil (fib)} + \text{bt} + \text{qtz}$ [12],

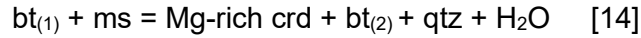
resulting in the overall polymorph transformation:

$\text{and} = \text{sil (fib)}$ [13].

Within the south-central regions of the Kluane Schist, a local assemblage contains prismatic sillimanite and is devoid of staurolite (sample 245b in Figs. 3.2 and 3.7a). Coarse, euhedral garnet is wrapped by biotite-rich S_{2b} fabrics and prismatic sillimanite (Fig. 3.7a). Garnet cores host inclusions of aligned quartz, biotite, and graphite while garnet rims domains lack inclusions (Fig. 3.7a). This distinct assemblage was likely the result of [9] moving to completion, where the kinetic barriers required for total staurolite consumption and were sufficiently lowered by the local presence of a fluid (e.g., Pattison & Tinkham, 2009).

Zone 6: Cordierite-in

Zone 6 is marked by the appearance of cordierite across the Kluane Schist (Fig. 3.7b). Within lower-grade units cordierite is primarily associated with the biotite-muscovite S_{2b} fabric and largely uncorroded andalusite and staurolite porphyroblasts (Fig. 3.7b). Coincident with the appearance of cordierite, muscovite shows a significant decrease in abundance and biotite shows recrystallization to more K-rich, less $\text{Mg}/(\text{Mg} + \text{Fe})$ compositions (Figs. 3.7b, 3.9c and 3.12d). These observations suggest the initial growth of cordierite occurred primarily at the expense of muscovite coupled with an increase in the Tschermak component of biotite (Figs. 3.9e and 3.12d; c.f., Ikeda, 1998):



where:

$\text{bt}_{(1)}$ = K-poor, Mg/(Mg/Fe)-rich biotite (Fig. 3.9c, e);

$\text{bt}_{(2)}$ = K-rich, Mg/(Mg/Fe)-poor biotite (Fig. 3.9c, e)

In AFM space, this shift in biotite composition can also be inferred to destabilise both garnet and aluminium silicate at the expense of cordierite (Fig. 3.12d). In thin section, we observe the direct replacement of garnet and fibrolitic sillimanite by cordierite (e.g., Fig. 3.7c). Moving up-grade through zone 6, cordierite abundance progressively increases while fibrolitic sillimanite decreases, until it is only observed as inclusions to cordierite (Figs. 3.7b *versus* 3.7c *versus* 3.3c). Within the highest-grade units of zone 6, garnet cores are preferentially replaced (atolled) and garnet rims show high-Mn, low-Mg chemistries consistent with resorption (Figs. 3.3c, 3.10 and Table E8). These observations are in accordance with:

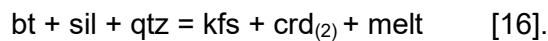


Reaction [15] is likely limited by the kinetic barriers associated with the sluggish dissolution of refractory garnet porphyroblasts (e.g., Pattison & Tinkham, 2009). However, fluid produced by the dehydration reaction [14] (Ikeda, 1998) could potentially act as catalyst to [15]. Microstructural and chemical evidence suggests garnet dissolution is common within zone 6 (e.g., Figs. 3.7c, 3.10 and Table E8). We therefore suggest the coeval occurrence of both [14] and [15], which together likely account for the observed abundance of cordierite across the Kluane Schist.

Zone 7: Migmatisation

The paleosome assemblage of zone 7 consists of biotite–plagioclase–cordierite–quartz–K-feldspar +/- garnet–sillimanite (Fig. 3.7e). Staurolite occurs as relic metastable porphyroblasts

and retrograde muscovite is randomly oriented (Fig. 3.7e). Leucosome domains comprise cordierite–quartz–plagioclase–muscovite (Fig. 3.7f) and are distinct in composition from the granodioritic Ruby Range batholith (K-feldspar–biotite–plagioclase–quartz +/- hornblende; e.g., Israel *et al.*, 2011a, b). This suggests zone 7 leucosome does not represent injectate from the nearby Ruby Range batholith. Peritectic K-feldspar and cordierite occur at the expense of S_{2b}-oriented biotite and fibrolitic sillimanite within the paleosome (Fig. 3.7e). This suggests the leucosome most likely represents the product of in-situ melting via the biotite dehydration reaction (e.g., Le Breton & Thomson, 1988):



Further evidence of this reaction is provided by the decreased abundance of biotite and fibrolitic sillimanite within zone 7 (e.g., Fig.3.7c *versus* 3.7e).

3.5.2. Petrological modelling and quantified *P–T* conditions of metamorphism

Combining our above reactions and microstructural observations, the metamorphic history of the Kluane Schist can be summarized as two distinct events, M₁ and M₂. The first, M₁, is expressed as S₁ bedding-parallel chlorite–muscovite–calcite–titanite fabrics (e.g., Fig. 3.5a, b). With the second, M₂, accompanying the progressive development of a transposition foliation that includes an earlier phase, S_{2a}, defined by chlorite–muscovite +/- biotite–zoisite fabrics that becomes fully transposed into a pervasive, planar, biotite-rich S_{2b} foliation (e.g., Figs. 3.3, 3.5c, d and 3.6). At higher metamorphic grade the transposition fabric consists of a cm-spaced, biotite–cordierite and plagioclase–quartz (+/- melt–garnet–sillimanite) gneissic fabric (e.g., Figs. 3.3 and 3.4).

Forward modelling

As the bulk composition of the Kluane Schist only shows a limited variation and no consistent trend with grade (e.g., Fig. 3.9a, b), our calculated phase diagram considers a single average bulk composition encompassing all XRF analyses across the Kluane Schist. Our resulting phase diagram uses *ds5.5*, its associated activity models and combines four regions of varying $a_{\text{H}_2\text{O}}$ which we consider to best account for the evolution of $a_{\text{H}_2\text{O}}$ during the metamorphism of the Kluane Schist (c.f., Figs. 3.11 and 3.13).

Our inferred evolution of $a_{\text{H}_2\text{O}}$ was constrained using the results of Raman spectroscopic analysis (see above; Fig. 3.11), forward petrological modelling (Fig. 3.13), thin section observation and the assumption of increasing $a_{\text{H}_2\text{O}}$ during prograde metamorphism due to progressive dehydration (e.g., Pattison, 2006). Raman spectroscopic analysis of the fluid-inclusion rich garnet domains typical of zones 3–4 suggests their mineral assemblages developed under a reduced $a_{\text{H}_2\text{O}}$ of 0.5 (Figs. 3.3g, 3.6c, d and 3.11). This low $a_{\text{H}_2\text{O}}$ value is supported by the presence of calcite mineral inclusions within garnet (e.g., Figs. 3.6c and A6). The cordierite-free, andalusite/sillimanite–garnet–biotite (+ quartz, plagioclase, ilmenite; e.g., Figs. 3.3e and 3.6e) assemblage typical of zone 5 requires an $a_{\text{H}_2\text{O}} < 0.65$ (Fig. 3.13). This result is further supported by P – T estimates from a zone 5 sample (Fig. 3.13; all P – T results found in Table 3.1). We therefore set $a_{\text{H}_2\text{O}} = 0.55$ for the T region associated with zone 5 assemblages (Fig. 3.13). Upgrade of zone 5, the cordierite–biotite +/- sillimanite–garnet (+ quartz, plagioclase, ilmenite; Figs. 3.3c and 3.7c) assemblage typical of zone 6 is produced at all values of $a_{\text{H}_2\text{O}}$ (Fig. 3.13). Therefore, to account for the increased $a_{\text{H}_2\text{O}}$ associated with prograde dehydration (e.g., Pattison, 2006), we set $a_{\text{H}_2\text{O}} = 0.95$ for T regions where graphite is present ($< 630^\circ\text{C}$; Fig. A1; Connolly & Cesare, 1993) while within graphite-free assemblages we assume $a_{\text{H}_2\text{O}} \sim 1$ (Figs. 3.13 and A1; Connolly & Cesare, 1993). Using the above constraints, we created a best-fit model for the evolution of $a_{\text{H}_2\text{O}}$ during prograde metamorphism of the Kluane Schist (Fig. 3.13f). This model is consistent with our independent P – T determinations from samples collected from zones 3, 5, and 6 (Fig. 3.13f and Table 3.1).

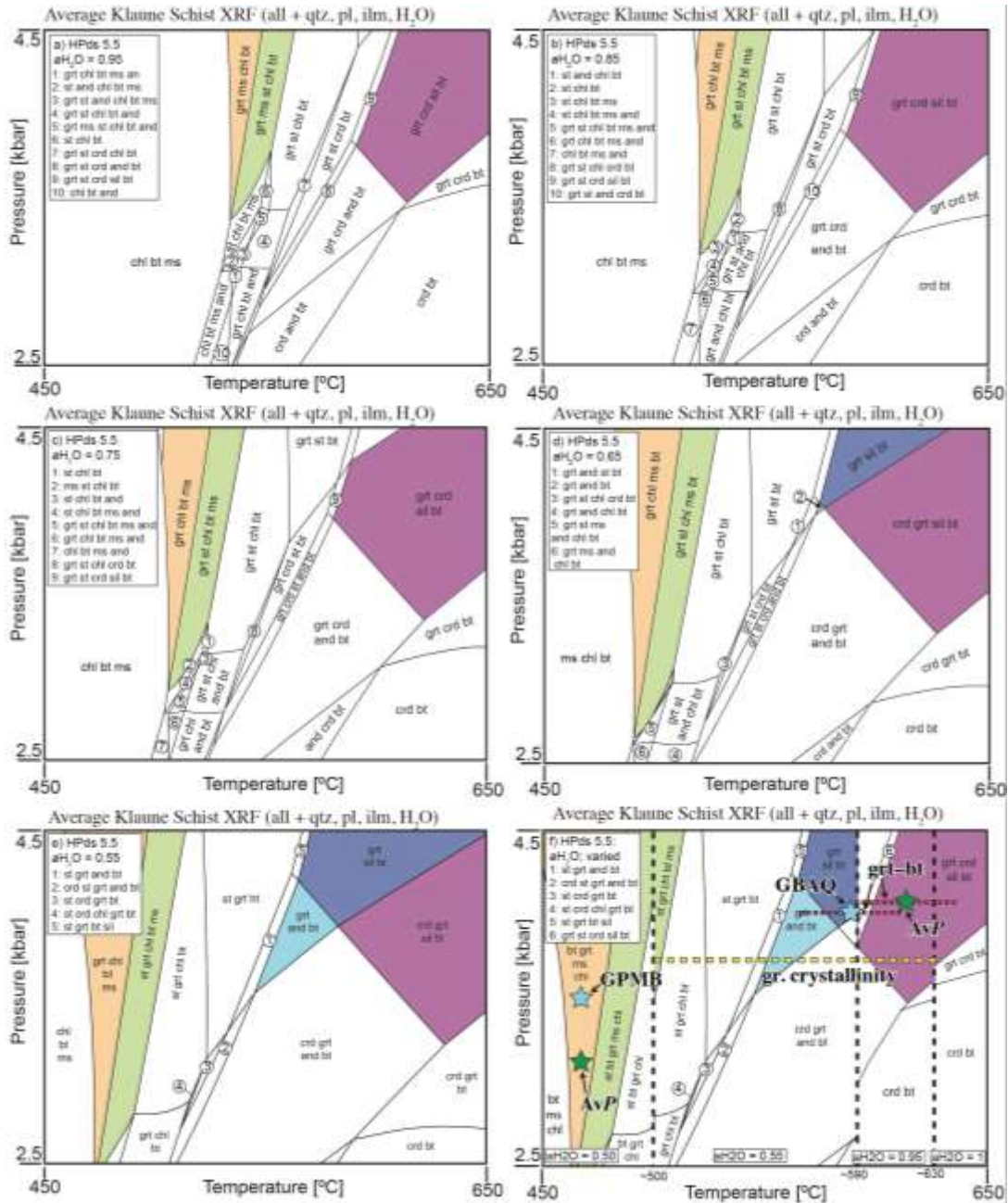
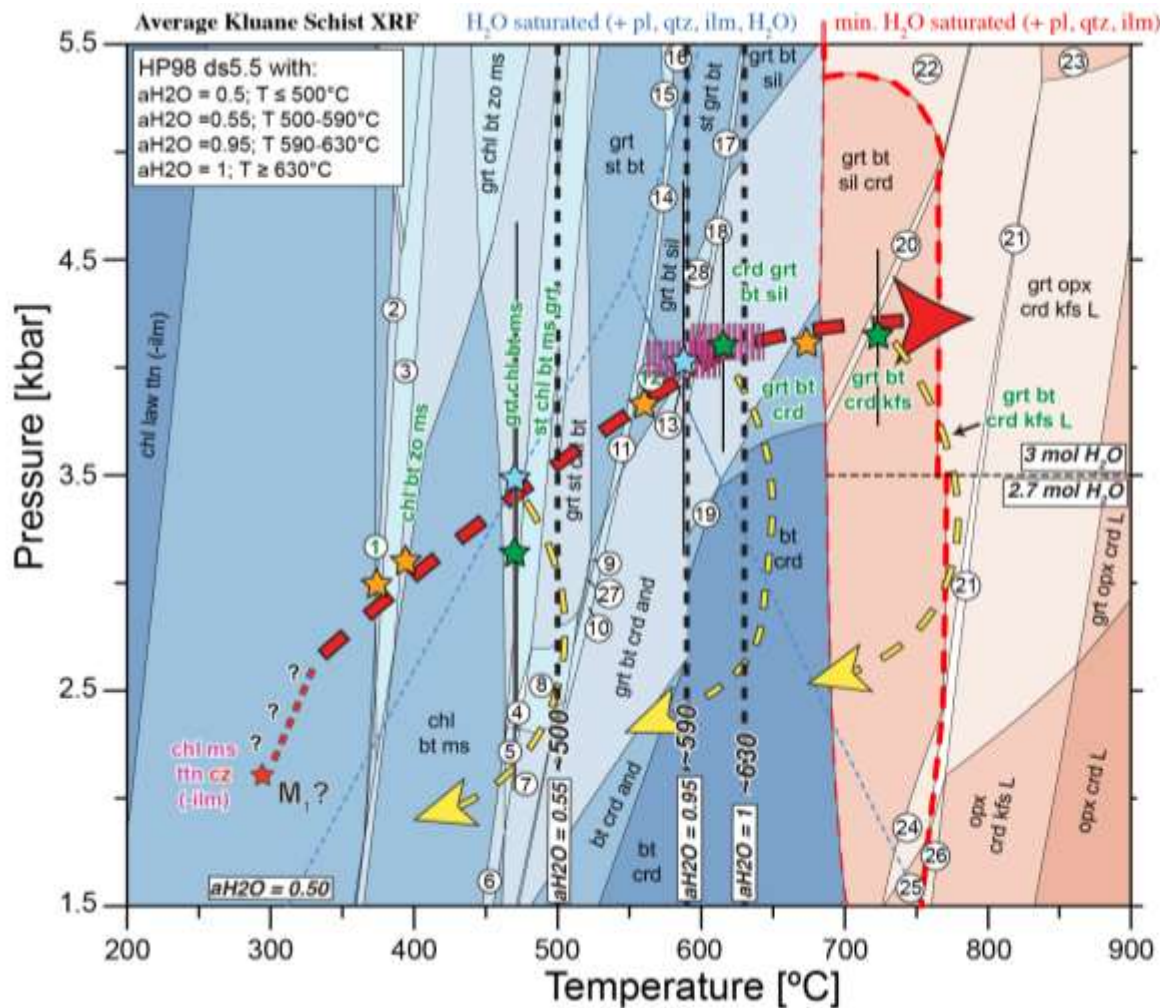


Figure 3.13. Phase diagrams calculated for an average Kluane Schist bulk composition over a select P - T area (450–650°C, 2.5–4.5 kbar) using ds5.5, the activity models described in the main text and a variety of aH_2O values. Zone 3 assemblages are highlighted in orange, zone 4 in green, zone 5 in blue and zone 6 in purple. A) $aH_2O = 0.95$, b) $aH_2O = 0.85$ c) $aH_2O = 0.75$, d) $aH_2O = 0.65$, e) $aH_2O = 0.55$. Across all diagrams we only observe the prediction of the zone 5 assemblage garnet–andalusite–biotite (+ quartz–plagioclase–ilmenite–H₂O; light blue) below aH_2O values of 0.65. f) A best-fit model accounting for observed natural assemblages across the Kluane Schist and their associated P - T estimates (see Table 3.1). Yellow dashed line shows range of temperatures returned from graphite crystallinity (see Fig. A1).

Petrologic zone	Zone 3				Zone 5	Zone 6	Zone 7	
Sample	19WM262				19WM120	19WM118	19WM123	
aH_2O	0.3	0.4	0.5	0.6	Not completed	1	0.4	1
AvP pressure (kbar)	3.56 +/- 0.8	3.42 +/- 0.9	3.12 +/- 1.1	3.35 +/- 1		4.1 +/- 0.5	4.13 +/- 0.37	4.43 +/- 0.57
Conventional barometry (kbar) [$aH_2O = 1$]	GPMB: 3.47 +/- 1.2				GBAQ: 3.94 +/- 1.8	Not completed	Not completed	
Conventional thermometry ($^{\circ}C$) [$aH_2O = 1$]	Not completed				Grt-Bt: 590 +/- 25	Grt-Bt: 615 +/- 25	Not completed	

Table 3.1. Summary of the P - T estimates completed across the Kluane Schist (see Fig. 3.2 for sample locations). AvP = average pressure estimate; GPMB = garnet–plagioclase–muscovite–biotite barometer estimate; GBAQ = garnet–biotite–Al–silicate–quartz barometer estimate; grt–bt = garnet–biotite thermometer estimate. “Not completed” indicates where obtaining a P - T estimate was not appropriate (see main text for detailed reasons why).

The resulting phase diagram (Fig. 3.14) is not a perfect representation of the phase relationships we observe, producing several inconsistencies compared with our petrological observations. These include: (1) the prediction of titanite with zoisite-bearing assemblages, where instead we typically observe ilmenite +/- hematite (c.f., Fig. 3.4). This likely arises from an inaccurate definition of XFe^{3+} within our model system (see Chapter 3.3 “*Forward petrological modelling*”; Forshaw & Pattison, 2021). (2) the prediction of clinozoisite (cz) within zone 1 assemblages. This likely results from the heightened XCa within the input bulk composition compared with that typical for zone 1 (c.f., Fig. 3.9b). (3) muscovite is predicted to leave the assemblage prior to chlorite and significantly downgrade of zone 6, where it is observed in prograde fabrics (c.f., Figs. 3.4 and 3.7b). (4) staurolite is observed to occur with both aluminium silicate and cordierite, which is not predicted by our model (e.g., Figs. 3.4, 3.6e and 3.7b). Thin section observations suggest these inconsistencies mostly likely relate to disequilibrium processes, in particular the sluggish dissolution of porphyroblasts such as staurolite and garnet (e.g., Pattison & Tinkham, 2009; Pattison & Spear, 2018).



Zone P-T estimates (values in table 1):

- zone 1: P-T by field: T < 350 °C, P < 2.5 kbar ★
- zone 2a: P-T by field: ★
- zone 2b: P-T by field: ★
- zone 3: T by field: ~460 °C, P by GPMB: ☆, AvP: ★
- zone 4: T by field: ~480 °C, (P not calculated)
- zone 5a: P-T by field: ★
- zone 5b: T by grt-bt: -----, P by GBAQ: ☆
- zone 6 lower: T by grt-bt: -----, P by AvP: ★
- zone 6 upper: P-T by field: ★
- zone 7 (paleosome): T by field: ~725 °C, P by AvP: ★

Petrological zones produced by model:

- zone 7: grt crd bt kfs + L
- zone 6 upper: grt crd bt
- zone 6 lower: grt crd bt sil
- zone 5b: bt grt sil
- zone 5a: grt bt and
- zone 4: st grt chl bt ms
- zone 3: bt ms grt chl
- zone 2b: bt ms zo chl
- zone 2a: ms zo chl ttm
- zone 1: ms chl ttm cz

Numbered fields:

11: grt bt st and	22: grt bt sil crd L
1: chl ttm zo ms (-ilm)	23: grt crd kfs L
2: chl bt ms ttm zo (-ilm)	13: grt bt crd sil
3: chl bt ms ttm zo	14: grt bt st sil
4: st chl bt ms and grt	15: grt st bt ky ms
5: chl bt ms and grt	16: grt bt ky
6: chl ms bt and	17: grt st bt sil
7: chl bt and grt	18: st grt crd bt sil
8: st chl bt and grt	19: bt crd and
9: grt st crd bt	20: grt bt sil crd kfs
10: grt bt crd and st	21: grt bt opx crd kfs L
	24: opx bt crd kfs
	25: opx bt crd kfs L
	26: opx bt crd kfs L
	27: grt st crd chl bt
	28: st grt crd bt

Legend:

- Red dashed arrow: M_1 Field Gradient ~ 200°C / kbar
- Yellow dashed arrow: Isomorphism path

Figure 3.14. Phase diagram calculated for an average bulk composition of the Kluane Schist using ds5.5 and the activity models described in the main text. Below 500°C $a_{\text{H}_2\text{O}} = 0.5$, from 500–590°C $a_{\text{H}_2\text{O}} = 0.55$, from 590–630°C $a_{\text{H}_2\text{O}} = 0.95$ and above 630°C $a_{\text{H}_2\text{O}} = 1$ (see Figs. 3.11, 3.13 and main text for discussion). Above the wet solidus (thin red dashed line; red shaded fields) models are run with minimally saturated water contents determined at 4.0 and 2.0 kbar (see Fig. A5 and Chapter 3.3 “*Forward petrological modelling*”). Bold assemblages highlight those best representative of the petrological zones across the Kluane Schist; pink text highlights zone 1 (M_1) and zones 2-7 (M_2) are highlighted in green. Red text refers to a discrepancy between model prediction and thin section observation (additionally, see text on right); these are discussed further in main text. Conventional barometry estimates are outlined by light blue stars. AvP estimates are highlighted by green stars. Pink dashed lines refer to temperature estimates from the garnet-biotite thermometer (Holdaway, 2000). All these P - T estimates, along with their 1-sigma uncertainties, can be found in Table 3.1. Collectively our results suggest the petrological zones across the Kluane Schist are best represented as a set of nested, clockwise P - T loops where peak conditions define a metamorphic field gradient of $\sim 200^\circ\text{C}/\text{kbar}$.

These inconsistencies aside, the overall topology of our model is consistent with the observed order of index mineral paragenesis as observed across the Kluane Schist (c.f., Figs. 3.2, 3.4 and 3.14). Further, we also see good agreement between our forward modelling and independent P - T estimates provided by thermobarometry (discussed further below; also see: Fig. 3.14 and Table 3.1). Equally, in comparison with the other combinations of dataset and activity-composition models outlined (see Chapter 3.3 “*Forward petrological modelling*”), which include ds6.2 of Holland & Powell (2011) coupled with the metapelite HPx-eos of White *et al.*, (2014) and the modified SPaC14 dataset of Spear & Cheney (1989) with activity models as described in Pattison & Debuhr (2015), our resulting ds5.5 model is more in line with natural phase observations (Figs. A3 and A4). Finally, the use of ds5.5 without varying $a_{\text{H}_2\text{O}}$ does not produce a result aligned with our thermobarometry or thin section observations (Fig. A2). We therefore consider our resulting model (Fig. 3.14) as the best approximation for quantifying the P - T conditions experienced during the metamorphic evolution of the Kluane Schist.

Thermobarometric estimates

AvP estimates below zone 5 were constrained using a range of $a\text{H}_2\text{O}$ (0.3, 0.4, 0.5, and 0.6; Table 3.1). We see a limited variability of ± 0.46 kbar when considering different $a\text{H}_2\text{O}$ within a single equilibrium assemblage (Table 3.1). Within zone 3, we chose an $a\text{H}_2\text{O}$ value of 0.5 to remain consistent with the results of garnet fluid inclusion analysis and our forward modelling (e.g., Figs. 3.11 and 3.14). Above zone 5, *AvP* is completed with $a\text{H}_2\text{O} = 1$ due to the largely graphite-free nature of the rock matrix (Fig. 3.7b, c and Table 3.1). *AvP* on migmatite units within zone 7 is completed with an $a\text{H}_2\text{O}$ of 0.4 and 1, showing a limited variation of ± 0.3 kbar between results (Table 3.1). We choose a value of 0.4 to remain consistent with the reduced $a\text{H}_2\text{O}$ commonly suggested for pelitic migmatites (e.g., Phillips, 1981; Lamb & Valley, 1988; Waters, 1988; Giorgetti *et al.*, 1996; Bader *et al.*, 2014; Waters, 2019). Our conventional barometry estimates, which assume $a\text{H}_2\text{O} = 1$ (see Chapter 3.3 “*Thermobarometry*”; Wu *et al.*, 2015, 2017), are considered reliable due to the lower susceptibility of a single barometer equilibria to changes in $a\text{H}_2\text{O}$ (e.g., Waters, 2019). Results from conventional barometry and *AvP*, where completed on the same sample, are within 1-sigma error of one another (Fig. 3.14 and Table 3.1).

Field gradient for the Kluane Schist

Combining the results from our phase diagram, *AvP*, and conventional barometry calculations we can constrain the main phase of Kluane Schist metamorphism (M_2) to between ~ 3 kbar at 375°C and $4.0\text{--}4.5$ kbar at $700\text{--}750^\circ\text{C}$, defining a field gradient of $\sim 200^\circ\text{C/kbar}$ or $\sim 55^\circ\text{C/km}$ (assuming a crustal density of 2.8 g/m^3) across the Kluane Schist (Fig. 3.14). These conditions largely align with other Buchan-style terranes worldwide, falling within the range of recent estimates for the Wopmay Orogen Buchan sequence ($34\text{--}68^\circ\text{C/km}$; St-Onge & Davis, 2017), close to estimates for progressive Buchan-style metamorphism across the western Pan-African Kaoko belt, Namibia ($\sim 50^\circ\text{C/km}$; Will *et al.*, 2004), and in line with the staurolite–andalusite–sillimanite sequences that define the western Buchan domain of northeast Scotland (~ 3.5 kbar at 550°C and $4.0\text{--}4.5$ kbar at $700\text{--}750^\circ\text{C}$; Pattison & Goldsmith, 2022). Integrating these results with our structural analysis, we observe the progressive intensification of deformation coinciding with increased metamorphic grade from the core of the Kluane Schist towards its northern, eastern, and southwestern edges (Figs. 3.2 and 3.3). To the north and east

we define an inverted metamorphic sequence between the greenschist facies and amphibolite-granulite transition while to the south a correct way up sequence culminates at staurolite-grade before exposure is lost under Kluane Lake (Figs. 3.2 and 3.3). Together these results suggest M_2 is reflected through the development of a Buchan-style metamorphic sequence between lower-grade zone 2 assemblages and higher-grade zone 7 assemblages (Fig. 3.14).

3.6. Discussion

3.6.1. Comparison with previous studies

Previous evaluation of the metamorphic conditions experienced by the Kluane Schist suggest it underwent two distinct episodes of metamorphism; an early regional event, peaking at $T \sim 510$ °C and $P \sim 7$ kbar, and a subsequent contact metamorphic episode at $T \sim 530$ – 720 °C and $P \sim 3.5$ – 4.5 kbar (Erdmer, 1991; Mezger *et al.*, 2001). In contrast, our findings suggest initial burial metamorphism of the Kluane Schist was limited to the sub-greenschist-facies ($P \ll 4$ kbar; Fig. 3.14) while its subsequent high- T , low- P metamorphism reflects a regional Buchan-style event coeval with deformation (Figs. 3.3, 3.4 and 3.14). The conditions we record for this second event are similar to those suggested by Mezger *et al.*, (2001) ($T \sim 400$ – 750 °C & $P \sim 3.0$ – 4.5 kbar; Fig. 3.14, Table 3.1), but we do not attribute it to a *static overprint* by a 5–6 km wide contact aureole. We discuss these inconsistencies further below.

Pressure–temperature conditions of M_1

To obtain the P - T conditions for M_1 , Mezger *et al.* (2001) consider a single zoned garnet in equilibrium with reversely zoned plagioclase (core $X_{an} = 0.24$; rim $X_{an} = 0.36$). Their resulting M_1 P - T path involves significant decompression across a limited range of temperatures (cores ~ 7.5 kbar at 510 °C to rims ~ 3.5 kbar at 550 °C; Mezger *et al.*, 2001). We note several inconsistencies between such a P - T trajectory and the observed phase relationships across the Kluane Schist. First, garnet cores overgrew a lower-grade fabric (S_1 ; muscovite–chlorite–graphite Figs. 3.5b and 3.6c) than which they are partially wrapped by (biotite-rich S_{2a} ; Fig. 3.6c, d). Second, the euhedral shape of garnet

crystals within zone 3 (e.g., Fig. 3.6c, d), their preserved zonation patterns (Table E8) and intra-sample crystal size distribution (Fig. 3.6d) are all more consistent with garnet growth during increasing P and T rather than isothermal decompression (e.g., Pattison & Tinkham, 2009; George & Gaidies, 2017). Third, we do not observe evidence of a distinct higher-pressure mineral assemblage (e.g., kyanite) associated with garnet cores or indeed elsewhere across the Kluane Schist. Fourth, we do not observe chemical or microstructural evidence for the overprinting of mineral assemblages that may be related to significant decompression (c.f., Vice *et al.*, 2020). Finally, the highest- P estimates provided by Mezger *et al.* (2001) (~ 7.5 – 7.0 kbar) were calculated using grossular-rich garnet in equilibrium with inferred oligoclase cores ($X_{\text{An}} = 0.32$ – 0.24); these plagioclase compositions contrast with the measured garnet-grade plagioclase compositions reported by Mezger *et al.* (2001) ($X_{\text{An}} = 0.37$ – 0.31) and those within this study (Fig. 3.9h, i). Instead, the zone 3 plagioclase we observe typically shows normal zonation with individual grains characterized by more anorthite-rich cores than that suggested by Mezger *et al.* (2001) ($X_{\text{An}} = 30$ – 40 ; Figs. 3.6b, d and 3.9h, i). Microstructural relationships suggest these more anorthite-rich plagioclase cores represent part of the same mineral assemblage as the grossular-rich garnet cores (e.g., Fig. 3.6b, c, d).

We instead suggest the development of these Ca-rich mineral cores (i.e., garnet, plagioclase) reflects fluid infiltration and/or variation in local composition rather than elevated pressures. This is evidenced by the distinct increase in whole rock $\text{Ca}/(\text{Ca} + \text{Na})$ upgrade of zone 1 (e.g., Fig. 3.9b, h), the calcite inclusions typical of garnet within zone 3 (e.g., Figs. 3.6c and A6), and the low $a_{\text{H}_2\text{O}}$ values that are suggested during the initial growth of garnet (Figs. 3.11, 3.13 and 3.14; e.g., Connolly & Cesare, 1993; Bader *et al.*, 2014). As such our zone 3 pressure estimates (~ 3.0 – 3.5 kbar; Fig. 3.14 and Table 3.1) are derived from an assumed equilibrium between the outer core domains of garnet and plagioclase with matrix phases chlorite–biotite–muscovite (+ H_2O , quartz) (c.f., Fig. 3.6d).

M₂: contact versus regional metamorphism

Mapped isograds relating to M_2 highlight a hot-side-up, inverted metamorphic field gradient which increases in grade towards the Ruby Range batholith (Figs. 3.2 and 3.3; see also Fig. 2 in Mezger *et al.*, 2001). Coincidence between this field gradient, the location of the Ruby Range batholith, and evidence for the static growth of the staurolite–aluminium-silicate–cordierite M_2 mineral sequence led Mezger *et al.*, (2001) to

suggest M_2 primarily reflected an extensive ~5–6 km contact aureole to the batholith. However, within this study we document the consistent entrainment of M_2 index minerals within prograde transposition fabrics of the Kluane Schist, where metamorphic grade appears directly related to the intensity and style of the deformational fabric preserved (Figs. 3.3, 3.4, 3.5, 3.6 and 3.7).

This observation of a coupled metamorphic-deformational evolution contrasts with previous hypotheses that suggest the mineral assemblages of staurolite-grade and above were developed statically across the Kluane Schist (e.g., Mezger, 1997; Mezger *et al.*, 2001). However, it does not refute their growth in response to a dynamic emplacement of the Ruby Range batholith, which has been suggested by its field relationships (e.g., Fig. 2.3d; Johnston and Canil, 2007; Israel *et al.*, 2011a). That said, we highlight that the post-deformational annealing and coarsening of mineral assemblages and microstructure is only observed within the structurally highest units of the Kluane Schist, < 1 Km from the contact with the overlying Ruby Range batholith (e.g., Fig. 3.3). This static fabric overgrowth may be related to the intrusion of the post-tectonic phase of the Ruby Range batholith, which is significantly more voluminous than its syn-tectonic phase (e.g., Israel *et al.*, 2011a). It therefore seems unlikely that the more minor, syn-tectonic phase of the Ruby Range batholith can act as the principal heat source during the development of the complete greenschist- to granulite-grade inverted metamorphic sequence preserved across the Kluane Schist (e.g., Figs. 3.2 and 3.3). Equally, we also note that our coupled metamorphic-deformational field gradient is not unique to the northern regions of the Kluane Schist (e.g., Figs. 3.2 and 3.3). We additionally documented a correct way up metamorphic sequence, to at least staurolite-grade (zone 4), along the southeast of Kluane Lake (Figs. 3.2 and 3.3). Unless a portion of the Ruby Range batholith was displaced by the Denali fault (c.f., Fig. 3.2), this increase in metamorphic grade away from the Ruby Range batholith is inconsistent with its intrusion acting as the principal heat source during the inverted metamorphism experienced by the Kluane Schist (e.g., Mezger *et al.*, 2001). Notwithstanding, our field and petrographic observations are most consistent with a coupled tectono-metamorphic history for the Kluane Schist where an increase in metamorphic grade is mirrored by the intensity of ductile deformation (e.g., Fig. 3.3). This highlights that M_2 was primarily a regional metamorphic event, facilitated in part by the intrusion of the Ruby Range

batholith, rather than being directly driven by the emplacement of the batholith itself (Figs. 3.3 and 3.4; e.g., Mezger *et al.*, 2001).

3.6.2. Tectonic evolution of the Kluane Schist

The northeast-dipping inverted metamorphic sequence preserved by the Kluane Schist combined with its pervasive tops-to-the-SW shear structures are similar to those observed within forearc assemblages farther south within the Cordillera that have undergone underplating below an inboard continental arc (e.g., Sierra de Salinas Schists, southern California; Swakane gneiss, North Cascades; Ducea & Chapman, 2018). We therefore suggest the Kluane Schist was most likely deposited in a forearc setting, as has been hypothesised previous workers (Israel *et al.*, 2011a; Canil *et al.*, 2015; Waldien *et al.*, 2021b). Our data provides new constraints on the style of Kluane Basin inversion, supporting its inferred deposition as part of a forearc. Below we summarize the metamorphic and structural evolution of the Kluane Schist within the context of Mesozoic Cordilleran orogenesis.

D1M1: After its deposition in Late Cretaceous time, the Kluane Schist experienced D₁M₁ which is expressed as the S₁ chlorite–muscovite–titanite–calcite fabric within its lowest-grade zone 1 units (e.g., Fig. 3.5a, b). Although the metamorphic conditions are difficult to quantify for M₁, the preserved S₁ assemblage suggests M₁ occurred around the prehnite-pumpellyite to greenschist transition (*P-T*: ~2–4 kbar, ~250–350 °C; Fig. 3.14).

The low-*P* conditions we record for M₁ suggest that the Kluane Schist only experienced limited tectonic burial at this time. As such, we suggest D₁M₁ reflects the initial stages of Kluane Basin collapse between the encroaching Insular terranes and the previously accreted Intermontane terranes, leading to its initial underthrusting below the Yukon-Tanana terrane, which was part of the North American plate within southwest Yukon at this time (e.g., Mezger *et al.*, 2001; Israel *et al.*, 2011a; Nelson *et al.*, 2013; Box *et al.*, 2019).

D2M2: The second and most intense period of metamorphism experienced by the Kluane Schist was coeval with a period of NE-SW compression (e.g., Fig. 3.3). D₂M₂ was largely responsible for the development of the metamorphic field gradient preserved

across the Kluane Schist along with its petrologic zones (Fig. 3.2). D_2M_2 involved the transposition of greenschist-grade S_1 fabrics through S_{2a} orientations, resulting in a penetrative S_{2b} folia at staurolite grade (Fig. 3.3). D_2M_2 is associated with symmetric F_2 folds which become progressively tighter with metamorphic grade, and eventually isoclinal at staurolite grade, with their axial planes parallel to S_{2b} fabrics (Fig. 3.3h, f). Rootless and isoclinal F_{2b} folds were progressively sheared to form a coarsened and fully transposed S_{2b} gneissosity within andalusite and cordierite grade units (e.g., Fig. 3.3b, d, f). This lockstep between metamorphic assemblage and fabric development strengthens our interpretation of a coupled metamorphic-deformational field gradient across the Kluane Schist, while illustrating how the deformation occurred within an evolving strain field (e.g., Figs. 3.3 and 3.4).

During D_2M_2 lower-grade assemblages were deformed within a dominantly coaxial strain field while higher-grade assemblages show a predominance of non-coaxial strain (Figs. 3.3, 3.4, 3.5, 3.6 and 3.7). This evolving strain field likely tracks the initial burial below and subsequent override of the Kluane Schist by the Yukon-Tanana terrane (e.g., Israel *et al.*, 2011a); initial coaxial flattening deformation occurred as the Kluane Schist underwent initial tectonic burial below the Yukon-Tanana terrane, with the evolution to a non-coaxial strain field, as recorded by S_{2b} fabric asymmetry (e.g., Figs. 3.3 and 3.4), tracking the subsequent override of the Kluane Schist by the Yukon-Tanana terrane (e.g., Israel *et al.*, 2011a). This accounts for the diachronous style of metamorphism and deformation recorded by D_2M_2 and development of the dominant WNW-striking, largely NNE-dipping S_{2b} transposition fabric across the Kluane Schist (Figs. 3.1b and 3.2). The structures, field gradient, and strain evolution preserved throughout D_2M_2 are consistent with their development during a period of largely orogen-normal compression, such as that hypothesized during the terminal accretion of the Insular terranes (e.g., the 120-60 Ma period of Monger & Gibson, 2019).

D3: D_3 lacks the development of a unique planar fabric. Instead, it is primarily expressed through the formation of F_3 shear folds (e.g., Fig. 3.8a), sheared lensoidal quartz veins (e.g., Fig. 3.8b), and a NE-SW trending mineral alignment lineation defined by tourmaline, mica, and plagioclase. Recorded throughout the Kluane Schist (e.g., Table K1–2), these features demonstrate that D_3 involved a period of pervasive, SW-directed non-coaxial strain. This non-coaxial strain field is best demonstrated through the folding of S_{2b} fabrics to form F_3 shear folds (e.g., Fig. 3.8). F_3 folds show consistent

vergence towards the SW and trend to the SE, suggesting D_3 occurred during a period of NE-SW compression (Fig. 3.8a). Asymmetrical lensoidal quartz stringers and boudins observed parallel to mineral alignment lineations also show a strong tops-to-the-WSW and SW shear sense (e.g., Figs. 3.3a and 3.8b).

The lack of a distinct fabric orientation associated with D_3 and the consistency in trend between F_2 and F_3 folds suggests that both D_2 and D_3 demonstrate a similar NE-SW-directed contractional event that likely reinforced pre-existing S_2 fabrics. The pervasive, non-coaxial SW-directed shear associated with D_3 likely results from the continued override of the Kluane Schist by the flanking components of the North American margin after its underthrusting below the Yukon-Tanana terrane during D_2M_2 (see above).

D_4 : The final episode of deformation expressed across the Kluane Schist relates to the formation of F_4 buckle folds (F_4 in Fig. 3.2). The buckled nature of these folds implies D_4 occurred when the Kluane Schist was cooler than during D_2 or D_3 . These folds trend E-W, suggesting D_4 occurred during a N-S period of compression. As such, D_4 likely occurred after the exhumation of the Kluane Schist, producing the larger-scale fold pattern of our mapped petrologic zones and isograds (Fig. 3.2).

Considering the above, we view the Kluane Basin as a Late Cretaceous depocenter (ca. 94 Ma; Israel *et al.*, 2011a) that was open during the late stages of Insular terrane accretion. This accounts for the metamorphic evolution of the Kluane Schist only involving a shallow underthrusting below the continental margin prior to its override by the Yukon-Tanana terrane. As such, the metamorphism of the Kluane Schist was primarily driven by initial limited burial below and subsequent override by a warm Yukon-Tanana terrane, which hosted significant magmatic activity during the Cretaceous (e.g., the Tanacross–Dawson Range belt and Tok–Tetlin belt of Hart *et al.*, 2004; and the ‘100–50 Ma magmatic belt’ of Gehrels *et al.*, 2009). This model provides a potential mechanism to develop the heightened geothermal gradient implied by the low-medium pressure, high temperature metamorphic regime we record across the Kluane Schist, while also accounting for the evolution of flattening to rotational fabrics during D_{2-3} (see above; e.g., Figs. 3.3 and 3.4; Israel *et al.*, 2011a).

3.6.3. Tectonic significance of the Kluane Schist within Southwest Yukon

Evaluation of the metamorphic conditions experienced by the Blanchard River assemblage to the south of the Kluane Schist (e.g., Fig. 3.1b) suggest it underwent two distinct episodes of regional metamorphism; an early Barrovian event, peaking at $T \sim 650$ °C and $P \sim 6.5$ kbar, followed regional exhumation and subsequent metamorphism at $P \sim 3$ kbar (Vice *et al.*, 2020). In contrast, the conditions and mineral assemblages we record across the Kluane Schist suggest it experienced initial metamorphism within the sub-greenschist-facies (our D₁M₁ above; Fig. 3.14) followed by a Buchan style event which peaked at ~ 700 – 750 °C and 4.0–4.5 kbar (our D₂M₂ above; Fig. 3.14). The initial high- P kyanite–garnet grade assemblages observed across the Blanchard River assemblage, along with their lower- P cordierite–andalusite/sillimanite–spinel coronas (Vice *et al.*, 2020) are not observed across the Kluane Schist. Instead, the cordierite–aluminium silicate assemblages we document across the Kluane Schist appear associated with its main phase of metamorphism, without evidence for these assemblages having overprinted a previous higher- P event (e.g., Figs. 3.3, 3.6 and 3.7). These observations suggest that the initial Barrovian event recorded in the Blanchard River assemblage (Vice *et al.*, 2020) was not experienced by the Kluane Schist.

Our interpretation does not preclude the potential for a later shared metamorphic history between the Kluane Schist and the Blanchard River assemblage. Both units preserve evidence for a distinct low- P , high- T metamorphic event that was synchronous with deformation and associated with the development of a common, continentally-dipping foliation (see above; Vice *et al.*, 2020). This similarity in P - T conditions suggests these unit may have been together during the latter Buchan event experienced by the Kluane Schist. Equally, similarity in graphitic-rich protolith for both the Kluane Schist and Blanchard River assemblage (Bordet *et al.*, 2015; Vice *et al.*, 2020) along with their similar detrital zircon age spectra (Israel *et al.*, 2011a; Vice, 2017) suggest both units were likely sourced from similar, inboard continental regions.

3.7. Conclusions

The Kluane Schist preserves an excellent example of a low-medium pressure, high temperature Buchan-style metamorphic field gradient. Our detailed reevaluation of the metamorphic-deformational history experienced by the Kluane Schist suggests it experienced two distinct phases of metamorphism; an initial (sub)-greenschist-facies event, expressed through the development of S_1 bedding-parallel chlorite–calcite–titanite fabrics and a second more penetrative episode demonstrated through the progressive transposition of the lower grade S_1 foliation initially into a S_{2a} oblique chlorite–muscovite fabric and eventually to the pervasive, planar, biotite-rich S_{2b} foliation and centimetre-spaced, biotite–sillimanite–cordierite (+/- melt) gneissic fabric. Combined, these events are reflected as a metamorphic field gradient across the Kluane Schist. We document isograd continuity relating to this metamorphism across the Kluane Schist which is at odds with previous suggestions that it represents the juxtaposition of two distinct regionally metamorphosed tectonic belts. Further, the coupled metamorphic-deformational evolution we record across the Kluane Schist suggests its mineral assemblages were not developed within an ~5–6 km wide static contact aureole to the Ruby Range batholith.

Instead, we view the Kluane Basin as a Late Cretaceous depocenter that was infilled during the very late stages of Insular terrane accretion. Metamorphism and deformation occurred during the waning stages of Insular terrane accretion when the Kluane Schist experienced limited tectonic burial below the North American margin followed by its underthrusting below a thermally mature Yukon-Tanana terrane. This process is documented by the development of an inverted Buchan-style metamorphic field gradient which records the evolution of coaxial to non-coaxial shear structures with increased metamorphic grade. Later tops-to-the-SW shear structures, which overprint S_{2b} fabrics and dominate the inverted basin, likely developed in response to the continued SW-directed override of the Yukon-Tanana terrane.

Combined, the structures, field gradient, and strain evolution preserved throughout the Kluane Schist are consistent with its metamorphism and deformation having occurred during a heightened geothermal regime, potentially reflecting its override by thickened continental crust during orogen-normal compression and the terminal accretion of the Insular terranes.

3.8. References

- Aranovich, L.Y. & Newton, R.C. (1999). Experimental determination of CO₂-H₂O activity-composition relations at 600–1000 C and 6–14 kbar by reversed decarbonation and dehydration reactions. *American Mineralogist*, v.84, n.9, p. 1319-1332. <https://doi.org/10.2138/am-1999-0908>
- Bader, T., Franz, L., De Capitani, C. & Zhang, L. (2014). The effect of water activity on calculated phase equilibria and garnet isopleth thermobarometry of granulites, with particular reference to Tongbai (east-central China). *European Journal of Mineralogy*, v.26, n.1, p.5-23. <https://doi.org/10.1127/0935-1221/2013/0025-2351>
- Beyssac, O., Goffé, B., Chopin, C. & Rouzaud, J.N. (2002). Raman spectra of carbonaceous material in metasediments: a new geothermometer. *Journal of Metamorphic Geology*, v.20, n.9, p. 859-871. <https://doi.org/10.1046/j.1525-1314.2002.00408.x>
- Bishop, D.G. (1972). Progressive metamorphism from prehnite-pumpellyite to greenschist facies in the Dansey Pass area, Otago, New Zealand. *Geological Society of America Bulletin*, v.83, n.11, p. 3177-3198. [https://doi.org/10.1130/0016-7606\(1972\)83\[3177:PMFPTG\]2.0.CO;2](https://doi.org/10.1130/0016-7606(1972)83[3177:PMFPTG]2.0.CO;2)
- Box, S.E., Karl, S.M., Jones, J.V., Bradley, D.C., Haeussler, P.J. & O'Sullivan, P.B., (2019). Detrital zircon geochronology along a structural transect across the Kahiltna assemblage in the western Alaska Range: Implications for emplacement of the Alexander-Wrangellia-Peninsular terrane against North America. *Geosphere*, v.15, n.6, p.1774-1808. <https://doi.org/10.1130/GES02060.1>
- Breton, N.L. & Thompson, A.B., (1988). Fluid-absent (dehydration) melting of biotite in metapelites in the early stages of crustal anatexis. *Contributions to Mineralogy and Petrology*, v.99, n.2, p.226-237. <https://doi.org/10.1007/BF00371463>
- Brown, M., Averkin, Y.A., McLellan, E.L. & Sawyer, E.W., (1995). Melt segregation in migmatites. *Journal of Geophysical Research: Solid Earth*, v.100, n.B8, p. 15655-15679. <https://doi.org/10.1029/95JB00517>

- Canil, D., Johnston, S.T., D'Souza, R.J. & Heaman, L.M., (2015). Protolith of ultramafic rocks in the Kluane Schist, Yukon, and implications for arc collisions in the northern Cordillera. *Canadian Journal of Earth Sciences*, v.52, n.7, p. 431-443. <https://doi.org/10.1139/cjes-2014-0138>
- Chu, X. & Ague, J.J., (2013). Phase equilibria for graphitic metapelite including solution of CO₂ in melt and cordierite: implications for dehydration, partial melting and graphite precipitation. *Journal of Metamorphic Geology*, v.31, n.8, p.843-862. <https://doi.org/10.1111/jmg.12047>
- Coggon, R. & Holland, T.J.B., (2002). Mixing properties of phengitic micas and revised garnet-phengite thermobarometers. *Journal of Metamorphic Geology*, v.20, n.7, p.683-696. <https://doi.org/10.1046/j.1525-1314.2002.00395.x>
- Colpron, M., Nelson, J.L., & Murphy, D.C. (2007). Northern Cordilleran terranes and their interactions through time. *GSA Today*, v.17, p.4–10 <https://doi.org/10.1130/GSAT01704-5A.1>
- Colpron, M. and Nelson, J.L., (2011). A Digital Atlas of terranes for the Northern Cordillera; British Columbia Ministry of Energy and Mines, BCGS GeoFile 2011-11.
- Connolly J. A. & Bodnar R. J. (1983) A modified Redlich–Kwong equation of state for H₂O–CO₂ mixtures: application to fluid inclusion studies. *EOS* 64, (abstr.), p. 350.
- Coombs, D.S., Nakamura, Y. & Vuagnat, M., (1976). Pumpellyite-actinolite facies schists of the Taveyanne Formation near Loèche, Valais, Switzerland. *Journal of Petrology*, v.17, n.4, p.440-471. <https://doi.org/10.1093/petrology/17.4.440>
- Davidson, C., Hollister, L.S. & Schmid, S.M., (1992). Role of melt in the formation of a deep-crustal compressive shear zone: The MaClaren Glacier metamorphic belt, south central Alaska. *Tectonics*, v.11, n.2, p.348-359. <https://doi.org/10.1029/91TC02907>

- Davidson, C., & McPhillips, D., (2007), Along strike variations in metamorphism and deformation of the strata of the Kahiltna basin, south-central Alaska, in Ridgway, K.D., Trop, J.M., Glen, J.M.G., & O'Neill, J.M., eds., Tectonic growth of a collisional continental margin: crustal evolution of southern Alaska: Geological Society of America Special Paper 431, p. 439–454. [https://doi.org/10.1130/2007.2431\(17\)](https://doi.org/10.1130/2007.2431(17))
- de Capitani, C. & Brown, T.H., (1987). The computation of chemical equilibrium in complex systems containing non-ideal solutions. *Geochimica et Cosmochimica Acta*, v.51, n.10, p.2639-2652. [https://doi.org/10.1016/0016-7037\(87\)90145-1](https://doi.org/10.1016/0016-7037(87)90145-1)
- de Capitani, C. & Petrakakis, K., (2010). The computation of equilibrium assemblage diagrams with Theriak/Domino software. *American mineralogist*, v.95, n.7, p.1006-101 <https://doi.org/10.2138/am.2010.3354>
- Dempster, T.J., La Piazza, J., Taylor, A.G., Beaudoin, N. & Chung, P., (2017). Chemical and textural equilibration of garnet during amphibolite facies metamorphism: The influence of coupled dissolution–reprecipitation. *Journal of Metamorphic Geology*, v.35, n.9, p.1111-1130. <https://doi.org/10.1111/jmg.12278>
- Ducea, M.N., and Chapman, A.D., (2018), Sub-magmatic arc underplating by trench and forearc materials in shallow subduction systems; a geologic perspective and implications: *Earth--Science Reviews*, v. 185, p. 763–779, <https://doi.org/10.1016/j.earscirev.2018.08.001>.
- Dyck, B., Goddard, R.M., Wallis, D., Hansen, L.N. & Martel, E., (2021). Metamorphic evolution of the Great Slave Lake shear zone. *Journal of Metamorphic Geology*, v.39, n.5, p.567-590. <https://doi.org/10.1111/jmg.12576>
- Eisbacher, G.H., (1976). Sedimentology of the Dezadeash flysch and its implications for strike-slip faulting along the Denali fault, Yukon Territory and Alaska. *Canadian Journal of Earth Sciences*, v.13, n.11, p.1495-1513. <https://doi.org/10.1139/e76-157>
- Erdmer, P. & Mortensen, J.K., 1993. A 1200-km-long Eocene metamorphic-plutonic belt in the northwestern Cordillera: Evidence from southwest Yukon. *Geology*, v.21, n.11, p.1039-1042. [https://doi.org/10.1130/0091-7613\(1993\)021<1039:AKLEMP>2.3.CO;2](https://doi.org/10.1130/0091-7613(1993)021<1039:AKLEMP>2.3.CO;2)

- Ernst, W.G., 1963. Significance of phengitic micas from low-grade schists. *American Mineralogist: Journal of Earth and Planetary Materials*, v.48, n.11-12, p.1357-1373.
- Forshaw, J.B., Pattison, D.R.M., (2021) Ferrous/ferric (Fe²⁺/Fe³⁺) partitioning among silicates in metapelites. *Contributions to Mineralogy and Petrology* v.176, n.63. <https://doi.org/10.1007/s00410-021-01814-4>
- Frezzotti, M.L., Tecce, F. & Casagli, A., (2012). Raman spectroscopy for fluid inclusion analysis. *Journal of Geochemical Exploration*, v.112, p.1-20. DOI: 10.1016/j.gexplo.2011.09.009
- Gehrels, G.E., McClelland, W.C., Samson, S.D., Patchett, P.J. & Orchard, M.J., (1992). Geology of the western flank of the Coast Mountains between Cape Fanshaw and Taku Inlet, southeastern Alaska. *Tectonics*, v.11, n.3, p.567-585. <https://doi.org/10.1029/92TC00482>
- Gehrels, G., Rusmore, M., Woodsworth, G., Crawford, M., Andronicos, C., Hollister, L., Patchett, J., Ducea, M., Butler, R., Klepeis, K. & Davidson, C., (2009). U-Th-Pb geochronology of the Coast Mountains batholith in north-coastal British Columbia: Constraints on age and tectonic evolution. *Geological Society of America Bulletin*, v.121, n.9-10, p.1341-1361. <https://doi.org/10.1130/B26404.1>
- Giorgetti, G., Frezzotti, M.L., Palmeri, R. & Burke, E.A.J., (1996). Role of fluids in migmatites: CO₂-H₂O fluid inclusions in leucosomes from the Deep Freeze Range migmatites (Terra Nova Bay, Antarctica). *Journal of Metamorphic Geology*, v.14, n.3, p.307-317. <https://doi.org/10.1111/j.1525-1314.1996.00307.x>
- Guidotti, C.V. & Dyar, M.D., (1991). Ferric iron in metamorphic biotite and its petrologic and crystallochemical implications. *American Mineralogist*, v.76, n.1-2, p.161-175.
- Holdaway, M.J., (2000). Application of new experimental and garnet Margules data to the garnet-biotite geothermometer. *American mineralogist*, v.85, n.7-8, p.881-892. <https://doi.org/10.2138/am-2000-0701>

- Hart, C.J., Goldfarb, R.J., Lewis, L.L. & Mair, J.L., (2004). The Northern Cordilleran Mid-Cretaceous plutonic province: Ilmenite/magnetite-series granitoids and intrusion-related mineralisation. *Resource Geology*, v.54, n.3, p.253-280.
<https://doi.org/10.1111/j.1751-3928.2004.tb00206.x>
- Holland, T.J.B. & Powell, R.T.J.B., 1998. An internally consistent thermodynamic data set for phases of petrological interest. *Journal of Metamorphic Geology*, v.16, n.3, p.309-343. <https://doi.org/10.1111/j.1525-1314.1998.00140.x>
- Holland, T. & Powell, R., (2003). Activity–composition relations for phases in petrological calculations: an asymmetric multicomponent formulation. *Contributions to Mineralogy and Petrology*, v.145, n.4, p.492-501. <https://doi.org/10.1007/s00410-003-0464-z>
- Holland, T.J.B. & Powell, R., (2009). AX: A program to calculate activities of mineral end members from chemical analysis. Retrieved from:
<https://filedn.com/IU1GlyFhv3UuXg5E9fbnWFF/TJBHpages/ax.html>. Last updated, October 2019.
- Holland, T.J.B. & Powell, R., (2011). An improved and extended internally consistent thermodynamic dataset for phases of petrological interest, involving a new equation of state for solids. *Journal of Metamorphic Geology*, v.29, n.3, p.333-383.
<https://doi.org/10.1111/j.1525-1314.2010.00923.x>
- Hults, C.P., Wilson, F.H., Donelick, R.A. & O'Sullivan, P.B., (2013). Two flysch belts having distinctly different provenance suggest no stratigraphic link between the Wrangellia composite terrane and the paleo-Alaskan margin. *Lithosphere*, v.5, n.6, p.575-594. <https://doi.org/10.1130/L310.1>
- Israel, S., Murphy, D., Bennett, V., Mortensen, J. and Crowley, J., 2011a. New insights into the geology and mineral potential of the Coast Belt in southwestern Yukon. In: *Yukon Exploration and Geology 2010*, MacFarlane, K.E., Weston, L.H., and Relf, C. (eds.), Yukon Geological Survey, p. 101-123.

- Israel, S., Cobbett, R., Westberg, E., Stanley, B. & Hayward, N., 2011b. Preliminary bedrock geology of the Ruby Ranges, southwestern Yukon, (Parts of NTS 115G, 115H, 115A and 115B) (1:150 000 scale). Yukon Geological Survey, Open File 2011-2.
- Israel, S., Colpron, M., Cubley, J., Moynihan, D., Murphy, D.C. & Relf, C., (2015). The Bear Creek assemblage: A latest Triassic volcano-sedimentary succession in southwest Yukon. In: Yukon Exploration and Geology 2014, K.E. MacFarlane, M.G. Nordling and P.J. Sack (eds.), Yukon Geological Survey, p. 99-112.
- Johnston, S.T., and Canil, D., 2007. Crustal architecture of SW Yukon, northern Cordillera: Implications for crustal growth in a convergent margin orogen: *Tectonics*, v.26, TC1006, doi: 10.1029/2006TC001950.
- Kent, D.V. & Irving, E., (2010). Influence of inclination error in sedimentary rocks on the Triassic and Jurassic apparent pole wander path for North America and implications for Cordilleran tectonics. *Journal of Geophysical Research: Solid Earth*, v.115, n.B10. <https://doi.org/10.1029/2009JB007205>
- Kohn, M.J. and Spear, F., 2000. Retrograde net transfer reaction insurance for pressure-temperature estimates. *Geology*, v.28, n.12, p.1127-1130. [https://doi.org/10.1130/0091-7613\(2000\)28<1127:RNTRIF>2.0.CO;2](https://doi.org/10.1130/0091-7613(2000)28<1127:RNTRIF>2.0.CO;2)
- Kohn, M. J. (2014). Geochemical zoning in metamorphic minerals. *Treatise on Geochemistry*, v.4, p.249-280. <https://doi.org/10.1016/B0-08-043751-6/03176-5>
- Lamadrid, H.M., Moore, L.R., Moncada, D., Rimstidt, J.D., Burruss, R.C. & Bodnar, R.J., (2017). Reassessment of the Raman CO₂ densimeter. *Chemical Geology*, v.450, p.210-222. <http://dx.doi.org/10.1016/j.chemgeo.2016.12.034>
- Lamb, W.M. & Valley, J.W., (1988). Granulite facies amphibole and biotite equilibria, and calculated peak-metamorphic water activities. *Contributions to Mineralogy and Petrology*, v.100, n.3, p.349-360. <https://doi.org/10.1007/BF00379744>
- Law, R.D., (1986). Relationships between strain and quartz crystallographic fabrics in the Roche Maurice quartzites of Plougastel, western Brittany. *Journal of Structural Geology*, v.8, n.5, p.493-515. [https://doi.org/10.1016/0191-8141\(86\)90001-5](https://doi.org/10.1016/0191-8141(86)90001-5)

- Lowey, G.W., (2018). Provenance analysis of the Dezadeash Formation (Jurassic–Cretaceous), Yukon, Canada: Implications regarding a linkage between the Wrangellia composite terrane and the western margin of Laurasia. *Canadian Journal of Earth Sciences*, v.56, n.1, p.77-100. <https://doi.org/10.1139/cjes-2017-0244>
- McClelland, W.C., Gehrels, G.E. & Saleeby, J.B., (1992). Upper Jurassic-Lower Cretaceous basinal strata along the Cordilleran margin: Implications for the accretionary history of the Alexander-Wrangellia-Peninsular terrane. *Tectonics*, v.11, n.4, p.823-835. <https://doi.org/10.1029/92TC00241>
- Mehnert, K. R., (1968). *Migmatites and the Origin of Granitic Rocks*. x 393 p., 138 figs. Elsevier Publishing Company, Amsterdam, London, New York. *Geological Magazine*. Cambridge University Press, v.106, n.2, p. 222–223. doi: 10.1017/S0016756800052092.
- Mezger, J.E., 1997. Tectonometamorphic evolution of the Kluane metamorphic assemblage, southwest Yukon: evidence for Late Cretaceous eastward subduction of oceanic crust underneath North America. Unpublished PhD thesis, University of Alberta, 306 p. <https://doi.org/10.7939/R3DJ58N76>
- Mezger, J.E., (2010). Rotation of irregular staurolite porphyroblasts in a simple shear dominated shear zone controlled by initial growth orientation and aspect ratio. *Journal of Structural Geology*, v.32, n.8, p.1147-1157. <https://doi.org/10.1016/j.jsg.2010.07.002>
- Mezger, J.E., 2000. 'Alpine-type' ultramafic rocks of the Kluane metamorphic assemblage, southwest Yukon: Oceanic crust fragments of a late Mesozoic back-arc basin along the northern Coast Belt. In: *Yukon Exploration and Geology 1999*, Emond, D.S. and Weston, L.W. (eds.), Exploration and Geological Sciences Division, Yukon Region, Indian and Northern Affairs Canada, p. 127-138.
- Mezger, J.E., Chacko, T. & Erdmer, P., (2001). Metamorphism at a late Mesozoic accretionary margin: a study from the Coast Belt of the North American Cordillera. *Journal of Metamorphic Geology*, v.19, n.2, p.121-137. <https://doi.org/10.1046/j.0263-4929.2000.00300.x>

- Monger, J.W., (2014). Logan Medallist 1. Seeking the suture: The Coast-Cascade conundrum. *Geoscience Canada*, v.41, n.4, p.379-398.
<https://doi.org/10.12789/geocanj.2014.41.058>
- Monger, J.W. & Gibson, H.D., (2019). Mesozoic-Cenozoic deformation in the Canadian Cordillera: The record of a “Continental bulldozer”? *Tectonophysics*, v.757, p.153-169. <https://doi.org/10.1016/j.tecto.2018.12.023>
- Monger, J.W.H., Price, R.A., & Tempelman-Kluit, D.J., (1982), Tectonic accretion and the origin of the two major metamorphic and tectonic welts in the Canadian Cordillera. *Geology*, v.10, n.2, 70–75. [https://doi.org/10.1130/0091-7613\(1982\)10<70:TAATOO>2.0.CO;2](https://doi.org/10.1130/0091-7613(1982)10<70:TAATOO>2.0.CO;2)
- Monger, J.W.H., van der Heyden, P., Journeay, J.M., Evenchick, C.A. & Mahoney, J.B., (1994). Jurassic-Cretaceous basins along the Canadian Coast Belt: Their bearing on pre-mid-Cretaceous sinistral displacements. *Geology*, v.22, n.2, p.175-178.
[https://doi.org/10.1130/0091-7613\(1994\)022<0175:JCBATC>2.3.CO;2](https://doi.org/10.1130/0091-7613(1994)022<0175:JCBATC>2.3.CO;2)
- Mukherjee, S., (2017). Review on symmetric structures in ductile shear zones. *International Journal of Earth Sciences*, v.106, n.5, p.1453-1468. DOI: 10.1007/s00531-016-1366-4
- Nelson, J. L., Colpron, M. & Israel, S. (2013). The Cordillera of British Columbia, Yukon, and Alaska: Tectonics and Metallogeny. In: Special Publication 17, M. Colpron, T. Bissig, B.G. Rusk, and J.F.H. Thompson (eds), Society of Economic Geologists, Inc., p. 53-110. <https://doi.org/10.5382/SP.17.03>
- Nokleberg, W.J., Jones, D.L. & Silberling, N.J., (1985). Origin and tectonic evolution of the Maclaren and Wrangellia terranes, eastern Alaska Range, Alaska. *Geological Society of America Bulletin*, v.96, n.10, p.1251-1270. [https://doi.org/10.1130/0016-7606\(1985\)96<1251:OATEOT>2.0.CO;2](https://doi.org/10.1130/0016-7606(1985)96<1251:OATEOT>2.0.CO;2)
- Pattison, D.R. & Goldsmith, S.A., (2022). Metamorphism of the Buchan type-area, NE Scotland and its relation to the adjacent Barrovian domain. *Journal of the Geological Society*, v.179, n.1. <https://doi.org/10.1144/jgs2021-0>

- Pattison, D.R.M. & DeBuhr, C.L., (2015). Petrology of metapelites in the Bugaboo aureole, British Columbia, Canada. *Journal of Metamorphic Geology*, v.33, n.5, p.437-462. <https://doi.org/10.1111/jmg.12128>
- Phillips, G.N., (1981). Water activity changes across an amphibolite-granulite facies transition, Broken Hill, Australia. *Contributions to Mineralogy and Petrology*, v.75, n.4, p.377-386. DOI: 0010-7999/80/0075/0377/.
- Powell, R. & Holland, T., (1994). Optimal geothermometry and geobarometry. *American Mineralogist*, v.79, n.1-2, p.120-133. DOI: 0003-004X/94/0102-0120.
- Powell, R. & Holland, T.J.B., (2008). On thermobarometry. *Journal of Metamorphic Geology*, v.26, n.2, p.155-179. <https://doi.org/10.1111/j.1525-1314.2007.00756.x>
- Ramsay, C.R., (1973) The origin of biotite in Archaean meta-sediments near Yellowknife, N. W. T., Canada. *Contributions to Mineralogy and Petrology*, v.42, p. 43–54. <https://doi.org/10.1007/BF00521646>
- Redler, C., White, R.W. & Johnson, T.E., (2013). Migmatites in the Ivrea Zone (NW Italy): Constraints on partial melting and melt loss in metasedimentary rocks from Val Strona di Omegna. *Lithos*, v.175, p.40-53. <https://doi.org/10.1016/j.lithos.2013.04.019>
- Sawyer, E.W., Dombrowski, C. & Collins, W.J., (1999). Movement of melt during synchronous regional deformation and granulite-facies anatexis, an example from the Wuluma Hills, central Australia. *Geological Society, London, Special Publications*, v.168, n.1, p.221-237. <https://doi.org/10.1144/GSL.SP.1999.168.01.15>
- Sigloch, K. & Mihalynuk, M.G., (2013). Intra-oceanic subduction shaped the assembly of Cordilleran North America. *Nature*, v.496, n.7443, p.50-56. <https://doi.org/10.1038/nature12019>
- Sigloch, K. & Mihalynuk, M.G., (2017). Mantle and geological evidence for a Late Jurassic–Cretaceous suture spanning North America. *Geological Society of America Bulletin*, v.129, n.11-12, p.1489-1520. <https://doi.org/10.1130/B31529.1>

- Smith, T.E., (1981), Geology of the Clearwater Mountains, south-central Alaska. Alaska Division of Geological & Geophysical Surveys Geologic Report 60, p.72, 3 sheets, scale 1:63,360. <https://doi.org/10.14509/406>
- Spear, F.S. & Cheney, J.T., (1989). A petrogenetic grid for pelitic schists in the system SiO₂-Al₂O₃-FeO-MgO-K₂O-H₂O. *Contributions to Mineralogy and Petrology*, v.101, n.2, p.149-164. <https://doi.org/10.1007/BF00375302>
- Spear, F.S., (1993). Metamorphic phase equilibria and pressure–temperature–time paths. *Mineralogical Society of America Monograph*, Washington, D.C., p. 1-799.
- Spry, A., (1974). *Metamorphic textures*. Pergamon Press, Oxford, p. 240–246
- Stanley, B., (2012). Structural geology and geochronology of the Kluane schist, southwestern Yukon Territory. UWSpace. <http://hdl.handle.net/10012/7096> (unpublished Master's thesis, University of Waterloo).
- Steele-MacInnis, M., (2018). Fluid inclusions in the system H₂O-NaCl-CO₂: An algorithm to determine composition, density and isochore. *Chemical Geology*, v.498, p.31-44. <https://doi.org/10.1016/j.chemgeo.2018.08.022>
- St-Onge, M.R. & Davis, W.J., (2018). Wopmay orogen revisited: Phase equilibria modeling, detrital zircon geochronology, and U-Pb monazite dating of a regional Buchan-type metamorphic sequence. *Geological Society of America Bulletin*, v.130, n.3-4, p.678-704. <https://doi.org/10.1130/B31809.1>
- Sugisaki, R., (1984). Relation between chemical composition and sedimentation rate of Pacific ocean-floor sediments deposited since the middle Cretaceous: basic evidence for chemical constraints on depositional environments of ancient sediments. *The Journal of Geology*, v.92, n.3, p.235-259. <https://doi.org/10.1086/628858>
- Sun, Q., Zhao, L., Li, N., Liu, J., (2010). Raman spectroscopic study for the determination of Cl⁻ concentration (molarity scale) in aqueous solutions: Application to fluid inclusions. *Chemical Geology*, v.272, n.1-4, p. 55-61. <https://doi.org/10.1016/j.chemgeo.2010.02.004>

- Tempelman-Kluit, D. J., (1974). Reconnaissance geology of Aishihik Lake, Snag and part of Stewart River map-areas, west-central Yukon; Tempelman-Kluit, D J. Geological Survey of Canada, Paper 73-41, 1974, 97 pages (3 sheets), <https://doi.org/10.4095/102542>
- Thompson Jr, J.B., (1957). The graphical analysis of mineral assemblages in pelitic schists. *American Mineralogist: Journal of Earth and Planetary Materials*, v.42, n.11-12, p.842-858.
- Utada, M., (2001). Zeolites in hydrothermally altered rocks. *Reviews in mineralogy and geochemistry*, v.45, n.1, p. 305-322. <https://doi.org/10.2138/rmg.2001.45.10>
- van der Heyden, P., (1992). A Middle Jurassic to early Tertiary Andean-Sierran arc model for the Coast belt of British Columbia. *Tectonics*, v.11, n.1, p.82-97. <https://doi.org/10.1029/91TC02183>
- Vice, L., Gibson, H. D. & Israel, S., (2020). Late Cretaceous to Paleocene Tectonometamorphic Evolution of the Blanchard River Assemblage, Southwest Yukon: New Insight into the Terminal Accretion of Insular terranes in the Northern Cordillera. *Lithosphere*, 2020, v.1: 2298288. <https://doi.org/10.2113/2020/2298288>
- Waldien, T.S., Roeske, S.M., Benowitz, J.A., Twelker, E. & Miller, M.S., (2021a). Oligocene-Neogene lithospheric-scale reactivation of Mesozoic terrane accretionary structures in the Alaska Range suture zone, southern Alaska, USA. *Geological Society of America Bulletin*, v,133, n.3-4, p.691-716. <https://doi.org/10.1130/B35665.1>
- Waldien, T.S., Roeske, S.M. & Benowitz, J.A., (2021b). Tectonic underplating and dismemberment of the Maclaren-Kluane schist records Late Cretaceous terrane accretion polarity and ~480 km of Post-52 Ma dextral displacement on the Denali fault. *Tectonics*, v.40, n.10, e2020TC006677. <https://doi.org/10.1029/2020TC006677>
- Waters, D. J., (1988), Partial melting and the formation of granulite facies assemblages in Namaqualand, South Africa: *Journal of Metamorphic Geology*, v.6, p.387–404. <https://doi.org/10.1111/j.1525-1314.1988.tb00430.x>

- Waters, D.J., (2019). Metamorphic constraints on the tectonic evolution of the High Himalaya in Nepal: the art of the possible. Geological Society, London, Special Publications, v.483, n.1, p.325-375. <https://doi.org/10.1144/SP483-2018-187>
- White, R.W., Powell, R. & Clarke, G.L., (2002). The interpretation of reaction textures in Fe-rich metapelitic granulites of the Musgrave Block, central Australia: constraints from mineral equilibria calculations in the system $K_2O-FeO-MgO-Al_2O_3-SiO_2-H_2O-TiO_2-Fe_2O_3$. *Journal of metamorphic Geology*, v.20, n.1, p.41-55. <https://doi.org/10.1046/j.0263-4929.2001.00349.x>
- White, R.W., Powell, R. & Holland, T.J.B., (2001). Calculation of partial melting equilibria in the system $Na_2O-CaO-K_2O-FeO-MgO-Al_2O_3-SiO_2-H_2O$ (NCKFMASH). *Journal of Metamorphic Geology*, v.19, n.2, p.139-153. <https://doi.org/10.1046/j.0263-4929.2000.00303.x>
- White, R.W., Powell, R. & Holland, T.J.B., (2007). Progress relating to calculation of partial melting equilibria for metapelites. *Journal of Metamorphic Geology*, v.25, n.5, p.511-527. <https://doi.org/10.1111/j.1525-1314.2007.00711.x>
- White, R.W., Powell, R.O.G.E.R., Holland, T.J.B., Johnson, T.E. & Green, E.C.R., (2014). New mineral activity–composition relations for thermodynamic calculations in metapelitic systems. *Journal of Metamorphic Geology*, v.32, n.3, p.261-286. <https://doi.org/10.1111/jmg.12071>
- Whitney, D.L. & Evans, B.W., (2010). Abbreviations for names of rock-forming minerals. *American Mineralogist*, v.95, n.1, p.185-187. <https://doi.org/10.2138/am.2010.3371>
- Will, T.M., Okrusch, M. & Gruner, B.B., (2004). Barrovian and Buchan type metamorphism in the Pan-African Kaoko belt, Namibia: implications for its geotectonic position within the framework of Western Gondwana. *South African Journal of Geology*, v.107, n.3, p.431-454. <https://doi.org/10.2113/107.3.431>
- Wu, C.M., (2015). Revised empirical garnet–biotite–muscovite–plagioclase geobarometer in metapelites. *Journal of Metamorphic Geology*, v.33, n.2, p.167-176. <https://doi.org/10.1111/jmg.12115>

Wu, C.M., (2017). Calibration of the garnet–biotite–Al₂SiO₅–quartz geobarometer for metapelites. *Journal of Metamorphic Geology*, v.35, n.9, p.983-998.
<https://doi.org/10.1111/jmg.12264>

Zwart, H.J., (1962). On the determination of polymetamorphic mineral associations, and its application to the Bosost area (Central Pyrenees). *Geologische Rundschau*, v.52, n.1, p.38-65. <https://doi.org/10.1007/BF01840064>

Chapter 4. A record of Late Cretaceous to early Paleogene Insular terrane accretion within the Northern Cordillera; insights from monazite petrochronology across the Kluane Schist, southwest Yukon

Will McKenzie¹, Brendan Dyck², H. Daniel Gibson¹ and Kyle Larson²

¹ *Department of Earth Sciences, Simon Fraser University, Burnaby, BC, Canada*

² *Department of Earth, Environmental and Geographical Sciences, University of British Columbia, Kelowna, BC, Canada*

Abstract

The Kluane Schist is a metamorphosed package of siliciclastic and calcareous rocks that lies between the inboard pericratonic Intermontane terranes and outboard Insular terranes of the North American Cordillera within Yukon, Canada. The metamorphic sequence of the Kluane Schist preserves a record of the tectono-thermal evolution and timing of Insular terrane accretion. Here we document the timing of metamorphism and deformation across the Kluane Schist using *in-situ* laser ablation inductively coupled plasma mass spectrometry U-Th-Pb monazite petrochronology. Monazite-bearing samples collected across an inverted metamorphic sequence preserved in the northern regions of the Kluane Schist yield dates ranging from ca. 70–55 Ma. Complementary phase equilibria modelling and thin section analysis indicate monazite grew between ~450 °C and 3.0–3.5 kbar to ~700–715 °C and 4.0–4.5 kbar, coeval with the development of the Kluane Schist's inverted metamorphic sequence. Dating the four chemical zones preserved by monazite demonstrates its protracted growth during three distinct periods of garnet crystallisation and breakdown, as well as coeval with melt generation. Our data illustrate that peak metamorphic conditions were reached at progressively younger ages with decreasing structural level within the Kluane Schist.

Our results are consistent with Buchan-style metamorphism associated with the terminal accretion of the outboard Insular terranes and southwest-directed overriding of the inboard Yukon-Tanana terrane from ca. 70–55 Ma. These findings are further consistent with a Late Cretaceous timing for the terminal accretion of the Insular terranes within southwest Yukon, facilitated by east-dipping subduction beneath a westward migrating North American continent.

4.1. Introduction

The boundary between the outboard Insular terranes and the inboard Intermontane terranes of the Northern Cordillera extends for over 2000 km from southern British Columbia to Alaska (Monger *et al.*, 1982; Rubin and Saleeby, 1991a; van der Heyden, 1992). Current tectonic models of the Mesozoic accretion of the Insular terranes to the western Laurentian margin differ on the timing, mechanism, and tectonic style of this accretionary event (e.g., Monger *et al.*, 1982; Gehrels *et al.*, 1991; Rubin and Saleeby, 1991a, b; McClelland *et al.*, 1992a, b; van der Heyden, 1992; Trop *et al.* 2002; Gehrels *et al.*, 2009; Sigloch and Mihalynuk, 2013, 2017; Box *et al.*, 2019; Monger and Gibson, 2019). These differences can be summarized in two end-member scenarios: (1) progressive accretion of the Insular terranes across an extensive ocean basin from the Late Jurassic to earliest Eocene, primarily driven by slab-pull and west-dipping subduction along the inboard margin of the Insular terranes (Sigloch and Mihalynuk, 2013, 2017), and (2) a diachronous accretionary history, from Middle Jurassic–Late Cretaceous, facilitated by east- and north-dipping subduction below a westerly migrating North American continent. In this second scenario, initial Middle Jurassic Insular terrane accretion occurred near west-central British Columbia and southernmost Alaska (present-day coordinates), and became progressively younger to the north and south accompanied by episodes of metamorphism, deformation and inversion of terrane-intervening basins up until the terminal accretion of the Insular terranes in mid–late Cretaceous (Monger *et al.*, 1982; Gehrels *et al.*, 1991; Rubin and Saleeby, 1991a, 1991b; McClelland *et al.*, 1992a, 1992b; van der Heyden, 1992; Trop *et al.* 2002; Gehrels *et al.*, 2009; Monger and Gibson, 2019; Box *et al.*, 2019).

Testing these different models of Insular terrane accretion against the geological record has been hampered by the fact that the Insular-Intermontane suture potentially accommodated >1000 Km of terrane translation during the Cenozoic and has been overprinted by multiple phases of deformation, magmatism, and metamorphism since the mid-Cretaceous (e.g., Monger, 2014). However, insight into the tectonic history of this suture zone can be gleaned from a series of variably metamorphosed and deformed Jurassic to Cretaceous (Jura-Cretaceous) aged basins that together are considered to represent a seaway, or series of seaways, that once separated the Insular and Intermontane terranes (van der Heyden, 1992; McClelland *et al.*, 1992b; Gehrels *et al.*, 1991; Monger *et al.*, 1994; Hults *et al.*, 2013; Box *et al.*, 2019). Recent and past studies largely agree that the collapse of these basins records both metamorphism and deformation associated with Insular terrane accretion (Monger *et al.*, 1994; Hults *et al.*, 2013; Box *et al.*, 2019; Vice *et al.*, 2020; Waldien *et al.*, 2021a, b; Chapter 3), and that analysis of the structures preserved in these basins provides evidence for their collective inversion during a period of orogen-normal compression (Smith, 1981; Monger *et al.*, 1982; van der Heyden, 1992; McClelland and Mattinson, 2000; Hults *et al.*, 2013; Moore and Box, 2016; Box *et al.*, 2019; Monger and Gibson, 2019; Chapter 3).

While there is general agreement about the broad correlations between these units and their restored structural positions, the precise timing at which some of these basins collapsed remains contentious. Past studies that combined structural analysis and detrital zircon datasets have inferred as much as a ca. 40 Myr difference in the timing of initial basin inversion between southern Alaska, southwest Alaska, and southwest Yukon (ca. 117–81 Ma; Manuszak *et al.*, 2007; Yokelson *et al.*, 2015; Box *et al.*, 2019). Equally, studies aimed at determining the timing of compressional events preserved within individual basins also report a disparity in ages (e.g., Mezger *et al.*, 2001; Israel *et al.*, 2011a; Box *et al.*, 2019; Waldien *et al.*, 2021b). Post-tectonic plutons are dated to ca. 90 Ma within the Gravina Belt of west-central British Columbia/southeast Alaska (e.g., McClelland and Mattinson, 2000), to ca. 75 Ma within the Kahiltna Basin south-central Alaska (e.g., Hults *et al.*, 2013; Box *et al.*, 2013; Moore and Box, 2016), and to between ca. 64–57 Ma within the Kluane Basin of southwest Yukon (Erdmer and Mortensen, 1993; Israel *et al.*, 2011a) implying a diachronous collapse of these basins during the Late Cretaceous (e.g., Box *et al.*, 2019). In contrast, the recent *in-situ* analysis of monazite within the Blanchard River assemblage of southwest Yukon (ca. 83–61 Ma,

Vice *et al.*, 2020) and dates from metamorphic zircon separates from the Maclaren Schist of southcentral Alaska (ca. 84–55 Ma, Waldien *et al.*, 2021a) provides evidence that these basins share a metamorphic and deformation history that extends into the latest Paleocene or early Eocene. Reconciling these disparate datasets remains key to unravelling the timing and style of Insular terrane accretion within the Northern Cordillera and quantifying the tectonic evolution of North American margin during the Mesozoic.

In this study we provide a comprehensive examination of the Kluane Schist, the major metasedimentary fill of the Cretaceous Kluane Basin, southwest Yukon, by integrating pressure-temperature-time (*P-T-t*) data with structural analyses to show the Kluane Schist: (1) preserves an inverted Buchan-style gradient within its northern region that resulted from a single, downward penetrating phase of metamorphism and deformation between ca. 70–55 Ma and (2) experienced limited thermal overprinting by the Ruby Range batholith.

4.2. Geological setting

The Kluane Basin is located within the Dezadeash and Ruby Ranges of southwest Yukon, to the southeast and north of Haines Junction and to the east of Kluane Lake (Fig. 4.1). The basin itself lies at the interface between the Yukon-Tanana terrane of the Intermontane belt and Alexander and Wrangellia terranes of the Insular belt (Fig. 4.1; e.g., Mezger *et al.*, 2001; Israel *et al.*, 2011a, b). The Denali fault truncates the Kluane Basin along its southwest flank, separating it from rocks of the Alexander and Wrangellia terranes, while the extensive Paleocene-Eocene Ruby Range batholith overprints the contact between the Kluane Schist and the overthrust Yukon-Tanana terrane towards the north, east and south (Fig. 4.1).

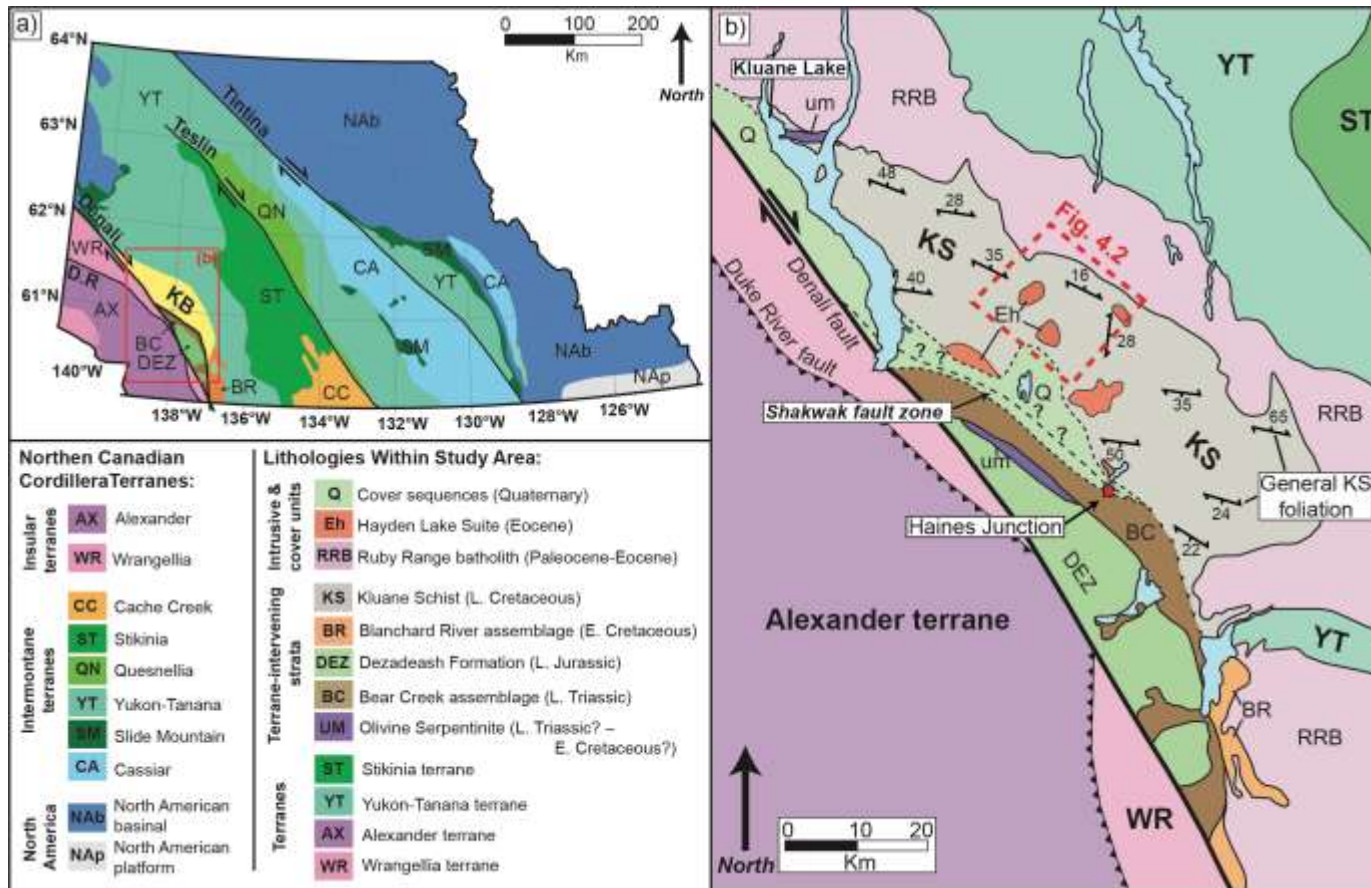


Figure 4.1. a) Terrane map of Yukon (after: Colpron & Nelson, 2011). Red box outlines location of the study area shown in b) (KB = Kluane Basin; D.R = Duke River Fault). b) Map showing the distribution of major lithologies within the Kluane Basin of southwest Yukon, other Jura-Cretaceous basins within this region of the Cordillera and their relationship to surrounding geological belts (modified from: Mezger *et al.*, 2001; Israel *et al.*, 2011b; Israel *et al.*, 2015). Within the study area the Intermontane terranes are primarily represented by the Yukon-Tanana terrane. Dashed box outlines approximate location of Figure 4.2.

The Kluane Basin hosts a range of lithologies including metapelites, ultramafic talc-schists, and carbonate enclaves (Fig. 4.1b). Young, undeformed diorite to quartz diorites of the Eocene Hayden Lake suite intrude across the major transposition fabric preserved in the Kluane Schist (Fig. 4.1b; Mezger *et al.*, 2001; Israel *et al.*, 2011b; Canil *et al.*, 2015). The predominant lithology of the Kluane Basin is the Kluane Schist, a 160 km long, largely northwest-striking belt of graphitic metapelites (Fig. 4.1b; e.g., Mezger *et al.*, 2001; Israel *et al.*, 2011a, b). Recent work has divided Kluane Schist into seven distinct petrological zones defined by similarity in their preserved metamorphic assemblage and deformation fabrics (Fig. 4.2; Chapter 3). Below, most pertinent characteristics of these petrological zones are summarized.

Towards the core of the basin, in its lowest exposed structural levels, the Kluane Schist comprises greenschist-facies schists that host a planar fabric defined by chlorite–muscovite +/- titanite–calcite (zone 1; Figs. 4.2 and B1a; Chapter 3). Within structurally higher samples, this planar fabric is initially overprinted by a biotite–zoisite crenulation and subsequently overgrown by plagioclase and garnet porphyroblasts (zones 2–3; Fig. 4.2; Chapter 3). Up structural section, complete fabric transposition occurs at the staurolite-grade (zone 4; Fig. 4.2; Chapter 3), defined by a pervasive, NNE-dipping biotite-rich folia that dominates this part of the Kluane Schist (Fig. 4.2; Chapter 3). Shearing and coarsening of this transposition fabric locally forms protogneissic banding at andalusite/fibrolite-grade (zone 5; Fig. 4.2; Chapter 3) and eventually a penetrative, outcrop-scale gneissosity at cordierite-grade (zone 6; Fig. 4.2 and B1b–e; Chapter 3). The progressive development of polymineralic leucosome within the northeast regions of the basin (zone 7; Fig. 4.2; Chapter 3) disrupts the coarse biotite–cordierite and plagioclase–quartz gneissic band preserved by the structurally highest units of the basin. This relationship between metamorphic grade and structural level across the Kluane Schist has been interpreted as a hot-side up metamorphic field gradient relating to the post-tectonic intrusion of the overlying Ruby Range batholith (Mezger *et al.*, 2001), a structurally inverted metamorphic sequence which represents part of a ~40 km thick crustal section that becomes younger and more juvenile with depth (Johnston and Canil, 2007), and as a cryptic structural discontinuity, which may in part represent the boundary between the Kluane Schist and the overlying rocks of the Yukon-Tanana terrane (Fig. 4.1b; Erdmer, 1991; Israel *et al.*, 2011a).

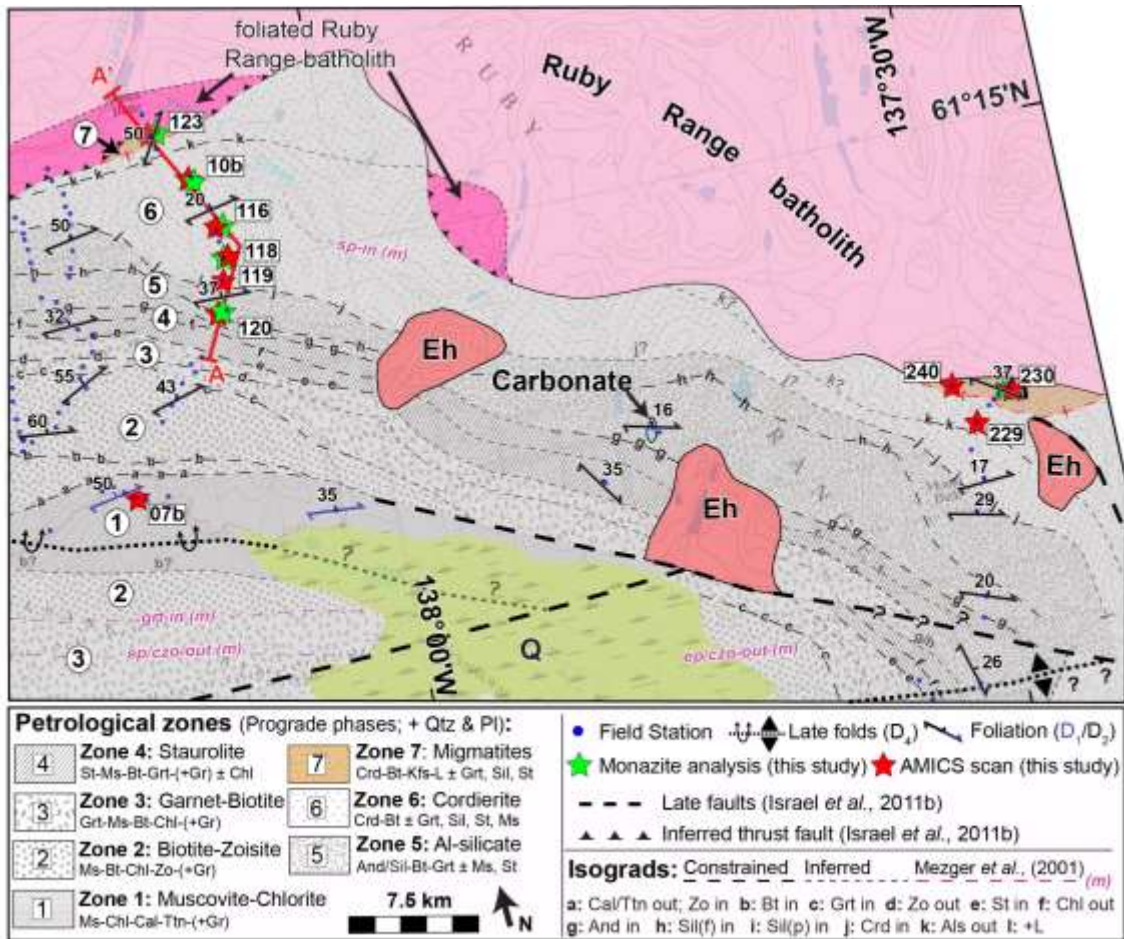


Figure 4.2. Geologic map including petrological zones within the central region of the Kluane Schist (see also Chapter 3). This map represents the red dashed area outlined in Figure 4.1b. All lithologies are the same colour as Figure 4.1b unless indicated (dark pink = foliated variety of the Ruby Range batholith; Blue = carbonate). Petrological zones are highlighted by different shading and fill patterns and labeled with circled numbers. The mineral assemblage characteristic of each zone is noted in the legend labeled “Petrological zones” (mineral abbreviations after Whitney & Evans, 2010). Field isograds within, and bounding, each petrological zone are shown by dashed lines and labelled with letters (a–l) that correspond to the phases used to define the isograds. Orange shading represents areas where leucosome is observed in Kluane Schist outcrops. Phase maps were made for samples highlighted by red stars, and green stars show the samples selected for monazite trace element analysis and U-Th-Pb petrochronology (full sample descriptions can be found within main text; sample numbers are represented in boxes).

Key to unravelling the principal driver of this structural-metamorphic relationship preserved within Kluane Schist is constraint on its timing of metamorphism and deformation. Kluane Schist peak metamorphism has been characterized through laser ablation inductively coupled plasma mass spectrometry (LA-ICP-MS) U-Pb analysis of zircon rims from a single sample, which indicated two major metamorphic episodes at ca. 82 and 72 Ma (Israel *et al.*, 2011a; Stanley, 2012). However, U-Pb isotope dilution-thermal ionization mass spectrometry (ID-TIMS) analyses on monazite and xenotime separates recovered from multiple samples across the Kluane Schist indicate a distinctly younger peak metamorphic age of ca. 58–56 Ma (Mortensen and Erdmer, 1992; Erdmer and Mortensen, 1993). Coincidence between those dates and the age of the Ruby Range batholith (ca. 64–57 Ma, Erdmer and Mortensen, 1993; Israel *et al.*, 2011a, b), have led to suggestions that they reflect a widespread recrystallisation event related to Ruby Range batholith intrusion (Mezger, 1997). Zircon from a dyke cross-cutting the major transposition fabric within the Kluane Schist indicates that the deformation occurred prior to ca. 72–68 Ma, in line with the dates provided by zircon rims (Mezger *et al.*, 2001; Israel *et al.*, 2011a). However, monazite within the same dyke provides a significantly younger age of 55.6 ± 0.6 Ma (Israel *et al.*, 2011a), indicating the dated zircon could be inherited from the host rock. Lastly, ^{40}Ar - ^{39}Ar mica dates are interpreted to reflect cooling during final exhumation and uplift of the Kluane Schist to between ca. 55–40 Ma (Mortensen and Erdmer, 1992; Mezger, 1997).

4.3. Methods

4.3.1. Analytical methods

Automated mineralogy

To aid in selecting amenable samples for detailed petrochronology, X-ray phase mapping was completed on nine samples that were collected across the Kluane Schist (Fig. 4.2 and B1). X-ray phase maps were obtained from Vidence Inc., Burnaby, Canada. Analysis was undertaken with a Hitachi SU3900 scanning electron microscope fitted with a single large area (60 mm²) Bruker SDD energy dispersive spectrometer and running the Advanced Mineral Identification and Characterization System (AMICS)

automated mineralogy package. An acceleration voltage of 20 kV was coupled with a beam current of 15 nA. A segmented field image mode was used, which subdivides the back scattered electron (BSE) image into the domains (segments) of similar brightness (i.e., different mineral grains) and then acquires a representative EDS X-ray spectrum from a point within the segment; the mineral identified is then assigned to the entire segment. As measurements are optimized to highlight both textural and modal mineralogical information an effective image resolution of 2.48 μm was used. These high-resolution thin section scans allowed us to identify monazite grains in different textural and microstructural positions.

Monazite back scattered electron (BSE) images and chemical maps

AMICS scans were used to aid the selection of six monazite-bearing samples for further analysis. These include: 19WM120, 19WM118, 19WM116, 18WM10b, 19WM123 and 19WM230 (Figs. 4.2 and B1–7). We targeted monazite within these samples that were generally aligned with the dominant micaceous foliation (AMICS scans with marked monazite are presented in Figs. B2–7). Elemental maps were made for select monazite grains using the CAMECA SX-5 Field Emission Electron Probe Micro-Analyser (EPMA) in the Fipke Laboratory for Trace Element Research (FiLTER) at the University British Columbia, Okanagan. Maps of Si, Ca, Th, U and Y were created using a 1 μm step size, 1 μm spot size, and dwell time of 100ms. The acceleration potential was set to 15 KeV and current was 200 nA. The chemical maps of monazite were used to guide spot selection during monazite U-Th-Pb age and trace element analysis and are presented in Figs. B2–7.

Monazite U-Th-Pb petrochronology and trace element chemistry

Monazite U-Th-Pb petrochronology was carried out via LA-ICP-MS at FiLTER. Samples were examined *in-situ* over 6 analytical sessions over a 3-day period using a Photon Machines Analyte 193 Excimer laser coupled to an Agilent 8900 triple quadrupole (QQQ) ICP-MS operated in single quadrupole mode. Signal was tuned for each analytical session to maximize signal for Pb, U, and Th, and optimize U/Th against the reference glass 'NIST610', while minimizing ThO production. A 15 μm diameter laser spot was used for all specimens with a repetition rate of 6.00 Hz and fluence of $\sim 3.95 \text{ J/cm}^2$. Each spot was pre-ablated with two laser bursts followed by a 30 second delay before 30 seconds of ablation. The ablated material was transported to the QQQ-ICP-

MS via 0.9 L/min Ar sample gas with a 0.375 L/min He carrier gas and mixed pre-plasma using an in-house glass signal smoothing device.

Analyses of unknown monazite were bracketed with material of known age/composition approximately every 10 spots. The monazite reference material '44069' ($^{206}\text{Pb}/^{238}\text{U}$ ID-TIMS age of 424.9 ± 0.4 Ma; Aleinikoff *et al.*, 2006) was used for primary age/ratio calibration with additional monazite reference materials 'Bananeira' ($^{206}\text{Pb}/^{238}\text{U}$ ID-TIMS age of 511.9 ± 1.5 Ma; Horstwood *et al.*, 2016; $^{206}\text{Pb}/^{238}\text{U}$ LA-ICP-MS age of 508 ± 1 Ma and over-dispersed $^{208}\text{Pb}/^{232}\text{Th}$ LA-ICP-MS age of 496.5 ± 1.6 Ma; Kylander-Clark *et al.*, 2013) and '554' ($^{208}\text{Pb}/^{232}\text{Th}$ date of 45.0 ± 1.3 Ma; M. Tatsumoto, as cited in Harrison *et al.*, 1999 and $^{206}\text{Pb}/^{238}\text{U}$ dates of $\sim 44.3 - 50.8$ Ma; Peterman *et al.*, 2012) analysed as unknowns to verify the analytical setup and quantify potential excess dispersion. Down-hole element fractionation and instrument drift were monitored based on the primary reference material and corrected for using the Lolite software package (v.4) (Paton *et al.*, 2010, 2011). Repeat analyses of Bananeira yielded weighted mean $^{208}\text{Pb}/^{232}\text{Th}$ ages of 501 ± 3 Ma (mean squared weighted deviation (MSWD) = 1.6, $n = 9/10$), 490 ± 3 Ma (MSWD = 1.6, $n = 8/8$), 487 ± 2 Ma (MSWD = 5, $n = 10/10$), 504 ± 6 Ma (MSWD = 5, $n = 5/8$), 497 ± 2 Ma (MSWD = 1.9, $n = 15/15$), and 493 ± 3 Ma (MSWD = 3.2, $n = 7/10$) and Stacey and Kramers (1975) based ^{207}Pb corrected $^{206}\text{Pb}/^{238}\text{U}$ ages of 510 ± 2 Ma (MSWD = 1.1, $n = 8/10$), 509 ± 3 Ma (MSWD = 0.58, $n = 8/8$), 506 ± 3 Ma (MSWD = 2.2, $n = 10/10$), 513 ± 5 Ma (MSWD = 3, $n = 6/8$), 505 ± 2 Ma (MSWD = 1.4, $n = 15/15$), and 503 ± 2 Ma (MSWD = 1.9, $n = 10/10$) for specimens 19WM118, 19WM230, 19WM123, 18WM10B, 19WM116 and 19WM120, respectively. Analysis of 554 across the same sessions yielded weighted mean $^{208}\text{Pb}/^{232}\text{Th}$ ages of 48.5 ± 0.3 Ma (MSWD = 1.1, $n = 5/6$), 47.2 ± 0.4 Ma (MSWD = 0.57, $n = 6/7$), 45.5 ± 0.3 Ma (MSWD = 15, $n = 4/4$), 47.3 ± 0.3 Ma (MSWD = 2.1, $n = 7/10$), 44.1 ± 0.3 Ma (MSWD = 1.3, $n = 9/9$), and 45.3 ± 0.3 Ma (MSWD = 1.1, $n = 12/12$), respectively. Excess dispersion calculated based on the $^{232}\text{Th}/^{208}\text{Pb}$, $^{207}\text{Pb}/^{206}\text{Pb}$ and $^{238}\text{U}/^{206}\text{Pb}$ ratios derived for NIST610 glass ranged between 0 and 1.5 %. The associated values were propagated through the isotopic ratios of the secondary reference materials and unknowns in quadrature for each associated run. The results of the secondary reference materials are within analytic reproducibility of the expected ages (e.g., Horstwood *et al.*, 2016); the variation in the results of the secondary monazite is consistent with known heterogeneity of the materials (see Kylander-Clark *et al.* 2013; Peterman *et al.*, 2012). The young age

of the monazite investigated in this study results in low radiogenic Pb signals (see Table F1). This precludes an accurate ^{204}Pb correction and can cause imprecision in both $^{207}\text{Pb}/^{235}\text{U}$ and $^{208}\text{Pb}/^{232}\text{Th}$ ages (e.g., Parish, 1990; Larson *et al.*, 2013). To address this issue, we used the ^{207}Pb -method of Ireland and Gibson (1998) in which the $^{207}\text{Pb}/^{206}\text{Pb}$ ratio, uncorrected for common Pb, is plotted against the uncorrected $^{238}\text{U}/^{206}\text{Pb}$ ratio within a Tera-Wasserburg diagram (Tera and Wasserburg, 1972). The ages we report are based on the lower intercept of a linear regression run through the analysis and the concordia curve, where the upper intercept is anchored at the common $^{207}\text{Pb}/^{206}\text{Pb}$ predicted for a concordant datum based on the two-stage model of Stacey and Kramers (1975). Herein, both single spot dates and multi-spot domain ages are reported using the ^{207}Pb -corrected $^{238}\text{U}/^{206}\text{Pb}$ system and are presented with 2σ uncertainty.

Trace element concentrations of the unknowns were measured at the same time as the U-Th-Pb isotopes for all monazite spots. A dwell time of 15 ms was used for each of ^{89}Y , ^{139}La , ^{140}Ce , ^{141}Pr , ^{146}Nd , ^{147}Sm , ^{153}Eu , ^{157}Gd , ^{159}Tb , ^{163}Dy , ^{165}Ho , ^{166}Er , ^{169}Tm , ^{172}Yb , ^{175}Lu , ^{181}Ta , and a 5 ms dwell time used for ^{31}P . Trace element concentrations in monazite were calculated using Iolite v.4 (Paton *et al.*, 2010, 2011) with Bananeira as the primary reference material for all samples excluding 18WM10B for which the glass NIST610 (GeoReM database, application version 27, <http://georem.mpch-mainz.gwdg.de>; Jochum *et al.*, 2005) was used due to heterogeneity in the Bananeira analyses for that sample run. Trace element concentrations were calculated based on assumed stoichiometric P in unknown monazite. Where an unstoichiometric monazite geochemistry (e.g., low [P]/high [Y]) is returned the analysis spot is typically observed to either hit a crack and/or inclusion within monazite, only partially clip the monazite grain or to have hit a different associatory phase (e.g., xenotime). This provides an additional filter by which data were rejected. Long-term reproducibility of trace element concentrations using Bananeira as a reference material is estimated to be approximately $\pm 5\%$ (Cottle *et al.* 2019), though for the present study absolute trace element concentrations are secondary to relative changes through time. Full U-Th-Pb and trace element monazite datasets can be found in Tables F1–2.

Petrological modelling and pressure-temperature determination

Petrological modelling was applied to three monazite- and garnet-bearing samples (19WM120, 19WM118 and 19WM123) that were collected from different

structural levels across the basin (Fig. 4.2) to determine a detailed *P-T-t* history for the Kluane Schist. Effective bulk compositions were calculated by combining mineral compositional data with the modal proportions determined by AMICS scans. Compositions of seven major assemblage minerals (chlorite, muscovite, biotite, garnet, staurolite, plagioclase and cordierite) were analysed using wavelength-dispersive (WDS) X-ray spectroscopy on a CAMECA SX-5 Field EPMA at the University British Columbia, Okanagan. The standards used for calibration were garnet spessartine for Si and Mn, titanite for Ti, garnet almandine for Al and Fe, wollastonite for Ca, albite for Na, diopside for Mg, orthoclase for K, apatite for P, fluorite for F and pure KCl for Cl. WDS quantification of Si, Al and F used the LTAP crystal; Ti, Ca, K, P and Cl used the LPET crystal; Fe and Mn used the LLIF crystal; and Na and Mg using the TAP crystal. A 20 keV acceleration voltage and 20 nA beam current was used to maximize analytical resolution and minimize sample damage. We analysed several spot locations across each porphyroblastic phase (garnet, staurolite, plagioclase, cordierite, and coarse biotite) to assess any chemical variations within individual grain. All mineral compositional data can be found in the supplemental Tables E1–7; calculated bulk compositions are presented in Table G1.

All phase diagrams were generated using the petrological modelling software Theriak-Domino (de Capitani and Brown, 1987; de Capitani and Petrakakis, 2010). Modelling of all samples was completed within the chemical system MnNCKFMASHO (MnO–Na₂O–CaO–K₂O–FeO–MgO–Al₂O₃–SiO₂–H₂O–TiO₂–O₂) using ds5.5 of Holland and Powell (1998) combined with activity models for plagioclase (Holland and Powell, 2003; ternary feldspar, Cbar 1 field); biotite, garnet and melt, (White *et al.* 2007); white mica (Coggon and Holland 2002; margarite omitted); ilmenite (White *et al.* 2000); orthopyroxene, (White *et al.* 2002); and staurolite, chlorite, cordierite and H₂O, (Holland and Powell 1998). Clinozoisite and zoisite were modelled as pure end-members within our ferric-free chemical system. We use ds5.5 rather than the more recent ds6.2 (Holland and Powell, 2011), as ds5.5 has been shown to more accurately produce the stable mineral assemblages observed across the Kluane Schist (also see Chapter 3).

Phase diagrams for all samples assume excess free H₂O below the solidus. For samples showing evolution above the solidus (e.g., migmatite sample 19WM123) our models assume only the amount of H₂O required to minimally saturate the assemblage in the immediate sub-solidus at 4 kbar (~5 mol H₂O; Fig. B8; c.f. Dyck *et al.*, 2020). To

account for both the graphitic nature of the Kluane Schist and evidence for low $a_{\text{H}_2\text{O}}$ fluids during metamorphism (see Chapter 3), we made our calculations with a reduced water activity ($a_{\text{H}_2\text{O}}$) of 0.5 at temperatures below 600 °C and an $a_{\text{H}_2\text{O}} = 1$ above 600 °C. Independent temperature constraints were acquired by applying the Ti-in-biotite thermometer (Henry *et al.*, 2005) to all graphite-free samples where the assumption of $a_{\text{H}_2\text{O}} = 1$ remains valid while also consistent with our forward modelling (Table G2). One-sigma standard uncertainties of Ti-in-biotite temperatures at such conditions is reported as ± 12 °C (Henry *et al.*, 2005; Table G2).

4.4. Results

4.4.1. Petrology of Samples

19WM120 (zone 5): Sample 19WM120, which comprises an assemblage containing andalusite/sillimanite–plagioclase–biotite–staurolite–garnet–muscovite (Fig. 4.3a), was collected from a structurally lower unit of zone 5 (Figs. 4.2 and 4.4). 19WM120 shows limited growth of aluminium silicates, preserving only rare knotty andalusite poikiloblasts and local clots of fibrolitic sillimanite intergrown with biotite-rich S_{2b} fabrics (Fig. 4.3a). Staurolite occurs as abundant subhedral porphyroblasts and inclusion-rich garnet have corroded rims (Fig. 4.3a). Structurally higher within zone 5, samples record the progressive replacement of staurolite by andalusite and garnet develops inclusion-free mantle domains that show a distinct chemistry versus their inclusion-rich cores (Fig. B1b; Chapter 3). The polymorphic transformation of andalusite to fibrolitic sillimanite is also observed with increased structural level within zone 5.

19WM119, 19WM118, 19WM116, 18WM10b and 19WM229 (zone 6): Collected from various structural levels within zone 6, these samples consist of cordierite–biotite–quartz–plagioclase +/- garnet–sillimanite/andalusite–muscovite (Fig. 4.3b). In general cordierite abundance increases to higher structural levels and metamorphic grades across zone 6 (Fig. B1b–d). Structurally lower samples (e.g., 19WM119; Fig. B1b) preserve fine, anhedral cordierite, which parallels biotite–muscovite–sillimanite S_{2b} fabrics (Fig. 4.3b). Relic andalusite and staurolite porphyroblasts are wrapped by cordierite (Fig. B1b). Within structurally higher samples

of zone 6 (e.g., 19WM118) staurolite, andalusite, and fibrolitic sillimanite show a reduced abundance and inclusion-free garnet mantles are strongly embayed and wrapped by cordierite (Figs. 4.3b and B1c–d). Garnet cores also show replacement by chlorite, muscovite, biotite, cordierite, and plagioclase (atolls, Fig. B1c). Across all zone 6 samples cordierite wraps plagioclase, staurolite, garnet, and andalusite (Figs. 4.3b and B1b–e). The structurally highest samples of zone 6 show coarse cordierite porphyroblasts with fibrolitic sillimanite inclusions (Fig. B1e). These samples generally lack staurolite, andalusite, and garnet (Fig. B1e). In general, the modal proportion of sillimanite is negatively correlated with increased structural level and cordierite abundance across zone 6 (Figs. 4.3b vs. 4.3c and B1b–e).

19WM123, 19WM240, 19WM230 (zone 7): These samples were collected from the structural top of the Kluane Schist and are migmatitic, exhibiting stromatic (Fig. 4.3c) and schollen (Fig. 4.3d) textures. Paleosome domains within both migmatite varieties show regularly spaced, centimetre-scale gneissic banding and consist of a mineral assemblage containing quartz–biotite–cordierite–plagioclase–K-feldspar +/- sillimanite/andalusite–garnet–staurolite (Fig. 4.3c and d). Cordierite exhibits two distinct populations within the migmatitic units; one roughly aligned with biotite-rich folia and a second population which shows an irregular shape, lacks aluminium silicate inclusions, and overgrows biotite fabrics (Fig. 4.3c–d). The inclusion-free cordierite population is interpreted here as peritectic (see Chapter 3). K-feldspar is observed in a similar microstructural position to peritectic cordierite and appears to have grown at the expense of biotite (Fig. 4.3c insert). Fibrolitic sillimanite and andalusite show a marked decrease in abundance compared with zone 6, only locally occurring as inclusions within cordierite (Figs. 4.3c and B1f). Local atoll garnet porphyroblasts are seen to host cordierite, muscovite, and chlorite (Fig. B1f). Leucosome domains within zone 7 consists of plagioclase, quartz, and peritectic cordierite (Fig. 4.3d). Peritectic cordierite is anhedral, fractured, free of any aluminum silicate inclusions, and shows limited microstructural relationship to surrounding biotite (Fig. 4.3d, insert; c.f. inserts in b, c). Plagioclase is euhedral and equant, lacking a shape preferred orientation as is seen in the paleosome (Fig. 4.3d). Spongy and randomly orientated muscovite and chlorite are interpreted as retrograde phases (Fig. 4.3d).

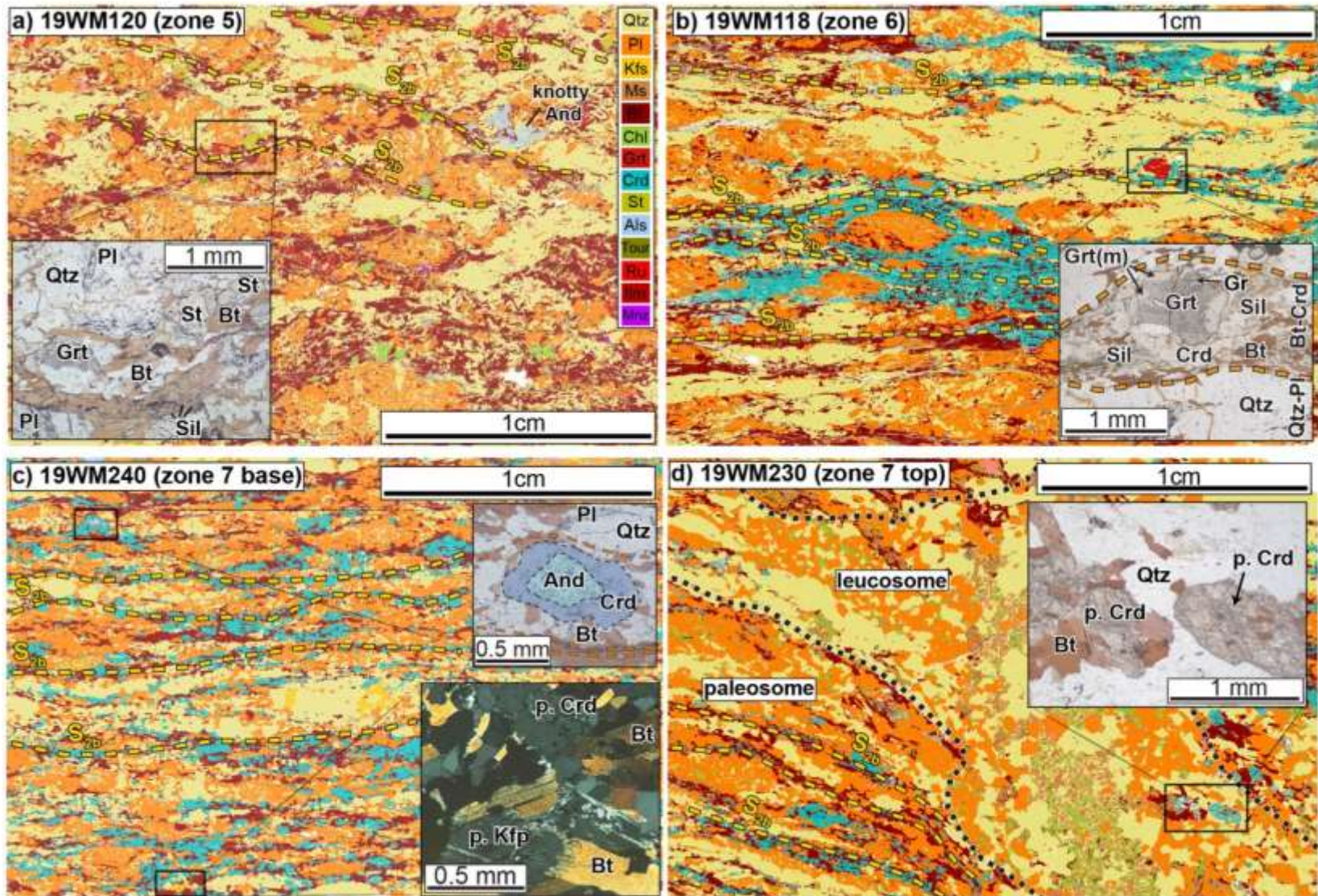


Figure 4.3. Advanced Mineral Identification and Characterization System (AMICS) scans highlighting key petrological relationships across the Kluane Schist; the colours used in all AMICS scans are keyed to their respective phases within the legend provided in (a). a) sample 19WM120 is typified by an assemblage containing aluminium silicate and staurolite. Both andalusite and fibrolitic sillimanite occur as rare anhedral phases; plagioclase and metastable staurolite define the dominant porphyroblasts. Insert shows a plain polarized (ppl) photomicrograph; staurolite appears subhedral and prismatic, whereas garnet is corroded and embayed, and fibrolitic sillimanite shows limited development within the biotite-rich fabric. b) Sample 19WM118 (zone 6). Cordierite is present within all zone 6 assemblages at the expense of both sillimanite and garnet (see insert). Also note the inclusion-rich cores and inclusion-free mantles (Grt(m)) typical of garnet within zones 5 & 6. c) Paleosome within sample 19WM240, a stromatic migmatite from the structural base of Zone 7. Coarse and equant cordierite is associated with fibrolitic sillimanite and andalusite (see insert). Inclusion free, peritectic cordierite (p. Crd) and K-feldspar (p.Kfs) overgrew the biotite-rich fabric (see cross-polarized photomicrograph in lower insert). d) schollen-style migmatite from the structural top of zone 7. Paleosome is like that of (c), with leucosome primarily consisting of plagioclase-quartz along with peritectic cordierite (p. Crd in insert). Muscovite and chlorite are considered retrograde phases.

4.4.2. Monazite microstructure and chemistry

There is a consistent change in the microstructure of monazite with respect to the structural level and corresponding metamorphic grade of the samples (Figs. 4.4 and 4.5). The structurally lower samples (e.g., 19WM120 and 19WM118) preserve coarse, skeletal monazite grains that are weakly aligned with the main foliation (Figs. 4.4a and B2, 3). Structurally higher samples (e.g., 19WM116, 19WM10b, 19WM123 and 19WM230) contain stubby-equant monazite that are generally aligned with their long axes parallel to the foliation and commonly occur as inclusions in plagioclase and cordierite (Figs. 4.4a, 4.5 and B4-7). Monazite grains within the upper region of zone 7 are subhedral with partially resorbed margins (Fig. 4.4a and B6, 7).

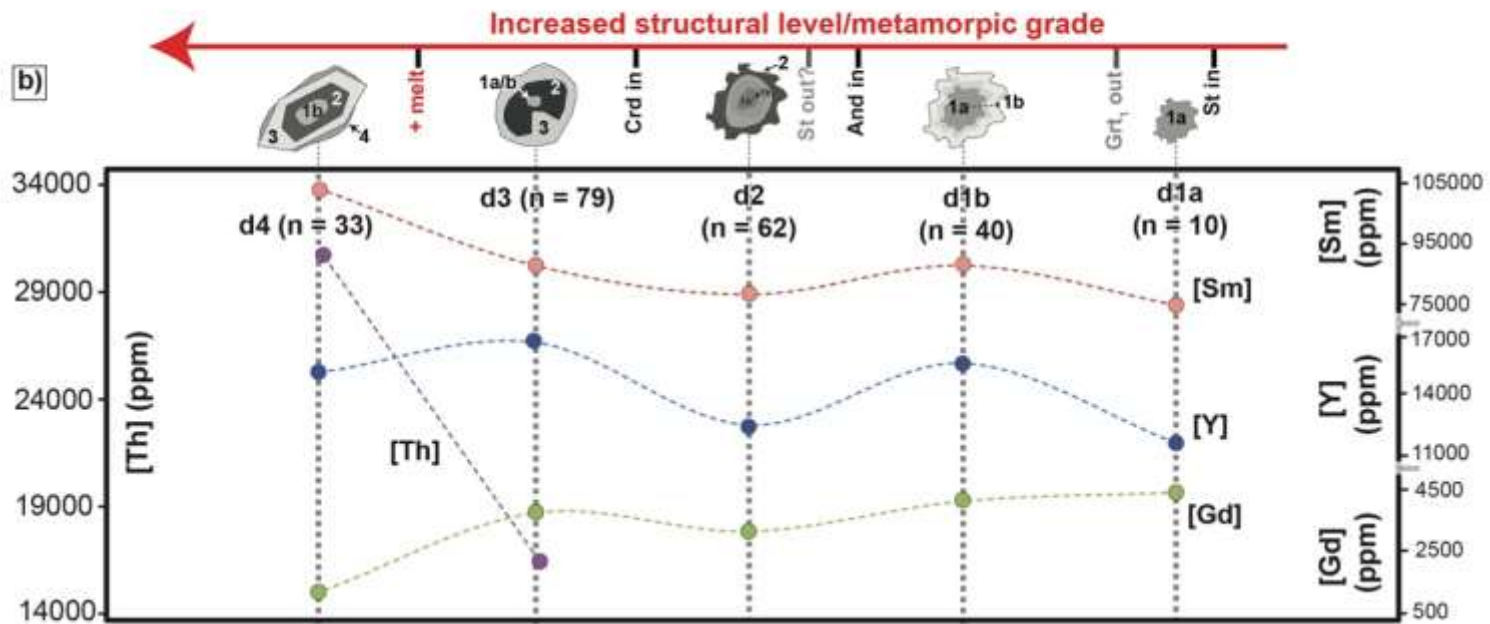
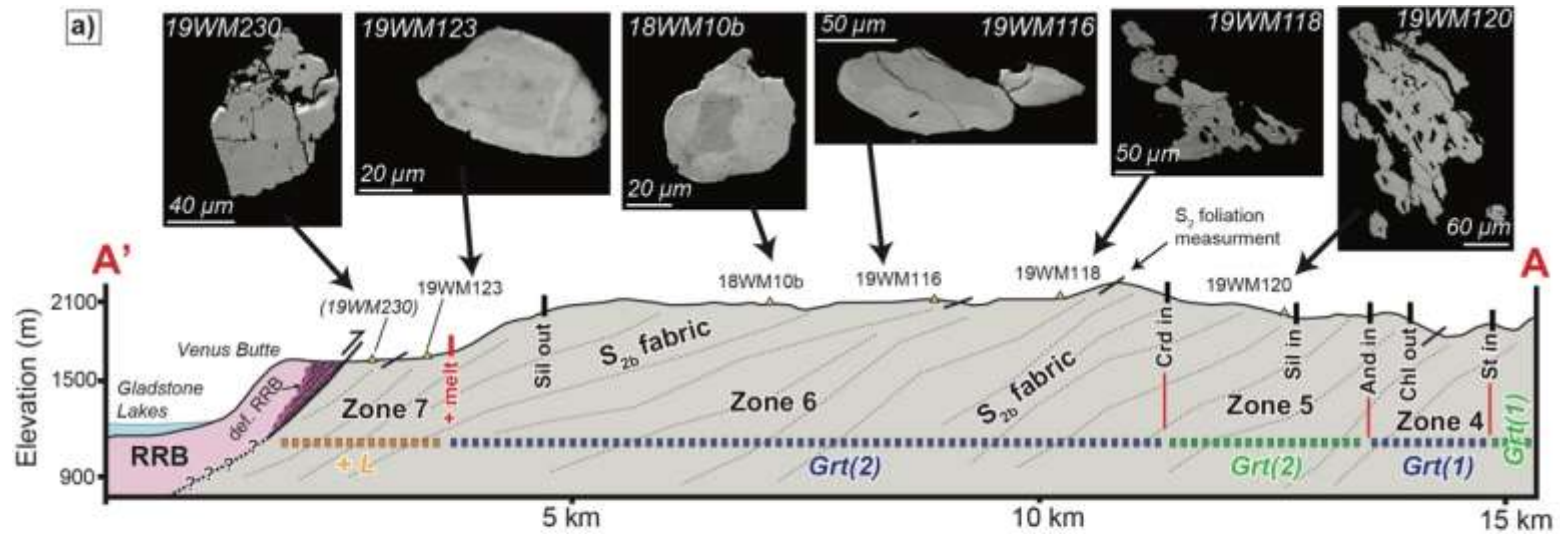


Figure 4.4. Cross section A-A' in Figure 4.2 (No vertical exaggeration). Metamorphic grade increases up structural level. Sample localities are highlighted by yellow triangles and average foliation measurements (S2) projected into the line of section are indicated by short solid lines. Isograds are directly labelled and indicated by thick solid lines. The observed growth and breakdown of distinct garnet populations is indicated by dashed green and blue lines respectively (see main text). Orange dashed line (+L) represents where melt domains were observed (see main text & Fig. 4.2). BSE images above the section show representative monazite with structural level and metamorphic grade. b) A schematic representation of the typical chemical zoning preserved by monazite with structural level and metamorphic grade across the Kluane Schist (see main text and Table 4.1). The average measured monazite [Y], [Sm], and [Gd] from all chemical domains and [Th] from domains 3 and 4 are indicated (see main text).

Yttrium distribution maps of monazite highlight four distinct chemical domains that, while not all present in each sample, show consistent textural and chemical relationships along our analysis transect (Figs. 4.4 and 4.5; Table 4.1 summarizes the chemical and microstructural characteristics used to differentiate monazite domains). In general, the complexity of the chemical zonation and the number of chemical domains preserved in individual grains increases up structural level (Figs. 4.4b and 4.5). Domain 1 is characterized by patchy zonation in Th, Y and Ca within lower grade samples (19WM120 and 19WM118; Fig. 4.5a-d) and forms the cores to monazite within higher-grade samples when present (e.g., 18WM10b; Fig. 4.5h). Domain 1 monazite is further subdivided based on its variable chemistry that includes either a local relative depletion in Y (domain 1a) or enrichment in Y (domain 1b) (Figs. 4.4b and 5a-d). Domain 1a is also characterized by a depletion in Sm (Fig. 4.4b). Domain 2 monazite have a depletion in Y, Sm and Gd and an enrichment in Th and Ca (Figs. 4.4b and 5). Domain 2 generally forms the cores to staurolite-free samples above the andalusite-in isograd (e.g., 19WM116, 18WM10b, 19WM123 and 19WM230; Figs. 4.4b, 4.5e-g and i, k); however, it consistently mantles domain 1 cores when they are present (e.g., Fig. 4.5h). Domain 3 monazite are typified by rims which truncate domain 2 in all samples above the cordierite-in isograd (Fig. 4.5 e-i). Domain 3 shows an enrichment in Y, Sm, and Gd and slight depletion in Th and Ca relative to domain 2 (Fig. 4.4b). Domain 4 monazite only occurs within the structurally highest samples of our transect, 19WM123 and 19WM230 where they form irregular overgrowths and thin rims on domain 3 (Fig. 4.5 i-l). These

domain 4 overgrowths typically show a depletion in Y, Ca, and Gd along with a strong enrichment in Th and Sm compared with domain 3 (Figs. 4.4b and 5 i-l).

4.4.3. Monazite petrochronology

Monazite dates returned from all individual sample are summarized in Fig. 4.6. Clear distinction can be made between each chemical domain present within an individual sample, with their overlapping ages indicating the sequential development of each chemical domain within monazite across the Kluane Schist, consistent with one metamorphic event.

Sample 19WM120: Thirty-seven spot analyses across 18 monazite grains produce overlapping dates between ca. 65 and ca. 56 Ma (Table F1). Typical monazite grains within this sample show < ca. 2 Myr difference in dates from core to rim, and are within uncertainty of one another (Fig. 4.5a-b). When all 38 spot analyses are considered together, there is a general chemical variation with date whereby young dates are returned from domains that are relatively enriched in [Y], middle and heavy rare earth elements (HREE; e.g., [Gd] and [Sm]; domain 1b; Fig. B9), and older dates for domains depleted in these elements (domain 1a; Fig. B9a and Table 4.1). Dates returned from domain 1b produce a lower intercept age of 57.4 +/- 0.2 (n = 32; MSWD = 1.7; Fig. 4.6a). Dates from domain 1a produce a lower intercept age at 62.8 +/- 1.8 Ma (n = 5; MSWD = 1.8; Fig. 4.6a). All grains preserve a negative Eu anomaly which is generally more pronounced with decreased age (Fig. B9).

Sample 19WM118: Fifty-two spot analysis across 19 grains produce dates between ca. 69 and ca. 56 Ma (Table F1). Domain 1a analyses yield the oldest dates with a lower intercept age of ca. 68.4 +/- 1.1 Ma (n = 4; MSWD = 0.6; Fig. 4.6b), whereas Domain 1b has a lower intercept age of 61.9 +/- 1.6 Ma (n = 3; MSWD = 0.3; Fig. 4.6b). Domain 2 dates define a lower intercept age of ca. 58.8 +/- 0.4 Ma (n = 28; MSWD = 1.1; Fig. 4.6b), and domain 3 rims yield a lower intercept age at 57.5 +/- 0.5 Ma (n = 17; MSWD = 1.2; Fig. 4.6b). A small negative Eu is noted for all domains; this is less pronounced for younger analyses (Fig. B9).

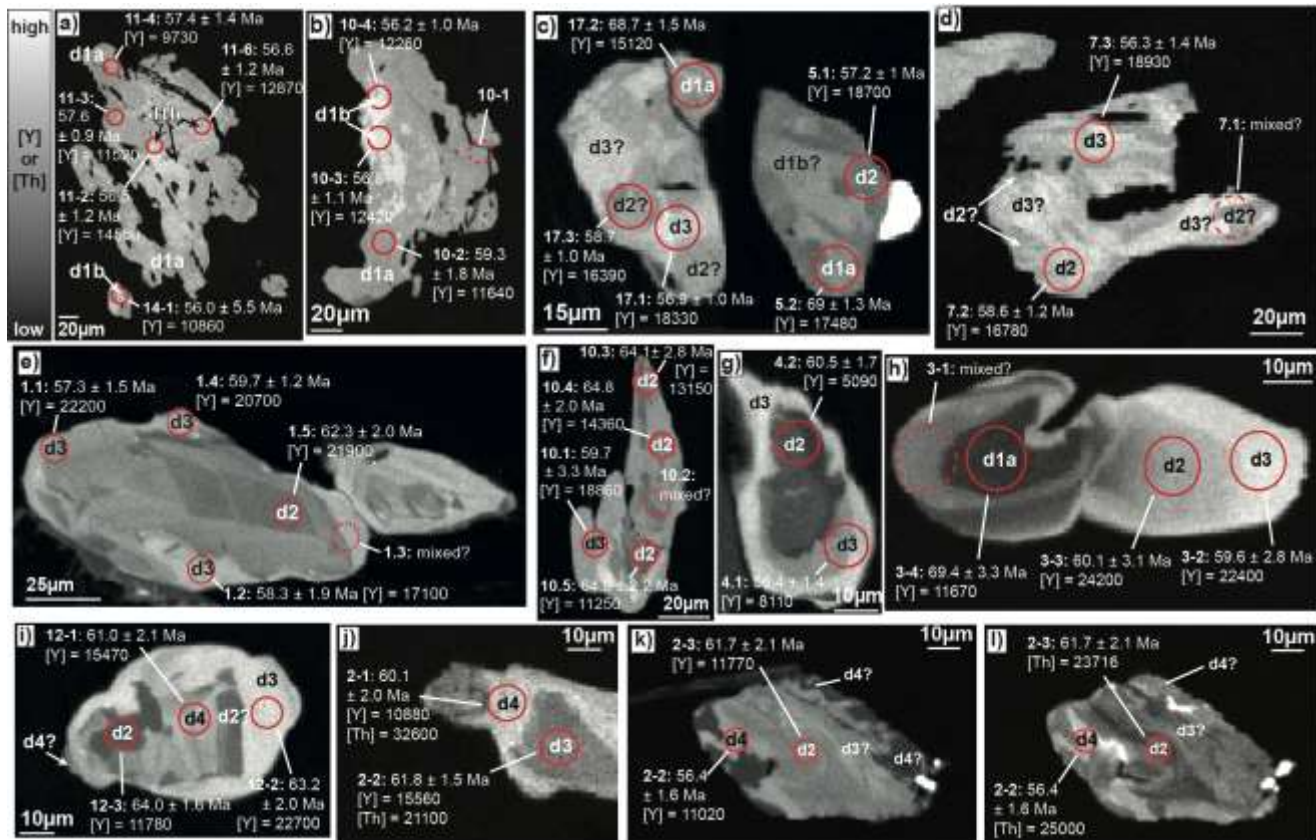








Figure 4.5. Chemical maps of monazite from all analysed samples across the Kluane Schist. For all chemical maps lighter shades of grey represent domains with higher relative concentrations of Y and Th versus domains with darker shades of grey. a-b) Yttrium [Y] maps of grains 11, 14 & 10 from 19WM120 (zone 5); c-d) Yttrium [Y] maps of grains 17, 5 & 7 from 19WM118 (zone 6 base); e-f) Yttrium [Y] maps of grains 1 & 10 from 19WM116 (zone 6 middle); g-h) Yttrium [Y] maps of grains 4 & 3 from 18WM10b (zone 6 top); i) Yttrium [Y] map of grain 12 from 19WM123 (zone 7 base); j) Thorium [Th] map of grain 2 from 19WM123, k) Yttrium [Y] map of grain 2 from 19MW230 (zone 7 top) and l) Thorium [Th] map of grain 2 from 19WM230.

	Sample (<i>petrologic zone</i>)	example grain	Domain 1a	Domain 1b	Domain 2	Domain 3	Domain 4
increasing structural level & metamorphic grade	19WM230 (7 upper)		<i>Not observed</i>	<i>Not observed</i>	64.6 ± 0.9 Ma; av. [Y] = 16465 av. [Th] = 22400 <i>HREE depleted</i>	61.4 ± 1.4 Ma; av. [Y] = 17540 av. [Th] = 24440 <i>HREE enriched</i>	58.4 ± 0.4 Ma; av. [Y] = 15830 av. [Th] = 26500 <i>HREE variable</i>
	19WM123 (7 base)		<i>Not observed</i>	67.6 ± 1.4 Ma; av. [Y] = 17500 <i>HREE enriched</i>	62.9 ± 0.8 Ma; av. [Y] = 13200 <i>HREE depleted</i>	60.8 ± 0.6 Ma; av. [Y] = 16100 av. [Th] = 29200 <i>HREE enriched</i>	59.2 ± 0.4 Ma; av. [Y] = 14400 [Th] = 34800 <i>HREE depleted</i>
	18WM10b (6 upper)		69.4 ± 3.2 Ma*; (n = 1) [Y] = 4540 <i>HREE depleted</i>	65.6 ± 2.1 Ma*; (n = 1) [Y] = 16200 <i>HREE enriched</i>	61.2 ± 1.5 Ma; av. [Y] = 8300 av. [Th] = 27300 <i>HREE variable</i>	57.6 ± 0.8 Ma av. [Y] = 14225 av. [Th] = 26200 <i>HREE enriched</i>	<i>Not observed</i>
	19WM116 (6 middle)		<i>Not observed</i>	<i>Not observed</i>	63.8 ± 1.0 Ma; av. [Y] = 19160 av. [Gd] = 2365 av. [Sm] = 114260	58.9 ± 0.6 Ma; av. [Y] = 20250 av. [Gd] = 2482 av. [Sm] = 105800	<i>Not observed</i>
	19WM118 (6 base)		68.4 ± 1.1 Ma; av. [Y] = 16450 av. [Gd] = 2400 av. [Sm] = 103575	61.9 ± 1.6 Ma; av. [Y] = 14620 av. [Gd] = 2020 av. [Sm] = 107030	58.8 ± 0.4 Ma; av. [Y] = 17035 av. [Gd] = 2190 av. [Sm] = 106870	57.5 ± 0.5 Ma; av. [Y] = 15250 av. [Gd] = 2230 av. [Sm] = 97230	<i>Not observed</i>
	19WM120 (5)		62.8 ± 1.8 Ma; av. [Y] = 13300 av. [Sm] = 105400 <i>HREE depleted</i>	57.4 ± 0.2 Ma; av. [Y] = 14010 av. [Sm] = 108300 <i>HREE enriched</i>	<i>Not observed</i>	<i>Not observed</i>	<i>Not observed</i>

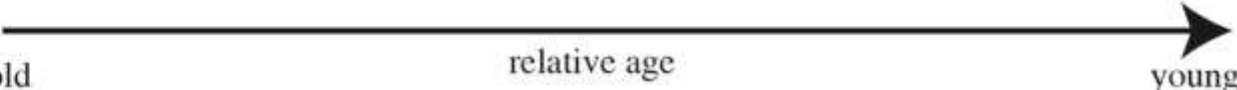


Table 4.1. Summary of the relationship between monazite grain structure, trace element chemistry and age with structural level and metamorphic grade across the Kluane Schist. All ages presented are lower intercept ages (see Fig. 4.6) unless denoted * where a single $^{238}\text{U}/^{206}\text{Pb}$ age (^{207}Pb corrected) is presented. Individual domains are labelled with numbers and coloured for their relative Y content; dark greys refer to relative depletions in Y while lighter greys relative Y enrichments.

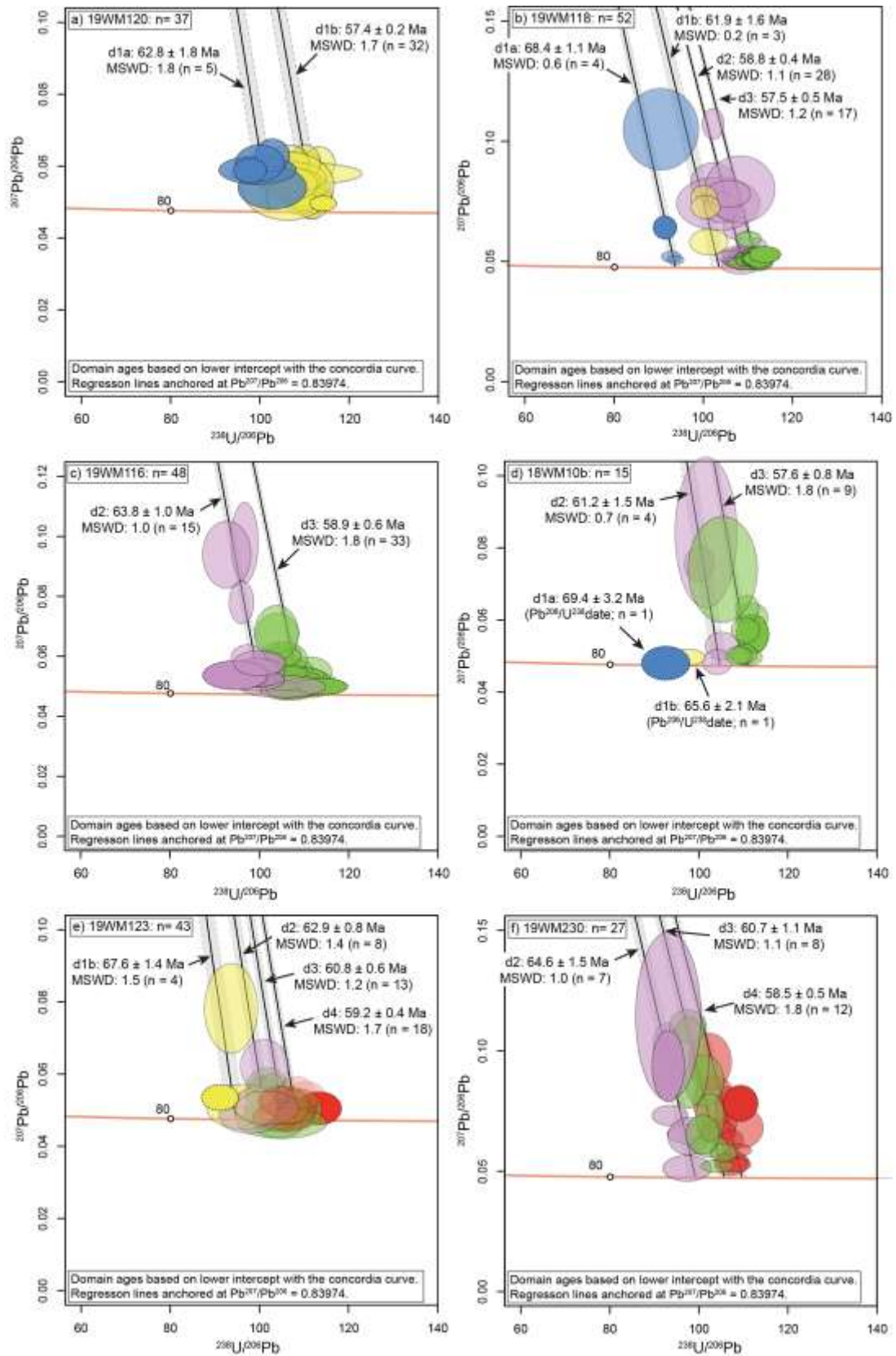


Figure 4.6. Terra-Wasserburg diagrams showing U-Pb isotope data from *in-situ* monazite analysis across the study area. Ellipses in all plots are provided at 2σ . Data are colour-coded for chemical domain (see main text). Regression lines are anchored on the initial $^{207}\text{Pb}/^{206}\text{Pb}$ ratio determined using the two-stage Pb evolution curve of Stacey & Kramers (1975) and the weighted mean age of all analyses (^{207}Pb corrected). The lower intercept age of each domain present within every sample is provided. The oldest and youngest single age ($^{235}\text{U}/^{206}\text{Pb}$) from each sample is highlighted by a solid ellipse. All ages were calculated, and diagrams created, using the IsoplotR software package (Vermeesch, 2018) for the open, free R platform.

19WM116: Forty-eight spot analyses across 18 grains produce dates between ca. 67 and ca. 56 Ma (Table F1). Domain 2 analyses yield a lower intercept age of 63.8 ± 1 Ma ($n = 15$; MSWD = 1; Fig. 4.6c). Domain 3 rims return a lower intercept age of 58.9 ± 0.6 Ma ($n = 33$; MSWD = 1.8; Fig. 4.6c). A negative Eu anomaly is noted in analyses from a few grains but shows limited relationship to domain age (Fig. B9).

18WM10b: Fifteen spot analyses across 8 grains range between ca. 69 and ca. 56 Ma (Table F1). Individual grains typically preserve domains 2 and 3 (Figs. 4.5g-h, 6d and Table 4.1). Domain 2 analyses yield a lower intercept age of 61.2 ± 1.5 Ma ($n = 4$; MSWD = 0.7), while domain 3 analyses yield a younger intercept age of 57.6 ± 0.8 Ma ($n = 9$; MSWD = 1.8; Fig. 4.6d). Domain 3 is enriched in Y and HREE compared to domain 2 (Fig. B9 and Table 4.1). Single spot analyses of domains 1a and 1b yield dates of 69.4 ± 3.2 Ma and 65.6 ± 2.1 Ma, respectively, with domain 1a showing both a depletion in Y and HREE compared with domain 1b (Figs. 4.6d, S9 and Table 4.1). Eu is depleted in domain 1a and enriched in domain 1b relative to domains 2 and 3 (Fig. B9).

19WM123: Forty-three spot analyses across 17 grains within sample 19WM123 produce dates between ca. 70 and ca. 56 Ma (Table F1). Domain 1b cores produce a lower intercept age of 67.6 ± 1.4 Ma ($n = 4$; MSWD = 1.5) and are Y-enriched compared with domain 2 analyses which produce a lower intercept age of 62.9 ± 0.8 Ma ($n = 8$; MSWD = 1.4). Domain 3 rims are Y and HREE enriched and produce a lower intercept age of 60.8 ± 0.6 Ma ($n = 13$; MSWD = 1.2; Fig. 4.6e, B9 and Table 4.1). The youngest dates come from domain 4 and produce a lower intercept age of 59.2 ± 0.4 Ma ($n = 18$; MSWD = 1.7). Domain 4 is strongly enriched in Th and shows a slight depletion in Y relative to domain 3 (Table 4.1). In general, a negative Eu anomaly is

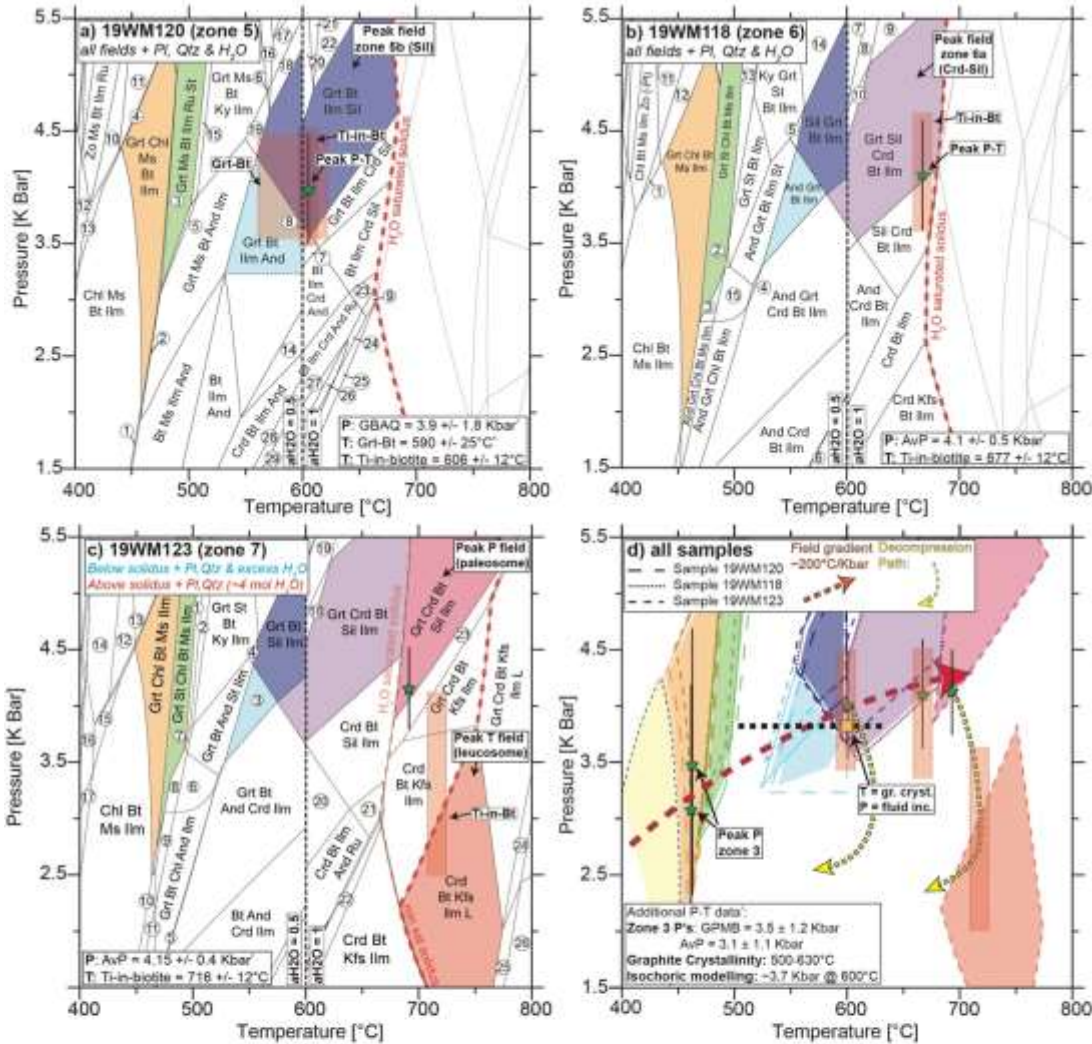
associated with domain 1b, which is less pronounced in domain 2 (Fig. B9). Between domains 2–4, Eu shows a progressive depletion to values akin to domain 1b (Fig. B9).

19WM230: Twenty-seven spot analyses across 19 grains produce spot dates between ca. 66 and ca. 56 Ma (Table F1). The oldest analyses come from Y-poor domain 2 which defines a lower intercept age of 64.6 ± 1.5 Ma ($n = 7$; MSWD = 1; Fig. 4.6f). Y-rich domain 3 rims produce a lower intercept age of 60.7 ± 1.1 Ma ($n = 8$; MSWD = 1.1). The youngest intercept age (58.5 ± 0.5 Ma; $n = 12$; MSWD = 1.8) is returned from domain 4. There is a slight relative depletion of HREE in domain 4 compared with domain 3 (Fig. B9). All domains exhibit a strong negative Eu anomaly (Fig. B9).

4.4.4. Petrological modelling

Calculated pseudosections are shown in detail in Figures 4.7a-c and summarized for all samples in Figure 4.7d.

Sample 19WM120 from zone 5 preserves a peak assemblage of garnet–biotite–sillimanite–andalusite–staurolite (+quartz–plagioclase–ilmenite) (Fig. 4.3a), with peak P - T conditions estimated at $\sim 606 \pm 12$ °C and 3.9 ± 1.8 kbar (Fig. 4.7a). Sample 19WM118 from zone 6 records a peak equilibrium assemblage comprising cordierite–biotite–garnet–sillimanite (+ quartz–plagioclase). The estimated peak conditions for 19WM118 are $\sim 675 \pm 12$ °C and 4.1 ± 0.5 kbar (Fig. 4.7b). The first occurrence of cordierite upgrade of andalusite/sillimanite is consistent with our observation of andalusite and sillimanite typically forming inclusions within cordierite porphyroblasts (e.g., Figs. 4.3c insert and S1b-e). Our estimated peak P - T conditions for 19WM123 are $\sim 715 \pm 12$ °C and 4.2 ± 0.4 kbar (Fig. 4.7c). This peak pressure estimate aligns with the assemblage we infer to have represented the peak pressure conditions experienced by the paleosome prior to leucosome development (e.g., cordierite–biotite–quartz–plagioclase–ilmenite +/- sillimanite–garnet; Figs. 4.3c and B1f), while the peak temperature estimate falls within a field where K-feldspar and cordierite are predicted to be stable in the presence of melt (Fig. 4.7c; c.f. Figs. 4.3c-d inserts).



Numbered Fields:

In (a):

- 1: Chi Bt Ms ilm And;
- 2: Grt Chi Bt Ms ilm And;
- 3: Grt Chi Ms Bt ilm St;
- 4: Grt Chi Zo Ms Bt ilm;
- 5: Grt St Ms Bt And ilm;
- 6: Grt Bt Ms ilm Sil Ru;
- 7: Grt Bt ilm Crd And;
- 8: Grt Bt ilm Sil;
- 9: Bt Crd Sil Kfs ilm Ru;
- 10: Zo Ms Bt ilm;
- 11: Grt Zo Ms Bt ilm;
- 12: Chi Zo Ms Bt ilm Ru;
- 13: Chi Ms Bt ilm Zo;
- 14: Grt Crd Bt ilm And;
- 15: Grt Ms Bt Ky ilm Ru St;
- 16: Grt Ms Bt Ky ilm Ru;
- 17: Grt Bt ilm Ky Ru;
- 18: Grt Bt ilm Sil Ru;
- 19: Grt Bt Ms ilm Sil;
- 20: Grt St ilm Sil;
- 21: Grt Bt ilm Sil Ru;
- 22: Grt Bt ilm Sil Ru;
- 23: Bt ilm Ru Crd Sil;
- 24: Bt Crd And Kfs ilm Ru;
- 25: Bt Crd Kfs Ru ilm;
- 26: Bt Crd And Kfs Ru;
- 27: Bt Crd And Ru;
- 28: Crd Bt ilm Kfs;
- 29: Crd Bt ilm And Kfs;

In (b):

- 1: Chi Bt Ms ilm Zo;
- 2: Grt St Chi St ilm;
- 3: And Grt St Chi Ms Bt ilm;
- 4: Crd And Grt Bt ilm St;
- 5: Sil Grt Bt ilm St;
- 6: Crd Bt ilm Kfs;
- 7: Grt St Bt ilm;
- 8: Grt Sil St Bt ilm;
- 9: Grt Sil Bt ilm;
- 10: Grt Sil St Bt ilm Crd;
- 11: Grt Chi Bt Ms ilm Zo (-PI);
- 12: Grt Chi Bt Ms ilm Zo;
- 13: Grt St Bt Ms ilm;
- 14: Ky Grt Bt ilm;
- 15: And Grt St Chi Bt ilm;

In (c):

- 1: Grt Chi Bt And Ms ilm Cld;
- 2: Chi Bt Ms ilm Cld;
- 3: Chi Bt And Ms ilm Cld;
- 4: Grt Chi Bt Cld Ms ilm;
- 5: Grt Bt St Ms ilm And;
- 6: Grt Sil Bt St ilm;
- 7: Grt Crd Bt St ilm And;
- 8: Grt Crd Chi Bt ilm And;
- 9: Grt Crd Sil Bt ilm +L;
- 10: Grt Crd Sil Kfs Bt ilm +L;
- 11: Grt Crd Kfs Bt ilm;
- 12: Grt Crd Bt Opx Kfs ilm +L;
- 13: Crd Sil Bt Kfs ilm Ru;
- 14: Crd Bt Kfs ilm Ru And;
- 15: Grt Bt St Ms ilm Ru;
- 16: Grt Bt St Ms ilm Ky;
- 17: Grt Bt St Chi ilm Ky;
- 18: Grt Chi Bt Ms ilm Zo (-PI);
- 19: Grt Chi Bt Ms ilm Zo;
- 20: Grt Bt St Ms Chi ilm Ky;
- 21: Grt Crd Bt Sil Kfs ilm;
- 22: Crd Bt Kfs ilm Sil;
- 23: Crd Sil Bt ilm Ru;
- 24: Chi Ms ilm Zo Ru;
- 25: Chi Ms ilm Zo;
- 26: Grt Chi Bt St Ms ilm And;
- 27: Chi Bt Ms And ilm;
- 28: Grt Chi Bt St Ms And ilm;
- 29: Grt Chi Bt St ilm And;
- 30: Grt Bt ilm And;
- 31: Grt Sil Bt St ilm;
- 32: Crd Bt Kfs ilm Ru;
- 33: Crd Bt Kfs ilm Ru;
- 34: Crd Bt Kfs Ru And;
- 35: Crd Bt Ru And;
- 36: Crd Bt Opx Kfs ilm +L;
- 37: Crd Opx Kfs ilm +L;

Figure 4.7. Pseudosections for samples 19WM120, 19WM118 and 19WM123, respectively. Coloured fields refer to assemblages characteristic of petrographic zones across the Kluane Schist; orange (zone 3), green (zone 4), light blue (zone 5a), dark blue (zone 5b), purple (zone 6), pink and red (zone 7, paleosome and leucosome, respectively; see Fig. 4.2). All samples are modelled with a varied aH_2O as described in the text. Samples experiencing peak conditions below the solidus (19WM120, 19WM118) are modelled assuming H_2O -saturation, and as such phase fields above the H_2O -saturated solidus are left blank. Samples modelled above the solidus (19WM123) assume only the amount of H_2O required to minimally saturate the assemblage in the immediate sub-solidus at 4 kbar. Ti-in-biotite thermometer results are plotted directly on their associated pseudosection and align with the temperatures predicted for each assemblage by our model. Additional P-T estimates (denoted * and presented in Chapter 3) were obtained using the crystallinity of graphite inclusions to garnet, isochor modelling of fluid inclusions in garnet, conventional thermobarometry and the Thermocalc average pressure (AvP) software (see main text & Chapter 3).

The peak P - T estimates recorded across the Kluane Schist outline a single apparent metamorphic field gradient of ~ 200 °C/kbar (Fig. 4.7d). This suggests that the Kluane Schist most likely represents a single lithological package that experienced progressive Buchan-style metamorphism (Fig. 4.7d). Further, there is a general younging pattern of ages returned from each chemical domain preserved within monazite and decreased structural height across the Kluane Schist (i.e., with decreased peak- T ; c.f., Fig. 4.4, 4.7 and Table 4.1). This is consistent with the development of the Kluane Schist's inverted metamorphic field gradient during a single, protracted phase of downward-penetrating metamorphism and deformation (c.f., Figs., 4.4, 4.5 and Table 4.1; Mottram *et al.*, 2014).

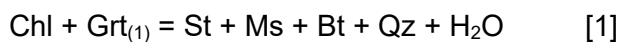
4.5. Discussion

4.5.1. Linking monazite age and petrologic zone

The monazite analyzed within this study is interpreted to have grown as the product of a single protracted metamorphic event during the prograde evolution of the Kluane Schist, with the ages returned having not been reset by later thermal or fluid activity. This inference is guided by three main observations: (1) the textual and petrological evidence

that peak metamorphism of the Kluane Schist did not exceed the closure temperature for monazite (~800°C e.g., Cherniak *et al.*, 2004; c.f., Fig. 4.7 and Table G2), (2) the presence of allanite/apatite and lack of monazite within the prograde fabrics of the lower grade, greenschist facies units of the Kluane Schist (e.g., Fig. B1a; c.f., Shrestha *et al.*, 2019), and (3) the discordant dates returned fall along single arrays that point back to an ancient Pb source that could not have a possible Cordilleran significance (>4 Ga; e.g., Fig. 4.6; Nelson *et al.*, 2013). In the context of (2) and (3), the spread of monazite ages away from concordia is more consistent with the incorporation of common Pb than the recrystallization of pre-existing, detrital monazite. Equally, our observation that allanite and apatite are entrained within the prograde fabrics of the Kluane Schist prior to the first appearance of monazite (e.g., Fig. B1a vs. Fig. 4.2) is in line with the common mineral association attributed to the growth of prograde monazite from precursor allanite and/or apatite during first-cycle, prograde metamorphism (e.g., Pyle *et al.*, 2001; Gibson *et al.*, 2004; Spear, 2010; Spear and Pyle, 2010; Shrestha *et al.*, 2019).

The initial growth of monazite within the Kluane Schist (domains 1a and 1b) is marked by the development of coarse skeletal grains that preserve patchy chemical zonation (e.g., Fig. 4.5a-d). These grains exclusively occur towards the structural base of our sample suite (e.g., samples 19WM120 and 19WM118; Figs. 4.4 and 4.5) < 3 km above the staurolite isograd (e.g., Figs. 4.2 and 4.4). We interpret the growth of domain 1 monazite as a response to the breakdown of garnet via reaction [1] (Fig. 4.8a; e.g., Foster and Parrish, 2003; Pyle and Spear, 2003; Gibson *et al.*, 2004). Similar chlorite dehydration reactions have been shown to promote rapid monazite nucleation where the continued breakdown of garnet and/or allanite is suggested to release their sequestered REE's, enriching the rock matrix Y during monazite growth (Figs. 4.4b and 4.8a; e.g., Kohn and Malloy, 2004; Fitzsimons *et al.*, 2005; Spear and Pyle, 2010). Our interpretation is supported by the observation of relic garnet in the presence of staurolite (e.g., Fig. 4.3a) and the relative Y enrichment seen within domain 1b compared with domain 1a (Figs. 4.4b, 4.5 and 4.8c).



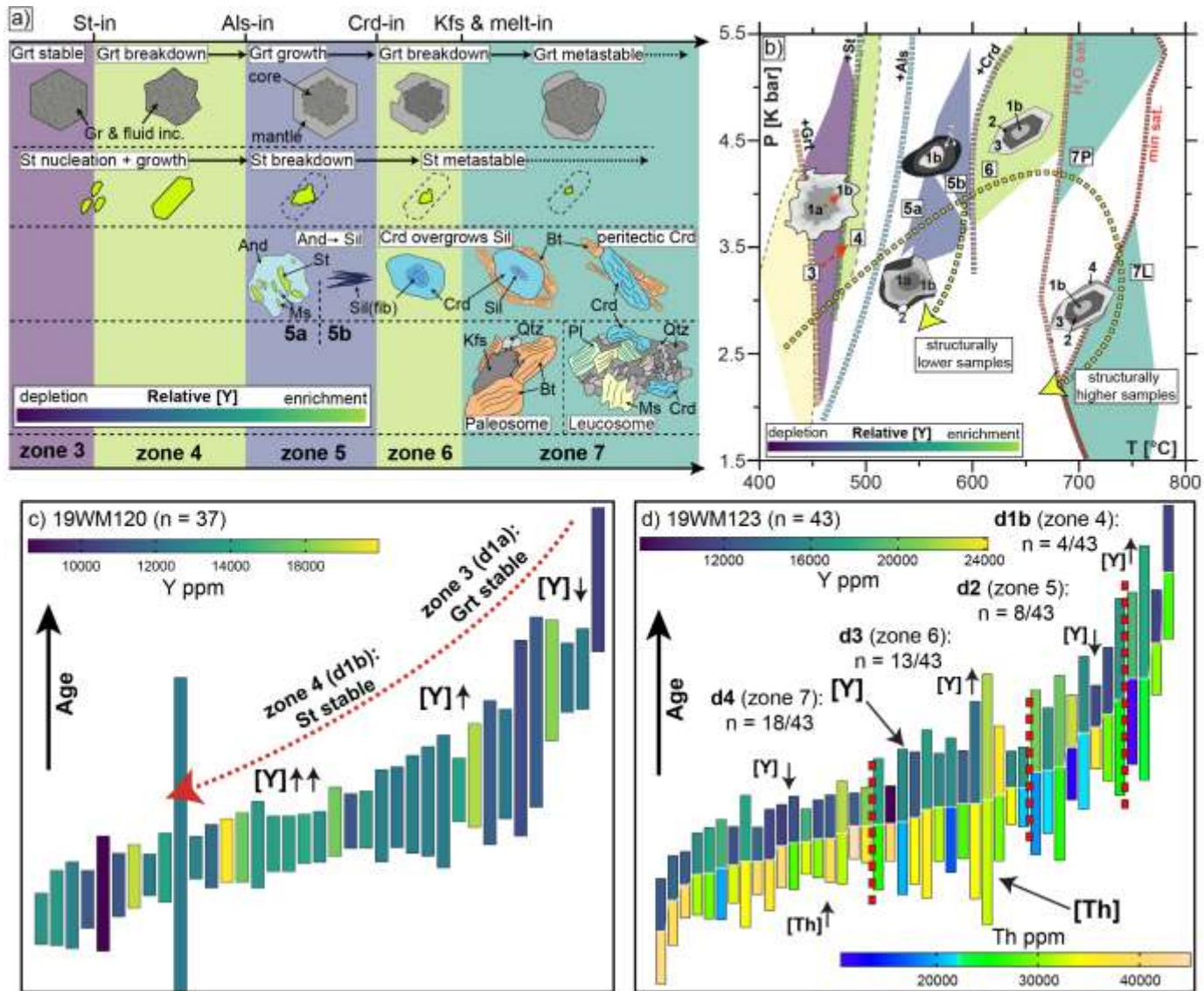
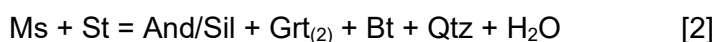


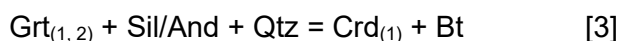
Figure 4.8. Summary of the relationships used for petrochronology within this study. Each phase relationship is associated with a relative enrichment or depletion in Yttrium [Y], based primarily on the stability of garnet (e.g., Foster *et al.*, 2002; Gibson *et al.*, 2004); this is reflected by the background colour assigned to each zone. These phase relationships and their effect on monazite growth are discussed in detail in the main text. b) Summary of the *P-T* conditions experienced by all samples across the Kluane Schist. Polygons refer to the stability field of assemblages characteristic of zones 3–7 (see Figs. 4.2 and 4.7) and are coloured for their inferred relative [Y] content that would be available for reacting minerals such as monazite (see (a) and Fig. 4.7d). Inset monazite grain sketches highlight the progressive development of observed individual monazite domains along our inferred *P-T* path. c-d) Age distribution plots for (c) 19WM120 (zone 5; structurally low) and (d) 19WM123 (zone 7; structurally high) documenting our inferred domain distinction in terms of absolute [Y] and [Th] with age. In (d) red dashed lines divide analyses from distinct monazite domains 1b, 2, 3, and 4 that are present in sample 19WM123 (see main text and Table 4.1). Diagrams in (d) were generated using the ChrontouR package for the open R platform (Larson, 2020).

Domain 2 monazite occurs in samples above the aluminosilicate isograd that lack staurolite porphyroblasts (e.g., 19WM118, 18WM10b, 19WM123, 19WM230; Figs. 4.2, 4.3, 4.4b and 4.5b–i and Table 4.1). These observations indicate that the production of domain 2 monazite was likely the result of staurolite breakdown coupled with the growth of aluminosilicate (reaction [2]; e.g., Foster and Parrish, 2003; Gibson *et al.*, 2004; Pattison and Tinkham, 2009; Shrestha *et al.*, 2019). Coincident with the breakdown of staurolite across the Kluane Schist a second generation of inclusion-free garnet is observed to mantle earlier, inclusion-rich garnet cores (Fig. 4.8a; c.f., Fig. 4.3b insert; Chapter 3). These observations are consistent with the production of domain 2 monazite in response to [2], where garnet growth likely sequestered Y, Gd, and Sm (Figs. 4.4b and 8a; e.g., Foster and Parrish, 2003; Gibson *et al.*, 2004; Spear and Pyle, 2010; Dumond *et al.*, 2014) and promoted the development of the MREE and Y depleted monazite typical of domain 2 (Figs. 4.4b, 4.5 and Table 4.1).



The kinetic limitations inherent with reaction [2] (e.g., Pattison and Tinkham, 2009; Chapter 3) further explain the lack of domain 2 monazite within the andalusite–sillimanite bearing sample 19WM120 (e.g., Figs. 4.3a and 4.5a-b). In this lower-grade zone 5 sample, the presence of abundant staurolite porphyroblasts and lack of evidence for a second period of garnet growth is consistent with initial Al-silicate growth across the Kluane Schist by $Ms + Chl + Qtz = And + Bt + H_2O$ (c.f., Fig. 4.3a–b and inserts; Pattison and Tinkham, 2009; Spear and Pattinson, 2017; see also Chapter 3). It is therefore likely that the metastable persistence of staurolite within these lower-grade Al-silicate assemblages (e.g., 19WM120; Fig. 4.3a) restricted the growth of a second garnet generation and the corresponding low-Y domain 2 in monazite. These observations further support the production of domain 2 monazite via [2] (Fig. 4.8a).

Above the cordierite-in isograd, monazite develops domain 3 rims (Figs. 4.4b, 4.5 and 4.8a, b). We interpret the relative enrichment in the HREE's in domain 3 monazite as an indication that monazite grew during a period of garnet breakdown (Figs. 4.4b and 4.8a; e.g., Foster and Parrish, 2003; Gibson *et al.*, 2004; Dumond *et al.*, 2014). Across the Kluane Schist garnet associated with cordierite bearing assemblages is typically anhedral and corroded with garnet cores showing replacement by chlorite–muscovite–biotite–cordierite–plagioclase atolls (e.g., Fig. 4.3b and S1b-c). Garnet chemical zonation profiles, which show a sharp increase in spessartine content coupled with a decrease in $Mg/(Mg + Fe)$ towards their rims, is consistent with period of garnet resorption (Pattison and Tinkham, 2009; see also Chapter 3). Combined with the petrological observation of cordierite replacing garnet and overgrowing fibrolitic sillimanite within zone 6 (e.g., Figs. 4.3b and B1c-e), and the occurrence of relic andalusite porphyroblasts and fibrolitic sillimanite included within cordierite within zones 6 and 7 (e.g., Figs. 4.3c, 4.8a and B1f), we infer the breakdown of garnet within zone 6 via [3], which in turn promotes the growth of the Y-enriched domain 3 monazite typical of cordierite-grade assemblages across the Kluane Schist (Figs. 4.4b and 4.8a).



The growth of domain 4 monazite exclusively occurs within the migmatitic units typical of zone 7 (Figs. 4.4b and 4.5). Domain 4 monazite is characterized by a strong relative enrichment in Th, not observed within any of the previous domains, along with a depletion in Y, Gd, and an enrichment in Sm compared with domain 3 (Figs. 4.4b, 4.5 i-l, 8d, B9 and Table 4.1). A slight depletion in Eu is also observed within domain 4 of sample 19WM123 (Fig. B9). These observations are consistent with previous models that link Th-rich, Eu-depleted monazite to the generation of melt and crystallization of K-feldspar in migmatites (c.f., [4] and Fig. 4.8a; e.g., Lederer *et al.*, 2013; Xing *et al.*, 2013; Mottram *et al.*, 2014; Dumond *et al.*, 2014; Dyck *et al.*, 2020).



Recent re-evaluation of these models, however, has suggested monazite breakdown, rather than growth likely occurs during prograde metamorphism at supra-solidus conditions (Yakymchuk and Brown, 2014; Shrestha *et al.*, 2019; Larson *et al.*, 2022). A period of breakdown is consistent with the finer, less euhedral nature of monazite crystals that typify the highest-grade migmatitic units of the Kluane Schist (e.g., 19WM230 in Figs. 4.4a, 4.5 and B7). However, monazite characteristic of these higher-grade units typically preserve the chemical domains developed during lower-grade metamorphism (e.g., Figs. 4.5i-l; Table 4.1). The preservation of these lower-grade monazite domains is likely the result of the dehydration associated with melt generation (e.g., [4]), which is considered to extend the stability field of monazite to higher *P-T* conditions (Larson *et al.*, 2022). Such a mechanism is consistent with the observations of this study where we observe a higher degree of monazite dissolution within schollen (e.g., 19M230; Figs. 4.3d, 4.4 and 4.5k) rather than in stromatic (e.g., 19WM123; Fig. 4.3c, 4.4 and 4.5i) style migmatites (c.f., Yakymchuk and Brown, 2014). Consequently, we consider domain 4 monazite to track the supra-solidus decompression associated with migmatite development across the Kluane Schist (Figs. 4.7 and 4.8 a, b). This is consistent with the strong Th-enrichment associated with domain 4 monazite (e.g., Fig. 4.4b and 4.8d) and the limited amount of monazite growth suggested by their thin,

veener-like form (e.g., Fig. 4.5i–l and Table 4.1; e.g., Yakymchuk and Brown, 2014; Williams *et al.*, 2018; Shrestha *et al.*, 2019).

4.5.2. The influence of the Ruby Range batholith

Previous monazite geochronology in the region by ID-TIMS analyses of monazite separates produced a smaller range of dates across the Kluane Schist than we document here (ca. 58–56 Ma; Mortensen and Erdmer, 1992). Coincidence between these previous monazite dates and the age of the Ruby Range batholith (ca. 64–57 Ma; Erdmer and Mortensen, 1993; Israel *et al.*, 2011a) underpinned the interpretation that intrusion of the batholith caused widespread (re)crystallisation of monazite across the Kluane Schist within an extensive ~5–6 km wide static contact aureole (Erdmer and Mortensen, 1993; Mezger, 1997; Mezger *et al.*, 2001).

Although accurately predicting the width of contact aureoles using analytical modelling alone is challenging (e.g., Annen *et al.*, 2017), key factors in developing the aureole widths required for wholesale monazite (re)crystallisation across the Kluane Schist (~6 km in structural height assuming an average dip of 35°; Fig. 4.4; Mezger, 1997; Mezger *et al.*, 2001) are the rate and geometry of intrusion emplacement (Annen, 2011). Recent modelling has shown that km-scale contact aureoles can develop within thickened crustal sequences due to the rapid emplacement (> 3 mm/yr) of under-accreting sill-like intrusive bodies (Annen, 2017) akin to the Ruby Range batholith (e.g., Erdmer and Mortensen, 1993; Israel *et al.*, 2011a). However, with such rapid emplacement rates, peak aureole temperatures are also likely to be reached quickly (on the order of 1×10^5 years; Annen, 2017). This contrasts by 2 orders of magnitude with the substantially longer ca. 15 Myr age range produced by our monazite analyses (ca. 70–55 Ma; Figs. 4.5 and 4.6; Table F1). Additionally, the similarity in the age of the youngest monazite population returned by all our samples, regardless of structural depth and distance from the Ruby Range batholith (< 2 Ma across ~6 km structural height; Figs. 4.4, 4.6 and Table 4.1 and F1), is inconsistent with time integrated cooling away from the Ruby Range batholith (c.f., Lihter *et al.*, 2020). Moreover, the direct observation and analysis of monazite recovered from contact metamorphic rocks shows that they are often typified by composite grains with inclusion-rich rims (e.g., Wing *et al.*, 2003) or

coarse grains that lack chemical zonation (Pandey *et al.*, 2013). Neither of these reflect the grain structure and concentric zonation patterns preserved within monazite from the Kluane Schist (e.g., Fig. 4.5).

Importantly, our results are derived from *in situ* analysis of monazite that link microstructural and petrological observations to the texture and chemistry preserved by individual crystals (e.g., Fig. 4.8). Our U-Th-Pb data are consistent with the metamorphism of the Kluane Schist between ca. 70 and ca. 55 Ma, which pre-dates the *main phase* of Ruby Range intrusion at ca. 64–57 Ma (Erdmer and Mortensen, 1993; Israel *et al.*, 2011a). We acknowledge that there is evidence for a *pre-main phase* to the Ruby Range batholith, dated using zircon separates from a single, cm-scale dyke to be between ca. 71–68 Ma (see Chapter 2; Israel *et al.*, 2011a), however, note that these dykes also include inherited Triassic zircon (Stanley, 2012) and contain monazite dated to ca. 57 Ma (Israel *et al.*, 2011a). Furthermore, zircon interpreted as magmatic, recovered from the early, foliated phase of the Ruby Range batholith (see chapter 2, Fig. 2.3d) produce an age of ca. 64 Ma (Crowley & Murphy, unpublished, as cited in Israel *et al.*, 2011a).

Taken together these considerations provide evidence that monazite growth across the Kluane Schist occurred as the product of widescale regional metamorphism (Fig. 4.8) largely independent of the intrusion of the Ruby Range batholith. This interpretation is consistent with the original structural juxtaposition of the Kluane Schist and overlying Yukon Tanana terrane having largely pre-dated the intrusion of Ruby Range batholith (e.g., Israel *et al.*, 2011a, b). This said, we do still consider the Ruby Range batholith as a potential source of heat during the later stages of Kluane Schist metamorphism (e.g., zone 7 migmatites), as is suggested by evidence for its emplacement during late-stage deformation (e.g., Fig. 2.3d; Israel *et al.*, 2011a, b). However, we highlight that the intrusion of the Ruby Range batholith alone was unlikely to act as the principal driver and heat source for developing the inverted metamorphic sequence preserved across the Kluane Schist (c.f., Figs. 4.2 and 4.4; Mezger, 1997; Mezger *et al.*, 2001).

4.5.3. *P-T-t* evolution of the Kluane Schist

Prior to the development of an inverted metamorphic sequence, the Kluane Schist experienced a distinct greenschist-facies metamorphic event, expressed as a bedding-parallel muscovite–chlorite fabric (c.f. Fig. B1a; Chapter 3). This metamorphic event is thought to track the initial collapse of the Kluane Basin between the encroaching Insular terranes and the previously accreted Intermontane terranes (Chapter 3). The timing of this event is poorly constrained; however, it must pre-date the growth of monazite during the amphibolite-facies metamorphism of the Kluane Schist (i.e., > 70 Ma; Figs. 4.7d, 4.8 and Table 4.1).

Together our results are in line with the Kluane Schist having experienced a clockwise *P-T-t* path involving a shallow prograde evolution followed by a largely isothermal decompression (Figs. 4.7d and 4.8b) and defined by: (1) an initial burial event that occurred as the basin collapsed against the continent prior to ca. 70 Ma, (2) a more protracted episode of downward penetrating metamorphism and deformation that led to the development of an inverted Buchan metamorphic sequence up until ca. 56 Ma, (3) a rapid and largely isothermal decompression concurrent with migmatite development between ca. 61 and ca. 56 Ma, (4) final exhumation and cooling from ca. 55–40 Ma (Figs. 4.7, 4.8b and Table 4.1; Mortensen and Erdmer, 1992; Mezger, 1997).

As outlined above, we do not consider the Ruby Range Batholith as the principal heat source during the Buchan-style metamorphism experienced by the Kluane Schist (c.f., our M2 above and in Chapter 3, and M2 of Mezger, 1997; Mezger *et al.*, 2001). Instead, our *P-T-t* results are consistent with the diachronous attainment of peak metamorphic conditions with structural height within the Kluane Schist over a period of ~15 Myr (Figs. 4.4, 4.7 and 4.8). This result is more in line with the Buchan-style metamorphism experienced by the Kluane Schist having been driven by its underthrusting below the warm Yukon-Tanana terrane from ca. 70–55 Ma, which hosted the roots of an active magmatic arc at this time (e.g., Coast Mountains Batholith; Gehrels *et al.*, 2009) and had experienced recent voluminous magmatism (e.g., the Tanacross–Dawson Range belt and Tok–Tetlin belt of Hart *et al.*, 2004). This provides a potential mechanism to develop the heightened geothermal gradient preserved within the Kluane Schist during its Late Cretaceous coupled metamorphic-deformational evolution (e.g., Figs. 4.2, 4.6 and 4.7; Chapter 3),

while additionally accounting for its regional tops-to-the-SW shear structures (e.g., Israel *et al.*, 2011a; Chapter 3).

It should also be noted, however, that there is a general coincidence between the age of Ruby Range Batholith (ca. 64–57 Ma; Israel *et al.*, 2011a) and the latest stages of Kluane Schist metamorphism (i.e., migmatite development, domain 4, ca. 61–55 Ma; Table F1). This suggests that although the Ruby Range batholith is not the primary heat source during Kluane Schist metamorphism, its emplacement likely facilitated the latest stages of Kluane Schist metamorphism and potentially aided in the development of its structurally highest migmatitic units (c.f., Figs. 4.2 and 4.4; Mezger *et al.*, 2001).

4.5.4. Implications for Insular terrane accretion

Along the Cordillera of North America, several Jura-Cretaceous basins show a similar high-temperature, low-pressure metamorphic event to that preserved by the Kluane Schist (Fig. 4.9). Within southwest Yukon, the Blanchard River assemblage contains high-pressure (~6.5 kbar) mineral assemblages that are overprinted by lower-pressure ones (~3 kbar) (Vice *et al.*, 2020). These lower-pressure assemblages are considered to develop in response to regional exhumation followed by high-temperature, low-pressure metamorphism from ca. 70–61 Ma (Vice *et al.*, 2020). In south-central Alaska, the Jura-Cretaceous metasedimentary rocks of the Maclaren Schist experienced a protracted metamorphic history between ca. 84–55 Ma (Waldien *et al.*, 2021b). Local kyanite-grade assemblages are overprinted by andalusite and cordierite during isothermal decompression along the Valdez Creek Shear zone from ca. 76–74 Ma, providing a ca. 75–55 Ma age range for its high-temperature, low-pressure metamorphic overprint (Fig. 4.9; e.g., Davidson and McPhillips, 2007; Waldien *et al.*, 2021b). Approximately 100 km southwest of the Maclaren Schist, rocks from the Devil Creek area show metamorphic fabrics and assemblages similar to those preserved by the Kluane Schist (Fig. 4.9; Davidson and McPhillips, 2007) with a ca. 68–63 Ma age for their metamorphism derived from syn-tectonic plutons (Davidson and McPhillips, 2007).

Recent restoration along the Denali fault indicates that the Kluane Schist, Blanchard River assemblage, Maclaren Schist, and rocks of Devil Creek area likely occupied a

similar position within the northern Cordillera prior to ca. 50 Ma (Fig. 4.9; e.g., Waldien *et al.*, 2021b). The general alignment in the age, duration, and conditions of metamorphism between these basins supports this restoration and additionally provides evidence for an extensive high-temperature, low-pressure metamorphic event within the southwest Yukon between ca. 75–55 Ma (Fig. 4.9; ca. 70–55 Ma, Kluane Schist; ca. 70–61 Ma, Blanchard River assemblage, ca. 75–55 Ma Maclaren Schist; ca. 68–63 Ma, Devil Creek). Similarity is also observed in the development of continentally dipping inverted metamorphic sequences in both the Kluane Schist and the Maclaren Schist (e.g., Smith, 1981; Davidson and McPhillips, 2007; this study) and consistent southwest- to south-oriented shear structures within the Kluane Schist (e.g., Israel *et al.*, 2011a), Devils Creek rocks (Davidson and McPhillips, 2007), Blanchard River assemblage (Vice *et al.*, 2020) and Maclaren Schist (Smith, 1981; Davidson and McPhillips, 2007; Waldien *et al.*, 2021a). These structures are all consistent with basin inversion during a period of southwesterly-directed tectonic underthrusting beneath the North American margin.

Reconstruction of the Mesozoic-Cenozoic trajectory of the North American craton highlights its dominant westward motion during this period in the Late Cretaceous (e.g., Monger and Gibson, 2019). As such, we infer this metamorphic event was likely driven by compression related to the wholesale overthrusting of these Jura-Cretaceous basins by flanking components of the North American continent (e.g., Yukon-Tanana terrane). This is inconsistent with models of Insular terrane accretion that envisage the collapse of an extensive Jura-Cretaceous ocean by west-dipping subduction (e.g., Sigloch and Mihalynuk, 2013, 2017; see also Pavlis *et al.*, 2019). Rather, our results are better reconciled by a model of Insular terrane accretion that involves the westward migration of the North American continent above an outboard east-dipping subduction zone (e.g., Monger & Gibson, 2019). Subsequent crustal thickening and overthrusting of terrane-intervening strata is driven primarily by override of the North American margin and facilitated by the emplacement of syn-tectonic plutons (e.g., Ruby Range batholith). Together these processes drove the inversion and metamorphism of the terrane-intervening Jura-Cretaceous basins accompanied by the development of their inverted metamorphic sequences and west- to southwest-directed compressional structures.

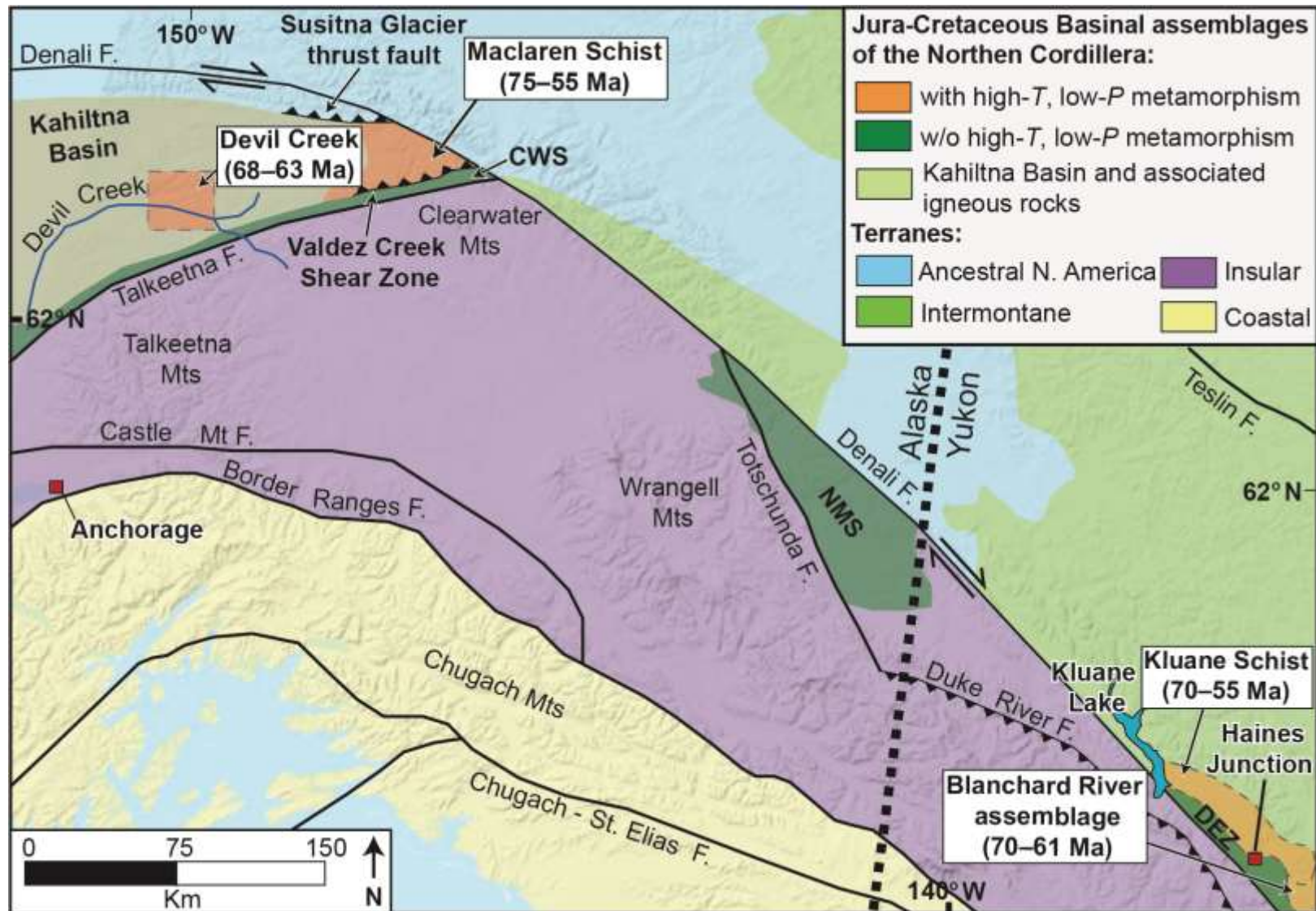


Figure 4.9. Terrane map showing the Northern Cordillera of southwest Yukon and south-central Alaska. Jura-Cretaceous basins are overlain and coloured based on their preserved metamorphic histories (Davidson & McPhillips, 2007; Hults *et al.*, 2013; Vice *et al.*, 2020; Waldien *et al.*, 2021a, b; Lowey, 2021; this study). Dextral offset along the Denali fault is considered to have led to the separation of the Kluane Schist-Blanchard River-Dezadeash (DEZ) within southwest Yukon from basins within south-central Alaska, including the Clearwater metasediments (CWS) and Maclaren Schist (Waldien *et al.*, 2021b). The location of the Devil Creek rocks within the Kahiltna Basin of south-central Alaska is also shown (Davidson & McPhillips, 2007). Within this region of the Cordillera, all basins reported to have experienced an episode of high-temperature, low-pressure metamorphism, along with the documented age of this event, are highlighted. See main text for discussion. NMS = Nutzotin Mountains Sequence.

4.6. Conclusions

The Kluane Schist preserves a high-temperature, low-pressure Buchan-style inverted metamorphic sequence which grades from greenschist-facies at its structural base to the amphibolite-granulite facies transition at its structural top. Within this sequence monazite grows continuously and as the product of distinct prograde reactions between the staurolite-grade (~450°C and 3.0–3.5 kbar) and the uppermost-amphibolite facies (~700–715°C and 4.0–4.5 kbar). The results of monazite petrochronology are consistent with diachronous metamorphism across the Kluane Schist whereby structurally higher samples to the northeast experience metamorphism prior to structurally lower samples to the southwest. Our findings reveal that the inverted Buchan-style metamorphic sequence preserved across the Kluane Schist most likely developed in response to a single phase of downward penetrating metamorphism and deformation during the southwest-directed override of the Yukon-Tanana terrane between ca. 70 and ca. 55 Ma.

Alignment in the conditions, timing, and duration of similar high-temperature, low-pressure metamorphic events within the Blanchard River assemblage, Maclaren Schist, and rocks of Devil Creek area provides strong evidence for a regional-scale metamorphic event within this region of the northern Cordillera between ca. 75 and 55 Ma. The similarity in the style of ductile deformation that these basins preserve is in accordance with their inversion during the southwesterly override of flanking

components of the North American continent (e.g., Yukon-Tanana terrane). This result provides strong evidence that the terminal accretion of the Insular terranes was primarily driven by the override of the North American continent rather than by slab pull related to west-dipping subduction that closed an extensive Jura-Cretaceous ocean basin.

4.7. References

- Aleinikoff, J.N., Schenck, W.S., Plank, M.O., Srogi, L., Fanning, C.M., Kamo, S.L. and Bosbyshell, H., 2006, Deciphering igneous and metamorphic events in high-grade rocks of the Wilmington Complex, Delaware: Morphology, cathodoluminescence and backscattered electron zoning, and SHRIMP U-Pb geochronology of zircon and monazite. *Geological Society of America Bulletin*, v.118, n.1-2, p. 39-64. <https://doi.org/10.1130/B25659.1>
- Annen, C., 2011, Implications of incremental emplacement of magma bodies for magma differentiation, thermal aureole dimensions and plutonism–volcanism relationships. *Tectonophysics*, v.500, n.1-4, p.3-10. <https://doi.org/10.1016/j.tecto.2009.04.010>
- Annen, C., 2017. Factors affecting the thickness of thermal aureoles. *Frontiers in Earth Science*, v.5, p.82. <https://doi.org/10.3389/feart.2017.00082>
- Box, S.E., Karl, S.M., Jones III, J.V., Bradley, D.C., Haeussler, P.J. and O’Sullivan, P.B., 2019. Detrital zircon geochronology along a structural transect across the Kahiltna assemblage in the western Alaska Range: Implications for emplacement of the Alexander-Wrangellia-Peninsular terrane against North America. *Geosphere*, v.15, n.6, p.1774-1808. <https://doi.org/10.1130/GES02060.1>
- Canil, D., Johnston, S.T., D’Souza, R.J. and Heaman, L.M., 2015. Protolith of ultramafic rocks in the Kluane Schist, Yukon, and implications for arc collisions in the northern Cordillera. *Canadian Journal of Earth Sciences*, v.52, n.7, p.431-443. <https://doi.org/10.1139/cjes-2014-0138>

- Cherniak, D.J., Watson, E.B., Grove, M. and Harrison, T.M., 2004. Pb diffusion in monazite: a combined RBS/SIMS study. *Geochimica et Cosmochimica Acta*, v.68, n.4, p.829-840. <https://doi.org/10.1016/j.gca.2003.07.012>
- Coggon, R. and Holland, T.J.B., 2002. Mixing properties of phengitic micas and revised garnet-phengite thermobarometers. *Journal of Metamorphic Geology*, v.20, n.7, p.683-696. <https://doi.org/10.1046/j.1525-1314.2002.00395.x>
- Cottle, J., Lederer, G. and Larson, K., 2019. The monazite record of pluton assembly: Mapping manaslu using petrochronology. *Chemical Geology*, v.530, p.119309. <https://doi.org/10.1016/j.chemgeo.2019.119309>
- Davidson, C., & McPhillips, D. 2007. Along strike variations in metamorphism and deformation of the strata of the Kahiltna basin, south-central Alaska. In K. D. Ridgway, J. M. Trop, J. M. G. Glen, & J. M. O'Neill (Eds.), *Special Paper 431: Tectonic growth of a collisional continental margin: Crustal evolution of Southern Alaska* (Vol. 431, pp. 439– 453). Geological Society of America. [https://doi.org/10.1130/2007.2431\(17\)](https://doi.org/10.1130/2007.2431(17))
- de Capitani, C. and Brown, T.H., 1987. The computation of chemical equilibrium in complex systems containing non-ideal solutions. *Geochimica et Cosmochimica Acta*, v.51, n.10, p.2639-2652. [https://doi.org/10.1016/0016-7037\(87\)90145-1](https://doi.org/10.1016/0016-7037(87)90145-1)
- de Capitani, C. and Petrakakis, K., 2010. The computation of equilibrium assemblage diagrams with Theriak/Domino software. *American Mineralogist*, v.95, n.7, p.1006-1016. <https://doi.org/10.2138/am.2010.3354>
- Dumond, G., Goncalves, P., Williams, M.L. and Jercinovic, M.J., 2015. Monazite as a monitor of melting, garnet growth and feldspar recrystallization in continental lower crust. *Journal of Metamorphic Geology*, v.33, n.7, p.735-762. <https://doi.org/10.1111/jmg.12150>
- Dyck, B., Waters, D.J., St-Onge, M.R. and Searle, M.P., 2020. Muscovite dehydration melting: Reaction mechanisms, microstructures, and implications for anatexis. *Journal of Metamorphic Geology*, v.38, n.1, p.29-52. <https://doi.org/10.1111/jmg.12511>

- Erdmer, P., 1991. Metamorphic terrane east of Denali fault between Kluane Lake and Kusawa Lake, Yukon Territory. Geological Survey of Canada Current Research, Part A, Paper 91-1A, 37–42. <https://doi.org/10.4095/132494>
- Erdmer, P. and Mortensen, J.K., 1993. A 1200-km-long Eocene metamorphic-plutonic belt in the northwestern Cordillera: Evidence from southwest Yukon. *Geology*, v.21, n.11, p.1039-1042. [https://doi.org/10.1130/0091-7613\(1993\)021<1039:AKLEMP>2.3.CO;2](https://doi.org/10.1130/0091-7613(1993)021<1039:AKLEMP>2.3.CO;2)
- Fitzsimons, I.C.W., Kinny, P.D., Wetherley, S. and Hollingsworth, D.A., 2005. Bulk chemical control on metamorphic monazite growth in pelitic schists and implications for U–Pb age data. *Journal of Metamorphic Geology*, v.23, n.4, p.261-277. <https://doi.org/10.1111/j.1525-1314.2005.00575.x>
- Foster, G., Gibson, H.D., Parrish, R., Horstwood, M., Fraser, J. and Tindle, A., 2002. Textural, chemical and isotopic insights into the nature and behaviour of metamorphic monazite. *Chemical Geology*, v.191, n.1-3, p.183-207. [https://doi.org/10.1016/S0009-2541\(02\)00156-0](https://doi.org/10.1016/S0009-2541(02)00156-0)
- Foster, G. and Parrish, R.R., 2003. Metamorphic monazite and the generation of P-T-t paths. Geological Society, London, Special Publications, v.220, n.1, p.25-47. <https://doi.org/10.1144/GSL.SP.2003.220.01.02>
- Gehrels, G.E., McClelland, W.C., Samson, S.D. and Patchett, P.J., 1991. U–Pb geochronology of detrital zircons from a continental margin assemblage in the northern Coast Mountains, southeastern Alaska. *Canadian Journal of Earth Sciences*, v. 28, n.8, p.1285-1300. <https://doi.org/10.1139/e91-114>
- Gehrels, G., Rusmore, M., Woodsworth, G., Crawford, M., Andronicos, C., Hollister, L., Patchett, J., Ducea, M., Butler, R., Klepeis, K. and Davidson, C., 2009. U-Th-Pb geochronology of the Coast Mountains batholith in north-coastal British Columbia: Constraints on age and tectonic evolution. *Geological Society of America Bulletin*, v.121, n.9-10, p.1341-1361. <https://doi.org/10.1130/B26404.1>

- Gibson, H.D., Carr, S.D., Brown, R.L. and Hamilton, M.A., 2004. Correlations between chemical and age domains in monazite, and metamorphic reactions involving major pelitic phases: an integration of ID-TIMS and SHRIMP geochronology with Y–Th–U X-ray mapping. *Chemical Geology*, v.211, n.3-4, p.237-260.
<https://doi.org/10.1016/j.chemgeo.2004.06.028>
- Harrison, M.T., Grove, M., Mckeegan, K.D., Coath, C.D., Lovera, O.M. and Fort, P.L., 1999. Origin and episodic emplacement of the Manaslu intrusive complex, central Himalaya. *Journal of Petrology*, v.40, n.1, p.3-19.
<https://doi.org/10.1093/petroj/40.1.3>
- Henry, D.J., Guidotti, C.V. and Thomson, J.A., 2005. The Ti-saturation surface for low-to-medium pressure metapelitic biotites: Implications for geothermometry and Ti-substitution mechanisms. *American Mineralogist*, v.90, n.2-3, p.316-328.
<https://doi.org/10.2138/am.2005.1498>
- Holland, T.J.B. and Powell, R.T.J.B., 1998. An internally consistent thermodynamic data set for phases of petrological interest. *Journal of Metamorphic Geology*, v.16, n.3, p.309-343. <https://doi.org/10.1111/j.1525-1314.1998.00140.x>
- Holland, T. and Powell, R., 2003. Activity–composition relations for phases in petrological calculations: an asymmetric multicomponent formulation. *Contributions to Mineralogy and Petrology*, v.145, n.4, p.492-501.
<https://doi.org/10.1007/s00410-003-0464-z>
- Holland, T.J.B. and Powell, R., 2011. An improved and extended internally consistent thermodynamic dataset for phases of petrological interest, involving a new equation of state for solids. *Journal of Metamorphic Geology*, v.29, n.3, p.333-383.
<https://doi.org/10.1111/j.1525-1314.2010.00923.x>
- Horstwood, M.S., Košler, J., Gehrels, G., Jackson, S.E., McLean, N.M., Paton, C., Pearson, N.J., Sircombe, K., Sylvester, P., Vermeesch, P. and Bowring, J.F., 2016. Community-derived standards for LA-ICP-MS U-(Th-) Pb geochronology–Uncertainty propagation, age interpretation and data reporting. *Geostandards and Geoanalytical Research*, v.40, n.3, p.311-332. <https://doi.org/10.1111/j.1751-908X.2016.00379.x>

- Hults, C.P., Wilson, F.H., Donelick, R.A. and O'Sullivan, P.B., 2013. Two flysch belts having distinctly different provenance suggest no stratigraphic link between the Wrangellia composite terrane and the paleo-Alaskan margin. *Lithosphere*, v.5, n.6, p.575-594. <https://doi.org/10.1130/L310.1>
- Israel, S., Cobbett, R., Westberg, E., Stanley, B. and Hayward, N., 2011b. Preliminary bedrock geology of the Ruby Ranges, southwestern Yukon, (Parts of NTS 115G, 115H, 115A and 115B) (1:150 000 scale). Yukon Geological Survey, Open File 2011-2.
- Israel, S., Murphy, D., Bennett, V., Mortensen, J. and Crowley, J., 2011a. New insights into the geology and mineral potential of the Coast Belt in southwestern Yukon. In: *Yukon Exploration and Geology 2010*, MacFarlane, K.E., Weston, L.H., and Relf, C. (eds.), Yukon Geological Survey, p. 101-123.
- Jochum, K.P., Nohl, U., Herwig, K., Lammel, E., Stoll, B. and Hofmann, A.W., 2005. GeoReM: a new geochemical database for reference materials and isotopic standards. *Geostandards and Geoanalytical Research*, v.29, n.3, p.333-338. <https://doi.org/10.1111/j.1751-908X.2005.tb00904.x>
- Johnston, S.T., and Canil, D., 2007. Crustal architecture of SW Yukon, northern Cordillera: Implications for crustal growth in a convergent margin orogen: *Tectonics*, v.26, TC1006, doi: 10.1029/2006TC001950.
- Kohn, M.J. and Malloy, M.A., 2004. Formation of monazite via prograde metamorphic reactions among common silicates: implications for age determinations. *Geochimica et Cosmochimica Acta*, v.68, n.1, p.101-113. [https://doi.org/10.1016/S0016-7037\(03\)00258-8](https://doi.org/10.1016/S0016-7037(03)00258-8)
- Kylander-Clark, A.R., Hacker, B.R. and Cottle, J.M., 2013. Laser-ablation split-stream ICP petrochronology. *Chemical Geology*, v.345, p.99-112. <https://doi.org/10.1016/j.chemgeo.2013.02.019>
- Larson, K.P., Gervais, F. and Kellett, D.A., 2013. A P–T–t–D discontinuity in east-central Nepal: Implications for the evolution of the Himalayan mid-crust. *Lithos*, v.179, p.275-292. <https://doi.org/10.1016/j.lithos.2013.08.012>

- Larson, K.P., 2020, ChrontouR: Scripts for plotting geochronological and petrochronological data in R. <https://doi.org/10.17605/OSF.IOP46MB>
- Larson, K.P., Shrestha, S., Cottle, J.M., Guilmette, C., Johnson, T.A., Gibson, H.D. and Gervais, F., 2022. Re-evaluating monazite as a record of metamorphic reactions. *Geoscience Frontiers*, v.13, n.2, p.101340. <https://doi.org/10.1016/j.gsf.2021.101340>
- Lederer, G.W., Cottle, J.M., Jessup, M.J., Langille, J.M. and Ahmad, T., 2013. Timescales of partial melting in the Himalayan middle crust: insight from the Leo Pargil dome, northwest India. *Contributions to Mineralogy and Petrology*, v.166, p.1415-1441. <https://doi.org/10.1007/s00410-013-0935-9>
- Lihter, I., Larson, K.P., Shrestha, S., Cottle, J.M. and Brubacher, A.D., 2020. Contact metamorphism of the Tethyan Sedimentary Sequence, Upper Mustang region, west-central Nepal. *Geological Magazine*, v.157, n.11, p.1917-1932. <https://doi.org/10.1017/S0016756820000229>
- Lowey, G.W., 2019. Provenance analysis of the Dezadeash Formation (Jurassic–Cretaceous), Yukon, Canada: Implications regarding a linkage between the Wrangellia composite terrane and the western margin of Laurasia. *Canadian Journal of Earth Sciences*, v.56, n.1, p.77-100. <https://doi.org/10.1139/cjes-2017-0244>
- Lowey, G.W., 2011. Volcaniclastic gravity flow deposits in the Dezadeash Formation (Jura-Cretaceous), Yukon, Canada: Implications regarding the tectonomagmatic evolution of the Chitina arc in the northern Cordillera of North America. *Lithos*, v.125, p.86-100. <https://doi.org/10.1016/j.lithos.2011.01.014>
- Lowey, G.W., 2000. The Tatshenshini shear zone (new) in southwestern Yukon, Canada: Comparison with the Coast shear zone in British Columbia and southeastern Alaska and implications regarding the Shikwak suture. *Tectonics*, v.19, n.3, p.512-528. <https://doi.org/10.1029/1999TC001119>

- Manuszak, J.D., Ridgway, K.D., Trop, J.M. and Gehrels, G.E., 2007. Sedimentary record of the tectonic growth of a collisional continental margin: Upper Jurassic–Lower Cretaceous Nutzotin Mountains sequence, eastern Alaska Range, Alaska, *in* K.D., Trop, J.M., Trop, Glen, J.M.G., O'Neill, M.J., eds., *Tectonic Growth of a Collisional Continental Margin: Crustal Evolution of Southern Alaska*, Geological Society Special Paper 431, p. 345–377, [https://doi.org/10.1130/2007.2431\(14\)](https://doi.org/10.1130/2007.2431(14))
- McClelland, W.C., Gehrels, G.E. and Saleeby, J.B., 1992b. Upper Jurassic-lower Cretaceous basinal strata along the Cordilleran margin: Implications for the accretionary history of the Alexander-Wrangellia-Peninsular terrane. *Tectonics*, v.11, n.4, p.823-835. <https://doi.org/10.1029/92TC00241>
- McClelland, W.C., Gehrels, G.E., Samson, S.D. and Patchett, P.J., 1992a. Structural and geochronologic relations along the western flank of the Coast Mountains batholith: Stikine River to Cape Fanshaw, central southeastern Alaska. *Journal of Structural Geology*, v.14, n.4, p.475-489. [https://doi.org/10.1016/0191-8141\(92\)90107-8](https://doi.org/10.1016/0191-8141(92)90107-8)
- McClelland, W.C. and Mattinson, J.M., 2000. Cretaceous-Tertiary evolution of the western Coast Mountains, central southeastern Alaska. *Special Paper of the Geological Society of America* 343, p.159-182. <https://doi.org/10.1130/0-8137-2343-4.159>
- Mezger, J.E., 1997. Tectonometamorphic evolution of the Kluane metamorphic assemblage, southwest Yukon: evidence for Late Cretaceous eastward subduction of oceanic crust underneath North America [unpublished PhD thesis]: University of Alberta, 306 p. <https://doi.org/10.7939/R3DJ58N76>
- Mezger, J.E., Chacko, T. and Erdmer, P., 2001. Metamorphism at a late Mesozoic accretionary margin: a study from the Coast Belt of the North American Cordillera. *Journal of Metamorphic Geology*, v.19, n.2, p.121-137. <https://doi.org/10.1046/j.0263-4929.2000.00300.x>
- Monger, J.W. and Gibson, H.D., 2019. Mesozoic-Cenozoic deformation in the Canadian Cordillera: The record of a “Continental bulldozer”? *Tectonophysics*, v.757, p.153-169. <https://doi.org/10.1016/j.tecto.2018.12.023>

- Monger, J.W.H., Price, R.A. and Tempelman-Kluit, D.J., 1982. Tectonic accretion and the origin of the two major metamorphic and plutonic belts in the Canadian Cordillera. *Geology*, v.10, n.2, p.70-75. [https://doi.org/10.1130/0091-7613\(1982\)10<70:TAATOO>2.0.CO;2](https://doi.org/10.1130/0091-7613(1982)10<70:TAATOO>2.0.CO;2)
- Monger, J.W.H., van der Heyden, P., Journeay, J.M., Evenchick, C.A. and Mahoney, J.B., 1994. Jurassic-Cretaceous basins along the Canadian Coast Belt: Their bearing on pre-mid-Cretaceous sinistral displacements. *Geology*, v.22, n.2, p.175-178. [https://doi.org/10.1130/0091-7613\(1994\)022<0175:JCBATC>2.3.CO;2](https://doi.org/10.1130/0091-7613(1994)022<0175:JCBATC>2.3.CO;2)
- Moore, T.E. and Box, S.E., 2016. Age, distribution and style of deformation in Alaska north of 60° N: Implications for assembly of Alaska. *Tectonophysics*, v.691, p.133-170. <https://doi.org/10.1016/j.tecto.2016.06.025>
- Mortensen, J.K., and Erdmer, P., 1992, U-Pb, ⁴⁰Ar-³⁹Ar, and K-Ar ages for metamorphism of the Kluane and Aishihik assemblages in southwestern Yukon Territory, in *Radiogenic Age and Isotopic Studies: Report 6*; by Geological Survey of Canada; Geological Survey of Canada, Paper n. 92-2, 1992, p. 135-140, <https://doi.org/10.4095/134174>
- Mottram, C.M., Warren, C.J., Regis, D., Roberts, N.M., Harris, N.B., Argles, T.W. and Parrish, R.R., 2014. Developing an inverted Barrovian sequence; insights from monazite petrochronology. *Earth and Planetary Science Letters*, v.403, p.418-431. <https://doi.org/10.1016/j.epsl.2014.07.006>
- Nelson, J. L., Colpron, M. & Israel, S., 2013. The cordillera of British Columbia, Yukon, and Alaska. *Society of Economic Geology, Special Publication 17*. <https://doi.org/10.5382/SP.17.03>
- Pandey, M., Pant, N.C. and Kumar, S., 2013. Criteria to distinguish between regional and contact zone monazite—a case study from Proterozoic North Delhi Fold Belt (NDFB), India. *Episodes Journal of International Geoscience*, v.36, n.4, p.275-289.
- Parrish, R.R., 1990. U–Pb dating of monazite and its application to geological problems. *Canadian Journal of Earth Sciences*, v.27, n.11, p.1431-1450. <https://doi.org/10.1139/e90-152>

- Paton, C., Hellstrom, J., Paul, B., Woodhead, J. and Hergt, J. 2011. Lolite: Freeware for the visualisation and processing of mass spectrometric data. *Journal of Analytical Atomic Spectrometry*. doi:10.1039/c1ja10172b.
- Paton, C., Woodhead, J., Hellstrom, J., Hergt, J., Greig, A. and Maas, R., 2010. Improved laser ablation U-Pb zircon geochronology through robust down-hole fractionation correction. *G Cubed*, v.11, doi:10.1029/2009GC002618.
- Pattison, D.R.M. and Tinkham, D.K., 2009. Interplay between equilibrium and kinetics in prograde metamorphism of pelites: an example from the Nelson aureole, British Columbia. *Journal of Metamorphic Geology*, v.27, n.4, p.249-279.
<https://doi.org/10.1111/j.1525-1314.2009.00816.x>
- Pavlis, T.L., Amato, J.M., Trop, J.M., Ridgway, K.D., Roeske, S.M. and Gehrels, G.E., 2019. Subduction polarity in ancient arcs: A call to integrate geology and geophysics to decipher the Mesozoic tectonic history of the Northern Cordillera of North America. *GSA Today*, v.29, n.11, p.4-10.
<https://doi.org/10.1130/GSATG465Y.1>
- Peterman, E.M., Mattinson, J.M. and Hacker, B.R., 2012. Multi-step TIMS and CA-TIMS monazite U–Pb geochronology. *Chemical Geology*, v.312, p.58-73.
<https://doi.org/10.1016/j.chemgeo.2012.04.006>
- Pyle, J.M. and Spear, F.S., 2003. Yttrium zoning in garnet: Coupling of major and accessory phases during metamorphic reactions. *American Mineralogist*, v.88, n.4, p.708-708.
- Pyle, J.M., Spear, F.S., Rudnick, R.L. and McDonough, W.F., 2001. Monazite–xenotime–garnet equilibrium in metapelites and a new monazite–garnet thermometer. *Journal of Petrology*, v.42, n.11, p. 2083-2107.
<https://doi.org/10.1093/petrology/42.11.2083>
- Rubin, C.M. and Saleeby, J.B., 1991a. Tectonic framework of the upper Paleozoic and lower Mesozoic Alava sequence: a revised view of the polygenetic Taku terrane in southern southeast Alaska. *Canadian Journal of Earth Sciences*, v.28, n.6, p.881-893. <https://doi.org/10.1139/e91-080>

- Rubin, C.M. and Saleeby, J.B., 1991b. The Gravina Sequence: Remnants of a Mid-Mesozoic oceanic arc in southern southeast Alaska. *Journal of Geophysical Research: Solid Earth*, v.96, n.B9, p.14551-14568.
<https://doi.org/10.1029/91JB00591>
- Shrestha, S., Larson, K.P., Duisterhoeft, E., Soret, M. and Cottle, J.M., 2019. Thermodynamic modelling of phosphate minerals and its implications for the development of PTt histories: A case study in garnet-monazite bearing metapelites. *Lithos*, v.334, p.141-160. <https://doi.org/10.1016/j.lithos.2019.03.021>
- Sigloch, K. and Mihalynuk, M.G., 2013. Intra-oceanic subduction shaped the assembly of Cordilleran North America. *Nature*, v.496, n.7443, p.50-56.
<https://doi.org/10.1038/nature12019>
- Sigloch, K. and Mihalynuk, M.G., 2017. Mantle and geological evidence for a Late Jurassic–Cretaceous suture spanning North America. *Geological Society of America Bulletin*, v.129, n.11-12, p.1489-1520. <https://doi.org/10.1130/B31529.1>
- Smith, T. E., 1981. Geology of the Clearwater Mountains, south-central Alaska. Alaska Division of Geological and Geophysical Surveys Geologic Report 60, scale 1:63,360, 3 sheets, 72 p., <https://doi.org/10.14509/406>
- Spear, F.S. and Pattison, D.R., 2017. The implications of overstepping for metamorphic assemblage diagrams (MADs). *Chemical Geology*, v.457, p.38-46.
<https://doi.org/10.1016/j.chemgeo.2017.03.011>
- Spear, F.S. and Pyle, J.M., 2010. Theoretical modeling of monazite growth in a low-Ca metapelite. *Chemical Geology*, v.273, n.1-2, p.111-119.
<https://doi.org/10.1016/j.chemgeo.2010.02.016>
- Spear, F.S., 2010. Monazite–allanite phase relations in metapelites. *Chemical Geology*, v.279, n.1-2, p.55-62. <https://doi.org/10.1016/j.chemgeo.2010.10.004>
- Stacey, J.T. and Kramers, J., 1975. Approximation of terrestrial lead isotope evolution by a two-stage model. *Earth and planetary science letters*, v.26, n.2, p.207-221.
[https://doi.org/10.1016/0012-821X\(75\)90088-6](https://doi.org/10.1016/0012-821X(75)90088-6)

- Stanley, B., 2012. Structural geology and geochronology of the Kluane Schist, southwestern Yukon Territory [unpublished master's thesis]: University of Waterloo], <http://hdl.handle.net/10012/7096>
- Trop, J.M., Ridgway, K.D., Manuszak, J.D. and Layer, P., 2002. Mesozoic sedimentary-basin development on the allochthonous Wrangellia composite terrane, Wrangell Mountains basin, Alaska: A long-term record of terrane migration and arc construction. *Geological Society of America Bulletin*, v.114, n.6, p.693-717. [https://doi.org/10.1130/0016-7606\(2002\)114<0693:MSBDOT>2.0.CO;2](https://doi.org/10.1130/0016-7606(2002)114<0693:MSBDOT>2.0.CO;2)
- Trop, J. M., & Ridgway, K. D. 2007. Mesozoic and Cenozoic tectonic growth of southern Alaska: A sedimentary basin perspective. In K. D. Ridgway, J. M. Trop, J. M. G. Glen, & J. M. O'Neill (Eds.), *Special Paper 431: Tectonic growth of a collisional continental margin: Crustal evolution of Southern Alaska*, v. 431, p. 55–94. Geological Society of America. [https://doi.org/10.1130/2007.2431\(04\)](https://doi.org/10.1130/2007.2431(04))
- van der Heyden, P., 1992. A Middle Jurassic to early Tertiary Andean-Sierran arc model for the Coast belt of British Columbia. *Tectonics*, v.11, n.1, p.82-97. <https://doi.org/10.1029/91TC02183>
- Vermeesch, P., 2018. IsoplotR: A free and open toolbox for geochronology. *Geoscience Frontiers*, v.9, n.5, p.1479-1493. <https://doi.org/10.1016/j.gsf.2018.04.001>
- Vice, L., 2017. Late Cretaceous to Paleocene evolution of the Blanchard River assemblage, southwest Yukon; implications for Mesozoic accretionary processes in the northwestern Cordillera [unpublished master's thesis]: Simon Fraser University.
- Vice, L., Gibson, H.D. and Israel, S. 2020. Late Cretaceous to Paleocene tectonometamorphic evolution of the Blanchard River Assemblage, Southwest Yukon: New insight into the terminal accretion of insular terranes in the Northern Cordillera. *Lithosphere*, v.2020, n.1, <https://doi.org/10.2113/2020/2298288>

- Waldien, T.S., Roeske, S.M. and Benowitz, J.A., 2021b. Tectonic underplating and dismemberment of the Maclaren-Kluane schist records Late Cretaceous terrane accretion polarity and ~ 480 km of Post-52 Ma dextral displacement on the Denali fault. *Tectonics*, v.40, n.10, p.e2020TC006677.
<https://doi.org/10.1029/2020TC006677>
- Waldien, T.S., Roeske, S.M., Benowitz, J.A., Twelker, E. and Miller, M.S., 2021a. Oligocene-Neogene lithospheric-scale reactivation of Mesozoic terrane accretionary structures in the Alaska Range suture zone, southern Alaska, USA. *Geological Society of America Bulletin*, v.133, n3-4, p.691-716.
<https://doi.org/10.1130/B35665.1>
- White, R.W., Powell, R. and Clarke, G.L., 2002. The interpretation of reaction textures in Fe-rich metapelitic granulites of the Musgrave Block, central Australia: constraints from mineral equilibria calculations in the system $K_2O-FeO-MgO-Al_2O_3-SiO_2-H_2O-TiO_2-Fe_2O_3$. *Journal of Metamorphic Geology*, v.20, n.1, p.41-55.
<https://doi.org/10.1046/j.0263-4929.2001.00349.x>
- White, R.W., Powell, R. and Holland, T.J.B., 2007. Progress relating to calculation of partial melting equilibria for metapelites. *Journal of Metamorphic Geology*, v.25, n.5, p.511-527. <https://doi.org/10.1111/j.1525-1314.2007.00711.x>
- White, R.W., Powell, R., Holland, T.J.B. and Worley, B.A., 2000. The effect of TiO_2 and Fe_2O_3 on metapelitic assemblages at greenschist and amphibolite facies conditions: mineral equilibria calculations in the system $K_2O-FeO-MgO-Al_2O_3-SiO_2-H_2O-TiO_2-Fe_2O_3$. *Journal of Metamorphic Geology*, v.18, n.5, p.497-511.
- Williams, M.A., Kelsey, D.E., Baggs, T., Hand, M. and Alessio, K.L., 2018. Thorium distribution in the crust: Outcrop and grain-scale perspectives. *Lithos*, v.320, p.222-235. <https://doi.org/10.1016/j.lithos.2018.09.016>
- Wing, B.A., Ferry, J.M. and Harrison, T.M., 2003. Prograde destruction and formation of monazite and allanite during contact and regional metamorphism of pelites: petrology and geochronology. *Contributions to Mineralogy and Petrology*, v.145, p.228-250. <https://doi.org/10.1007/s00410-003-0446-1>

Xing, L., Trail, D. and Watson, E.B., 2013. Th and U partitioning between monazite and felsic melt. *Chemical Geology*, v.358, p.46-53.

<https://doi.org/10.1016/j.chemgeo.2013.07.009>

Yakymchuk, C. and Brown, M., 2014. Behaviour of zircon and monazite during crustal melting. *Journal of the Geological Society*, v.171, n.4, p.465-479.

<https://doi.org/10.1144/jgs2013-115>

Yokelson, I., Gehrels, G.E., Pecha, M., Giesler, D., White, C. and McClelland, W.C., 2015. U-Pb and Hf isotope analysis of detrital zircons from Mesozoic strata of the Gravina belt, southeast Alaska. *Tectonics*, v.34, n.10, p.2052-2066.

<https://doi.org/10.1002/2015TC003955>

Chapter 5. Insights into the timing and style of Cretaceous Insular terrane accretion from detrital zircon geochronology across the Kluane Schist, southwest Yukon.

Will McKenzie¹, H. Daniel Gibson¹ & Brendan Dyck²

¹ Department of Earth Sciences, Simon Fraser University, Burnaby, BC, Canada

² Department of Earth, Environmental and Geographical Sciences, University of British Columbia, Kelowna, BC, Canada

Abstract

The Kluane Schist, southwest Yukon, represents one of the largest continuous exposures of metasedimentary rocks at the interface between the inboard pericratonic Intermontane terranes and outboard Insular terranes of the North American Cordillera. Consisting of an 160 km long belt of metamorphosed siliciclastic and calcareous rocks interleaved with ultramafic bodies and local carbonate, the Kluane Schist preserves a detailed record of Insular terrane accretion throughout the latest Mesozoic and into the early Cenozoic. To determine the nature of the paleo-western margin of North America and its relationship to the Insular terranes prior to their accretion, we report U-Pb age and Hf-isotope determinations of detrital zircon samples collected from various structural levels within the Kluane Schist. Our results highlight the Kluane Schist as a young depocenter within this region of the Cordillera with strong provenance ties to the paleo-western margin of North America. These characteristics are compatible with its deposition as the uppermost part of a contractional forearc assemblage to an arc built upon the Yukon-Tanana terrane. Combined with similar datasets from other Jura-Cretaceous metasedimentary units within the Northern Cordillera we suggest the tectonic setting for the Kluane Schist is best reconciled with models of Insular terrane accretion that involve east-dipping subduction below a westward migrating North American continent.

5.1. Introduction

The Cordilleran orogen of western North America experienced a protracted history of terrane accretion which can be broadly divided into two phases: 1) initial accretion of the Intermontane terranes to the passive margin of North America during the latest Permian and early Mesozoic, followed by 2) the accretion of the Insular terranes, as early as ca. 175 Ma or as late as ca. 70 Ma (e.g., van der Heyden, 1992; Gehrels, 2001; Dickinson, 2004; Colpron *et al.*, 2007; Gehrels *et al.*, 2009; Beranek & Mortensen, 2011; Monger & Gibson, 2019; Box *et al.*, 2019; Vice *et al.*, 2020; Waldien *et al.*, 2021b; Chapter 4). Today the boundary between the Insular and Intermontane terranes extends for over 2000 km from southern British Columbia to Alaska where it is extensively overprinted by multiple episodes of metamorphism, deformation, and magmatism (Fig. 5.1; e.g., the Coast Plutonic Complex; Monger *et al.*, 1982; Rubin & Saleeby, 1991; van der Heyden, 1992). Nevertheless, a record of the timing and tectonic processes driving Insular terrane accretion is preserved in numerous Jurassic to Cretaceous (Jura-Cretaceous) metasedimentary belts that are considered to have once represented the intervening seaway separating the Insular and Intermontane terranes (Fig. 5.1; e.g., van der Heyden, 1992; Monger *et al.*, 1994; Hults *et al.*, 2013; Yokelson *et al.*, 2015; Box *et al.*, 2019; Waldien *et al.*, 2021a, b). Although recent and past studies largely agree that the collapse of these Jura-Cretaceous basins records both metamorphism and deformation associated with Insular terrane accretion (Monger *et al.*, 1994; Hults *et al.*, 2013; Box *et al.*, 2019; Vice *et al.*, 2020; Waldien *et al.*, 2021a, b; Chapter 3), controversy surrounds their original geodynamic position within the Cordillera and their tectonic significance during Insular terrane accretion (e.g., Monger, 2014).

Current models of Insular terrane accretion interpret the Jura-Cretaceous basins as having formed in one of the following three tectonic settings:

- 1) A combination of back-arc basins, entrapped forearc assemblages and post-accretionary rifts collectively record the diachronous closure of a series of finite seaways developed within the back-arc region of long-lived, east-dipping subduction zone outboard of the Insular terranes (e.g., Monger *et al.*, 1982; Gehrels *et al.*, 1991; Rubin & Saleeby, 1991a, b; McClelland *et al.*, 1992a, b; van der Heyden, 1992; Trop *et al.* 2002; Gehrels *et al.*, 2009). According to this model, initial Middle Jurassic Insular terrane accretion occurred near west-central British Columbia and southernmost Alaska

(present-day coordinates), and became progressively younger to the north and south until the terminal accretion of the Insular terranes in mid–Late Cretaceous (Monger *et al.*, 1982; Gehrels *et al.*, 1991; Rubin & Saleeby, 1991a, b; McClelland *et al.*, 1992a, b; van der Heyden, 1992; Trop *et al.* 2002; Gehrels *et al.*, 2009).

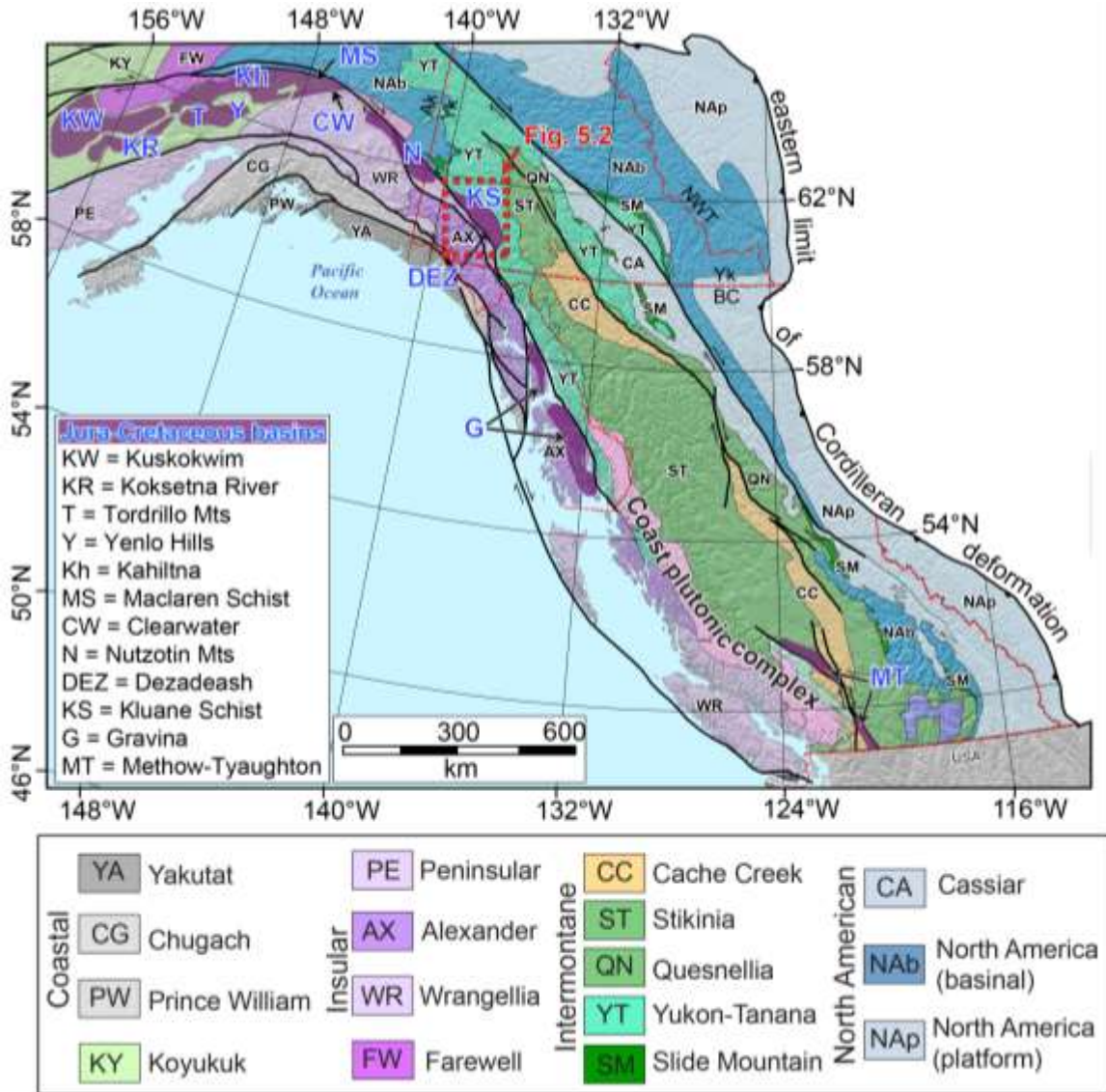


Figure 5.1. Terrane map of the Northern Canadian Cordillera (modified from Colpron & Nelson, 2011), with the location of the study area highlighted in the red dashed box. Jura-Cretaceous basinal assemblages situated at the interface between the Insular and Intermontane terranes are highlighted in dark purple.

2) The basins are interpreted as two unique, terrane-specific lithofacies that were originally separated by an ocean of unknown width until at least the mid-Cretaceous (ca. 117 Ma; Box *et al.*, 2019). The diachronous juxtaposition of these terrane-specific lithofacies is considered to occur atop a north- and east-dipping subduction zone below the paleo-western margin of North America. Initial basin juxtaposition is considered to occur near to the Yukon-Alaska border in the Early Cretaceous (present-day coordinates; ca. 117 Ma; Nutzotin-Dezadeash in Fig. 5.1; e.g., Box *et al.*, 2019) and propagated southeast and northwest until the final collapse of basins within southwest Alaska during the mid–Late Cretaceous (present-day coordinates; Kuskokwim-Koksetna in Fig. 5.1; ca. 81 Ma; e.g., Hampton *et al.*, 2010; Box *et al.*, 2019).

3) The basins represent vestiges of a once extensive ocean that was open and interconnected throughout Late Jurassic to earliest Eocene (the Mezcalera-Angayucham Ocean; Sigloch & Mihalynuk, 2013, 2017). Following this interpretation, progressive Insular terrane accretion across this wide, 2000–4000 km oceanic basin was largely driven by slab-pull of a west-dipping subduction system along the inboard margin of the Insular terranes (Sigloch & Mihalynuk, 2013, 2017).

Understanding the original geodynamic position of these basins and their tectonic significance is key to integrating their extensive post-depositional datasets with current models of Cordilleran orogenesis (e.g., Monger, 2014). Here we present the results of U-Pb age and Hf-isotope data acquired from five detrital zircon samples collected across the Cretaceous Kluane Schist, which represents a metasedimentary assemblage at the interface between the Insular and Intermontane terranes within southwest Yukon (Figs. 5.1 & 5.2; e.g., Mezger *et al.*, 2001; Israel *et al.*, 2011a). Our data not only bears provenance and depositional age information for the Kluane Schist but also provide key insight into the original geodynamic setting of its deposition. We integrate our zircon dataset with recent structural restorations and metamorphic revaluations (Chapter 3), along with monazite petrochronology (Chapter 4), to build a new tectonic model for the Kluane Schist from its initial deposition to collapse and final exhumation. Combined with similar datasets from other Jura-Cretaceous basins within the Canadian-Alaska (“Northern”) Cordillera (Fig. 5.1 & 5.3; Berg *et al.*, 1972; Wallace *et al.*, 1989; McClelland *et al.*, 1991; Gehrels *et al.*, 1992; Kapp & Gehrels, 1998; Lowey, 2000, 2011, 2019, 2021; Trop *et al.*, 2002; Manuszak *et al.*, 2007; Davidson & McPhillips, 2007; Miller *et al.*, 2007; Bradley *et al.*, 2009; Israel *et al.*, 2011a; Wilson *et al.*, 2012; Hulst *et al.*, 2013;

Yokelson *et al.*, 2015; Vice, 2017; Box *et al.*, 2019; Vice *et al.*, 2020; Fasulo *et al.*, 2020; Waldien *et al.*, 2021a, b), we also offer a five-stage model to account for their tectonic histories during Insular terrane accretion and address key questions relating to the Mesozoic tectonic architecture of the Northern Cordillera including: 1) the width and geometry of the ocean separating the Insular and Intermontane terranes during the Mesozoic, 2) the timing and driving mechanism of Insular terrane accretion, and 3) the polarity of subduction during Insular terrane accretion.

5.2. Geological Setting

The Cordillera of western North America is an accretionary orogen that was constructed by the accretion of two main terrane groups to the western margin of Laurentia from the mid-Paleozoic to Cenozoic; the Intermontane terranes and Insular terranes (Fig. 5.1 and 5.2; e.g., Monger *et al.*, 1972; Coney *et al.*, 1980; Nelson *et al.*, 2013). We detail some key characteristics of these accreted terranes below, with focus of the study area within southwest Yukon (Fig. 5.2; e.g., Israel *et al.*, 2011a).

5.2.1. Intermontane terranes: the Yukon-Tanana terrane

Within southwest Yukon the Intermontane terranes are primarily composed of the Yukon-Tanana terrane (Fig. 5.1; e.g., Mortensen, 1992). The Yukon-Tanana terrane is considered pericratonic with respect to the North American continent (e.g., Nelson *et al.*, 2013). It preserves a long deformational, metamorphic, and magmatic history that reflects mid-Paleozoic rifting away from the western Laurentian margin and early Mesozoic re-accretion (e.g., Monger *et al.*, 1982; Colpron *et al.*, 2007; Beranek & Mortensen, 2011; Nelson *et al.*, 2013). Within the study area, the Yukon-Tanana terrane occupies the structurally highest panel, overlying all basinal assemblages, including the Kluane Schist (Fig. 5.2; e.g., Israel *et al.*, 2011a), and is comprised of two main units, the Snowcap and Finlayson assemblages (e.g., Israel *et al.*, 2011a).

The Snowcap assemblage forms the basement of much of the Yukon-Tanana terrane within the Northern Cordillera (e.g., Colpron *et al.*, 2006; Piercey & Colpron,

2009). It consists of quartzite, psammite, greenstone, marble, and calc-silicate rocks deposited on the distal western Laurentian margin prior to rifting of Yukon-Tanana terrane away from the continent during the mid-Paleozoic opening of the Slide Mountain Ocean (e.g., Gehrels *et al.*, 1992; Colpron *et al.*, 2006; Piercey & Colpron, 2009). The Devonian to Mississippian volcanic and sedimentary rocks of the Finlayson assemblage lie unconformably above the Snowcap assemblage and are typified by volcanic and sedimentary rocks with arc and back-arc affinity (Colpron *et al.*, 2006; Murphy *et al.*, 2009; Piercey & Colpron, 2009; Israel & Westberg, 2012).

Collectively the Snowcap and Finlayson assemblages, along with the western and northern parts of the Yukon-Tanana terrane, experienced greenschist to amphibolite facies metamorphism and penetrative deformation during the Late Triassic, Early-Middle Jurassic and Early Cretaceous (e.g., Berman *et al.*, 2007; Staples *et al.*, 2016; Clark, 2017). Within these units, significant magmatic episodes are recorded across southwest Yukon during the Late Devonian–Mississippian (ca. 365–345 Ma; e.g., Grass Lakes and Simpson Range suites; e.g., Nelson *et al.*, 2006), the latest Permian to Early Triassic (ca. 265–250 Ma; e.g., Sulphur Creek suite; e.g., Nelson *et al.*, 2006), Late Triassic to Early Jurassic (ca. 205–175; e.g., Long Lake and Minto suites; Mortensen *et al.*, 1999; Joyce *et al.*, 2015; Colpron *et al.*, 2022), Early to mid-Cretaceous (ca. 115–100 Ma; e.g., Whitehorse suite; e.g., Hart *et al.*, 2006), Late Cretaceous (ca. 80–70 Ma; e.g., Prospector Mountain and Casino suites; Allan *et al.*, 2013; Mortensen *et al.*, 2016) and Paleocene to Early Eocene (ca. 64–57 Ma; e.g., Ruby Range batholith; Fig. 5.2; Israel *et al.*, 2011a). Together these metamorphic and magmatic episodes are suggested to record the initial rifting of the Yukon-Tanana terrane away from the North American margin during the Carboniferous followed by its re-accretion to the North American margin during the Permo-Triassic and the subsequent development of an evolving, west-facing arc build upon the Yukon-Tanana terrane in response to subduction outboard of its western margin from the Late Triassic onward (e.g., Mortensen *et al.*, 1992; Nelson *et al.*, 2013; Colpron *et al.*, 2022).

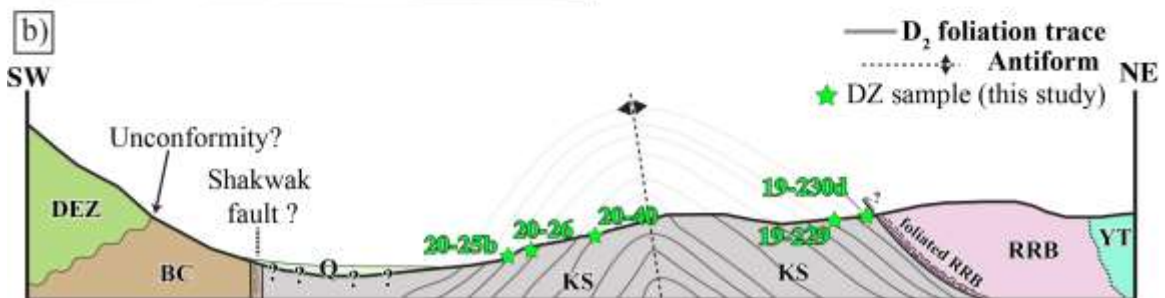
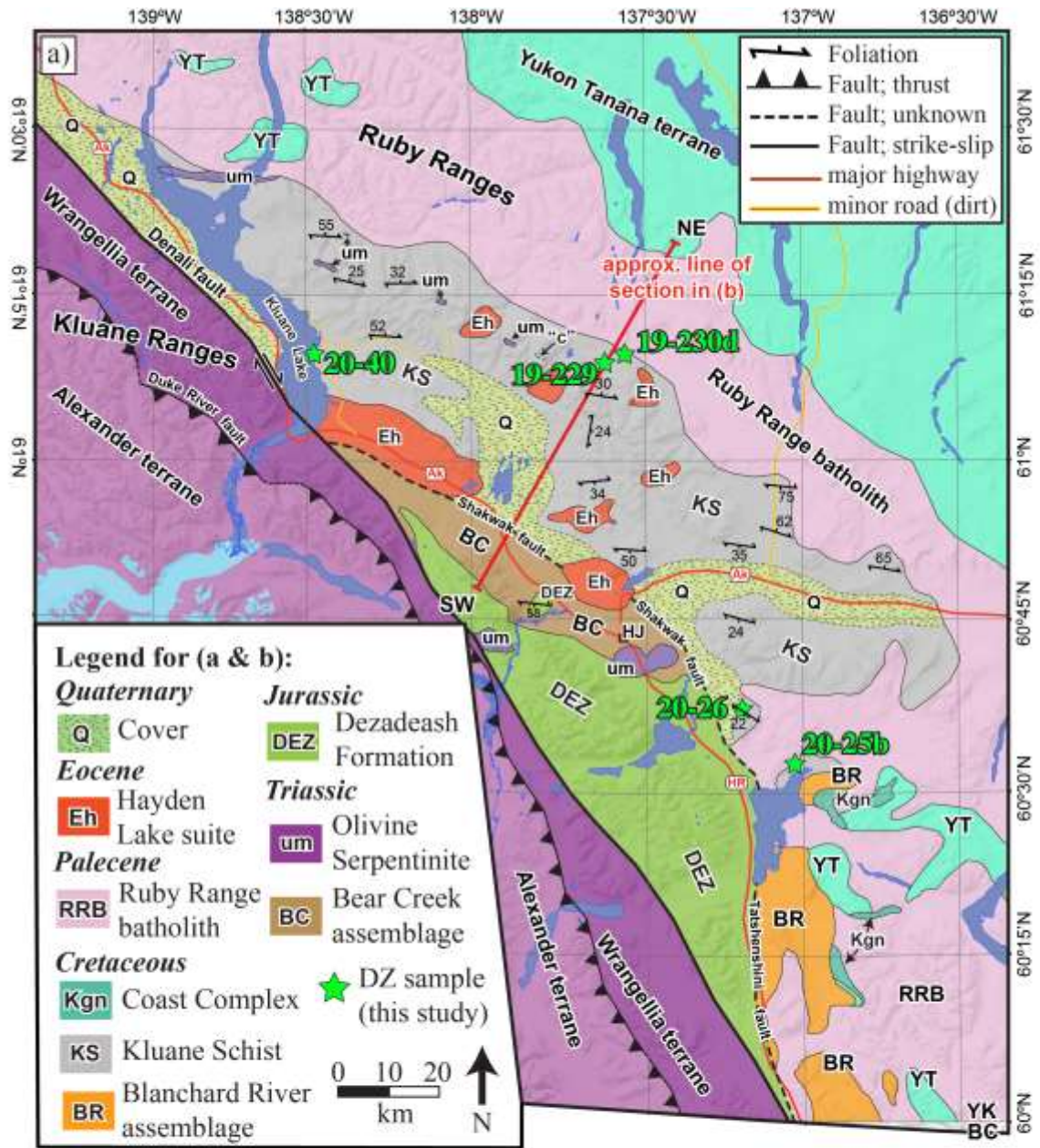


Figure 5.2 a) Map of the Kluane Basin and its surrounding geology. Location of detrital zircon samples collected for analysis in this study are highlighted by green stars. The distribution of the major lithologies within the Kluane Basin and their relationships to surrounding geological belts is shown (based on Mezger, 1997; Mezger *et al.*, 2001; Israel *et al.*, 2015; Vice *et al.*, 2020; this study). (carb = carbonate). b) Schematic cross section drawn from southwest to northeast and roughly through the centre of the study area (line of section shown in (a); modified after: Israel *et al.*, 2011a). Our detrital zircon samples are projected along strike onto the line of section to highlight their relative structural position across the Kluane Schist. The major structures bounding and within the Kluane Schist are also shown (see also: Mezger *et al.*, 2001a, b; Israel *et al.*, 2011a, b; Israel & Kim, 2014; Israel *et al.*, 2015; Chapter 3).

5.2.2. Insular terranes: Alexander and Wrangellia terranes

The Alexander and Wrangellia terranes comprise the majority of the Insular terranes within the Northern Cordillera (Fig. 5.1). Due to their well-documented shared evolution from at least the Pennsylvanian (e.g., Beranek *et al.*, 2014) and potentially as early as the Late Devonian (Israel *et al.*, 2014) the term “Insular terranes” is herein used to refer to both the Alexander and Wrangellia terranes (e.g., Monger *et al.*, 1982).

The Insular terranes are considered exotic within the Cordillera, with paleogeographic affinity to Baltican, Siberian and Caledonian realms (e.g., Colpron & Nelson, 2009). Faunal and provenance relationships track the initial transport of the Insular terranes into the paleo-Pacific around the northern margin of Laurentia during the mid-Paleozoic (e.g., Colpron & Nelson, 2009; Beranek *et al.*, 2013). Subsequent southward transport of the Insular terranes is then recorded from the Carboniferous after which they are considered to have evolved within an isolated intra-arc oceanic setting until the Early-Middle Jurassic (e.g., Gehrels *et al.*, 1996; Amato *et al.*, 2009; Colpron & Nelson, 2009, 2011; Nelson *et al.*, 2013). This period of intra-arc evolution is recorded by largely juvenile volcanic-plutonic arc successions exposed throughout the Insular terranes including the Lower Cretaceous Chisana Formation (U-Pb zircon age ca. 135–130 Ma, zircon $\epsilon_{\text{Hf}}(t) \sim +7$ to $+15$; Manselle *et al.*, 2020; Fasulo *et al.*, 2020), the Jurassic–Late Cretaceous Chitina Arc (U-Pb zircon age ca. 175–135 Ma; Plafker *et al.*, 1989; Day *et al.*, 2016; Manselle *et al.*, 2020), the Late Jurassic St. Elias plutonic suite (U-Pb zircon age ca. 155–147 Ma, whole rock $\epsilon_{\text{Nd}}(t) \sim +3$ to $+5$; Beranek *et al.*, 2017),

the Jurassic Talkeetna Arc (U-Pb zircon age ca. 200–155 Ma, whole rock $\epsilon\text{Nd}(t) \sim +4$ to $+8$; Rioux *et al.*, 2007) and the Mississippian–Pennsylvanian Skolai Arc (U-Pb zircon age ca. 320–290 Ma, whole rock $\epsilon\text{Nd}(t) \sim +0$ to $+8$; Beard & Barker, 1989; Beranek *et al.*, 2014).

The earliest evidence for the accretion of the Insular terranes with the paleo-western margin of North America is observed as Early-Middle Jurassic overlap sequences and cross-cutting plutons within west central British Columbia and southeast Alaska (ca. 180–175 Ma; e.g., van der Heyden, 1992; Gehrels, 2001; Gehrels *et al.*, 2009). Farther north within the Cordillera, the youngest depositional ages recorded for the Maclaren Schist (Fig. 5.1; 86 Ma; Waldien *et al.*, 2021a), parts of the Kahiltna assemblage (Fig. 5.1; ca. 81 Ma; Box *et al.*, 2019) and the Upper Koksetna River sequence (Fig. 5.1; ca. 85 Ma; Hults *et al.*, 2013), are consistent with an open ocean basin or seaway between the Insular and Intermontane terranes at this time (e.g., Hults *et al.*, 2013; Box *et al.*, 2019). This interpretation suggests initial accretion of the Insular terranes was likely diachronous along strike within the Northern Cordillera (c.f., Box *et al.*, 2019) with tectonic coupling between the Insular and inboard terranes (e.g., Intermontane) from the Early-Middle Jurassic until their terminal collision in the latest Mesozoic (e.g., van der Heyden, 1992; McClelland *et al.*, 1992; Nelson *et al.*, 2013; Colpron *et al.*, 2015; Sigloch & Mihalynuk, 2013, 2017; Monger, 2014; Box *et al.*, 2019; Trop *et al.*, 2020). Although the geodynamic setting, tectonic driver(s), and the precise timing of Insular terrane accretion remains hotly debated (e.g., Sigloch & Mihalynuk, 2013, 2017; Monger 2014), most agree that the geologic history preserved in the intervening Jura-Cretaceous basins provide important constraints for reconciling this controversy (e.g., McClelland *et al.*, 1992; Hults *et al.*, 2013; Sigloch & Mihalynuk 2017; Box *et al.*, 2019; Lowey, 2019; Trop *et al.*, 2020; Waldien *et al.*, 2021a).

5.2.3. Terrane-intervening strata: Jura-Cretaceous basins

The Jura-Cretaceous basinal strata juxtaposed between the Insular and Intermontane terranes range from Early Jurassic to Late Cretaceous in age (Fig. 5.3). Older units (e.g., Kahiltna basin, Gravina basin; Fig. 5.3) commonly show a terrane specific affinity to either outboard (i.e., Insular terranes) or inboard (i.e., Intermontane

terrane) sources (Fig. 5.3). Jura-Cretaceous sequences derived from outboard sources (e.g., Nutzotin, Clearwater, western Gravina) are typified by low-grade volcanic-turbidites which yield unimodal Late Jurassic detrital zircon signatures (Fig. 5.3; e.g., Hulst *et al.*, 2013), while sequences derived from inboard sources can record higher grades of metamorphism and are typically composed of volcanic-free turbidite or clastic sequences that yield multi-mode detrital zircon signatures with age populations extending into the Precambrian (e.g., Hulst *et al.*, 2013; Box *et al.*, 2019; Waldien *et al.*, 2021a, b). Younger mid-Late Cretaceous units have yielded evidence for a mixed provenance between inboard and outboard sources (e.g., Kuskokwim Group; Fig. 5.3; Elder & Box, 1992; Box *et al.*, 1993; Miller & Bundtzen, 1994; Patton *et al.*, 2009).

Figure 5.3 summarizes key information relating to the provenance, age of deposition and lithological features of each basin discussed within this study. Where possible, constraint on the timing of basin metamorphism and deformation is also provided (Fig. 5.3). The descriptions below focus on those that directly outcrop within the southwest Yukon (Fig. 5.2).

The Jura-Cretaceous basin of southwest Yukon

Three inverted Jura-Cretaceous basins outcrop within the immediate study area, the Dezadeash Formation, Blanchard River assemblage, and Kluane Schist (Fig. 5.2; Lowey, 2011; Israel *et al.*, 2011a; Israel *et al.*, 2015; Vice *et al.*, 2020). These units are all considered to unconformably overly, at least in part, rocks of the enigmatic Bear Creek assemblage; a sequence of Upper Triassic marine strata along with greenschist-facies intermediate to mafic volcanic rocks, pillow basalt and volcano-clastic interbeds that may represent a fragment of the ocean floor which once separated the Insular and Intermontane terranes (Fig. 5.2; Israel *et al.*, 2015; Chapter 2).

Dezadeash Formation: The Jurassic to Early Cretaceous Dezadeash Formation comprises sub-greenschist to greenschist-facies (Fig. 5.2; $P \sim 2.5$ kbar, $T \sim 250^\circ\text{C}$; Lowey, 2021) submarine fan deposits that are cut by the Denali fault to the southwest (Fig. 5.2; e.g., Eisbacher, 1976). Provenance, compositional, and paleocurrent indicators suggest it is primarily derived from arcs within the Insular terranes to the southwest (Fig. 5.3; e.g., Eisbacher, 1976; Lowey, 2007; 2011; Lowey, 2019), with both a collapsing back-arc (e.g., Eisbacher, 1976; Lowey, 2007; 2011) or forearc (Lowey, 2019) setting suggested for its deposition. Based on the age of volcanoclastic interbeds and granitic

conglomerate clasts, restoration of the Denali fault, and their similar detrital zircon spectra and lithology, the Dezadeash Formation has been considered correlative with the Nutzotin Mountain sequence, Clearwater metasediments, and the western parts of the Gravina belt (Fig. 5.3; e.g., Lowey, 2011; Hults *et al.*, 2013; Box *et al.*, 2019; Waldien *et al.*, 2021b).

Blanchard River assemblage: The Tatshenshini shear zone separates the Dezadeash Formation from the overlying Blanchard River assemblage (Fig. 5.2; Vice, 2017; Vice *et al.*, 2020). The Blanchard River assemblage consists of intensely deformed and interlayered units of quartz-biotite pelitic and psammitic schist along with locally migmatitic paragneiss that record metamorphism up to kyanite-grade conditions (Fig. 5.3; ~6.5 kbar; Bordet *et al.*, 2015; Vice *et al.*, 2020). These kyanite-grade assemblages are typically overprinted by cordierite–andalusite, recording the subsequent regional exhumation of the Blanchard River assemblage and its metamorphism at lower-pressure conditions (Fig. 5.3; ~3 kbar; Vice *et al.*, 2020). Detrital zircon constrain the depositional age of the Blanchard River assemblage to the Early Cretaceous and has been used to infer derivation primarily from units of the inboard Yukon-Tanana terrane with minor input from the outboard Insular terranes (Fig. 5.3; Vice, 2017).

Kluane Schist: Exposed as a 160 km long, largely northwest-striking belt of graphitic mica-quartz schist and cordierite bearing paragneiss, the Kluane Schist represents the most extensive package of metasedimentary rocks within the Insular-Intermontane suture zone of southwest Yukon (Fig. 5.2; e.g., Mezger *et al.*, 2001; Israel *et al.*, 2011a, b). Direct observation of the structural relationship between the Kluane Schist and its surrounding geological units are sparse (Fig. 5.2; Israel *et al.*, 2011a). To the southeast, the Shawkak fault, an inferred structural feature of unknown kinematics, separates the Kluane Schist from the Bear Creek assemblage and Dezadeash Formation (Fig. 5.2, c; e.g., Mezger, 1997; Colpron & Nelson, 2011; Israel *et al.*, 2015), while to the southwest the Kluane Schist is truncated by the Denali fault, separating it from rocks of the Insular terranes (Fig. 5.2). The northern and eastern contacts of the Kluane Schist with the overlying Yukon-Tanana terrane are obscured by the extensive Paleocene-Eocene Ruby Range batholith (Fig. 5.2; Israel *et al.*, 2011a, b). Across the Kluane Schist both schist and gneiss units are locally interlayered with carbonate enclaves, interpreted as olistoliths of Yukon-Tanana affinity (Stanley, 2012), and olivine

serpentinite bodies (Fig. 5.2) which are suggested to either represent fragments of dismembered oceanic crust (Mezger, 2000) or parts of deeper seated ultramafic cumulates, exhumed from arcs within northern Stikinia and entrained within the Kluane Schist during its deposition (Canil *et al.*, 2015).

Metamorphic grade generally increases from the core of the Kluane Schist, which is characterized by a graphitic muscovite-rich schist, towards its northern and eastern edges where the Kluane Schist becomes increasingly gneissic and locally migmatitic, preserving a cm-scale banding defined by darker layers of biotite-cordierite and lighter layers of quartz-feldspar (Mezger *et al.*, 2001; Israel *et al.*, 2011b; Chapter 3). Its resulting northeast-dipping inverted metamorphic sequence documents the terminal accretion of the Insular terranes from ca. 70–55 Ma through the overprinting of a distinct sub-greenschist facies burial event by regional Buchan-style metamorphism (Fig. 5.2; 3.0–3.5 kbar at 375–400 °C to 4–4.5 kbar at 700–750 °C; Chapter 3).

Combined structural and metamorphic analyses generally agree that the Kluane Schist developed on the upper plate of an east-dipping subduction system (e.g., Mezger *et al.*, 2001; Israel *et al.*, 2011a; Chapter 3). However, significant differences in interpretation have been made regarding the timing and tectonic environment of Kluane Schist deposition along with its significance during the Mesozoic evolution of the Northern Cordillera (e.g., Erdmer & Mortensen, 1993; Mezger *et al.*, 2001; Israel *et al.*, 2011a; Canil *et al.*, 2015; Waldien *et al.*, 2021b; Chapter 3). Currently only eight, low-n (~20–70 grains) detrital zircon samples characterize the Kluane Schist and have been used to infer a Late Cretaceous age for its deposition (ca. 94 Ma; Fig. 5.3; Israel *et al.*, 2011a) and its primary derivation from the inboard Yukon-Tanana terrane (Israel *et al.*, 2011a; Stanley, 2012). However, the recent restoration of ~480 km of dextral slip along the Denali fault since ca. 52 Ma (Waldien *et al.*, 2021b) makes possible an abundance of potential new source areas for the Kluane Schist that are located outboard of the Denali fault and several hundred kilometres to the northwest of its current position (c.f., Fig. 5.1; Waldien *et al.*, 2021b). Consequently, to provide further insight into the key questions regarding the provenance, timing, and depositional setting of the Kluane Schist we have undertaken a systematic detrital zircon U-Pb age study accompanied by Hf-isotope compositions.

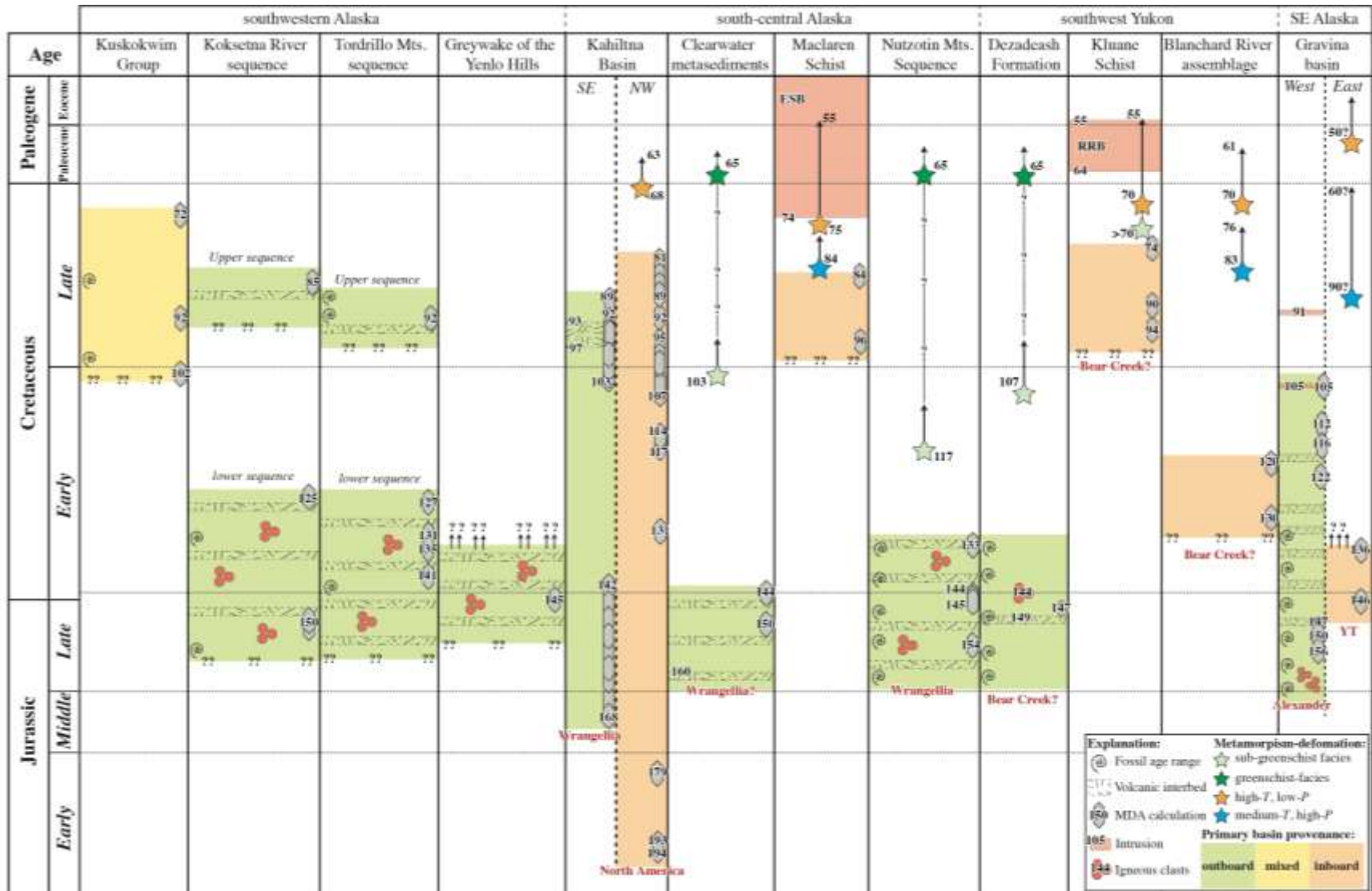


Figure 5.3. Stratigraphic chart showing the inferred provenance, depositional ages, lithological characteristics, and metamorphic-deformational constraints for the Jura-Cretaceous basins considered in this study (see also Fig. 5.1). See legend in lower right corner for explanation of symbols and colours. Red bold text indicates inferred basement unit (YT = Yukon-Tanana terrane). Time scale from Walker & Geissman (2022). (Data from: ESB = East Susitna Batholith; Waldien *et al.*, 2021b and references therein; RRB = Ruby Range batholith; Israel *et al.*, 2011a; Kuskokwim Group: Miller *et al.*, 2007; Bradley *et al.*, 2009; Hults *et al.*, 2013; Koksetna River Sequence: Wallace *et al.*, 1989; Hults *et al.*, 2013; Tordrillo Mountains sequence: Bradley *et al.*, 2009; Wilson *et al.*, 2012; Hults *et al.*, 2013; Yenlo Hills: Hults *et al.*, 2013; Kahiltna Basin: Davidson & McPhillips, 2007; Box *et al.*, 2019; Clearwater metasediments and Maclaren Schist: Waldien *et al.*, 2021a, b; Nutzotin Mountains sequence: Berg *et al.*, 1972; Trop *et al.*, 2002; Manuszak *et al.*, 2007; Hults *et al.*, 2013; Fasulo *et al.*, 2020; Dezadeash Formation: Eisbacher, 1976; Lowey, 2000, 2011, 2019, 2021; Kluane Schist: Israel *et al.*, 2011a; Chapters 3 & 4; Blanchard River assemblage: Vice, 2017; Vice *et al.*, 2020; Gravina Basin: McClelland *et al.*, 1991; Gehrels *et al.*, 1992; Kapp & Gehrels, 1998; Yokelson *et al.*, 2015).

5.3. Methods

5.3.1. Zircon Uranium-Lead (U-Pb) geochronology and Hafnium-isotope geochemistry by LA-MC-ICP-MS

Five Kluane Schist samples were collected for detrital zircon U-Pb geochronology and Hafnium(Hf)-isotope geochemistry (Fig. 5.2). Samples were selected to encompass the full range of metamorphic conditions experienced by the Kluane Schist, while also sampling the full geographical range and structural section currently exposed (Fig. 5.2). Selected samples included: (1) 19WM230d, a migmatite gneiss representing the northernmost, structurally highest unit of the Kluane Schist, (2) 19WM229, a cordierite-garnet-sillimanite bearing gneiss, typical of much of the northeast region of the basin, (3) 20WM40, a staurolite-garnet bearing schist, typical of structurally lower outcrops within the basin's far western regions, (4) 20WM26 an andalusite-grade protogneiss and (5) 20WM25b a cordierite bearing gneiss that collectively characterize the far southern regions of the currently exposed Kluane Schist (Fig. 5.2).

Zircon separation was performed at Simon Fraser University, Burnaby, British Columbia using standard crushing, Wilfley table, magnetic and heavy liquid (methylene

iodide) density-separation procedures. Analysis of zircon U-Th-Pb isotopes was then conducted at Geotop labs in the Université du Québec à Montréal (UQAM). Zircon were annealed in a muffle furnace at 1000 degrees for 48 hours. Zircon were then mounted in epoxy, polished, and imaged on a Hitachi S-3400 Variable Pressure SEM at an accelerating voltage of 20 kV using a Centaurus Cathodoluminescence (CL) detector. The CL images highlighted growth zoning, rims, and inherited cores when present within individual grains, and helped to guide the spot selection for the in-situ laser ablation analysis.

Zircon U-Th-Pb isotopes were measured using laser-ablation, multi-collector, inductively coupled plasma mass spectrometry (LA-MC-ICP-MS) across 5 individual analytical sessions. A Nu Attom single collector mass spectrometer attached to a photon machines G2 193nm excimer laser was used with a spot size of 30µm, following the general procedures reported in Perrot *et al.* (2017). In addition, 3 ml/min N₂ was added before the torch to reduce oxide formation in the plasma and the sensitivity of the mass spectrometer was optimized using U from a NIST610 glass, ensuring that the NIST glass produced U/Th of 1 and a Th/ThO of 1.10⁻³. Specific LA-MC-ICP-MS parameters are detailed in Tables H1 and H3, as recommended by Horstwood *et al.* (2016).

For each session, Lolite 4 software was used to process the data and correct for down-hole fractionation. We used 91500 (Wiedenbeck *et al.*, 1995) as the primary reference material for calibration, while Plešovice (Sláma *et al.*, 2008) was analysed as a secondary reference material for quality control and validation purposes. During each session, repeat analyses of Plešovice and GJ1 produced weighted mean ages within error with their known ages (Sláma *et al.*, 2008; Jackson *et al.*, 2004). Individual secondary reference material data and ages are given in Tables H2 and H4. After processing the raw data, Isoplot R (Vermeesch, 2018a) was used to generate Concordia diagrams and weighted mean ages.

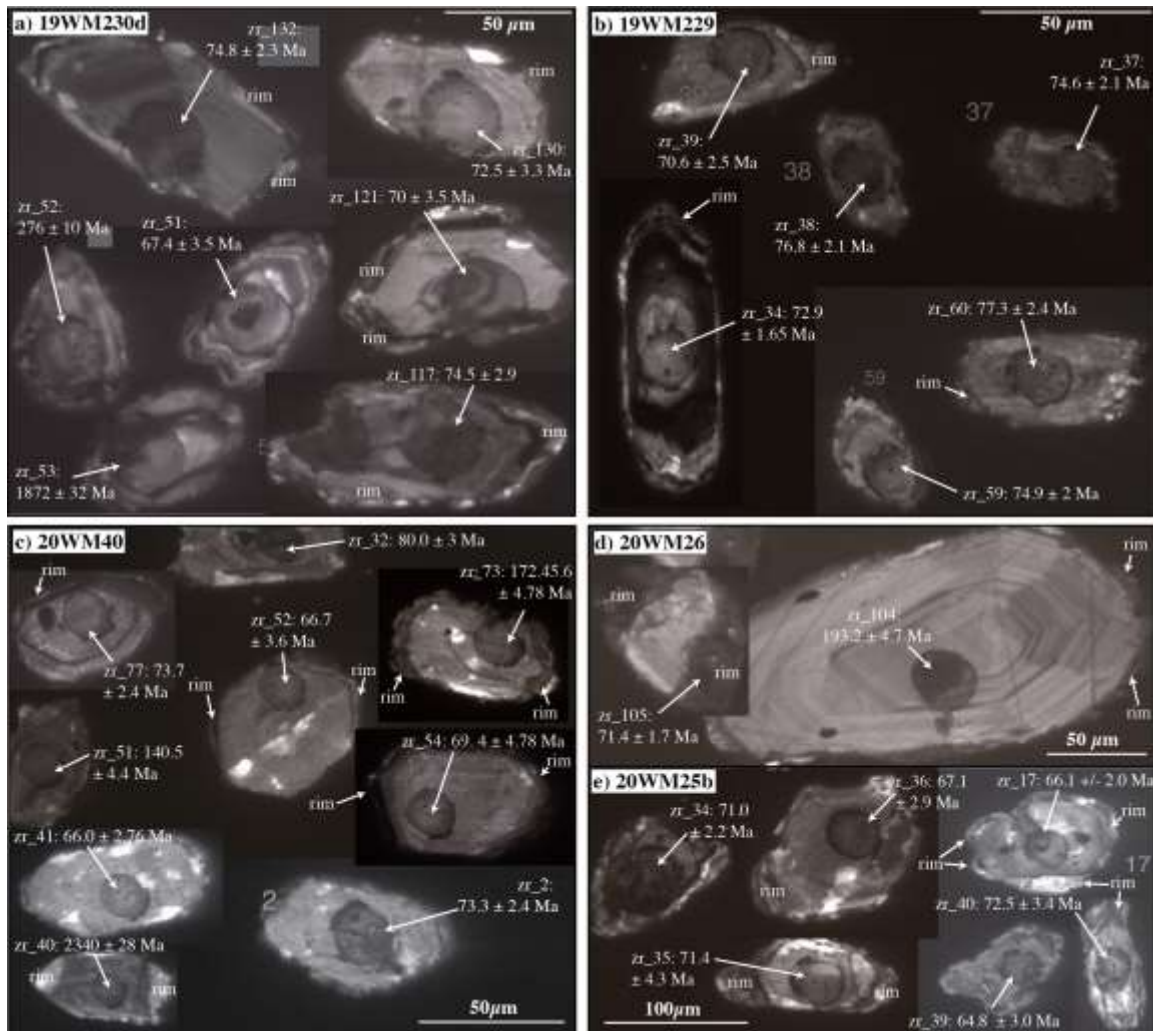


Figure 5.4. Representative cathodoluminescence (CL) images of detrital zircon grains from (a) 19WM230d, (b) 19WM229, (c) 20WM40, (d) 20WM26 & (e) 20WM25b. The location of the analysis pit and associated age with 2σ uncertainty is shown.

Based on the LA-MC-ICP-MS U-Pb dates, Hafnium-isotope geochemistry was determined for a subset of concordant zircon grains at the Pacific Centre for Isotope and Geochemical Research, University of British Columbia, Vancouver. Hafnium-isotopes were measured using a New Wave Research 193 nm laser ablation system paired with a Nu instruments Nu Plasma (NP021) MC-ICP-MS. A 35 μm spot was used for Hf analyses which was placed directly on the pre-existing, smaller U-Pb ablation pit. The laser fluence was $\sim 6 \text{ J/cm}^2$ with a repetition rate of 5 Hz, ablating a $\sim 30 \mu\text{m}$ deep pit. The ablated material was transported to the MC-ICP-MS via 0.9 L/min Ar sample gas

with a 0.950 L/min He carrier gas and mixed pre-plasma using a Y-piece 70 cm from the torch. The detection system consisted of a Faraday cup array which measured in static mode. Plešovice ($^{176}\text{Hf}/^{177}\text{Hf} = 0.282482 \pm 12$; Sláma *et al.*, 2008) was used as primary reference material and 91500 ($^{176}\text{Hf}/^{177}\text{Hf} = 0.282308 \pm 0.000006$; Blichert-Toft, 2008), FC1 ($^{176}\text{Hf}/^{177}\text{Hf} = 0.282183 \pm 12$; Fisher *et al.*, 2014), GJ1 ($^{176}\text{Hf}/^{177}\text{Hf} = 0.282000 \pm 0.000005$; Morel *et al.*, 2008) and Temora2 ($^{176}\text{Hf}/^{177}\text{Hf} = 0.282686 \pm 0.000024$; Woodhead *et al.*, 2004) used as secondary reference materials. Measured $^{176}\text{Hf}/^{177}\text{Hf}$ values for Plešovice were 0.282482 ± 0.000112 ($n = 43$) and for the secondary reference materials were: 0.282310 ± 0.000113 ($n = 21$), 0.282199 ± 0.000104 ($n = 21$), 0.282013 ± 0.000047 ($n = 1$) and 0.282664 ± 0.000113 ($n = 21$) respectively. $^{176}\text{Hf}/^{177}\text{Hf}$ ratios were normalized relative to Plešovice ($^{176}\text{Hf}/^{177}\text{Hf} = 0.282482 \pm 12$; Sláma *et al.*, 2008). Data reduction for internal standardization, interference correction, mass bias correction, isotopic determination, and uncertainty propagation was carried out using the Iolite software package (v.4) (Paton *et al.*, 2010, 2011). For the calculation of ϵ_{Hf} values and initial $^{176}\text{Hf}/^{177}\text{Hf}$ ratios we used the chondritic uniform reservoir (CHUR) Lu-Hf values of Bouvier *et al.* (2008) and the ^{176}Lu decay constant determination of Söderlund *et al.* (2004). All raw zircon Hf-isotope data and specific LA-MC-ICP-MS parameters for isotopic analyses can be found in supplemental Tables I1-3.

As all the zircon analysed within this study were extracted from samples that had experienced staurolite through upper-amphibolite/granulite grade metamorphism (Mezger *et al.*, 2001b; Israel *et al.*, 2011a; Chapter 3), we additionally screened analyses for evidence of metamorphic recrystallisation and/or lead loss. This was done by applying discordance filters, using zircon U/Th ratios, U contents and through observing post-ablation CL images to rule out analyses that had inadvertently partially clipped recrystallized domains from our detrital dataset (Figs. 5.4; see also section 5.5.1; e.g., Israel *et al.*, 2011a; Andersen *et al.*, 2019). However, within young metamorphic assemblages such as the Kluane Schist, any lead loss due to metamorphic recrystallisation and/or fluid alteration shortly after deposition can be difficult to ascertain because younger zircon populations (i.e., post-late Phanerozoic) whose $^{207}\text{Pb}/^{235}\text{U}$ error is large could still appear concordant (Ireland & Williams, 2003; Mezger & Krogstad, 2004; Spencer *et al.*, 2016; Andersen *et al.*, 2019). We therefore additionally consider the age of known metamorphic events and intrusions within the Kluane Schist to evaluate the significance of our youngest zircon populations in comparison to the

constraints provided by the surrounding geology. These include the well constrained age of the Ruby Range batholith which intrudes across the major foliation of the Kluane Schist between ca. 64–55 Ma (Fig. 5.3; Israel *et al.*, 2011a) and the age of Kluane Schist metamorphism as determined by monazite petrochronology (Fig. 5.3; ca. 70–55 Ma; Chapter 4).

5.3.2. Zircon U-Pb dating by Chemical Abrasion-Thermal Ionization Mass Spectrometry (CA-TIMS)

To increase the precision of our maximum depositional age calculations, CA-TIMS was additionally performed at UQAM Geotop labs on the youngest concordant grains analysed by LA-MC-ICP-MS (c.f., Vermeesch, 2021; Figs. C1–5). Analysed grains were extracted from the epoxy mount, and then washed in 7N nitric acid and ultra-sonically cleaned. Following this, the grains were chemically abraded (Mattinson, 2005; Widmann *et al.*, 2019) in a solution of 29N HF at 180°C for 12h, the grains were then fluxed on a hotplate in 6N HCl overnight before being ultra-sonically cleaned 4 times in 3N HNO₃. Grains were then loaded into teflon microcapsules in a solution of 29N HF, trace of HNO₃ and 2.5µL of ²⁰⁵Pb + ²³³U + ²³⁵U EARTHTIME tracer ET535 (Condon *et al.*, 2015; McLean *et al.*, 2015), the capsules were placed into a Parr digestion vessel and then into the oven for 48h at 210°C. Following dissolution, the samples were dried down on a hotplate and the fluoride salts were converted to chloride by fluxing in a Parr bomb in the oven at 180°C for 24h. The samples were then dried down again before being brought back into solution in 3N HCl for AG1X8 anion exchange separation of U and Pb from the rest of the zircon matrix. A modified version of the procedure of Krogh (1973) was used to separate U and Pb fractions, which were finally collected in pre-cleaned 7 ml Savillex beakers and dried with one drop of 0.04N H₃PO₄.

The U-Pb TIMS measurements were performed on a TRITON mass spectrometer. Each sample was loaded onto an outgassed Re-filament with one drop of silica gel emitter (modified from the Gerstenberger & Haase, 1997 recipe). Lead-isotopes were measured in dynamic mode on a MasCom secondary electron multiplier. Uranium-isotopes were analyzed as UO₂ in static mode on Faraday cups attached to 10¹³ ohm resistors using a ¹⁸O/¹⁶O ratio of 0.00205 which has been determined from

multiple measurements of U500. The mass fractionation for Pb was corrected using repeat measurements of SRM981 at the same running conditions as the samples. For uranium the in-run fractionation was corrected using a $^{233}\text{U}/^{235}\text{U}$ of 0.99506, and the uranium isotopic composition of the analyzed zircon was assumed to be $^{238}\text{U}/^{235}\text{U}$ of 137.818 ± 0.045 (2σ ; Hiess *et al.*, 2012). Uranium-lead data were reduced, and uncertainties were propagated using the Tripoli and U-Pb Redux software (Bowring *et al.*, 2011) which uses the algorithms of McLean *et al.* (2011). $^{238}\text{U}/^{206}\text{Pb}$ dates are reported with $[X]/[Y]/[Z]$ 2σ uncertainties (Schoene *et al.*, 2006), where X is the internal uncertainty, Y is tracer calibration error and Z includes both tracer calibration and decay constant uncertainties and are Th-corrected for initial Th/U disequilibrium using a partition coefficient relationship between the Th/U of the zircon and the Th/U ratio of magma from which zircon crystallized (e.g., Wotzlaw *et al.*, 2014). All common Pb was assumed to be procedural blank and was corrected according to the following long-term lab blank isotopic composition: $^{206}\text{Pb}/^{204}\text{Pb} = 18.102 \pm 0.23$, $^{207}\text{Pb}/^{204}\text{Pb} = 15.35 \pm 0.14$, $^{208}\text{Pb}/^{204}\text{Pb} = 38.01 \pm 0.55$ (all 1σ absolute errors). Analytical results are given in Table J1.

5.3.3. Data Presentation and Statistical Tests

We determine the potential source areas of the Kluane Schist by identifying distinctive populations of detrital zircon based on their U-Pb dates and Hf-isotope compositions. We present the distribution of our U-Pb data as both Kernel Density Estimate (KDE) and cumulative probability plots developed using the IsoplotR geochronology toolbox (Vermeesch, 2018a).

To both mitigate and further investigate potential issues related to zircon Pb loss via recrystallization and/or fluid alteration (see section 5.5.1), we have chosen to calculate the maximum depositional age (MDA) of each sample using 5 different methods: (1) the youngest graphical peak age which is calculated from the youngest mode in our KDE plot that contains 2 or more grains (YPP; Dickinson & Gehrels, 2009), (2) the weighted mean of the youngest cluster of 2 or more grains whose uncertainties overlap at 1σ (YGC1s; Dickinson & Gehrels, 2009), (3) the weighted mean of the youngest cluster of 3 or more grains whose uncertainties overlap at 2σ (YGC2s;

Dickinson & Gehrels, 2009), (4) the youngest statistical population (YSP) of Coutts *et al.*, (2019), and (5) the maximum likelihood age (MLA) method of Vermeesch (2021). We then test these MDA estimates against well-established geological relationships within and surrounding the Kluane Schist (i.e., MDA must be older than the cross-cutting Ruby Range batholith and metamorphism of the schist itself; e.g., Israel *et al.*, 2001a; Chapter 4).

The multidimensional scaling (MDS) function within the R package 'Provenance' (Vermeesch *et al.*, 2016) was used to assess the similarity between our Kluane Schist detrital zircon U-Pb dates and those recovered from other Jura-Cretaceous assemblages within the Northern Cordillera, including the Maclaren Schist and Clearwater metasediments of south-central Alaska, and the Dezadeash Formation and Blanchard River assemblage in southwest Yukon (c.f., Fig. 5.1 and 5.2). Specifically, we used the Kolmogorov-Smirnov (K-S) distance (test D statistic) and the Kuiper statistic to assess the dissimilarity between the single grain U-Pb age distribution of each sample. The non-parametric K-S and Kuiper tests are selected over standard parametric dissimilarity tests (e.g., t- or chi-squared tests) as they have been shown to be largely independent of sample size effects and do not require dataset pre-treatment (e.g., binning/averaging), which may introduce bias and a loss of dataset information (e.g., Vermeesch, 2018b). More complex dissimilarity measures that can account for both age distributions and their associated analytical uncertainties (e.g., likeness, cross-correlation; Satkoski *et al.*, 2013; Saylor *et al.*, 2016) may provide a more robust dataset comparison, however, the reproducibility of these dissimilarity tests has been questioned (e.g., Vermeesch, 2018b). Furthermore, as our comparison only considers U-Pb age distributions measured using the same analytical procedure (LA-MC-ICP-MS), the relative differences in analytical uncertainty are likely small and will have a negligible effect on our calculations (e.g., Vermeesch, 2018b). As such, for the purpose of this study, we consider the K-S and Kuiper tests to provide a valid measure of sample dissimilarity such that we can quantify the relative differences between the U-Pb age distribution of individual samples independent of their sample size or complexity (c.f., Vermeesch, 2013, 2018b).

5.4. Results

5.4.1. Detrital zircon U-Pb geochronology and Hafnium-isotope geochemistry

19WM230d & 19WM229; Northeast Kluane Schist: Samples 19WM230d and 19WM229, from the northeast region of the study area, represent two of the structurally highest units of the Kluane Schist (Fig. 5.2). Zircon grains from both samples are similar in appearance (Fig. 5.4a, b). Grains range in shape from prismatic to irregular and generally preserve oscillatory or sector zonation patterns (Fig. 5.4a, b). In the most irregularly shaped grains CL reveals a mottled internal texture (Fig. 5.4a, b). Rim domains with irregular internal textures are apparent in CL and occur across both samples (“rim” in Fig. 5.4a, b).

Sample 19WM230d ($n = 92$) shows prominent age populations at ca. 83 Ma ($n = 19$), ca. 109 Ma ($n = 29$) and ca. 197 Ma ($n = 15$) (Fig. 5.5a). The $\epsilon\text{Hf}(t)$ values for these populations range from -0.6 to +12.2 ($n = 13$), -8.0 to +17.9 ($n = 29$) and -1.1 to +9.2 ($n = 8$) respectively, with the majority of zircon showing $\epsilon\text{Hf}(t)$ values above the chondritic uniform reservoir (CHUR in Fig. 5.6a, b). Only the ca. 109 Ma population shows a significant contribution of evolved zircon with $\epsilon\text{Hf}(t)$ values dropping to -8.0 (Fig. 5.6b). 19WM230d shows a minor zircon population between ca. 290–250 Ma ($n = 3$), at ca. 346 Ma ($n = 2$) and between ca. 460–400 Ma ($n = 5$) (Fig. 4a). Scattered single Proterozoic grain ages occur between ca. 1085–600 Ma with varied $\epsilon\text{Hf}(t)$ values (Figs. 5.5a & 5.6a).

Sample 19WM229 ($n = 79$) shows a similar age distribution to 19WM230d with prominent Cretaceous and Jurassic populations at ca. 79 Ma ($n = 31$), ca. 102 Ma ($n = 9$), ca. 127 Ma ($n = 11$) and ca. 193 Ma ($n = 7$) (Fig. 5.5b). The $\epsilon\text{Hf}(t)$ values for these populations are -1.8 to +10.1 ($n = 17$), -1.25 to +11.9 ($n = 7$), -0.7 to +13.8 ($n = 7$) and -4.4 to +4.8 ($n = 5$) respectively (Fig. 5.6a, b). Across these prominent Cretaceous and Jurassic populations only 6 zircon show $\epsilon\text{Hf}(t) < 0$ (Fig. 5.6a, b). Minor Paleozoic populations occur between ca. 280–270 Ma ($n = 2$) and ca. 380–340 Ma, centred around

ca. 375 Ma ($n = 3$) (Fig. 5.5b). Scattered single Proterozoic grains occur between ca. 2093–730 Ma with varied $\epsilon\text{Hf}(t)$ values (Figs. 5.5b & 5.6a).

20WM40; West Kluane Schist: Our detrital zircon sample from the eastern shore of Kluane Lake represents the structurally lowest sample analysed in this study (Fig. 5.2). Zircon grains from 20WM40 are generally prismatic to subrounded with most grains preserving evidence for weak oscillatory or sector zoning (Fig. 5.4c). In some zircon their original internal growth textures are overprinted, giving them a saccharoidal appearance in CL (Fig. 5.4c). Distinct but irregularly developed rim domains are apparent in a few grains within sample 20WM40 (“rim” in Fig. 5.4c).

20WM40 ($n = 163$) shows significant age populations at ca. 79 Ma ($n = 38$), ca. 106 Ma ($n = 24$), ca. 160 Ma ($n = 17$) and ca. 182 Ma ($n = 24$) (Fig. 5.5c). The $\epsilon\text{Hf}(t)$ values for these populations are -11.0 to +14.6 ($n = 31$), -20.6 to +13.6 ($n = 21$), +3.3 to +13.3 ($n = 16$) and -38.3 to +14.6 ($n = 21$), respectively (Fig. 5.6a, c). Like the mid-Cretaceous population within the samples from the northeast Kluane Schist, the ca. 106 population in 20WM40 is the only Mesozoic population to show a significant abundance of zircon with $\epsilon\text{Hf}(t)$ values < -5 (Fig. 5.6c). The spread of $\epsilon\text{Hf}(t)$ values (~ -5 to +10; Fig. 5.6c) recorded by the Early Jurassic zircon population within 20WM40 also aligns well with similar aged populations in 19WM229 and 19WM230d (Fig. 5.6a, c). Minor populations occur at ca. 125 Ma ($n = 14$), between ca. 280–250 Ma ($n = 3$), ca. 338 Ma ($n = 6$) and ca. 368 Ma ($n = 10$) (Fig. 5.5c). These minor populations show a disparity in their $\epsilon\text{Hf}(t)$ value; the populations at ca. 125 Ma and between ca. 280–250 Ma largely return juvenile $\epsilon\text{Hf}(t)$ values ranging from +1.9 to +13.3 ($n = 12$) and +6.8 to +11.6 ($n = 2$), respectively whereas the zircon populations at ca. 338 Ma and ca. 368 Ma show more evolved $\epsilon\text{Hf}(t)$ values ranging from -24.0 to +2.4 ($n = 13$) (Fig. 5.6a). Two grains within the ca. 125 Ma population are more evolved with $\epsilon\text{Hf}(t)$ values of -5.5 and -13.5 (Fig. 5.6c). Scattered single grains return Proterozoic and Archean dates and varied $\epsilon\text{Hf}(t)$ values (Figs. 5.6a). A distinct age population at ca. 1090 Ma is characterized by more evolved $\epsilon\text{Hf}(t)$ values which range from -12.5 to +6.0 ($n = 6$) (Figs. 5.5c & 5.6a). The small ca. 2072 Ma age population shows $\epsilon\text{Hf}(t)$ values which range from +3.3 to +6.1 ($n = 3$) (Figs. 5.5c & 5.6a).

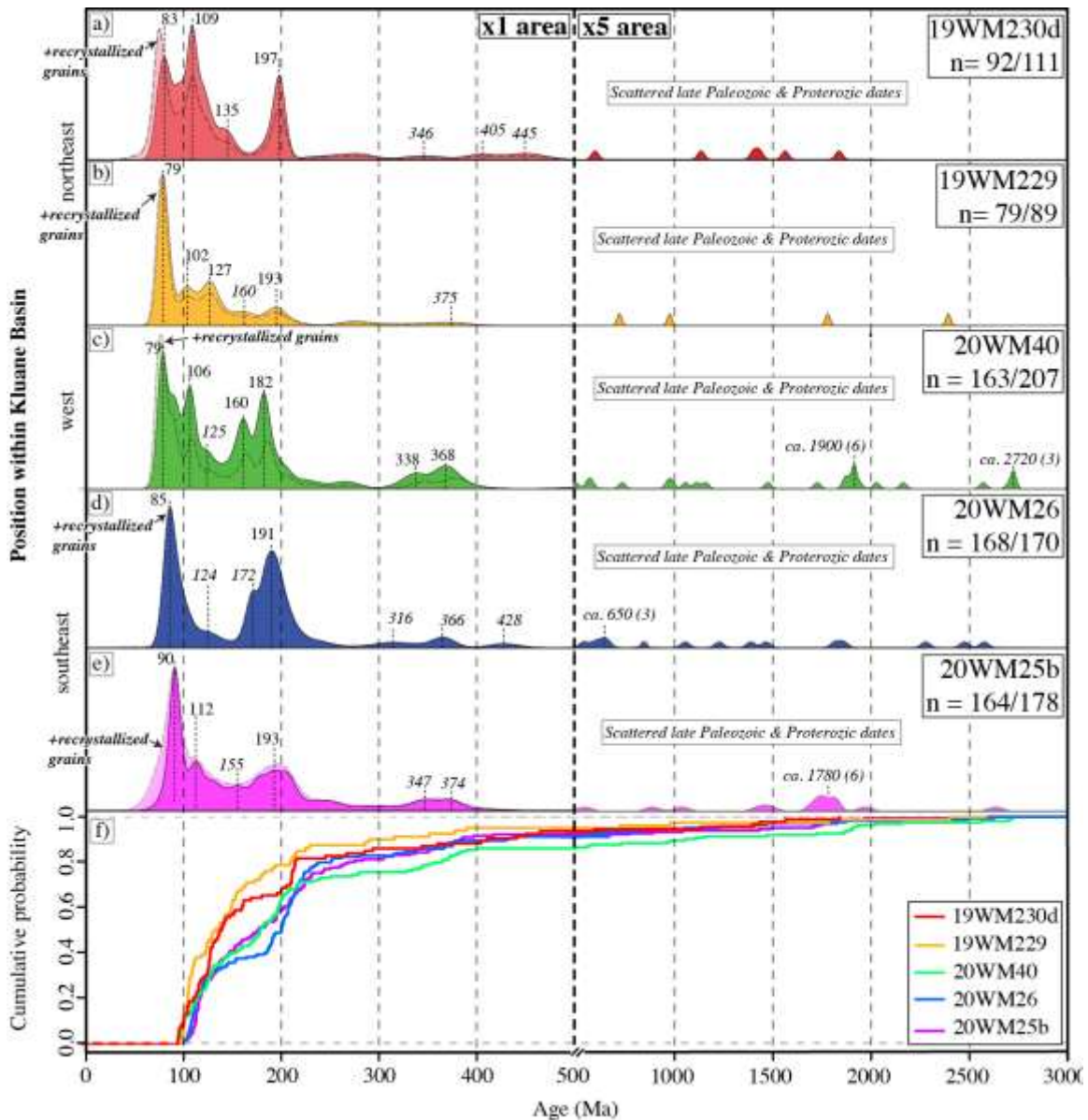


Figure 5.5. Kernel density estimate (KDE) plots of the ages of zircon across the Kluane Schist. (a) 19WM230d, (b) 19WM229, (c) 20WM40, (d) 20WM26, (e) 20WM25b. KDE plots outlined by dashed lines represent plots considering all zircon analyses, whereas KDE plots with solid outlines represent just detrital analyses (see main text sections 5.5.1 and 5.5.2 for full explanation). (f) Cumulative probability function including just detrital grains from all samples. In all plots note change in x-axis at 500 Ma. Precambrian ages are represented by x5 the area of Phanerozoic ages.

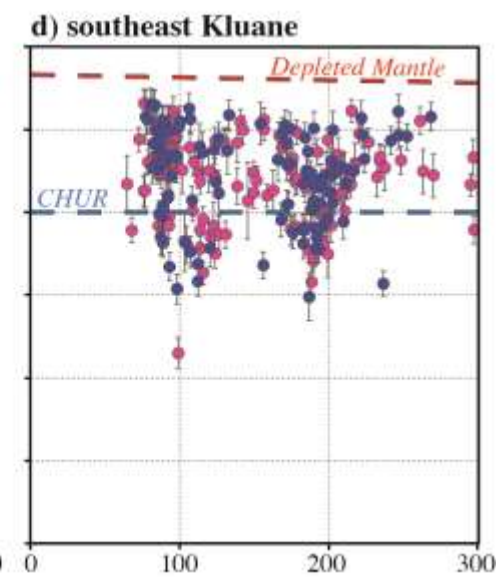
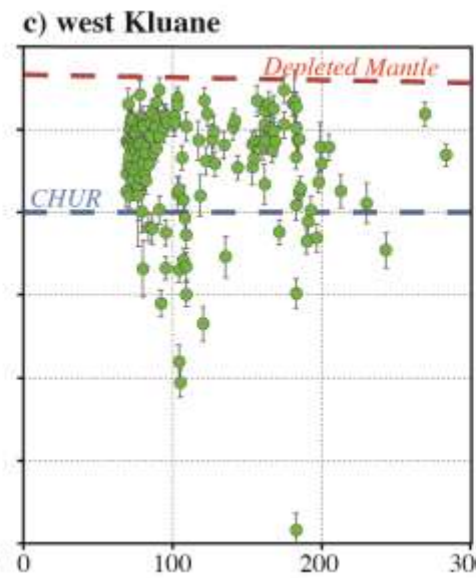
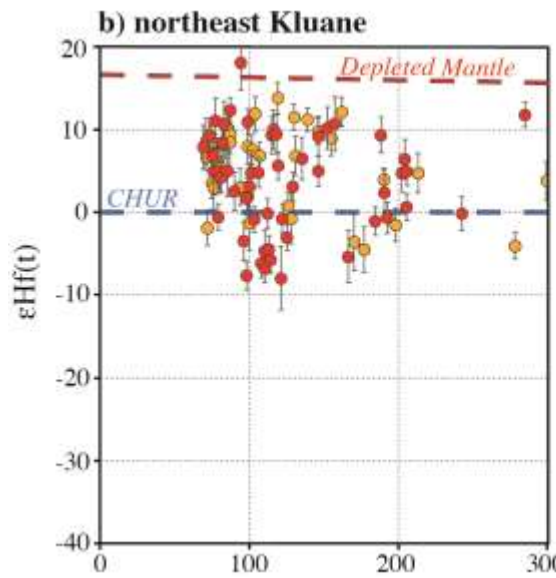
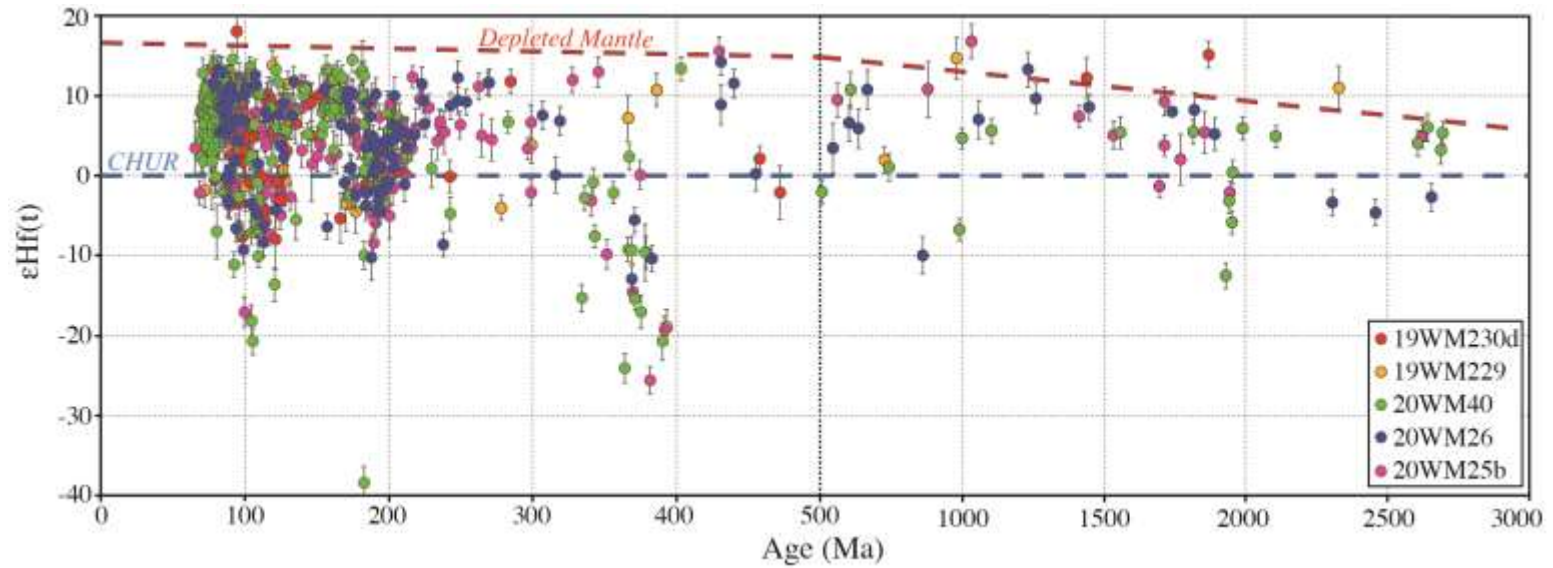


Figure 5.6. $\epsilon\text{Hf}(t)$ versus age plot across the Kluane Schist; colours as in Figure 5.5. All $\epsilon\text{Hf}(t)$ values are shown with 2σ uncertainties. (a) All Kluane Schist samples combined. Note change in x-axis at 500 Ma. Plots (b-d) show only grains with ages <300 Ma from (b) the northeast Kluane Schist, (c) west Kluane Schist and (d) southeast Kluane Schist (see Fig. 5.2). CHUR = chondritic uniform reservoir.

20WM26 & 20WM25; Southeast Kluane Schist: Samples 20WM26 and 20WM25b are from the southeast region of the Kluane Schist (Fig. 5.2). Detrital zircon from 20WM26 are mostly prismatic to subrounded with oscillatory or sector zoning (Fig. 5.4d). Few grains show dark, narrow, and homogenous rims that appear poorly developed (e.g., grain 105 in Fig. 5.4d). Grains from sample 20WM25b are prismatic to subrounded (Fig. 5.4e). Zircon grains generally preserve internal oscillatory or sector zonation, however, they can commonly be mottled with bright patches in CL (Fig. 5.4e). Rim domains are more apparent within 20WM25b than 20WM26, with these generally being dark, irregularly developed, and stubby (“rim” in Fig. 5.4d, e).

Both samples yield similar age distributions (Fig. 5.5d, e). As with the other Kluane Schist samples, 20WM26 ($n = 168$) shows significant Late Cretaceous (ca. 85 Ma; $n = 56$) and Early Jurassic (ca. 191 Ma; $n = 55$) age populations, however, it appears to lack the mid-Cretaceous peak common to all other samples (Fig. 5.5d). The $\epsilon\text{Hf}(t)$ values for the Late Cretaceous population range from -9.3 to +13.2 ($n = 44$). Generally, the younger zircon within this Late Cretaceous population are restricted to $\epsilon\text{Hf}(t)$ values of $> +5$ while the older portion of this population is more evolved with an abundance of zircon returning $\epsilon\text{Hf}(t)$ values ≤ -5 (Fig. 5.6d). This distribution of zircon $\epsilon\text{Hf}(t)$ values is like that of samples returning a distinct mid-Cretaceous population (Figs. 5.5 & 5.6; samples: 19WM229, 19WM230d, 20WM40, 20WM25b). The Early Jurassic population in 20WM26 is characterized by a spread of $\epsilon\text{Hf}(t)$ values between -10.2 to +11.5 ($n = 41$; Fig. 5.6d), the majority of which occur between ~ -5 to +10 (Fig. 5.6d). Minor Mesozoic age populations occur at ca. 124 Ma ($n = 10$) and ca. 172 Ma ($n = 14$) and return $\epsilon\text{Hf}(t)$ values of -8.3 to +11.8 ($n = 10$) and -6.3 to +10.8 ($n = 13$) respectively (Figs. 5.5d & 5.6d). Minor Paleozoic peaks in 20WM26 occur at ca. 316 Ma ($n = 5$), ca. 366 Ma ($n = 6$) and ca. 428 Ma ($n = 4$) (Fig. 5.5d). $\epsilon\text{Hf}(t)$ values for these minor populations are +0.1 to +7.6 ($n = 3$), -12.9 to -5.5 ($n = 3$) and +0.3 to +14.2 ($n = 4$) respectively (Fig. 5.6a). Scattered single grains return Proterozoic and Archean dates and varied $\epsilon\text{Hf}(t)$ values; in

general, zircon return evolved Hf-isotopic signatures prior to 2000 Ma and more juvenile signatures after (Fig. 5.6a). A small Neoproterozoic peak centred around ca. 605 Ma ($n = 3$) consists of juvenile zircon with $\epsilon\text{Hf}(t)$ values between +6.0 to +10.8 ($n = 3$; Figs. 5.5d & 5.6a).

Sample 20WM25b ($n = 164$) yields detrital zircon populations at ca. 90 Ma ($n = 51$), ca. 112 Ma ($n = 12$) and ca. 193 Ma ($n = 38$) which return a range of $\epsilon\text{Hf}(t)$ values that align well with our other Kluane Schist samples (-17.1 to +13.2; $n = 41$, -7.4 to +8.6; $n = 12$, and -8.5 to +12.3; $n = 11$, respectively; Fig. 5.5e & 5.6a, d). A minor Late Jurassic population occurs at ca. 155 Ma ($n = 6$) with exclusively juvenile $\epsilon\text{Hf}(t)$ values between +2.0 to +11.2 ($n = 6$) (Figs. 5.5e & 5.6d). Paleozoic populations occur between ca. 270–240 Ma ($n = 6$) and ca. 374–347 Ma ($n = 12$), returning $\epsilon\text{Hf}(t)$ values of +4.5 to +11.1 ($n = 4$) and -25.6 to +12.9 ($n = 9$) respectively (Figs. 5.5e & 5.6a, d). Scattered single grains return Proterozoic and Archean dates with $\epsilon\text{Hf}(t)$ values generally $\geq +5$ (Fig. 5.6a). A distinct minor population at ca. 1078 Ma ($n = 6$; Fig. 5.5e) consists of zircon with $\epsilon\text{Hf}(t)$ values between -1.3 and +9.3 ($n = 5$; Fig. 5.6a).

5.4.2. CA-TIMS U-Pb geochronology

CA-TIMS analysis was performed on thirteen grains. One of two grains analysed from sample 19WM230d produced a concordant date of 66.76 ± 0.35 Ma (Fig. 5.7a). The second grain from this sample produced a discordant date (Fig. 5.7a). Three grains from sample 20WM25b produce two concordant dates of 65.06 ± 0.36 Ma and 73.23 ± 0.09 Ma (Fig. 5.7a). A single grain analysed from sample 20WM26 produced a concordant date of 54.51 ± 0.1 Ma (Fig. 5.7a). Three grains from sample 20WM40 produced a discordant date and two concordant dates of 60.36 ± 0.33 Ma and 61.51 ± 0.08 Ma (Fig. 5.7b). Four grains analysed from sample 19WM229 produce three concordant single grain ages between 66.34 and 68.50 Ma (Fig. 5.7b). In general, we observe that TIMS dates are consistently younger than those returned by LA-MC-ICP-MS when the age of the same grain is compared (Fig. 5.7 insert). Commonly these ages are statistically separable from one another (Fig. 5.7).

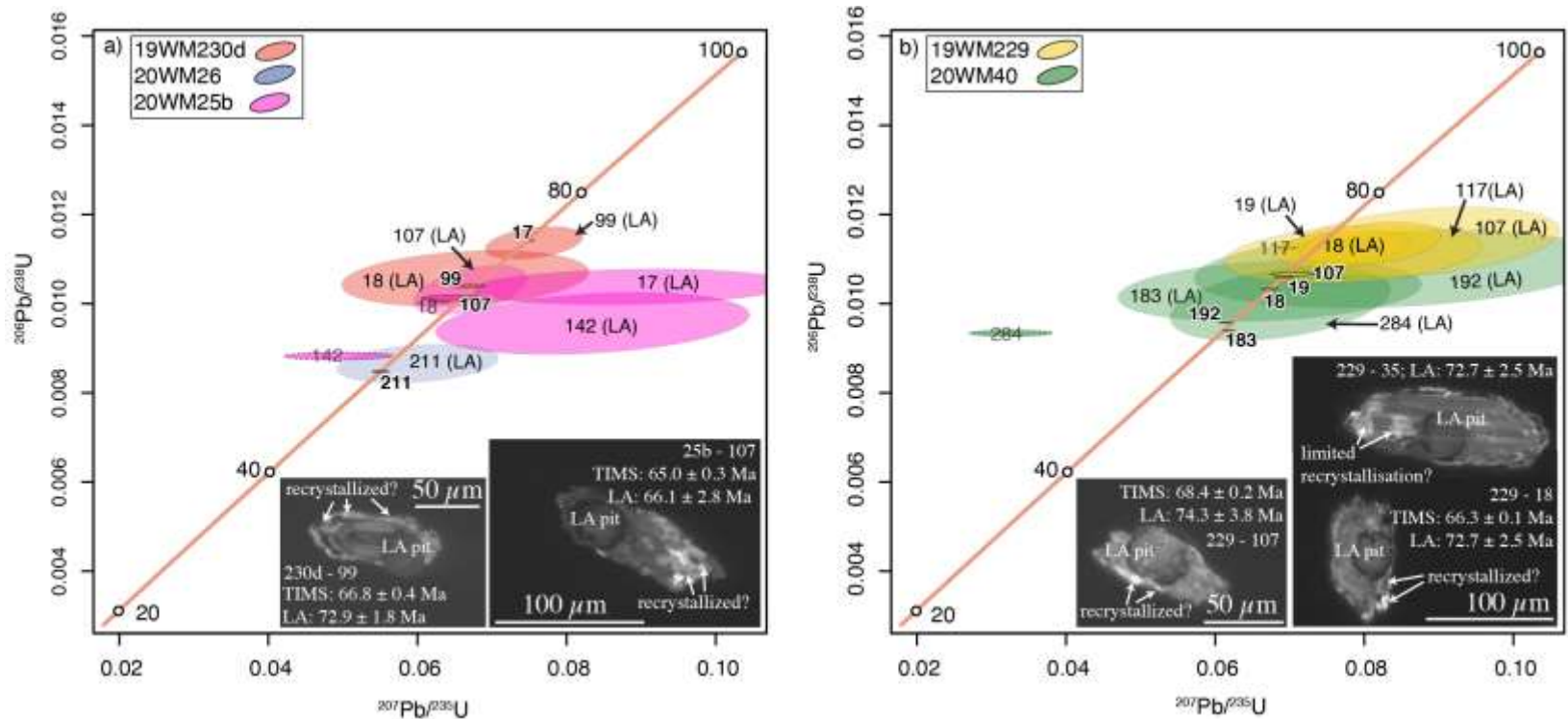


Figure 5.7. The results of Chemical Abrasion-Thermal Ionization Mass Spectrometry (CA-TIMS) completed on a subset of the youngest zircon grains across the Kluane Schist. U-Pb concordia plots summarize both laser-ablation, multi-collector, inductively coupled plasma mass spectrometry (LA-MC-ICP-MS; “(LA)”) and CA-TIMS dates (bold; black outline around the ellipse) when completed on the same grain (2σ uncertainty) (note: ellipse labels also indicate the zircon number for that sample). (a) Samples 19WM230d, 20WM40 and 20WM25b and (b) 19WM229 and 20WM40. Insert grain examples present a direct comparison of the LA-MC-ICP-MS (LA) and CA-TIMS dates, with 2σ uncertainty, returned from each individual grain. CA-TIMS dates are commonly younger than, and in cases statistically separable from, the laser ablation dates from the same grains (see main text, section 5.5.1 for full explanation).

5.5. Discussion

5.5.1. Evidence for partial zircon recrystallization

A portion of the zircon from all samples analysed by both LA-MC-ICP-MS and CA-TIMS return concordant dates that are younger than the age of Kluane Schist metamorphism and the Ruby Range batholith (Figs. 5.3 & 5.7; Table H5; Israel *et al.*, 2011a; Chapter 4). Zircon cores that return these young dates all show evidence for partial recrystallization and the mottling of their original internal growth textures in CL (e.g., grains 41 and 52 in sample 20WM40 Fig. 5.4c; grains 36 and 39 in 20WM25b, Fig. 5.4e & all grains in insert of Fig. 5.7). This contrasts with core domains of zircon that return older dates, which typically preserve original internal zoning structures (oscillatory, sector, diffuse; e.g., grain 132 in 19WM230d, Fig. 5.4a; grain 60 in 19WM229, Fig. 5.4b; grain 26 in 20WM40, Fig. 5.4c & grain 104 in 20WM26, Fig. 5.4d). Zircon which show evidence for rim growth also typically produces ages <70 Ma when analysed by CA-TIMS or when these rims are hit by LA-MC-ICP-MS spots (Fig. 5.7 inserts). This partial recrystallization of zircon may also explain the difference between our LA-MC-ICP-MS and TIMS dates (Fig. 5.7); TIMS dates are routinely younger, and often statistically separable from, their equivalent LA-MC-ICP-MS spot date except in one case (20WM25b, grain 17; Fig. 5.4e & 5.7a) where the LA-MC-ICP-MS spot was almost entirely within a recrystallized domain (Fig. 5.4e & 5.7). By volume, the TIMS analyses would have incorporated more of the recrystallized domains in the zircon grains that were analysed versus the LA-MC-ICP-MS spots that may have inadvertently clipped a recrystallized domain.

In general, we do not observe a trend in the abundance of recrystallized grains when compared against structural level, metamorphic grade, or geographic location across the Kluane Schist (c.f., Figs. 5.2 & 5.5; Table H5). Within the next sections (provenance analysis and MDA calculations) we remove zircon with evident partial recrystallization from our detrital dataset (c.f., Table H5).

5.5.2. Provenance of the Kluane Schist

After removing analyses that have been affected by recrystallization, all our samples produce similar detrital zircon spectra; there are no significant or systematic variations with structural level, metamorphic grade, or geographic position across the Kluane Schist (Figs. 5.2 & 5.5). Considering this similarity and the improved reliability of provenance determination with high-n datasets (e.g., Vermeesch, 2004; Gehrels, 2014; Sharman & Malkowski, 2020) we combine our Kluane Schist samples to consider a single dataset for provenance analysis (U-Pb age, $n = 666$; Hafnium-isotope determinations, $n = 568$; Fig. 5.8). Additionally, our provenance analysis of the Kluane Schist recognises a potential ~480 km of post-depositional dextral transport along the Denali fault (see section 5.2; Waldien *et al.*, 2021b).

Detrital zircon analysed across the Kluane Schist are predominately Mesozoic in age (~80%; Table H6). Late Cretaceous zircon (ca. 95–75 Ma) contribute the most significant population recorded by all samples and are characterized by a cluster of juvenile $\epsilon\text{Hf}(t)$ values between ~ +5 to +12 (Fig. 5.8). A similar distribution of Late Cretaceous U-Pb age and $\epsilon\text{Hf}(t)$ values are determined for detrital zircon recovered from the Upper Matanuska Formation in south-central Alaska, which is considered to represent part of the forearc that was deposited along the outboard margin of the Insular terranes prior to and during their Mesozoic accretion (MF; Fig. 5.8a & 5.9a; Reid *et al.*, 2018). This could suggest the Kluane Schist, like the Upper Matanuska Formation, may source its Late Cretaceous zircon from a ca. 90–68 Ma intrusive suite within the Talkeetna Mountains (mlK in Fig. 5.9a; Stevens-Goddard *et al.*, 2018). Recent U-Pb geochronology and Lu-Hf isotope geochemistry of zircon recovered from coeval granitoids within the central Talkeetna Range produces juvenile $\epsilon\text{Hf}(t)$ values that overlap with those produced by both our Kluane Schist samples and the Upper Matanuska Formation (green star in Fig. 5.8a; Todd *et al.*, 2017).

Equally, the ca. 100–50 Ma intrusive suite within the Coast Plutonic Complex of southern Alaska and British Columbia (Gehrels *et al.*, 2009; Cecil *et al.*, 2011) could act as a source of Late Cretaceous zircon to the Kluane Schist. Zircon analysed from ca. 100–50 Ma plutons across the Coast Plutonic Complex of southern Alaska and British Columbia produce a varied distribution of $\epsilon\text{Hf}(t)$ values (~ +2 to +13; Cecil *et al.*, 2011; Fig. 5.8a) that largely encompass the range of $\epsilon\text{Hf}(t)$ values returned from the Late

Cretaceous zircon population recovered from the Kluane Schist (Fig. 5.8a). Further, the ca. 95–75 Ma zircon population collected from the Kluane Schist coincides well with the high flux of magmatism documented within the northern portions of the Coast Plutonic Complex from ca. 100–80 Ma (Gehrels *et al.*, 2009; Cecil *et al.*, 2011). Of note, the timing of high-flux magmatism within the Coast Plutonic Complex appears to vary along strike, suggesting it is influenced by local factors such as the timing and style of upper plate deformation, the variability in forearc/wedge materials, or the accretion of small terrane fragments (Gehrels *et al.*, 2009; Cecil *et al.*, 2018). As such this high flux of magmatism from ca. 100–80 Ma may record crustal thickening in response to the accretion of the Insular terranes within the northern regions of the Cordillera (e.g., Gehrels *et al.*, 2009). In turn, this suggests the possible emergence of an active continental arc in proximity to the Kluane Basin during Kluane Schist deposition, with the alignment in the range of $\epsilon_{\text{Hf}}(t)$ values returned from the Coast Plutonic Complex providing evidence for the direct shedding of zircon from this active arc into the Kluane Basin (Fig. 5.8a).

Further potential sources for Late Cretaceous zircon occur throughout southwest Yukon (Fig. 5.9b). These include the Casino suite (Fig. 5.9b; ca. 79–74 Ma; Selby *et al.*, 1999; Friend, 2022), the Rancheria suite (ca. 82–77 Ma; Morris & Creaser, 2008; Rasmussen, 2013), the Carmacks Group (ca. 72–65; Grond *et al.*, 1984; Lowey *et al.*, 1986; Joyce *et al.*, 2015), and the Prospector Mountain suite (ca. 72–68 Ma; Allen *et al.*, 2013; Friend, 2022). Unfortunately, no Hf-isotope datasets are available from these units for comparison. However, whole rock $\epsilon_{\text{Nd}}(t)$ values from the Casino suite ($\epsilon_{\text{Nd}}(t) \sim -6$ to $+3$; Selby *et al.*, 1999; Bineli-Betsi *et al.*, 2012; Friend, 2022), the Prospector Mountain suite ($\epsilon_{\text{Nd}}(t) \sim -1$ to $+2$; Selby *et al.*, 1999; Friend, 2022; Sack, unpublished data), Rancheria suite ($\epsilon_{\text{Nd}}(t) \sim -15$ to $+3$; Morris & Creaser, 2008; Rasmussen, 2013; Sack, unpublished data), and the Carmacks Group ($\epsilon_{\text{Nd}}(t) \sim +2$; Sack, unpublished data), converted to Hf-equivalent using the method of Vervoort *et al.* (2011), produce $\epsilon_{\text{Hf}}(t)$ values between ~ -17 to $+8$ (Fig. 5.8a). These values largely align with the range of Hf-isotope compositions ($\epsilon_{\text{Hf}}(t) \sim -5$ to $+12$; Fig. 5.8a) determined from the Late Cretaceous zircon population within the Kluane Schist (Fig. 5.8a).

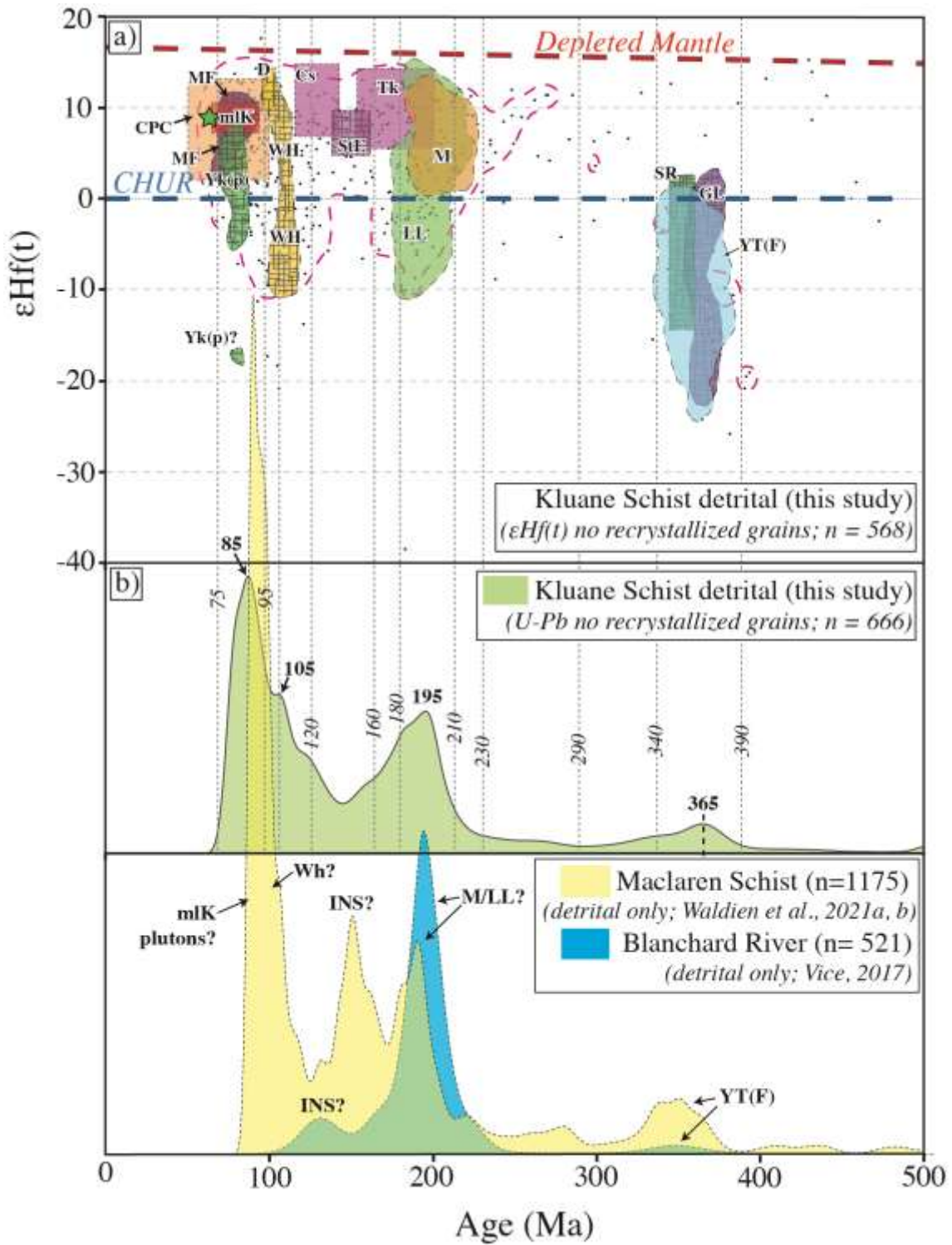


Figure 5.8. (a) Contoured $\epsilon\text{Hf}(t)$ data versus age for detrital zircon analyses (all grains < 500 Ma) across the Kluane Schist. Pink dashed line reflects 95th percentile contour. We overlay the age and $\epsilon\text{Hf}(t)$ values of potential Kluane Schist zircon sources (see main text, sections 5.2 and 5.5.2 for full explanation and data sources). MF = Upper Matanuska Formation; mlK = mid-Late Cretaceous plutons in the southern Talkeetna Mountains; CPC = Coast Plutonic Complex (ca. 100–50 Ma); Yk(p) = Late Cretaceous plutons in Yukon including Casino suite, Prospector Mountain suite, Carmacks Group, Rancheria suite; WH = Whitehorse suite; D = Dawson Range Batholith; Cs = Chisana Formation; Tk = Talkeetna Arc; StE = St. Elias plutonic suite; LL = Long Lake; M = Minto; SR = Simpson Range suite; GL = Grass Lakes suite; YT(F) = Yukon-Tanana (Finlayson) (see also Fig. 5.9). Note where overlays have a hachure pattern $\epsilon\text{Hf}(t)$ values are calculated from whole rock $\epsilon\text{Nd}(t)$ values using the method of Vervoort *et al.*, (2011). Plot developed using the HafniumPlotter routine of Sundell *et al.*, (2019). CHUR = Chondritic Uniform Reservoir. (b) Kernel density estimate (KDE) plots showing all detrital zircon ages across the Kluane Schist (this study) in comparison to all Phanerozoic detrital zircon ages from the Maclaren Schist (Yellow, Waldien *et al.*, 2021a, b) and the Blanchard River assemblage (Blue, Vice, 2017).

From data currently available it is challenging to tie the Late Cretaceous population within the Kluane Schist to a single source region (c.f., Fig. 5.8a). The overlap in ages between the detrital zircon recovered from the Upper Matanuska Formation and the Kluane Schist (Fig. 5.8a) highlights a potential source as the ca. 90–68 Ma intrusive suite within the Talkeetna Mountains (mlK in Fig. 5.9a; Stevens-Goddard *et al.*, 2018). Equally, the ca. 100–50 Ma intrusive suite within the Coast Plutonic Complex of southern Alaska and British Columbia (Gehrels *et al.*, 2009; Cecil *et al.*, 2011) shows a good match with our Kluane Schist data (Fig. 5.8a). However, neither of these sources alone can account for the Late Cretaceous evolved zircon ($\epsilon\text{Hf}(t) < 0$) recovered from the Kluane Schist (Fig. 5.8a). Clear overlap is also observed between converted whole rock whole rock $\epsilon\text{Nd}(t)$ values from Late Cretaceous plutons within southwest Yukon and the Late Cretaceous zircon population within the Kluane Schist (Fig. 5.8a; e.g., Casino, Rancheria, Prospector Mountain, Carmacks Group). These Late Cretaceous plutons could potentially also account for the evolved ($\epsilon\text{Hf}(t) < 0$) Late Cretaceous zircon recovered from the Kluane Schist (Fig. 5.8a). However, due to a lack of Hf-isotope datasets for these units, a potential inboard Intermontane-bound source cannot be definitively identified (or ruled out).

The next significant zircon population recorded in the Kluane Schist occurs in the mid-Cretaceous (ca. 110–100 Ma) and is characterized by zircon which have a significantly wider range of juvenile to evolved $\epsilon\text{Hf}(t)$ values (~ -10 to $+12$; Fig. 5.8a). During this time, widespread magmatism is recorded across the southern Yukon-Tanana terrane with the intrusion of the ca. 112–98 Ma Whitehorse suite providing multiple source areas for mid-Cretaceous zircon within ~ 100 km of the Kluane Schist, particularly to its north and west (Whitehorse “Wh” & Dawson Range Batholith “Wh(D)” in Fig. 5.9b; e.g., Selby *et al.*, 1999; Morris & Creaser, 2008). The $\epsilon\text{Nd}(t)$ values from the Whitehorse suite (e.g., Selby *et al.*, 1999; Morris & Creaser, 2008), converted to Hf-equivalent using the method of Vervoort *et al.* (2011), produce a range of $\epsilon\text{Hf}(t)$ values that align well with those produced by our mid-Cretaceous zircon population (Fig. 5.8a). The alignment in both age and isotopic signature along with the increased abundance of mid-Cretaceous zircon within the northern and western regions of the Kluane Schist (ca. 110–100 Ma peak heights in Figs. 5.5a-c vs. 5.5d-e) provides evidence that the mid-Cretaceous population within the Kluane Schist was sourced from proximal intrusions within the Yukon-Tanana terrane (Figs. 5.8 & 5.9b).

The last significant contribution of Mesozoic zircon recorded by all our Kluane Schist samples show ages between the Late Triassic to Early Jurassic (ca. 210–180 Ma; Fig. 5.8a). This population shows a range of ages and $\epsilon\text{Hf}(t)$ values (ca. 210–180 Ma and $\epsilon\text{Hf}(t) \sim -10$ to $+10$; Fig. 5.8a) that are well matched with those known for intrusive suites within southern Yukon including the Long Lake and Minto suites (Figs. 5.8a & 5.9b; e.g., Sack *et al.*, 2020; Colpron *et al.*, 2022). Late Triassic to Early Jurassic U-Pb zircon ages are also common to Talkeetna arc rocks from the Chugach Mountains (Fig. 5.9a), however, these rocks display a more restricted range of juvenile isotopic signatures which are poorly matched with our Kluane samples (Fig. 5.8; e.g., Rioux *et al.*, 2007).

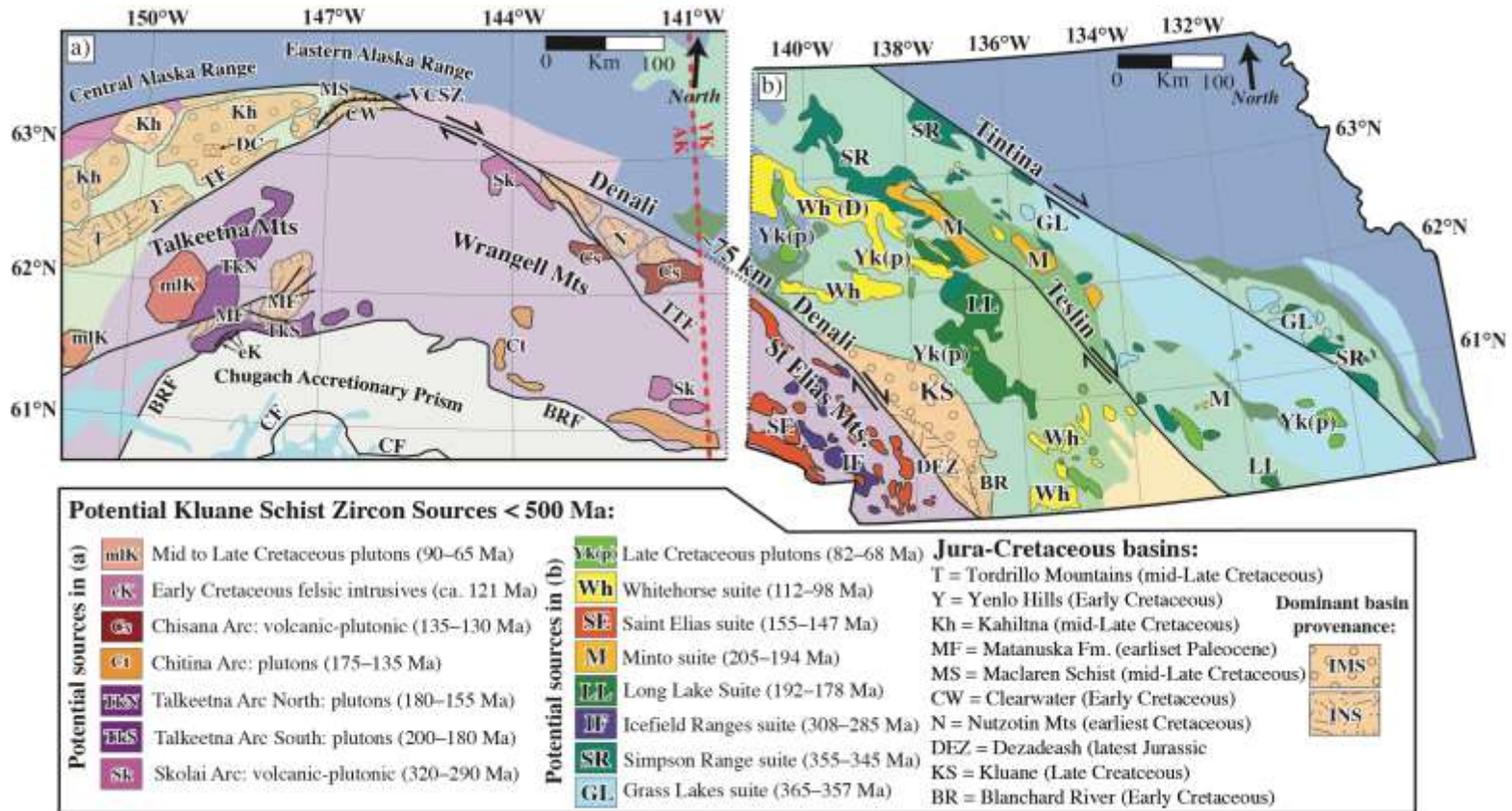


Figure 5.9. Maps highlighting the location of potential sources of Kluane Schist zircon each side of the Denali fault (adapted from: Colpron *et al.*, 2016; Stevens Goddard *et al.*, 2018; Fasulo *et al.*, 2020; all ages reported are zircon U-Pb). Note the omission of ~75 km between panels (a) and (b). Underlying terrane maps are not labelled but coloured the same as in Fig. 5.1 (i.e., after: Colpron & Nelson, 2011). (a) Potential sources in south-central Alaska and (b) in Yukon (see also Fig. 5.6). In both maps Jura-Cretaceous basins are highlighted and patterned for their dominant provenance (see Fig. 5.3 and main text section 5.5.2 for explanation and references). DC = Devil Creek area of Davidson & McPhillips (2007).

Minor contribution from Paleozoic (~11%; Table H6) sources is apparent across all our Kluane Schist samples with the most significant being from Late Devonian to Carboniferous zircon (ca. 390–340 Ma). These Late Devonian to Carboniferous zircon record progressively more juvenile Hf-isotope signatures moving from the Late Devonian into the Carboniferous (Figs. 5.5a & 5.7a). This distinct “pull-up” from strongly negative $\epsilon_{\text{Hf}}(t)$ values (~ -20) within the Devonian to more juvenile $\epsilon_{\text{Hf}}(t)$ values (~ 0) in the Carboniferous shows a noticeable overlap with the detrital zircon recovered from the Finlayson and Klinkit assemblages of the Yukon-Tanana terrane (YT(F) in Fig. 5.8a; Kroeger *et al.*, 2023). This suggests the recycling of zircon from the overlying Yukon-Tanana terrane including the Late Devonian to Mississippian Grass Lakes suite, Simpson Range suite and the Finlayson assemblage (Fig. 5.8a & 5.9; e.g., Grass Lakes suite; age and converted $\epsilon_{\text{Nd}}(t)$ from: Manor *et al.*, 2022; Simpson Range suite; converted $\epsilon_{\text{Nd}}(t)$ from: Piercey *et al.*, 2003, 2006; age from: Mortensen, 1992; Colpron *et al.*, 2006).

Approximately 9% of grains analysed within our samples return Precambrian dates (Table H6). The ubiquitous presence of Precambrian grains across all our samples generally implies recycling of zircon from basement sources such as regions of the Yukon-Tanana terrane (e.g., Snowcap assemblage) and parts of the Laurentian craton (Figs. 5.5 & 5.6; Piercey & Colpron, 2009; Gehrels & Pecha, 2014; Pecha *et al.*, 2016; Parsons *et al.*, 2022).

Previous detrital zircon geochronology completed across the Kluane Schist has suggested its derivation primarily from inboard sources (e.g., Yukon-Tanana; Israel *et al.*, 2011a; Stanley, 2012). Although these datasets comprise a low number of analyses (Israel *et al.*, 2011a, n = 71; Stanley, 2012; n < 50), the combined detrital zircon dataset of the Kluane Schist (n = 666; Fig. 5.8a) presented in this study supports these previous studies and identifies the paleo-western margin of North America as being a major source of zircon to the Kluane Schist (Fig. 5.8a; e.g., Coast Plutonic Complex, Whitehorse suite, Minto suite, Long Lake suite, Yukon-Tanana terrane). However, potential sourcing from a suite of Late Cretaceous plutons within the Talkeetna Mountains (mLK in Figs. 5.8a & 5.9a; Reid *et al.*, 2018; Stevens-Goddard *et al.*, 2018) also provides evidence for the Kluane Schist possibly having source areas within the outboard Insular terranes. Conversely, a clear overlap is observed between the whole

rock $\epsilon\text{Nd}(t)$ values determined for Late Cretaceous plutonic suites within southern Yukon (e.g., Casino, Rancheria, Prospector Mountain, Carmacks Group) and the Late Cretaceous detrital zircon population returned from the Kluane Schist (e.g., Fig. 5.8a). However, a lack of Hafnium-isotope determinations of zircon recovered from these Late Cretaceous plutons makes it challenging to conclude if they represent a unique source for the restricted, juvenile, Late Cretaceous zircon population recovered from the Kluane Schist (Fig. 5.8a).

Our combined U-Pb age and $\epsilon\text{Hf}(t)$ results imply the protolith of the Kluane Schist was primarily derived from inboard (i.e., Intermontane/North American margin) sources. Limited evidence for a unique outboard (i.e., Insular) source is consistent with the Kluane Schist having been deposited on the paleo-western margin of North America (i.e., Yukon-Tanana terrane; e.g., Israel *et al.*, 2011a). This interpretation is further supported by the lack of a significant contribution from Late Jurassic to Early Cretaceous zircon across all Kluane Schist samples (ca. 160–120 Ma; Figs. 5.5 & 5.8a) in comparison to the widespread Late Jurassic to Early Cretaceous magmatism recorded within the Insular terranes (Fig. 5.9a; St. Elias plutonic suite; Beranek *et al.*, 2017; Talkeetna, Chitina & Chisana arcs; Plafker *et al.*, 1989; Rioux *et al.*, 2007; Day *et al.*, 2016; Manselle *et al.*, 2020). That said, the limited Late Jurassic to Early Cretaceous zircon (ca. 160–120 Ma) recovered from the Kluane Schist do show $\epsilon\text{Hf}(t)$ values (~ 0 to $+13$; Fig. 5.8a) that align with Insular derived sources (Fig. 5.8a).

5.5.3. Maximum depositional age (MDA) for the Kluane Schist

In this study we calculate MDA using 5 different methods (see section 5.3.3): (1) the youngest graphical peak age which is calculated from the youngest mode in our KDE plot that contains 2 or more grains (YPP; Fig. 5.10a and Table H5; Dickinson & Gehrels, 2009), (2) the weighted mean of the youngest cluster of 2 or more grains whose uncertainties overlap at 1σ (YGC1s; Fig. 5.10b and Table H5; Dickinson & Gehrels, 2009), (3) the weighted mean of the youngest cluster of 3 or more grains whose uncertainties overlap at 2σ (YGC2s; Fig. 5.10b and Table H5; Dickinson & Gehrels, 2009), (4) the youngest statistical population (YSP; Fig. 5.10b and Table H5) of Coutts *et al.*, (2019), and (5) the maximum likelihood age (MLA; Fig. 5.10b, C11 and Table H5)

method of Vermeesch (2021). These 5 methods are chosen as they include a subset of the most widely applied methodologies (YPP, YGC2s, YGC1s; e.g., Dickinson & Gehrels, 2009; Coutts *et al.*, 2019) and have been shown to produce reasonably accurate MDA values in scenarios where the abundance of near depositional aged zircon is high, while not imposing a negative bias on the calculation (Coutts *et al.*, 2019; Vermeesch, 2021). This is an important consideration because of the potential younging bias zircon recrystallization may introduce to our depositional age estimates (see above, section 5.5.1).

Previously a mid-Late Cretaceous MDA for the Kluane Schist had been suggested based on the youngest detrital zircon populations returned from two samples, after stripping away any dates inferred to be the result of metamorphism or later alteration (Fig. 5.3; ca. 94 Ma, Israel *et al.*, 2011a). Israel *et al.* (2011a) noted these metamorphic zircon as dark overgrowths in CL within their Kluane Schist samples that are characterized by high U/Th ratios ($\gg 10$; [U] = 879–8129 ppm & [Th] = 4–88 ppm; Israel *et al.*, 2011a). These overgrowths contrast to the lower U and higher Th contents typical of detrital zircon cores (Israel *et al.*, 2011a). Across all of our Kluane Schist samples the majority of zircon comprising our youngest age population (ca. 85 Ma; e.g., Figs. 5.5 & 5.8) returns a U/Th ratio < 10 with limited variation between this younger population and older detrital grains (Fig. 5.10c). The few zircon which do return higher U/Th ratios (i.e., $\geq \sim 50$; Fig. 5.10c) are largely represented by the recrystallized fraction which was removed during our MDA calculations (see sections 5.3.1 & 5.5.1; Fig. 5.10c). Additionally, because we completed targeted analysis on zircon guided by CL images (e.g., Fig. 5.4), we were able to exclude any LA-MC-ICP-MS spot analyses from our detrital dataset that hit either a recrystallized domain or metamorphic overgrowth (see sections 5.3.1 & 5.5.1).

The results of our MDA calculations are presented in Figures 5.10b and C11, and in Table H5. Calculated MDAs across the Kluane Schist range from ca. 90–79 Ma using the YPP method, from ca. 79–74 Ma using the MLA method, from ca. 83–76 Ma using the YSP method, from ca. 76–72 Ma using the YGC1s method, and from ca. 77–72 Ma using the YGC2s method (Fig. 5.10b and Table H5). As expected, the more conservative YPP method consistently produces an older MDA estimate than all other methods (Fig. 5.10b). In all but one case (sample 20WM26) the YGC1s method produces an MDA estimate within error of the known age of Kluane Schist

metamorphism (Fig. 5.10b; see Chapter 4); we therefore do not consider the YGC1s method as a reliable measure of MDA for the Kluane Schist. In two cases (19WM229 and 20WM40) the YGC2s method produces an MDA estimate within error of the known age of Kluane Schist metamorphism, suggesting it too tends to underestimate the MDA of the Kluane Schist (Fig. 5.10b; c.f., Vermeesch, 2021). We therefore do not consider the YGC2s method within our final MDA determination.

Our collective MDA estimate of ca. 90–74 Ma for the Kluane Schist considers 3 independent methods (YPP, YSP, and MLA) and is in general agreement with previous studies (94.9 +/- 1.1 Ma; Israel *et al.*, 2011a), with the improved statistics our larger-n dataset (n = 666 in this study vs. n ~ 70 in Israel *et al.*, 2011a) likely providing a refined estimate of this previous MDA value (e.g., Vermeesch, 2021).

There is a general lack of correlation between the abundance of recrystallized zircon within a given sample and the difference in MDA estimate provided by each method (Fig. 5.10b). This said, the two samples which show the highest relative abundance of young, recrystallized zircon (i.e., < ca. 70 Ma; 19WM230d & 20WM25b) produce the greatest variation in MDA estimates (Fig. 5.10b). This likely stems from the structural position of these samples within the Kluane Schist (Fig. 5.2); both samples are collected from the structurally highest units currently exposed across the Kluane Schist (Fig. 5.2) where the highest grades of metamorphism were experienced between ca. 70–55 Ma (c.f., Chapters 3 & 4). This increased grade of metamorphism (i.e., higher *T*) could therefore have potentially driven enhanced zircon recrystallization within these samples from ca. 70 Ma. These results highlight the identification and exclusion of individual recrystallized zircon grains is paramount to obtaining an accurate MDA.

As such we consider our Late Cretaceous MDA for the Kluane Schist to be a reliable, if not a slightly conservative estimate for the age of deposition of the Kluane Schist, with this MDA estimate being consistent with the surrounding geological relationships of the Kluane Schist (Figs. 5.2, 5.3 & 5.10a; e.g., Israel *et al.*, 2011a).

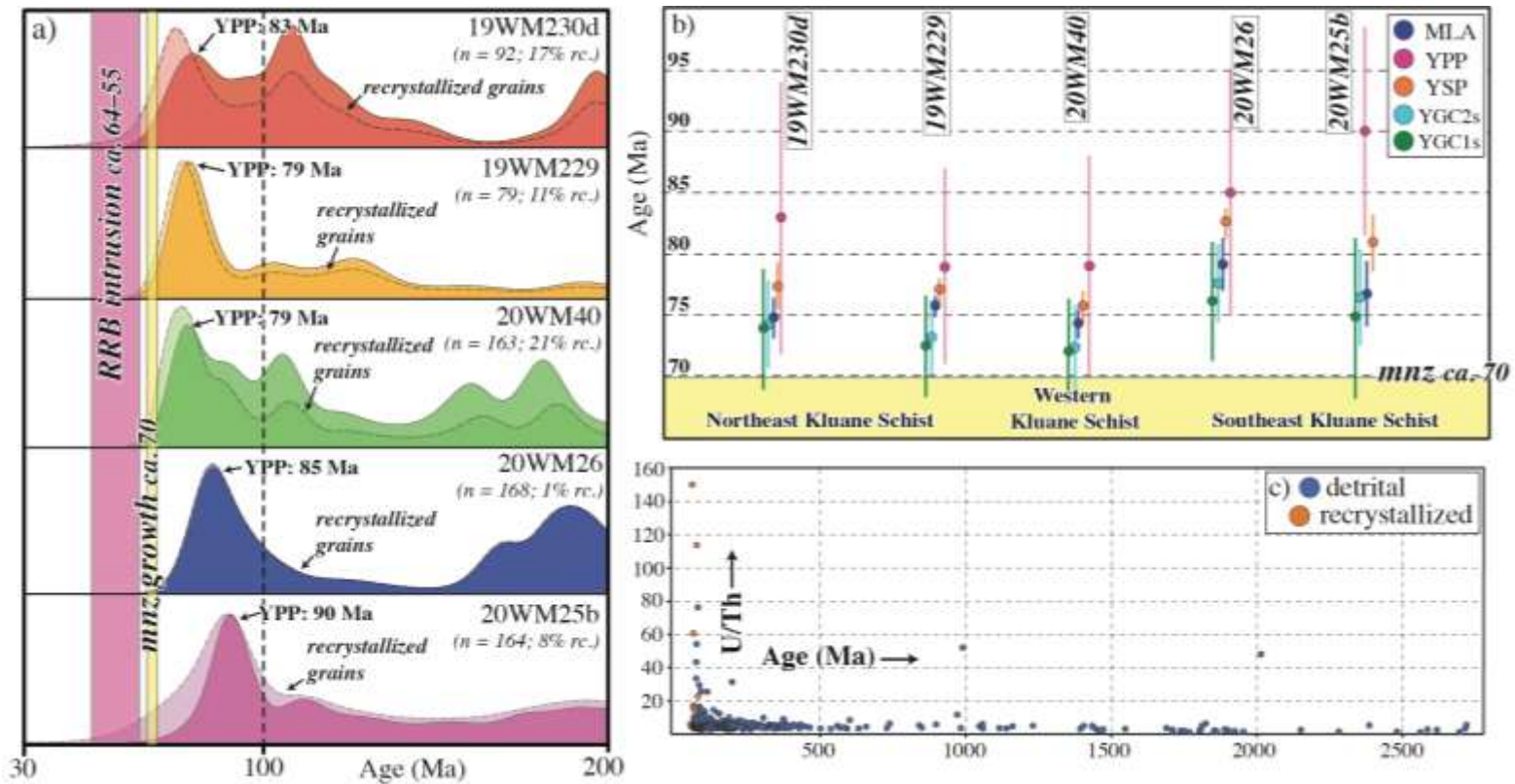


Figure 5.10. Maximum depositional age (MDA) constraints across the Kluane Schist. (a) Kernel Density Estimate plots showing the distribution and amount of detrital and recrystallized (rc.) zircon within each of our Kluane samples. We compare these against established geological constraints within the Kluane Basin (Israel *et al.*, 2011a, b; Chapter 4). Combined, we used these KDE plots to determine the youngest graphical peak age (YPP; see main text, section 5.5.3 and Table H5). (b) Comparison of the MDA estimates returned from YPP, YSP, YGC2s, YGC1s, and MLA methods and sample location across the Kluane Schist (see also Table H5). The timing of metamorphic monazite growth in the Kluane Schist is also indicated (see chapter 4). (c) U/Th ratios of all detrital and recrystallized zircon with age across the Kluane Schist see also Table H7).

5.5.4. Correlative rock packages within the North American Cordillera and geodynamic setting of the Kluane Schist

Recent detrital zircon analysis of the Maclaren Schist, a Barrovian inverted metamorphic belt within south-central Alaska that grades from lower greenschist facies metasedimentary strata in the south to amphibolite facies pelitic and quartzofeldspathic schist and gneiss in the north (Figs. 5.3 & 5.8; e.g., Smith, 1981; Waldien *et al.*, 2021a), has been used to suggest its primary derivation from terranes comprising the inboard North American margin and its deposition in the mid-Late Cretaceous (Fig. 5.3; MDA: 94–86 Ma, YSP method; Waldien *et al.*, 2021a, b). Limited sourcing of Maclaren Schist detritus from the outboard Insular terranes is also inferred from its distinct mid-Late Cretaceous (ca. 90 Ma) and Late Jurassic (ca. 150 Ma) juvenile zircon populations (Fig. 5.8b; $\varepsilon_{\text{Hf}}(t) \sim +8$ to $+13$ and $\sim +2$ to $+15$, respectively; Waldien *et al.*, 2021b). Detrital zircon analysis across the Early Cretaceous Blanchard River assemblage, southwest Yukon, has also been used to infer its derivation largely from the inboard, North American margin with only minor Insular terrane input (Vice, 2017). Comparison of the detrital zircon, metamorphic, and structural datasets acquired from these basins with those previously available for the Kluane Schist (Mezger *et al.*, 2001b; Israel *et al.*, 2011a, b; Stanley, 2012) has provided evidence that these units were all once part of the same contractional, west-verging forearc to a Cretaceous arc built on the Yukon-Tanana terrane and underwent contemporaneous Late Cretaceous Barrovian metamorphism shortly after their collective mid-Cretaceous deposition (Mezger *et al.*, 2001b; Davidson & McPhillips, 2007; Israel *et al.*, 2011a; Vice, 2017; Vice *et al.*, 2020; Waldien *et al.*, 2021a, b). Juxtaposition of the Kluane-Maclaren-Blanchard River(?) assemblages against the underlying Dezadeash-Nutzotin-Clearwater sequence is then suggested to track the terminal accretion of the Insular terranes between ca. 75–65 Ma (Waldien *et al.*, 2021a, b).

Comparison of our new detrital zircon U-Pb age dataset from the Kluane Schist with similar datasets from the Maclaren Schist (Waldien *et al.*, 2021a, b), Blanchard River assemblage (Vice, 2017), Dezadeash Formation (Lowey, 2019), and Clearwater metasediments (Waldien *et al.*, 2021a, b) provides further insight into these potential correlations (Fig. 5.11a, b). Dataset comparisons were completed using MDS analysis (Vermeesch *et al.*, 2016); we prefer the K-S distance (test D statistic; e.g., Fig. 5.11a) over

the Kuiper statistic to assess sample dissimilarity as it consistently produces lower stress values, indicating an overall better fit, when producing final plots (stress values were 6.22 and 0.016 for equivalent Kuiper statistic dissimilarities in 5.11a and 5.11b respectively; e.g., Vermeesch, 2018; see section 5.3.3 for full description of MDS methods).

In general, the results of our MDS analysis highlight similarity between our new detrital zircon datasets from the Kluane Schist and those from the Maclaren Schist (Fig. 5.11a). Limited correlation is seen between zircon datasets from Kluane Schist, Blanchard River assemblage, Dezadeash Formation or Clearwater metasediments (Fig. 5.11a, b).

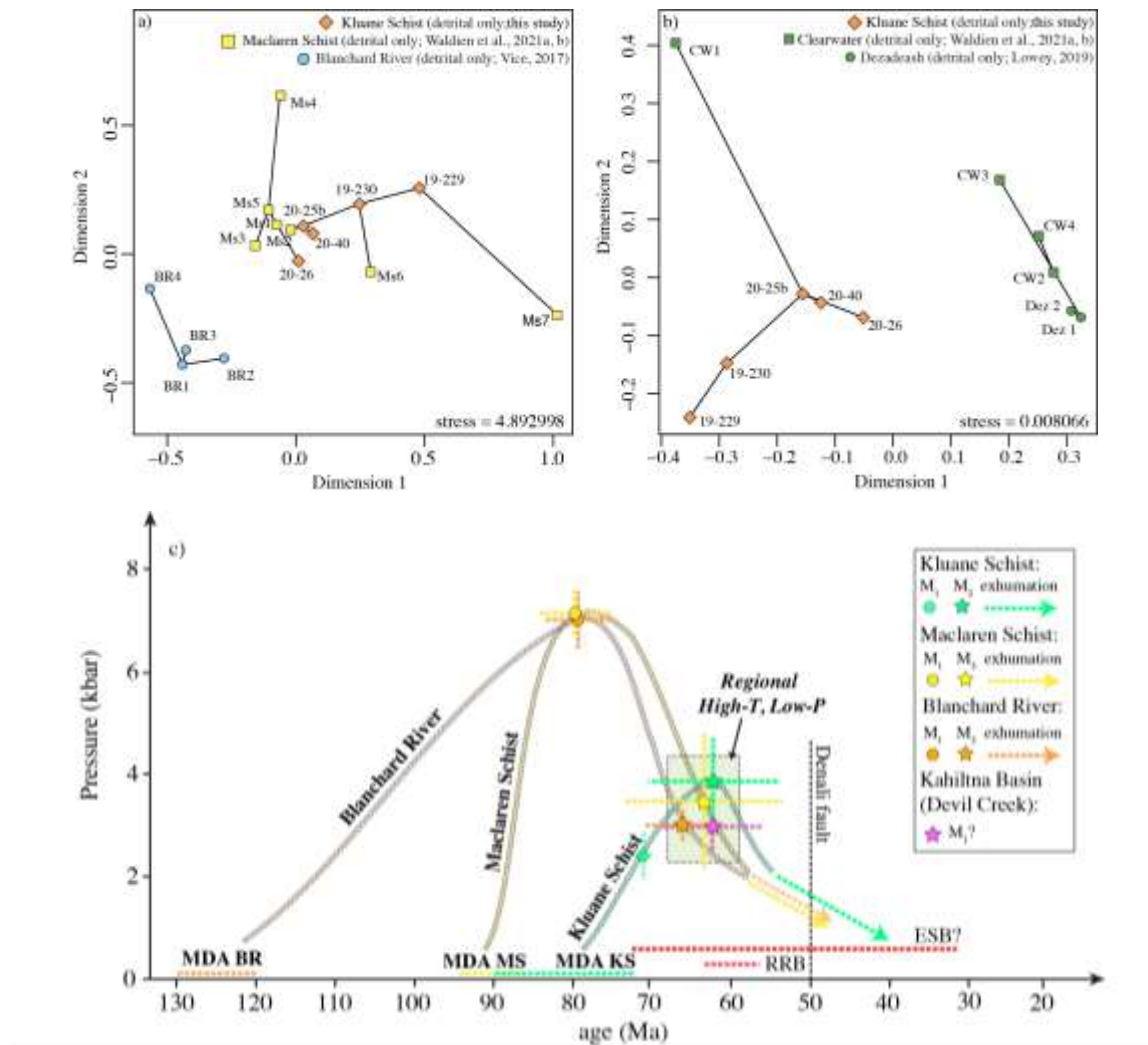


Figure 5.11. Comparison of potentially correlative Jura-Cretaceous rock packages within the Northern Cordillera (see Fig. 5.9). (a-b) Multidimensional scaling (MDS) plots of U-Pb age spectra from individual samples across the Kluane Schist (this study), Maclaren Schist (Waldien *et al.*, 2021a, b), Blanchard River assemblage (Vice, 2017), Clearwater metasediments (Waldien *et al.*, 2021a) and Dezadeash Formation (Lowey, 2019); (a) comparison of the Kluane Schist with the Blanchard River assemblage and Maclaren Schist, and (b) comparison of the Kluane Schist with the Dezadeash Formation and Clearwater metasediments. c) Pressure-age graph summarising equivalent depositional, metamorphic, and geochronological datasets extracted from continentally derived Jura-Cretaceous metasedimentary units within the Northern Cordillera (see main text section 5.5.4 for full explanation). DC = Devil Creek rocks (see Fig. 5.9; Davidson & McPhillips, 2007); BR = Blanchard River assemblage (Vice, 2017; Vice *et al.*, 2020); KS = Kluane Schist (this study; Chapter 4); MS = Maclaren Schist (Davidson & McPhillips, 2007; Waldien *et al.*, 2021a, b). ESB = East Susitna Batholith (Nokleberg, 2015); RRB = Ruby Range batholith (Israel *et al.*, 2011a, b).

Overall, our results suggest a largely similar source region for both the Kluane Schist and Maclaren Schist, particularly when considering inboard terrane and plutonic sources (Figs. 5.8b & 5.9b; i.e., Whitehorse, Minto, Long Lake, recycled Yukon-Tanana terrane). Direct comparison of the detrital zircon U-Pb age spectra from the Blanchard River assemblage with these same source regions (e.g., Fig. 5.8b) also highlights it was likely sourced from a similar inboard region to the Maclaren Schist and Kluane Schist, however, with zircon being restricted to older ages (Fig. 5.8b; i.e., Minto, Long Lake, recycled Yukon-Tanana; Vice, 2017). This suggests the Maclaren Schist, Blanchard River assemblage, and Kluane Schist potentially occupied a similar, along-strike position relative to the North American margin during their deposition (Fig. 5.9; e.g., Waldien *et al.*, 2021 b).

A similar source region for the Kluane Schist and Maclaren Schist is further supported by both the age and isotopic signature of the mid-Late Cretaceous juvenile zircon population returned from the Maclaren Schist (ca. 90 Ma, $\epsilon_{\text{Hf}}(t) \sim +8$ to $+13$; see Fig. 6 in Waldien *et al.*, 2021b) and the older portion of the ca. 95–75 Ma juvenile population recorded across the Kluane Schist ($\epsilon_{\text{Hf}}(t) \sim +5$ to $+12$; Figs. 5.6 & 5.8a). Due to the lack of a significant contribution of Late Jurassic to Early Cretaceous zircon in all Kluane Schist samples (ca. 160–120 Ma; Figs. 5.5, 5.8a and 5.9; see above) we infer that this mid-Late Cretaceous juvenile zircon was most likely derived from inboard,

Intermontane-bound sources (c.f. Fig. 5.9). We suggest either (or a combination of) the Coast Plutonic Complex and/or several intrusive suites across southwestern Yukon as a likely source for these zircon (Figs. 5.8a & 5.9; e.g., Casino, Rancheria, Prospector Mountain, Carmacks Group; see section 5.5.2). Our inference is supported by whole rock $\epsilon\text{Nd}(t)$ values from these intrusive suites in southwest Yukon, which when converted to Hf-equivalent using the method of Vervoort *et al.* (2011), produce a range of $\epsilon\text{Hf}(t)$ values that align well with the mid-Late Cretaceous zircon recovered from both the Kluane Schist and Maclaren Schist (c.f., Yk(p) in Fig. 5.8a; Waldien *et al.*, 2021b). Either way, the good overlap between the $\epsilon\text{Hf}(t)$ values of this age population between both the Maclaren Schist and Kluane Schist provides strong evidence for a shared source region for both units (e.g., Waldien *et al.*, 2021b).

In addition to the similarities in the zircon U-Pb spectra of the of the Kluane Schist, Maclaren Schist and Blanchard River assemblage, we also note some key differences. Firstly, the younger (< ca. 85 Ma) mid-Late Cretaceous peak that dominates all Kluane Schist spectra (e.g., Figs. 5.5 & 5.6) is not present within any Maclaren Schist or Blanchard River assemblage samples (Fig. 5.8b; Vice, 2017; Waldien *et al.*, 2021a, b). Secondly, the distinct Early Cretaceous (ca. 125–120 Ma) peak within the zircon spectra of the Blanchard River assemblage (INS in Fig. 5.8b; Vice, 2017) and the Late Jurassic juvenile zircon population within the Maclaren Schist (INS in Fig. 5.8b; ca. 150 Ma; $\epsilon\text{Hf}(t) \sim +2$ to $+15$; Waldien *et al.*, 2021b) are not well represented within the Kluane Schist (Fig. 5.8). These Late Jurassic (for Maclaren Schist) and Early Cretaceous (for Blanchard River assemblage) populations have been suggested to reflect sourcing from the Insular terranes (c.f., Figs. 5.8 & 5.9a; Vice, 2017; Waldien *et al.*, 2021b). A lack of a significant contribution of zircon of this age within the Kluane Schist suggests it only received limited Insular derived detritus compared with either the Maclaren Schist or Blanchard River assemblage (Fig. 5.8).

Although the Blanchard River assemblage, Maclaren Schist, and Kluane Schist likely shared a similar along-strike position relative to the North American margin during their deposition, their apparent differences in abundance of Insular derived detritus indicates they occupied different positions within the seaway separating the Intermontane and Insular terranes. This also suggests they likely do not represent directly correlative lithological units as has been previously suggested (e.g., Vice, 2017; Waldien *et al.*,

2021b). Instead, we propose a model where the Blanchard River assemblage, Maclaren Schist, and Kluane Schist were deposited sequentially as part of a west-facing forearc; all three units are primarily derived from the paleo-western margin of North America with the Blanchard River assemblage and Maclaren Schist representing the more distal accretionary wedge on top of which the Kluane Schist was deposited within a forearc-style basin (Fig. 5.12). This model puts the Maclaren Schist and Blanchard River assemblage in a slightly more outboard position in the Jura-Cretaceous ocean compared to the Kluane Schist, which would account for their increased abundance in Insular-derived detritus (e.g., Figs. 5.8 and 5.12). Equally, this model is consistent with the age and inferred metamorphic evolution for each unit (Fig. 5.11c; Chapter 3); the Blanchard River assemblage (MDA: 130–120 Ma; Vice, 2017) and Maclaren Schist (MDA: 94–86 Ma; Waldien *et al.*, 2021a, b) form the accretionary wedge and were contemporaneously metamorphosed to kyanite-grade between ca. 90–83 Ma (Figs. 5.11c and 5.12c; Davidson & McPhillips, 2007; Vice *et al.*, 2020; Waldien *et al.*, 2021b) during which time the Kluane Schist was likely still being deposited (MDA: 90–74 Ma; see section 5.5.3). This, along with its lack of Insular derived zircon and distinct metamorphic evolution (c.f., Chapters 3 & 4; Figs. 5.8 & 5.11c), is consistent with the Kluane Schist having been deposited within a continentally bound forearc-style basin above both the Blanchard River assemblage and Maclaren Schist (Fig. 5.12).

5.5.5. Implications for Insular terrane accretion

The detrital zircon dataset presented within this study is consistent with the Kluane Schist representing a young continentally bound, forearc-style depocenter that remained open until the waning stages of Insular terrane accretion. We combine this new detrital zircon dataset with existing metamorphic, structural, and geochronological data from the Kluane Schist (Chapters 3 & 4; Mezger, 2000; Mezger *et al.*, 2001a, b; Israel *et al.*, 2011a) and similar datasets derived from other Jura-Cretaceous basinal assemblages within the Northern Cordillera (e.g., Fig. 5.3) to infer the evolution of the paleo-western margin of North America between Late Jurassic through Eocene. Our tectonic model is centred around the Yukon-Alaska border (141°W, present coordinates; Fig. 5.1) and summarized in five time slices, detailed below and in Figure 5.12.

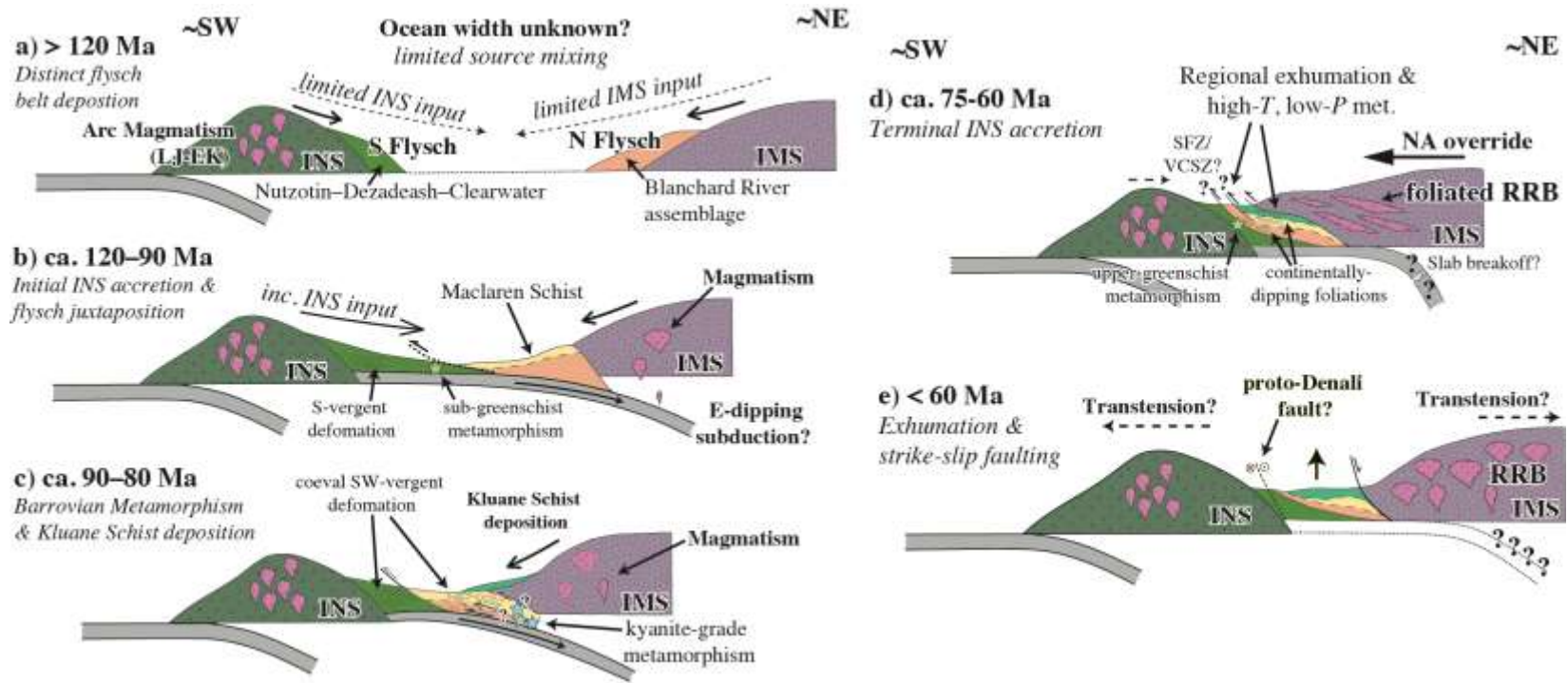


Figure 5.12. Tectonic model accounting for the accretion of the Insular terranes to the paleo-western margin of North America, centered around the current location of the Alaska-Yukon border. Specific events defining the time periods outlined in the model (t1 to t5) are discussed in detail in the main text, section 5.5.5. Based on geologic evidence recovered from Jura-Cretaceous basinal assemblages we prefer a model involving a second east-dipping subduction zone below the paleo-western margin of North America during the latest Mesozoic (c.f., Hults *et al.*, 2013; Box *et al.*, 2019; Trop *et al.*, 2020; Waldien *et al.*, 2021b). However, note that such a subduction zone is not a fundamental requirement for our model when considering the current uncertainties regarding the nature of the crust separating the Insular and Intermontane terranes during the Mesozoic (see main text, section 5.5.5 for discussion). (INS = Insular terranes; IMS = Intermontane terranes; SFZ = Shakhwak fault zone; VCSZ = Valdez Creek Shear Zone).

Time 1 - ca. 150–120 Ma: Jurassic through Early Cretaceous basinal assemblages within the Northern Cordillera are defined by two distinct and terrane-specific lithofacies (Figs. 5.3, 5.9 & 5.12a); one being primarily derived from and deposited upon the inboard margin of the Insular terranes (Fig. 5.3; e.g., southern flysch; Nutzotin-Dezadeash-Clearwater sequence; Hults *et al.*, 2013; western Gravina Belt; Yokelson *et al.*, 2015; southeast Kahiltna; Box *et al.*, 2019) and another being largely sourced from and overlapping the paleo-western margin of North America (northern flysch; e.g., eastern Gravina Belt; Yokelson *et al.*, 2015; Blanchard River assemblage; Vice, 2017; northwestern Kahiltna; Box *et al.*, 2019). Correlation between these terrane-specific units (e.g., Hults *et al.*, 2013; Box *et al.*, 2019) implies there was more than 2000 km of along-strike connectivity within the seaway separating the Insular and Intermontane terranes during the latest Jurassic to Early Cretaceous (Fig. 5.12a). The width of this inter-connected seaway remains poorly constrained (e.g., Hults *et al.*, 2013; Trop *et al.*, 2020). However, evidence for mixed outboard and inboard detrital zircon signatures within the parts of the Kahiltna assemblage (e.g., Hampton *et al.*, 2010; Box *et al.*, 2019) and the Early Cretaceous Blanchard River assemblage (e.g., Fig. 5.8b; Vice, 2017), suggests the Insular and Intermontane terranes were likely tectonically coupled by at least the Early Cretaceous and not separated by an extensive ocean 1000's of km wide (Fig. 5.12a). Equally the record provided by Early-Middle Jurassic overlap sequences and cross-cutting plutons within west central British Columbia and southeast Alaska (ca. 180–175 Ma; e.g., van der Heyden, 1992; Gehrels, 2001; Gehrels *et al.*, 2009) implies initial Insular terranes had already occurred further south within the Cordillera (present coordinates) by this time.

Time 2 - ca. 120–90 Ma: Initial accretion of the Insular terranes within the northernmost Cordillera is recorded by Early Cretaceous south-verging deformation in the Nutzotin Mountains sequence (Fig. 5.3; ca. 117 Ma; Manuszak *et al.*, 2007) and sub-greenschist facies metamorphism and deformation (Fig. 5.3; ca. 106; Lowey, 2021) within the Dezadeash Formation (Fig. 5.12b). Farther north, parts of the Kahiltna Basin and the Maclaren Schist were undergoing deposition in a contractional setting (Figs. 5.1 & 5.3; Box *et al.*, 2019; Waldien *et al.*, 2021b) while to the south, parts of the Gravina Basin remained open until the mid-Cretaceous (Fig. 5.1 & 5.3; ca. 112–105 Ma; Kapp & Gehrels, 1998; Yokelson *et al.*, 2015). Due to its similar source regions but distinctly younger MDA (e.g., Figs. 5.8b & 5.11c), it is likely the Maclaren Schist was deposited as

a separate unit atop the Blanchard River assemblage during this initial accretionary event (Figs. 5.11c & 5.12b; Vice, 2017; Waldien *et al.*, 2021b). However, to acknowledge the fact that the *true* depositional age of the Blanchard River assemblage may significantly pre-date its MDA we note our model is insensitive to this specific order of deposition and only relies on the inferred provenance of these units (c.f., Fig. 5.12a-c).

The presence of paired east-dipping subduction zones during the initial accretion of the Insular terranes remains uncertain (Fig. 5.12b; e.g., Trop *et al.*, 2020; Waldien *et al.*, 2021b). There is evidence that the Jura-Cretaceous basins of southwest Yukon were floored by oceanic crust during their deposition (e.g., Bear Creek assemblage in Fig. 5.2; Israel *et al.*, 2015), with the possibility of a subduction zone between the Insular and Intermontane terranes supported by the presence of potential ophiolitic fragments interleaved with Jura-Cretaceous metasedimentary units, including the Kluane Schist (Mezger, 2000), and the inferred presence of an interconnected seaway separating the Intermontane and Insular terranes during the Late Jurassic and Early Cretaceous (see above Fig. 5.12b; e.g., Hults *et al.*, 2013; Box *et al.*, 2019; Trop *et al.*, 2020). However, southwest Yukon lacks a paired magmatic belt to account for this subduction zone in addition to that suggested to record paleo-east dipping subduction below the outboard Insular terranes (e.g., Whitehorse suite in Fig. 5.9 e.g., Hart *et al.*, 2004; Gehrels *et al.*, 2009). The record of deposition and accretion within the outboard Chugach Accretionary Prism coeval with migration of a single magmatic belt in southwest Yukon (e.g., Gehrels *et al.*, 2009; Amato *et al.*, 2013) therefore provides evidence against oceanic subduction beneath the paleo-western margin of North America during the mid-Cretaceous.

However, alternative models that envisage west-dipping subduction below the eastern margin of the Insular terranes at this time (Sigloch & Mihalynuk, 2013, 2017; Lowey, 2019) are inconsistent with this record of paleo-east dipping subduction and coeval inboard-migrating magmatism (e.g., Clift *et al.*, 2005; Gehrels *et al.*, 2009; Amato *et al.*, 2013; Cecil *et al.*, 2018; Pavlis *et al.*, 2019; Trop *et al.*, 2020). Further, the consistent south to southwest-verging structures and low-grades of metamorphism recorded by Jura-Cretaceous basinal assemblages that overlap the inboard margin of the Insular terranes (Figs. 5.3 & 5.12b; e.g., Nutzotin–Clearwater–Dezadeash–SE Kahiltna) along with their well-documented connection with the Insular terranes from the Late Jurassic (Fig. 5.3; ca. 160 Ma; e.g., Lowey, 2000; Hults *et al.*, 2013; Yokelson *et al.*,

2015; Box *et al.*, 2019; Lowey, 2019; 2021) provides strong evidence against paleo-west dipping subduction along the inboard margin of the Insular terranes.

Following these arguments (see also detailed discussions in Monger, 2014; Pavlis *et al.*, 2019; Trop *et al.*, 2020) we include in our tectonic model a second east-dipping subduction zone inboard of the Insular terranes (Fig. 5.12b-d). However, we note that such a subduction zone is not a fundamental requirement for our model, accounting for the current uncertainties regarding the nature of the crust separating the Insular and Intermontane terranes during the Mesozoic (e.g., Trop *et al.*, 2020; Waldien *et al.*, 2021b).

Time 3 - ca. 90–80 Ma: The youngest depositional ages recorded for the Maclaren Schist (Fig. 5.3; 86 Ma; Waldien *et al.*, 2021a), parts of the Kahiltna assemblage (Fig. 5.3; ca. 81 Ma; Box *et al.*, 2019), Upper Koksetna River sequence (Fig. 5.3; ca. 85 Ma; Hults *et al.*, 2013), and the Kluane Schist (MDA: 90–74 Ma; section 5.5.3) imply the Insular-Intermontane seaway within the Alaska-Yukon regions of the Northern Cordillera (present-day coordinates) remained open during the mid-Late Cretaceous (Fig. 5.12c). Increased contribution from outboard sources to the zircon spectra of these units also suggests the increased proximity of the Insular terranes to the paleo-western margin during this time (Fig. 5.8b; e.g., Hampton *et al.*, 2010; Box *et al.*, 2019; Waldien *et al.*, 2021b).

Shortly after its deposition, the Maclaren Schist, along with other Jura-Cretaceous basins that primarily include continentally derived detritus within southeast Alaska, southwest Yukon, and parts of northern British Columbia (e.g., Figs. 5.3 & 5.9) experienced Barrovian-style metamorphism associated with their collective underplating below the western margin of North America (ca. 90–83 Ma; Figs. 5.3 & 5.12c; e.g., Maclaren Schist, Blanchard River assemblage, Gravina Belt; $P \sim 6.5\text{--}7$ kbar; McClelland *et al.*, 1991; Davidson & McPhillips, 2007; Vice *et al.*, 2020; Waldien *et al.*, 2021b). Coeval with this period of deep-seated metamorphism the Kluane Schist (MDA, 90–74 Ma; see above; Figs. 5.3, 5.10, 5.11 & C11; section 5.5.3) was being deposited (Figs. 5.11c & 5.12c). Due to its limited provenance ties to the Insular terranes (e.g., Fig. 5.8a), it is likely the deposition of the Kluane Schist occurred within a finite, continentally bound forearc-style basin atop the Maclaren Schist (Fig. 5.12c; section 5.5.4). However, the metamorphic evolution of the Kluane Schist, which includes a distinct sub-greenschist

facies burial event (< 3 kbar; Fig. 5.3; Chapter 3) prior to override by the North American margin (c.f., Fig. 5.12c; Chapters 3 & 4), is consistent with its deposition within a forearc-style basin just before the final docking of the Insular terranes with the paleo-western margin of North America (Chapter 3). Further, its lack of a mixed provenance signal as well as the presence of interleaved ultramafic bodies (Mezger, 2000; Canil *et al.*, 2015) is inconsistent with the Kluane Schist representing a post-accretionary pull apart basin (e.g., Cowan, 1978; 1985) as has been suggested previously (McClelland *et al.*, 1992a). The strong provenance ties between the Kluane Schist and the North American margin (Fig. 5.8a; Israel *et al.*, 2011a) are also inconsistent with the deposition of the Kluane Schist within a back-arc basin distal from a continental source (Mezger *et al.*, 2001b). Instead, these relationships are consistent with the Kluane Schist representing the uppermost part of a contractional forearc assemblage to a west-facing arc built on the paleo-western margin of North America (Fig. 5.12c). The lack of a distinct high-pressure M₁ event across the Kluane Schist in comparison to the Blanchard River assemblage and Maclaren Schist (Figs. 5.3 & 5.11c; Vice *et al.*, 2020; Waldien *et al.*, 2021b; Chapter 3) reflects its limited underplating below the North American margin prior to terminal accretion of the Insular terranes (Fig. 5.12c-d).

Time 4 - ca. 75–60 Ma: Shortly after the sub-greenschist facies metamorphism experienced by the Kluane Schist, ca. 70–68 Ma regional exhumation is recorded across the Blanchard River assemblage (Vice *et al.*, 2020) while top-to-the-south thrusting of the Maclaren Schist over its Clearwater-Dezadeash footwall is associated with decompression melting and migmatite formation from ca. 74–72 Ma (Fig. 5.11d; Davidson *et al.*, 1992; Davidson & McPhillips, 2007; Waldien *et al.*, 2021b). Upper greenschist facies metamorphism within the Clearwater-Dezadeash footwall occurs at ca. 65 Ma (Figs. 5.3 & 5.12d; Lowey, 2000; 2021; Waldien *et al.*, 2021a). The regional exhumation experienced by the Blanchard River assemblage and Maclaren Schist has been associated with the reactivation of basin bounding structures including the Valdez Creek and Tatshenshini-Shakwak shear zones (Fig. 5.12d; Davidson *et al.*, 1992; Vice *et al.*, 2020; Waldien *et al.*, 2021b). Within southwest Alaska (present coordinates), the Upper Cretaceous Kuskokwim Group (Figs. 5.1 & 5.3; MDA, 72 Ma; Miller *et al.*, 2007) records deposition within a series of finite, pull-apart basins coeval with this regional exhumation (Miller *et al.*, 2007; Hulst *et al.*, 2013). Together these events hint at a potential period of post-accretionary extension along the newly developed Insular-

Intermontane suture, which may reflect slab breakoff within the inboard subduction zone (Fig. 5.12d; e.g., Waldien *et al.*, 2021b). Potential evidence for a slab breakoff event at this time is provided by the Late Cretaceous (ca. 70 Ma) eruption of thick subaerial, primitive volcanic successions in Yukon on recently uplifted terranes inboard of the continental margin (Carmacks Group; e.g., Davies & von Blanckenburg, 1995; Johnston *et al.*, 1996).

Following this period of regional exhumation, a collective high- T , low- P metamorphic event is recorded by multiple Jura-Cretaceous assemblages along the paleo-western margin of North America (ca. 75–60 Ma; Figs. 5.3 & 5.11c; Davidson & McPhillips, 2007; Vice *et al.*, 2020; Waldien *et al.*, 2021b; Chapter 4). This high- T , low- P metamorphism is associated with the south- and southwest-directed overthrusting of these Jura-Cretaceous assemblages and their subsequent intrusion by syn- to post-deformational plutons (e.g., Ruby Range batholith, Israel *et al.*, 2011a, Fig. 5.12d; East Susitna batholith, Nokleberg *et al.*, 2015). Collectively this high- T , low- P event lead to the development of continentally dipping inverted metamorphic sequences in both the Kluane Schist and the Maclaren Schist (Fig. 5.12d; e.g., Smith, 1981; Mezger *et al.*, 2001b; Davidson & McPhillips, 2007; Chapters 3 and 4) and consistent southwest- to south-oriented shear structures within the Kluane Schist (Fig. 5.12d; e.g., Israel *et al.*, 2011a; Chapter 3), Blanchard River assemblage (Fig. 5.12d; Vice *et al.*, 2020), Maclaren Schist (Fig. 5.12d; Smith, 1981; Davidson & McPhillips, 2007; Waldien *et al.*, 2021a), and parts of the Kahiltna Basin (e.g., Devils Creek rocks of Davidson & McPhillips, 2007; DC in Figs. 5.9a & 5.11b). These structures are all consistent with the collective inversion of these Jura-Cretaceous basins by the southwesterly-directed override of the North American margin (Fig. 5.12d; Chapters 3 and 4). As such we consider the westward migration of the North American continent and the overthrusting of its thermally mature flanking components (e.g., Yukon-Tanana terrane) to be the primary driver of terminal Insular terrane accretion within this region of the Cordillera. This is consistent with reconstructions of the Mesozoic-Cenozoic trajectory of the North American craton (e.g., Monger & Gibson, 2019) and is best reconciled by a model of Insular terrane accretion that involves eastward, continentally dipping subduction and the North American continent in the upper plate position (Fig. 5.12d).

Time 5 - <ca. 60 Ma: After regional high- T , low- P metamorphism ceases, the cooling and exhumation of Jura-Cretaceous basins is recorded from ca. 60–40 Ma (Figs.

5.11c & 5.12e; Mortensen & Erdmer, 1992; Mezger, 1997; Vice *et al.*, 2020; Waldien *et al.*, 2021a). Across the Kluane Schist initial exhumation involved isothermal decompression and migmatite development from ca. 59 Ma (Chapter 4) while later cooling and uplift is recorded by ^{40}Ar - ^{39}Ar mica cooling dates between ca. 55–40 Ma (Fig. 5.11b; Mortensen & Erdmer, 1992; Mezger, 1997). Isothermal decompression across the Maclaren Schist occurred from ca. 62 Ma following cessation of slip along the Valdez Creek shear zone (Ridgway *et al.*, 2002; Davidson and McPhillips, 2007; Waldien *et al.*, 2021b). Final exhumation and cooling of the Blanchard River assemblage is considered to occur during the latest Cretaceous to early Paleogene (Vice *et al.*, 2020).

The timing of exhumation recorded by these Jura-Cretaceous basins largely coincides with the transition from orogen-normal to orogen-parallel tectonics within the Cordillera (ca. 60–50 Ma; Monger & Gibson, 2019). After this time dextral strike slip faulting begins to dominate within the Northern Cordillera (Fig 5.12e; e.g., Denali fault; ca. 52 Ma, Waldien *et al.*, 2021b), while within the Cordillera of south-central British Columbia rapid regional extension and exhumation of deep crustal rocks occurs from ca. 55–45 Ma (e.g., Okanagan & Columbia River normal fault systems; e.g., Tempelman-Kluit & Parkinson, 1986; Parrish, 1995; Johnson & Brown, 1996; Brown *et al.*, 2012; Damant *et al.*, 2023). Across west-central British Columbia and southeastern Alaska significant latest Cretaceous to Eocene exhumation and uplift of high-grade rocks occurs synchronous with pluton emplacement along the east side of the Coast shear zone (Hollister, 1982; Crawford *et al.*, 1999; McClelland & Mattinson, 2000; Andronicos *et al.*, 2003; Rushmore *et al.*, 2005). Thus, our model incorporates the uplift and exhumation of these Jura-Cretaceous basinal assemblages coeval with voluminous plutonism within the Coast Plutonic Complex (e.g., Figs. 5.11b & 5.12e; Ruby Range batholith & East Sustina Batholith). We suggest this exhumation was primarily driven by a transition to dextral transtension along North American continental margin (e.g., Ewing, 1980; Engebretson *et al.*, 1984; Parrish *et al.*, 1988; Price, 1994) and the associated shift of the Cordillera from an orogen dominated by largely orogen-normal tectonics to one dominated by orogen-parallel tectonics in the Cenozoic (c.f., Monger & Gibson, 2019).

5.6. Conclusions

New detrital zircon analyses across the Late Cretaceous Kluane Schist provide insight into the tectonic processes operating during the final stages of Insular terrane accretion within the Northern Cordillera. A Late Cretaceous maximum depositional age and provenance ties to inboard terranes (e.g., Yukon-Tanana terrane) suggest the Kluane Schist was deposited in a finite, continentally bound basin and represents the youngest part of a contractional forearc to an arc built on the Yukon-Tanana terrane. Integration of this geodynamic setting for Kluane Schist deposition with existing structural, metamorphic, and geochronological constraints provides strong evidence that the North American continental margin was in an upper plate position above an east-dipping subduction system during the Late Mesozoic. Furthermore, we suggest the Kluane Schist is unlikely to be directly correlative with either the Maclaren Schist or Blanchard River assemblage, as has been previously proposed. Instead, these units likely represent more distal parts of the forearc assemblage build upon the same arc within the Yukon-Tanana terrane.

Combined with similar datasets from other Jura-Cretaceous basins within the Northern Cordillera we offer a five-stage model to account for their tectonic histories during Insular terrane accretion. Our findings strongly favor a model of Insular terrane accretion that involves continentally dipping eastward subduction and the subsequent override of these Jura-Cretaceous basins by a westward migrating North American continent in the upper plate position. Our results are poorly reconciled with models of Insular terrane accretion that involve the progressive closure of an extensive Jura-Cretaceous ocean basin bounded by a west-dipping subduction zone.

5.7. Acknowledgements

Drs. Joshua Davies and Morgann Perrot (UQAM) are thanked for the collection and processing of detrital zircon U-Pb LA-MC-ICP-MS and CA-TIMS datasets. Dr. Corey Wall (UBC, Vancouver) is thanked for the collection and processing of detrital zircon Hf-isotope datasets. The authors are also grateful to the Yukon Geological Survey for supporting fieldwork with equipment and helicopter time. Maurice Colrpon and Steve

Israel are thanked for their insightful discussions regarding the Kluane Schist and detrital zircon analyses, and for their accompaniment during early fieldwork. Alex Rea and Raj Aulakh are thanked for their assistance during fieldwork.

5.8. References

- Allan, M. M., Mortensen, J. K., Hart, C. J. R., Bailey, L. A., Sánchez, M. G., Ciolkiewicz, W., McKenzie, G. G. and Creaser, R. A., 2013. Magmatic and metallogenic framework of west-central Yukon and eastern Alaska: Tectonics, Metallogeny, and Discovery: The North American Cordillera and Similar Accretionary Settings. Society of Economic Geologists, Special Publication, v.17, p.111–168
- Amato, J.M., Pavlis, T.L., Cliff, P.D., Kochelek, E.J., Hecker, J.P., Worthman, C.M. and Day, E.M., 2013. Architecture of the Chugach accretionary complex as revealed by detrital zircon ages and lithologic variations: Evidence for Mesozoic subduction erosion in south-central Alaska. *Geological Society of America Bulletin*, v.125, n.11-12, p.1891-1911. <https://doi.org/10.1130/B30818.1>
- Andersen, T., Elburg, M.A. and Magwaza, B.N., 2019. Sources of bias in detrital zircon geochronology: Discordance, concealed lead loss and common lead correction. *Earth-Science Reviews*, v.197, p.102899. <https://doi.org/10.1016/j.earscirev.2019.102899>
- Andersen, T., van Niekerk, H. and Elburg, M.A., 2022. Detrital zircon in an active sedimentary recycling system: Challenging the ‘source-to-sink’ approach to zircon-based provenance analysis. *Sedimentology*, v.69, n.6, p.2436-2462. <https://doi.org/10.1111/sed.12996>
- Andronicos, C.L., Chardon, D.H., Hollister, L.S., Gehrels, G.E. and Woodsworth, G.J., 2003. Strain partitioning in an obliquely convergent orogen, plutonism, and synorogenic collapse: Coast Mountains Batholith, British Columbia, Canada. *Tectonics*, v.22, p.2. <https://doi.org/10.1029/2001TC001312>

- Bacon, C.R., Vazquez, J.A. and Wooden, J.L., 2012. Peninsular terrane basement ages recorded by Paleozoic and Paleoproterozoic zircon in gabbro xenoliths and andesite from Redoubt volcano, Alaska. *Geological Society of America Bulletin*, v.124, n.1-2, p.24-34. <https://doi.org/10.1130/B30439.1>
- Beard, J.S. and Barker, F., 1989. Petrology and tectonic significance of gabbros, tonalites, shoshonites, and anorthosites in a late Paleozoic arc-root complex in the Wrangellia terrane, southern Alaska. *The Journal of Geology*, v.97, n.6, p.667-683. <https://doi.org/10.1086/629351>
- Beranek, L.P. and Mortensen, J.K., 2011. The timing and provenance record of the Late Permian Klondike orogeny in northwestern Canada and arc-continent collision along western North America. *Tectonics*, v.30, p.5. <https://doi.org/10.1029/2010TC002849>
- Beranek, L.P., van Staal, C.R., McClelland, W.C., Israel, S. and Mihalynuk, M.G., 2013. Baltican crustal provenance for Cambrian–Ordovician sandstones of the Alexander terrane, North American Cordillera: evidence from detrital zircon U–Pb geochronology and Hf isotope geochemistry. *Journal of the Geological Society*, v.170, n.1, p.7-18. <https://doi.org/10.1130/31066.1>
- Beranek, L.P., van Staal, C.R., McClelland, W.C., Joyce, N. and Israel, S., 2014. Late Paleozoic assembly of the Alexander-Wrangellia-Peninsular composite terrane, Canadian and Alaskan Cordillera. *Geological Society of America Bulletin*, v.126, n.11-12, p.1531-1550. <https://doi.org/10.1130/31066.1>
- Beranek, L.P., McClelland, W.C., van Staal, C.R., Israel, S., and Gordee, S.M., 2017, Late Jurassic flare-up of the Coast Mountains arc system, NW Canada, and dynamic linkages across the northern Cordilleran orogen: *Tectonics*, v.36, p.877–901, <https://doi.org/10.1002/2016TC004254>.
- Berg, H.C., Jones, D.L., and Richter, D.H., 1972, Gravina-Nutzotin Belt; tectonic significance of an upper Mesozoic sedimentary and volcanic sequence in southern and southeastern Alaska, in U.S. Geological Survey, *Geological survey research 1972*, Chapter D: U.S. Geological Survey Professional Paper 800-D, p.D1-D24.

- Bleick, H.A., Till, A.B., Bradley, D.C., O'Sullivan, P.B., Wooden, J.L., Bradley, D.B., Taylor, T.A., Friedman, S.B., and Hults, C.P., 2012, Early Tertiary exhumation of the flank of a forearc basin, southwest Talkeetna Mountains, Alaska: U.S. Geological Survey Open-File Report 2012–1232 (Available at <http://pubs.usgs.gov/of/2012/1232/>).
- Blichert-Toft, J., 2008. The Hf isotopic composition of zircon reference material 91500. *Chemical Geology*, v. 253, n.3-4, p.252-257. <https://doi.org/10.1016/j.chemgeo.2008.05.014>
- Bineli Betsi, T., Lentz, D., McInnes, B., and Evans, N.J., 2012, Emplacement ages and exhumation rates for intrusion-hosted Cu-Mo-Sb-Au mineral systems at Freegold Mountain (Yukon, Canada): Assessment from U-Pb, Ar-Ar, and (U-Th)/He geochronometers: *Canadian Journal of Earth Sciences*, v.49, n.5, p.653–670, <https://doi.org/10.1139/e2012-009>.
- Bordet, E., Israel, S. and D. Moynihan, 2015. Geology of the Takhanne River (NTS 115A/2) and Kluhini River (115A/7) map areas, southwest Yukon. In: *Yukon Exploration and Geology 2014*, K.E. MacFarlane, M.G. Nordling and P.J. Sack (eds.), Yukon Geological Survey, p.1-16.
- Bouvier, A., Vervoort, J.D. and Patchett, P.J., 2008. The Lu–Hf and Sm–Nd isotopic composition of CHUR: constraints from unequilibrated chondrites and implications for the bulk composition of terrestrial planets. *Earth and Planetary Science Letters*, v.273, n.1-2, p.48-57. <https://doi.org/10.1016/j.epsl.2008.06.010>
- Bowring, J.F., McLean, N.M. and Bowring, S.A., 2011. Engineering cyber infrastructure for U-Pb geochronology: Tripoli and U-Pb_Redux. *Geochemistry, Geophysics, Geosystems*, v.12, p.6. <https://doi.org/10.1029/2010GC003479>
- Box, S.E., Karl, S.M., Jones, J.V., Bradley, D.C., Haeussler, P.J. & O'Sullivan, P.B., (2019). Detrital zircon geochronology along a structural transect across the Kahiltna assemblage in the western Alaska Range: Implications for emplacement of the Alexander-Wrangellia-Peninsular terrane against North America. *Geosphere*, v.15, n.6, p.1774-1808. <https://doi.org/10.1130/GES02060.1>

- Box, S.E., Moll-Stalcup, E.J., Frost, T.P. and Murphy, J.M., 1993. Preliminary geologic map of the Bethel and southern Russian Mission quadrangles, southwestern Alaska. US Department of the Interior, US Geological Survey.
- Bradley, D., Haeussler, P.J., O'Sullivan, P., Friedman, R., Till, A., Bradley, D. and Trop, J., 2009. Detrital zircon geochronology of Cretaceous and Paleogene strata across the south-central Alaskan convergent margin (No. 1760-F). US Geological Survey. <https://doi.org/10.3133/pp1760F>
- Brown, S.R., Gibson, H.D., Andrews, G.D., Thorkelson, D.J., Marshall, D.D., Vervoort, J.D. and Rayner, N., 2012. New constraints on Eocene extension within the Canadian Cordillera and identification of Phanerozoic protoliths for footwall gneisses of the Okanagan Valley shear zone. *Lithosphere*, v.4, n.4, p.354-377. <https://doi.org/10.1130/L199.1>
- Canil, D., Johnston, S.T., D'Souza, R.J. & Heaman, L.M., (2015). Protolith of ultramafic rocks in the Kluane Schist, Yukon, and implications for arc collisions in the northern Cordillera. *Canadian Journal of Earth Sciences*, v.52, n.7, p.431-443. <https://doi.org/10.1139/cjes-2014-0138>
- Cecil, M.R., Gehrels, G., Ducea, M.N. and Patchett, P.J., 2011. U-Pb-Hf characterization of the central Coast Mountains batholith: Implications for petrogenesis and crustal architecture. *Lithosphere*, v.3, n.4, p.247-260. <https://doi.org/10.1130/L134.1>
- Cecil, M.R., Rusmore, M.E., Gehrels, G.E., Woodsworth, G.J., Stowell, H.H., Yokelson, I.N., Chisom, C., Trautman, M. and Homan, E., 2018. Along-strike variation in the magmatic tempo of the Coast Mountains batholith, British Columbia, and implications for processes controlling episodicity in arcs. *Geochemistry, Geophysics, Geosystems*, v.19, n.11, p.4274-4289. <https://doi.org/10.1029/2018GC007874>
- Clift, P.D., Draut, A.E., Kelemen, P.B., Blusztajn, J. and Greene, A., 2005. Stratigraphic and geochemical evolution of an oceanic arc upper crustal section: The Jurassic Talkeetna Volcanic Formation, south-central Alaska. *Geological Society of America Bulletin*, v.117, n.7-8, p.902-925. <https://doi.org/10.1130/B25638.1>

- Colpron, M., Sack, P.J., Crowley, J.L., Beranek, L.P. and Allan, M.M., 2022, Late Triassic to Jurassic magmatic and tectonic evolution of the Intermontane terranes in Yukon, northern Canadian Cordillera: Transition from arc to syn-collisional magmatism and post-collisional lithospheric delamination: *Tectonics*, v.41, 10.1029/2021TC007060.
- Colpron, M. and Nelson, J.L., 2011. A Digital Atlas of terranes for the Northern Cordillera; British Columbia Ministry of Energy and Mines, BCGS GeoFile 2011-11.
- Colpron, M., Israel, S. and Friend, M. (compilers), 2016. Yukon Plutonic Suites. Yukon Geological Survey, Open File 2016-37, scale 1:750000.
- Colpron, M., Nelson, J.L., and Murphy, D.C., 2006, A tectonostratigraphic framework for the pericratonic terranes of the Northern Cordillera, in Colpron, M., and Nelson, J.L., eds., *Paleozoic Evolution and Metallogeny of Pericratonic terranes at the Ancient Pacific Margin of North America, Canadian and Alaskan Cordillera*: Geological Association of Canada Special Paper 45, p.1– 23.
- Colpron, M., Nelson, J.L., & Murphy, D.C. 2007. Northern Cordilleran terranes and their interactions through time. *GSA Today*, v.17, p.4–10
<https://doi.org/10.1130/GSAT01704-5A.1>
- Condon, D.J., Schoene, B., McLean, N.M., Bowring, S.A. and Parrish, R.R., 2015. Metrology and traceability of U–Pb isotope dilution geochronology (EARTHTIME Tracer Calibration Part I). *Geochimica et Cosmochimica Acta*, v.164, p.464-480.
<https://doi.org/10.1016/j.gca.2015.05.026>
- Coutts, D.S., Matthews, W.A. and Hubbard, S.M., 2019. Assessment of widely used methods to derive depositional ages from detrital zircon populations. *Geoscience Frontiers*, v.10, n.4, p.1421-1435. <https://doi.org/10.1016/j.gsf.2018.11.002>
- Cowan, D.S., 1978. Origin of blueschist-bearing chaotic rocks in the Franciscan Complex, San Simeon, California. *Geological Society of America Bulletin*, v.89, n.9, p.1415-1423. [https://doi.org/10.1130/0016-7606\(1978\)89<1415:OOBCRI>2.0.CO;2](https://doi.org/10.1130/0016-7606(1978)89<1415:OOBCRI>2.0.CO;2)

- Cowan, D.S., 1985. Structural styles in Mesozoic and Cenozoic mélanges in the western Cordillera of North America. *Geological Society of America Bulletin*, v.96, n.4, p.451-462. [https://doi.org/10.1130/0016-7606\(1985\)96<451:SSIMAC>2.0.CO;2](https://doi.org/10.1130/0016-7606(1985)96<451:SSIMAC>2.0.CO;2)
- Crawford, M.L., Klepeis, K.A., Gehrels, G. and Isachsen, C., 1999. Batholith emplacement at mid-crustal levels and its exhumation within an obliquely convergent margin. *Tectonophysics*, v.312, n.1, p.57-78. [https://doi.org/10.1016/S0040-1951\(99\)00170-5](https://doi.org/10.1016/S0040-1951(99)00170-5)
- Damant, K.A., Enkelmann, E. and Jess, S., 2023. Prolonged post-orogenic extension in the southeastern Canadian Cordillera: Miocene reactivation of the Columbia River Fault. *Tectonophysics*, v.850, p.229763. <https://doi.org/10.1016/j.tecto.2023.229763>
- Davidson, C., & McPhillips, D., (2007), Along strike variations in metamorphism and deformation of the strata of the Kahiltna basin, south-central Alaska, in Ridgway, K.D., Trop, J.M., Glen, J.M.G., & O'Neill, J.M., eds., *Tectonic growth of a collisional continental margin: crustal evolution of southern Alaska: Geological Society of America Special Paper 431*, p. 439–454. [https://doi.org/10.1130/2007.2431\(17\)](https://doi.org/10.1130/2007.2431(17))
- Davidson, C., Hollister, L.S. and Schmid, S.M., 1992. Role of melt in the formation of a deep-crustal compressive shear zone: The McClaren Glacier Metamorphic Belt, south central Alaska. *Tectonics*, v.11, n.2, p.348-359. <https://doi.org/10.1029/91TC02907>
- Day, E.M., Pavlis, T.L. and Amato, J.M., 2016. Detrital zircon ages indicate an Early Cretaceous episode of blueschist-facies metamorphism in southern Alaska: Implications for the Mesozoic paleogeography of the northern Cordillera. *Lithosphere*, v.8, n.5, p.451-462. <https://doi.org/10.1130/L525.1>
- Davies, J.H. and von Blanckenburg, F., 1995. Slab breakoff: a model of lithosphere detachment and its test in the magmatism and deformation of collisional orogens. *Earth and planetary science letters*, v.129, n.1-4, p.85-102. [https://doi.org/10.1016/0012-821X\(94\)00237-S](https://doi.org/10.1016/0012-821X(94)00237-S)

- Dickinson, W.R. and Gehrels, G.E., 2009. Use of U–Pb ages of detrital zircons to infer maximum depositional ages of strata: a test against a Colorado Plateau Mesozoic database. *Earth and Planetary Science Letters*, v.288, n.1-2, p.115-125.
<https://doi.org/10.1016/j.epsl.2009.09.013>
- Dickinson, W.R., 2004. Evolution of the North American Cordillera. *Annual Review of Earth and Planetary Sciences* v.32, p.13-45.
<https://doi.org/10.1146/annurev.earth.32.101802.120257>
- Elder, W., & Box, S. (1992). Late Cretaceous Inoceramid Bivalves of the Kuskokwim Basin, Southwestern Alaska, and Their Implications for Basin Evolution. *Journal of Paleontology*, v.66, n.S26, p.1-39. doi:10.1017/S0022336000061400
- Engebretson, D.C., Cox, A., and Thompson, G.A., 1984. Correlation of plate motions with continental tectonics: Laramide to Basin-Range. *Tectonics*, v.3, n.2, p.115-119. <https://doi.org/10.1029/TC003i002p00115>
- Erdmer, P. & Mortensen, J.K., 1993. A 1200-km-long Eocene metamorphic-plutonic belt in the northwestern Cordillera: Evidence from southwest Yukon. *Geology*, v.21, n.11, p.1039-1042. [https://doi.org/10.1130/0091-7613\(1993\)021<1039:AKLEMP>2.3.CO;2](https://doi.org/10.1130/0091-7613(1993)021<1039:AKLEMP>2.3.CO;2)
- Ewing, T.E., 1980. Paleogene tectonic evolution of the Pacific Northwest. *The Journal of Geology*, v.88, n.6, p.619-638. <https://doi.org/10.1086/628551>
- Fasulo, C.R., Ridgway, K.D. and Trop, J.M., 2020. Detrital zircon geochronology and Hf isotope geochemistry of Mesozoic sedimentary basins in south-central Alaska: Insights into regional sediment transport, basin development, and tectonics along the NW Cordilleran margin. *Geosphere*, v.16, n.5, p.1125-1152.
<https://doi.org/10.1130/GES02221.1>
- Fisher, C.M., Vervoort, J.D. and DuFrane, S.A., 2014. Accurate Hf isotope determinations of complex zircons using the “laser ablation split stream” method. *Geochemistry, Geophysics, Geosystems*, v.15, n.1, p.121-139.
<https://doi.org/10.1002/2013GC004962>

- Friend, M., 2022. "Tectonomagmatic Framework for Late Cretaceous postsubduction Magmatism in West-Central and Southern Yukon." [Unpublished master's thesis], University of British Columbia. <http://dx.doi.org/10.14288/1.0407250>.
- Gehrels, G. and Pecha, M., 2014. Detrital zircon U-Pb geochronology and Hf isotope geochemistry of Paleozoic and Triassic passive margin strata of western North America. *Geosphere*, v.10, n.1, p.49-65. <https://doi.org/10.1130/GES00889.1>
- Gehrels, G., 2014. Detrital zircon U-Pb geochronology applied to tectonics. *Annual Review of Earth and Planetary Sciences*, v.42, p.127-149. <https://doi.org/10.1146/annurev-earth-050212-124012>
- Gehrels, G., Rusmore, M., Woodsworth, G., Crawford, M., Andronicos, C., Hollister, L., Patchett, J., Ducea, M., Butler, R., Klepeis, K. & Davidson, C., (2009). U-Th-Pb geochronology of the Coast Mountains batholith in north-coastal British Columbia: Constraints on age and tectonic evolution. *Geological Society of America Bulletin*, v.121, n.9-10, p.1341-1361. <https://doi.org/10.1130/B26404.1>
- Gehrels, G.E., 2001. Geology of the Chatham Sound region, southeast Alaska and coastal British Columbia. *Canadian Journal of Earth Sciences*, v.38, n.11, p.1579-1599. <https://doi.org/10.1139/e01-040>
- Gehrels, G.E., McClelland, W.C., Samson, S.D. and Patchett, P.J., 1991. U-Pb geochronology of detrital zircons from a continental margin assemblage in the northern Coast Mountains, southeastern Alaska. *Canadian Journal of Earth Sciences*, v.28, n.8, p.1285-1300. <https://doi.org/10.1139/e91-114>
- Gehrels, G.E., McClelland, W.C., Samson, S.D., Patchett, P.J. and Orchard, M.J., 1992. Geology of the western flank of the Coast Mountains between Cape Fanshaw and Taku Inlet, southeastern Alaska. *Tectonics*, v.11, n.3, p.567-585. <https://doi.org/10.1029/92TC00482>
- Gerstenberger, H. and Haase, G., 1997. A highly effective emitter substance for mass spectrometric Pb isotope ratio determinations. *Chemical Geology*, v.136, n.3-4, p.309-312. [https://doi.org/10.1016/S0009-2541\(96\)00033-2](https://doi.org/10.1016/S0009-2541(96)00033-2)

- Goldfarb, R.J., Ayuso, R., Miller, M.L., Ebert, S.W., Marsh, E.E., Petsel, S.A., Miller, L.D., Bradley, D., Johnson, C. and McClelland, W., 2004. The Late Cretaceous Donlin Creek gold deposit, Southwestern Alaska: Controls on epizonal ore formation. *Economic Geology*, v.99, n.4, p.643-671.
<https://doi.org/10.2113/gsecongeo.99.4.643>
- Grond, H.C., Churchill, S.J., Armstrong, R.L., Harakal, J.E., and Nixon, G.T., 1984, Late Cretaceous age of the Hutshi, Mount Nansen, and Carmacks Groups, southwestern Yukon Territory and northwestern British Columbia: *Canadian Journal of Earth Sciences*, v. 21, p.554–558.
- Greene, A.R., Scoates, J.S. and Weis, D., 2008. Wrangellia flood basalts in Alaska: A record of plume-lithosphere interaction in a Late Triassic accreted oceanic plateau. *Geochemistry, Geophysics, Geosystems*, v.9, n.12.
<https://doi.org/10.1029/2008GC002092>
- Greene, A.R., Scoates, J.S., Weis, D. and Israel, S., 2009. Geochemistry of Triassic flood basalts from the Yukon (Canada) segment of the accreted Wrangellia oceanic plateau. *Lithos*, v.110, n.1-4, p.1-19.
<https://doi.org/10.1016/j.lithos.2008.11.010>
- Hampton, B.A., Ridgway, K.D. and Gehrels, G.E., 2010. A detrital record of Mesozoic island arc accretion and exhumation in the North American Cordillera: U-Pb geochronology of the Kahiltna basin, southern Alaska. *Tectonics*, v.29, n.4.
<https://doi.org/10.1029/2009TC002544>
- Hart, C.J., Goldfarb, R.J., Lewis, L.L. and Mair, J.L., 2004. The Northern Cordilleran Mid-Cretaceous plutonic province: Ilmenite/magnetite-series granitoids and intrusion-related mineralisation. *Resource Geology*, v.54, n.3, pp.253-280.
<https://doi.org/10.1111/j.1751-3928.2004.tb00206.x>
- Hiess, J., Condon, D.J., McLean, N. and Noble, S.R., 2012. $^{238}\text{U}/^{235}\text{U}$ systematics in terrestrial uranium-bearing minerals. *Science*, v.335, n.6076, p.1610-1614. DOI: 10.1126/science.1215507

- Hollister, L.S., 1982. Metamorphic evidence for rapid (2 mm/yr) uplift of a portion of the Central Gneiss Complex, Coast Mountains, BC. *The Canadian Mineralogist*, v.20, n.3, p.319-332.
- Horstwood, M.S., Košler, J., Gehrels, G., Jackson, S.E., McLean, N.M., Paton, C., Pearson, N.J., Sircombe, K., Sylvester, P., Vermeesch, P. and Bowring, J.F., 2016. Community-derived standards for LA-ICP-MS U-(Th-) Pb geochronology– Uncertainty propagation, age interpretation and data reporting. *Geostandards and Geoanalytical Research*, v.40, n.3, p.311-332. <https://doi.org/10.1111/j.1751-908X.2016.00379.x>
- Hults, C.P., Wilson, F.H., Donelick, R.A. and O’Sullivan, P.B., 2013. Two flysch belts having distinctly different provenance suggest no stratigraphic link between the Wrangellia composite terrane and the paleo-Alaskan margin. *Lithosphere*, v.5, n.6, p.575-594. doi: <https://doi.org/10.1130/L310.1>
- Ireland, T.R. and Williams, I.S., 2003. Considerations in zircon geochronology by SIMS. *Reviews in Mineralogy and Geochemistry*, v.53, n.1, p.215-241. <https://doi.org/10.2113/0530215>
- Israel, S., Cobbett, R., Westberg, E., Stanley, B. & Hayward, N., 2011b. Preliminary bedrock geology of the Ruby Ranges, southwestern Yukon, (Parts of NTS 115G, 115H, 115A and 115B) (1:150 000 scale). Yukon Geological Survey, Open File 2011-2.
- Israel, S., Murphy, D., Bennett, V., Mortensen, J. and Crowley, J., 2011a. New insights into the geology and mineral potential of the Coast Belt in southwestern Yukon. In: *Yukon Exploration and Geology 2010*, MacFarlane, K.E., Weston, L.H., and Relf, C. (eds.), Yukon Geological Survey, p.101-123.
- Jackson, S.E., Pearson, N.J., Griffin, W.L. and Belousova, E.A., 2004. The application of laser ablation-inductively coupled plasma-mass spectrometry to in situ U–Pb zircon geochronology. *Chemical Geology*, v.211, n.1-2, p.47-69. <https://doi.org/10.1016/j.chemgeo.2004.06.017>

- Johnson, B.J. and Brown, R.L., 1996. Crustal structure and early Tertiary extensional tectonics of the Omineca belt at 51 N latitude, southern Canadian Cordillera. *Canadian Journal of Earth Sciences*, v.33, n.12, p.1596-1611.
<https://doi.org/10.1139/e96-121>
- Johnston, S.T., Jane Wynne, P., Francis, D., Hart, C.J., Enkin, R.J. and Engebretson, D.C., 1996. Yellowstone in Yukon: the late Cretaceous Carmacks Group. *Geology*, v.24, n.11, p.997-1000.
[https://doi.org/10.1130/0091-7613\(1996\)024<0997:YIYTLC>2.3.CO;2](https://doi.org/10.1130/0091-7613(1996)024<0997:YIYTLC>2.3.CO;2)
- Jones, J.V., Todd, E., Box, S.E., Haeussler, P.J., Holm-Denoma, C.S., Karl, S.M., Graham, G.E., Bradley, D.C., Kylander-Clark, A.R., Friedman, R.M. and Layer, P.W., 2021. Cretaceous to Oligocene magmatic and tectonic evolution of the western Alaska Range: Insights from U-Pb and $^{40}\text{Ar}/^{39}\text{Ar}$ geochronology. *Geosphere*, v.17, n.1, p.118-153.
<https://doi.org/10.1130/GES02303.1>
- Joyce, N.L., Colpron, M., Allan, M.M., Sack, P.J., Crowley, J.L and Chapman, J.B., 2016. New U-Pb zircon dates from the Aishihik batholith, southern Yukon. In: *Yukon Exploration and Geology 2015*, K.E. MacFarlane and M.G. Nordling (eds.), Yukon Geological Survey, p.131-149, plus digital appendices.
- Kalbas, J. L., Ridgway, K. D., & Gehrels, G. E., 2007. Stratigraphy, depositional systems, and provenance of the Lower Cretaceous Kahiltna assemblage, western Alaska Range: Basin development in response to oblique collision. In K. D. Ridgway, J. M. Trop, J. M. G. Glen & J. M. O'Neill (Eds.), *Tectonic Growth of a Collisional Continental Margin: Crustal Evolution of Southern Alaska*. v.431, p.307–343. *Geology Society of America Special Paper*.
[https://doi.org/10.1130/2007.2431\(13\)](https://doi.org/10.1130/2007.2431(13))
- Kapp, P.A. and Gehrels, G.E., 1998. Detrital zircon constraints on the tectonic evolution of the Gravina belt, southeastern Alaska. *Canadian Journal of Earth Sciences*, v.35, n.3, p.253-268. <https://doi.org/10.1139/e97-110>

- Krogh, T. E., 1973. A low-contamination method for hydrothermal decomposition of zircon and extraction of U and Pb for isotopic age determinations. *Geochimica et Cosmochimica Acta* v. 37, n.3, p.485-494. [https://doi.org/10.1016/0016-7037\(73\)90213-5](https://doi.org/10.1016/0016-7037(73)90213-5)
- Lowey, G.W., Sinclair, W.D. and Hills, L.V., 1986. Additional K–Ar isotopic dates for the Carmacks Group (Upper Cretaceous), west central Yukon. *Canadian Journal of Earth Sciences*, v.23, n.11, p.1857-1859. <https://doi.org/10.1139/e86-171>
- Lowey, G.W., 2000. The Tatshenshini shear zone (new) in southwestern Yukon, Canada: Comparison with the Coast shear zone in British Columbia and southeastern Alaska and implications regarding the Shakwak suture. *Tectonics*, v.19, n.3, p.512-528. <https://doi.org/10.1029/1999TC001119>
- Lowey, G.W., 2007. Lithofacies analysis of the Dezadeash Formation (Jura–Cretaceous), Yukon, Canada: The depositional architecture of a mud/sand-rich turbidite system. *Sedimentary Geology*, v.198, n.3-4, p.273-291. <https://doi.org/10.1016/j.sedgeo.2006.12.011>
- Lowey, G.W., 2011. Volcaniclastic gravity flow deposits in the Dezadeash Formation (Jura-Cretaceous), Yukon, Canada: Implications regarding the tectonomagmatic evolution of the Chitina arc in the northern Cordillera of North America. *Lithos*, v.125, n.1-2, p.86-100. <https://doi.org/10.1016/j.lithos.2011.01.014>
- Lowey, G.W., 2019. Provenance analysis of the Dezadeash Formation (Jurassic–Cretaceous), Yukon, Canada: Implications regarding a linkage between the Wrangellia composite terrane and the western margin of Laurasia. *Canadian Journal of Earth Sciences*, v.56, n.1, p.77-100. <https://doi.org/10.1139/cjes-2017-0244>
- Lowey, G.W., 2021. Very low-grade metamorphism of the Dezadeash Formation (Jura–Cretaceous): Constraints on the tectonometamorphic history of the Dezadeash flysch basin and implications regarding the tectonic evolution of the Northern Cordillera of Alaska and Yukon. *AIMS Geosciences*, v.7, n.3, p.355-389. doi: 10.3934/geosci.2021022

- Manor, M.J., Piercey, S.J., Murphy, D.C. and Wall, C.J., 2022. Age and Chemostratigraphy of the Finlayson Lake District, Yukon: Implications for Volcanogenic Massive Sulfide (VMS) Mineralization and Tectonics along the Western Laurentian Continental Margin. *Lithosphere*, v.1, p.4584611. <https://doi.org/10.2113/2022/4h584611>
- Manselle, P., Brueseke, M.E., Trop, J.M., Benowitz, J.A., Snyder, D.C. and Hart, W.K., 2020. Geochemical and stratigraphic analysis of the Chisana Formation, Wrangellia terrane, eastern Alaska: Insights into Early Cretaceous magmatism and tectonics along the northern Cordilleran margin. *Tectonics*, v.39, n.8, p.e2020TC006131. <https://doi.org/10.1029/2020TC006131>
- Manuszak, J.D., Ridgway, K.D., Trop, J.M., and Gehrels, G.E., 2007. Sedimentary record of the tectonic growth of a collisional continental margin: Upper Jurassic-Lower Cretaceous Nutzotin Mountains sequence, eastern Alaska Range, Alaska, in Ridgway, K.D., Trop, J.M., Glen, J.M.G., and O'Neill, J.M., eds., *Tectonic Growth of a Collisional Continental Margin: Crustal Evolution of Southern Alaska*: Geological Society of America Special Paper 431, [https://doi.org/10.1130/2007.2431\(14\)](https://doi.org/10.1130/2007.2431(14))
- Mattinson, J.M., 2005. Zircon U–Pb chemical abrasion (“CA-TIMS”) method: combined annealing and multi-step partial dissolution analysis for improved precision and accuracy of zircon ages. *Chemical Geology*, v.220, n.1-2, p.47-66. <https://doi.org/10.1016/j.chemgeo.2005.03.011>
- McClelland, W. C., & Mattinson, J. M. (2000). Cretaceous-Tertiary evolution of the western Coast Mountains, central southeastern Alaska. In H. H. Stowell, & W. C. McClelland (Eds.), *Tectonics of the Coast Mountains, southeastern Alaska and British Columbia*, v.343, p.159–182. Boulder, CO: Geological Society of America Special Paper.
- McClelland, W.C., Anovitz, L.M. and Gehrels, G.E., 1991. Thermobarometric constraints on the structural evolution of the Coast Mountains batholith, central southeastern Alaska. *Canadian Journal of Earth Sciences*, v.28, n.6, p.912-928. <https://doi.org/10.1139/e91-083>

- McClelland, W.C., Gehrels, G.E. & Saleeby, J.B., (1992a). Upper Jurassic-Lower Cretaceous basinal strata along the Cordilleran margin: Implications for the accretionary history of the Alexander-Wrangellia-Peninsular terrane. *Tectonics*, v.11, n.4, p.823-835. <https://doi.org/10.1029/92TC00241>
- McClelland, W.C., Gehrels, G.E., Samson, S.D. and Patchett, P.J., 1992b. Structural and geochronologic relations along the western flank of the Coast Mountains batholith: Stikine River to Cape Fanshaw, central southeastern Alaska. *Journal of Structural Geology*, v.14, n.4, p.475-489. [https://doi.org/10.1016/0191-8141\(92\)90107-8](https://doi.org/10.1016/0191-8141(92)90107-8)
- McLean, N.M., Bowring, J.F. and Bowring, S.A., 2011. An algorithm for U-Pb isotope dilution data reduction and uncertainty propagation. *Geochemistry, Geophysics, Geosystems*, v.12, n.6. <https://doi.org/10.1029/2010GC003478>
- McLean, N.M., Condon, D.J., Schoene, B. and Bowring, S.A., 2015. Evaluating uncertainties in the calibration of isotopic reference materials and multi-element isotopic tracers (EARTHTIME Tracer Calibration Part II). *Geochimica et Cosmochimica Acta*, v.164, p.481-501. <https://doi.org/10.1016/j.gca.2015.02.040>
- Mezger, J.E., 1997. Tectonometamorphic evolution of the Kluane metamorphic assemblage, southwest Yukon: evidence for Late Cretaceous eastward subduction of oceanic crust underneath North America. [Unpublished PhD thesis, University of Alberta], 306 p. <https://doi.org/10.7939/R3DJ58N76>
- Mezger, J.E., 2000. 'Alpine-type' ultramafic rocks of the Kluane metamorphic assemblage, southwest Yukon: Oceanic crust fragments of a late Mesozoic back-arc basin along the northern Coast Belt. In: Yukon Exploration and Geology 1999, D.S. Emond and L.H. Weston (eds.), Exploration and Geological Services Division, Yukon, Indian and Northern Affairs Canada, p.127-138.
- Mezger, J.E., Chacko, T. and Erdmer, P., 2001b. Metamorphism at a late Mesozoic accretionary margin: a study from the Coast Belt of the North American Cordillera. *Journal of Metamorphic Geology*, v.19, n.2, p.121-137. <https://doi.org/10.1046/j.0263-4929.2000.00300.x>

- Mezger, J.E., Creaser, R.A., Erdmer, P. and Johnston, S.T., 2001a. A Cretaceous back-arc basin in the Coast Belt of the northern Canadian Cordillera: evidence from geochemical and neodymium isotope characteristics of the Kluane metamorphic assemblage, southwest Yukon. *Canadian Journal of Earth Sciences*, v.38, n.1, p.91-103. <https://doi.org/10.1139/e00-076>
- Mezger, K. and Krogstad, E.J., 1997. Interpretation of discordant U-Pb zircon ages: An evaluation. *Journal of Metamorphic Geology*, v.15, n.1, p.127-140. <https://doi.org/10.1111/j.1525-1314.1997.00008.x>
- Miller, M.L., and Bundtzen, T.K., 1994, Generalized geologic map of the Iditarod Quadrangle, Alaska, showing potassium-argon, major-oxide, trace-element, fossil, paleocurrent, and archaeological sample localities: U.S. Geological Survey Miscellaneous Field Studies Map 2219-A, 48 p., 1 sheet, scale 1:250,000. <https://doi.org/10.3133/mf2219A>
- Miller, M.L., Bradley, D., Kalbas, J.L., Friedman, R. and O'Sullivan, P.B., 2007. Detrital zircon geochronology of the Upper Cretaceous Kuskokwim Group, Southwestern Alaska. In *Geological Society of America Abstracts with Programs*, v.39, n.6, p. 489.
- Monger, J.W. & Gibson, H.D., 2019. Mesozoic-Cenozoic deformation in the Canadian Cordillera: The record of a "Continental bulldozer"? *Tectonophysics*, v.757, p.153-169. <https://doi.org/10.1016/j.tecto.2018.12.023>
- Monger, J.W., (2014). Logan Medallist 1. Seeking the suture: The Coast-Cascade conundrum. *Geoscience Canada*, v.41, n.4, p.379-398. <https://doi.org/10.12789/geocanj.2014.41.058>
- Monger, J.W.H., Price, R.A., & Tempelman-Kluit, D.J., 1982. Tectonic accretion and the origin of the two major metamorphic and tectonic belts in the Canadian Cordillera. *Geology*, v.10, n.2, p.70-75. [https://doi.org/10.1130/00917613\(1982\)10<70:TAATOO>2.0.CO](https://doi.org/10.1130/00917613(1982)10<70:TAATOO>2.0.CO)

- Monger, J.W.H., van der Heyden, P., Journeay, J.M., Evenchick, C.A. & Mahoney, J.B., (1994). Jurassic-Cretaceous basins along the Canadian Coast Belt: Their bearing on pre-mid-Cretaceous sinistral displacements. *Geology*, v.22, n.2, p.175-178. [https://doi.org/10.1130/0091-7613\(1994\)022<0175:JCBATC>2.3.CO;2](https://doi.org/10.1130/0091-7613(1994)022<0175:JCBATC>2.3.CO;2)
- Mooney, P.R., 2010, *Geology of the Clearwater Mountains and southern boundary of the Alaska Range Suture Zone* [M.S. thesis]: Davis, University of California, 93 p.
- Morris, G.A. and Creaser, R.A., 2008. Correlation of mid-Cretaceous granites with source terranes in the northern Canadian Cordillera. *Canadian Journal of Earth Sciences*, v.45, n.3, p.389-403. <https://doi.org/10.1139/E08-002>
- Mortensen, J.K., and Erdmer, P., 1992, U-Pb, ⁴⁰Ar-³⁹Ar, and K-Ar ages for metamorphism of the Kluane and Aishihik assemblages in southwestern Yukon Territory, in *Radiogenic Age and Isotopic Studies: Report 6*; by Geological Survey of Canada; Geological Survey of Canada, n. 92-2, p. 135-140, <https://doi.org/10.4095/134174>
- Mortensen, J.K., Emon, K., Johnston, S.T. and Hart, C.J.R., 2000. Age, geochemistry, paleotectonic setting and metallogeny of Late Triassic- Early Jurassic intrusions in the Yukon and eastern Alaska: A preliminary report. In: *Yukon Exploration and Geology 1999*, D.S. Emond and L.H. Weston (eds.), Exploration and Geological Services Division, Yukon, Indian and Northern Affairs Canada, p.139-144.
- Mortensen, J.K., Hart, C.J.R., Tarswell, J. and Allan, M.M., 2016. U-Pb zircon age and Pb isotopic constraints on the age and origin of porphyry and epithermal vein mineralization in the eastern Dawson Range, Yukon. In: *Yukon Exploration Geology 2015*, K.E. MacFarlane and M.G. Nordling (eds.), Yukon Geological Survey, p.165-185, including appendices.
- Nokleberg, W.J., Jones, D.L. and Silberling, N.J., 1985. Origin and tectonic evolution of the Maclaren and Wrangellia terranes, eastern Alaska Range, Alaska. *Geological Society of America Bulletin*, v.96, n.10, p.1251-1270. [https://doi.org/10.1130/0016-7606\(1985\)96<1251:OATEOT>2.0.CO;2](https://doi.org/10.1130/0016-7606(1985)96<1251:OATEOT>2.0.CO;2)

- Nokleberg, W.J., Aleinikoff, J.N., Bond, G.C., Ferrians, O.J., Jr., Herzon, P.L., Lange, I.M., Miyaoka, R.T., Richter, D.H., Schwab, C.E., Silva, S.R., Smith, T.E., and Zehner, R.E., 2015, Geologic maps of the eastern Alaska Range, Alaska (44 quadrangles, 1:63,360 scale), with descriptions and interpretations of map units: Alaska Division of Geological & Geophysical Surveys Report of Investigation 2015-6, 64 p., 45 sheets, scale 1:63,360. <https://doi.org/10.14509/29444>
- Parrish, R.R., 1995. Thermal evolution of the southeastern Canadian Cordillera. *Canadian Journal of Earth Sciences*, v.32, n.10, p.1618-1642. <https://doi.org/10.1139/e95-130>
- Parrish, R.R., Carr, S.D. and Parkinson, D.L., 1988. Eocene extensional tectonics and geochronology of the southern Omineca Belt, British Columbia and Washington. *Tectonics*, v.7, n.2, p.181-212. <https://doi.org/10.1029/TC007i002p00181>
- Parsons, A.J., McClelland, W.C., Zagorevski, A., Ryan, J.J., Coleman, M.J., Clevens, N. and van Staal, C.R., 2022. U-Pb Zircon Geochronology from the Northern Cordillera, Central Yukon, With Implications for Its Tectonic Assembly. *Tectonics*, v.41, n.2, p.e2021TC006918. <https://doi.org/10.1029/2021TC006918>
- Paton, C., Hellstrom, J., Paul, B., Woodhead, J. and Hergt, J., 2011. Lolite: Freeware for the visualisation and processing of mass spectrometric data. *Journal of Analytical Atomic Spectrometry*. doi:10.1039/c1ja10172b.
- Paton, C., Woodhead, J., Hellstrom, J., Hergt, J., Greig, A. and Maas, R., 2010 Improved laser ablation U-Pb zircon geochronology through robust down-hole fractionation correction. *G Cubed*, v.11, doi:10.1029/2009GC002618.
- Patton, William W., Jr., Wilson, Fredric H, Labay, Keith A., and Shew, Nora, 2009, Geologic map of the Yukon-Koyukuk Basin, Alaska: U.S. Geological Survey Scientific Investigations Map 2909, scale 1:500,000, 2 sheets and pamphlet <https://pubs.usgs.gov/sim/2909/>.

- Pavlis, T.L., Amato, J.M., Trop, J.M., Ridgway, K.D., Roeske, S.M. and Gehrels, G.E., 2019. Subduction polarity in ancient arcs: A call to integrate geology and geophysics to decipher the Mesozoic tectonic history of the Northern Cordillera of North America. *GSA Today*, v.29, n.11, p.4-10.
<https://doi.org/10.1130/GSATG465Y.1>
- Pecha, M.E., Gehrels, G.E., McClelland, W.C., Giesler, D., White, C. and Yokelson, I., 2016. Detrital zircon U-Pb geochronology and Hf isotope geochemistry of the Yukon-Tanana terrane, Coast Mountains, southeast Alaska. *Geosphere*, v.12, n.5, p.1556-1574. <https://doi.org/10.1130/GES01303.1>
- Perrot, M., Tremblay, A. and David, J., 2017. Detrital zircon U-Pb geochronology of the Magog Group, southern Quebec—stratigraphic and tectonic implications for the Quebec Appalachians. *American Journal of Science*, v.317, n.10, p.1049-1094. DOI: <https://doi.org/10.2475/10.2017.01>
- Piercey, S.J., Mortensen, J.K. and Creaser, R.A., 2003. Neodymium isotope geochemistry of felsic volcanic and intrusive rocks from the Yukon–Tanana terrane in the Finlayson Lake Region, Yukon, Canada. *Canadian Journal of Earth Sciences*, v.40, n.1, p.77-97. <https://doi.org/10.1139/e02-094>
- Piercey, S.J., Nelson, J.L., Colpron, M., Dusel-Bacon, C., Simard, R.L. and Roots, C.F., 2006. Paleozoic magmatism and crustal recycling along the ancient Pacific margin of North America, northern Cordillera. *Paleozoic Evolution and Metallogeny of Pericratonic terranes at the Ancient Pacific Margin of North America, Canadian and Alaskan Cordillera: Geological Association of Canada, Special Paper*, v.45, p.281-322.
- Plafker, G., Nokleberg, W.J. and Lull, J.S., 1989. Bedrock geology and tectonic evolution of the Wrangellia, Peninsular, and Chugach terranes along the Trans-Alaska Crustal Transect in the Chugach Mountains and southern Copper River Basin, Alaska. *Journal of Geophysical Research: Solid Earth*, v.94, n.B4, p.4255-4295.
<https://doi.org/10.1029/JB094iB04p04255>

- Price, R. A., 1994, Cordilleran tectonics and the evolution of the western Canada sedimentary basin, in Mossop, G., and Shestin, I., eds., *Geologic atlas of the Western Canada Sedimentary Basin: Alberta Research Council and Canadian Society of Petroleum Geologists*, p.13–24.
- Rasmussen, K. L. (2013). The timing, composition, and petrogenesis of syn- to post-accretionary magmatism in the northern Cordilleran miogeocline, eastern Yukon and southwestern Northwest Territories (PhD thesis). The University of British Columbia, Vancouver, BC. Retrieved from:
<https://qopen.library.ubc.ca/cIRcle/collections/ubctheses/24/items/1.0071986>
- Reid, M., Finzel, E.S., Enkelmann, E., and McClelland, W.C., 2018, Detrital zircon provenance of Upper Jurassic–Upper Cretaceous forearc basin strata on the Insular terranes, south-central Alaska, *in* Ingersoll, R.V., Lawton, T.F., and Graham, S.A., eds., *Tectonics, Sedimentary Basins, and Provenance: A Celebration of William R. Dickinson's Career: Geological Society of America Special Paper 540*, p.1–20, [https://doi.org/10.1130/2018.2540\(25\)](https://doi.org/10.1130/2018.2540(25)).
- Ridgway, K.D., Trop, J.M., Nokleberg, W.J., Davidson, C.M. and Eastham, K.R., 2002. Mesozoic and Cenozoic tectonics of the eastern and central Alaska Range: Progressive basin development and deformation in a suture zone. *Geological Society of America Bulletin*, v.114, n.12, p.1480-1504.
[https://doi.org/10.1130/0016-7606\(2002\)114<1480:MACTOT>2.0.CO;2](https://doi.org/10.1130/0016-7606(2002)114<1480:MACTOT>2.0.CO;2)
- Rioux, M., Hacker, B., Mattinson, J., Kelemen, P., Blusztajn, J., and Gehrels, G., 2007, Magmatic development of an intra-oceanic arc: High-precision U-Pb zircon and whole-rock isotopic analyses from the accreted Talkeetna arc, south-central Alaska. *Geological Society of America Bulletin*, v.119, p.1168–1184,
<https://doi.org/10.1130/B25964.1>.
- Rubin, C.M. and Saleeby, J.B., 1991a. The Gravina Sequence: Remnants of a Mid-Mesozoic oceanic arc in southern southeast Alaska. *Journal of Geophysical Research: Solid Earth*, v.96, n.B9, p.14551-14568.
<https://doi.org/10.1029/91JB00591>

- Rubin, C.M. and Saleeby, J.B., 1991b. Tectonic framework of the upper Paleozoic and lower Mesozoic Alava sequence: a revised view of the polygenetic Taku terrane in southern southeast Alaska. *Canadian Journal of Earth Sciences*, v.28, n.6, p.881-893. <https://doi.org/10.1139/e91-08>
- Ruks, T.W., Piercey, S.J., Ryan, J.J., Villeneuve, M.E. and Creaser, R.A., 2006. Mid-to late Paleozoic K-feldspar augen granitoids of the Yukon-Tanana terrane, Yukon, Canada: Implications for crustal growth and tectonic evolution of the northern Cordillera. *Geological Society of America Bulletin*, v.118, n.9-10, p.1212-1231. <https://doi.org/10.1130/B25854.1>
- Rusmore, M.E., Woodsworth, G.J. and Gehrels, G.E., 2005. Two-stage exhumation of midcrustal arc rocks, Coast Mountains, British Columbia. *Tectonics*, v.24, n.5. <https://doi.org/10.1029/2004TC001750>
- Sack, P.J., Colpron, M., Crowley, J.L., Ryan, J.J., Allan, M.M., Beranek, L.P., Joyce, N.L., Mortensen, J.K., Israel, S. and Chapman, J.B., 2020. Atlas of Late Triassic to Jurassic plutons in the Intermontane terranes of Yukon. Yukon Geological Survey Open File 2020-1, p.365. <http://data.geology.gov.yk.ca/Reference/95839>
- Satkoski, A.M., Wilkinson, B.H., Hietpas, J., Samson, S.D., 2013. Likeness among detrital zircon populations - An approach to the comparison of age frequency data in time and space. *Geological Society of America Bulletin*, v.125, n.11-12, p.1783–1799. <https://doi.org/10.1130/B30888.1>
- Saylor, J.E. and Sundell, K.E., 2016. Quantifying comparison of large detrital geochronology data sets. *Geosphere*, v.12, n.1, p.203-220. <https://doi.org/10.1130/GES01237.1>
- Schoene, B., Crowley, J.L., Condon, D.J., Schmitz, M.D. and Bowring, S.A., 2006. Reassessing the uranium decay constants for geochronology using ID-TIMS U–Pb data. *Geochimica et Cosmochimica Acta*, v.70, n.2, p.426-445. <https://doi.org/10.1016/j.gca.2005.09.007>

- Selby, D., Creaser, R.A. and Nesbitt, B.E., 1999. Major and trace element compositions and Sr-Nd-Pb systematics of crystalline rocks from the Dawson Range, Yukon, Canada. *Canadian Journal of Earth Sciences*, v.36, n.9, p.1463-1481.
<https://doi.org/10.1139/e99-058>
- Sharman, G.R. and Malkowski, M.A., 2020. Needles in a haystack: Detrital zircon U-Pb ages and the maximum depositional age of modern global sediment. *Earth-Science Reviews*, v.203, p.103109.
<https://doi.org/10.1016/j.earscirev.2020.103109>
- Sigloch, K. & Mihalynuk, M.G., 2013. Intra-oceanic subduction shaped the assembly of Cordilleran North America. *Nature*, v.496, n.7443, p.50-56.
<https://doi.org/10.1038/nature12019>
- Sigloch, K. & Mihalynuk, M.G., 2017. Mantle and geological evidence for a Late Jurassic–Cretaceous suture spanning North America. *Geological Society of America Bulletin*, v.129, n.11-12, p.1489-1520. <https://doi.org/10.1130/B31529.1>
- Sláma, J., Košler, J., Condon, D.J., Crowley, J.L., Gerdes, A., Hanchar, J.M., Horstwood, M.S., Morris, G.A., Nasdala, L., Norberg, N. and Schaltegger, U., 2008. Plešovice zircon—a new natural reference material for U–Pb and Hf isotopic microanalysis. *Chemical Geology*, v.249, n.1-2, p.1-35.
<https://doi.org/10.1016/j.chemgeo.2007.11.005>
- Smith, T.E., 1981. *Geology of the Clearwater Mountains, south-central Alaska*, v.60. Division of Geological & Geophysical Surveys.
- Smith, T.E., and Turner, D.L., 1973, *Geochronology of the MaClaren metamorphic belt, south-central Alaska; A progress report: Isochron/West*, v.7, p.21-25.
- Söderlund, U., Patchett, P.J., Vervoort, J.D. and Isachsen, C.E., 2004. The ^{176}Lu decay constant determined by Lu–Hf and U–Pb isotope systematics of Precambrian mafic intrusions. *Earth and Planetary Science Letters*, v.219, n.3-4, p.311-324.
[https://doi.org/10.1016/S0012-821X\(04\)00012-3](https://doi.org/10.1016/S0012-821X(04)00012-3)

- Spencer, C.J., Kirkland, C.L. and Taylor, R.J., 2016. Strategies towards statistically robust interpretations of in situ U–Pb zircon geochronology. *Geoscience Frontiers*, v.7, n.4, p.581-589. <https://doi.org/10.1016/j.gsf.2015.11.006>
- Stanley, B., 2012. Structural geology and geochronology of the Kluane schist, southwestern Yukon Territory. [M.S. thesis]: University of Waterloo. <http://hdl.handle.net/10012/7096>.
- Stevens Goddard, A.L., Trop, J.M. and Ridgway, K.D., 2018. Detrital zircon record of a Mesozoic collisional forearc basin in south central Alaska: The tectonic transition from an oceanic to continental arc. *Tectonics*, v.37, n.2, p.529-557. <https://doi.org/10.1002/2017TC004825>
- Stout, J. H., 1965. Bedrock geology between Rainy Creek and the Denali fault, Eastern Alaska Range, Alaska. (Unpublished master's thesis). Fairbanks, AK: University of Alaska.
- Tempelman-Kluit, D. and Parkinson, D., 1986. Extension across the Eocene Okanagan crustal shear in southern British Columbia. *Geology*, v.14, n.4, p.318-321. [https://doi.org/10.1130/0091-7613\(1986\)14<318:EATEOC>2.0.CO;2](https://doi.org/10.1130/0091-7613(1986)14<318:EATEOC>2.0.CO;2)
- Thomas, W.A., 2011. Detrital-zircon geochronology and sedimentary provenance. *Lithosphere*, v.3, n.4, p.304-308. <https://doi.org/10.1130/RF.L001.1>
- Todd, E., Kylander-Clark, A., Wypych, A., Twelker, E. and Sicard, K.R., 2017. U-Pb and Lu-Hf isotope, age, and trace-element data from zircons at four sites in the western Alaska Range and Talkeetna Mountains, Alaska. State of Alaska, Department of Natural Resources, Division of Geological & Geophysical Surveys, Raw Data File 2017-2.
- Trop, J.M., Benowitz, J.A., Koepf, D.Q., Sunderlin, D., Brueseke, M.E., Layer, P.W. and Fitzgerald, P.G., 2020. Stitch in the ditch: Nutzotin Mountains (Alaska) fluvial strata and a dike record ca. 117–114 Ma accretion of Wrangellia with western North America and initiation of the Totschunda fault. *Geosphere*, v.16, n.1, p.82-110. <https://doi.org/10.1130/GES02127.1>

- Trop, J.M., Ridgway, K.D., Manuszak, J.D. and Layer, P., 2002. Mesozoic sedimentary-basin development on the allochthonous Wrangellia composite terrane, Wrangell Mountains basin, Alaska: A long-term record of terrane migration and arc construction. *Geological Society of America Bulletin*, v.114, n.6, p.693-717.
[https://doi.org/10.1130/0016-7606\(2002\)114<0693:MSBDOT>2.0.CO;2](https://doi.org/10.1130/0016-7606(2002)114<0693:MSBDOT>2.0.CO;2)
- van der Heyden, P., 1992. A Middle Jurassic to early Tertiary Andean-Sierran arc model for the Coast belt of British Columbia. *Tectonics*, v.11, n.1, p.82-97.
<https://doi.org/10.1029/91TC02183>
- Vermeesch, P. (2013), Multi-sample comparison of detrital age distributions, *Chemical Geology*. v.341, p.140–146. <http://dx.doi.org/10.1016/j.chemgeo.2013.01.010>
- Vermeesch, P., 2004. How many grains are needed for a provenance study? *Earth and Planetary Science Letters*, v.224, n.3-4, p.441-451.
<https://doi.org/10.1016/j.epsl.2004.05.037>
- Vermeesch, P., 2018a. IsoplotR: A free and open toolbox for geochronology. *Geoscience Frontiers*, v.9, n.5, p.1479-1493.
<https://doi.org/10.1016/j.gsf.2018.04.001>
- Vermeesch, P., 2018b. Dissimilarity measures in detrital geochronology. *Earth-Science Reviews*, v.178, p.310-321. <https://doi.org/10.1016/j.earscirev.2017.11.027>
- Vermeesch, P., 2021. Maximum depositional age estimation revisited. *Geoscience Frontiers*, v.12, n.2, p.843-850. <https://doi.org/10.1016/j.gsf.2020.08.008>
- Vermeesch, P., Resentini, A. and Garzanti, E., 2016. An R package for statistical provenance analysis. *Sedimentary Geology*, v.336, p.14-25.
<https://doi.org/10.1016/j.sedgeo.2016.01.009>
- Vervoort, J.D., Plank, T. and Prytulak, J., 2011. The Hf–Nd isotopic composition of marine sediments. *Geochimica et Cosmochimica Acta*, v.75, n.20, p.5903-5926.
<https://doi.org/10.1016/j.gca.2011.07.046>

- Vice L., 2017. Late Cretaceous to Paleocene evolution of the Blanchard River assemblage, southwest Yukon; implications for Mesozoic accretionary processes in the northwestern Cordillera, [M.S. Thesis], 2017, Burnaby, BC, Simon Fraser University.
- Vice, L., Gibson, H. D. & Israel, S., 2020. Late Cretaceous to Paleocene Tectonometamorphic Evolution of the Blanchard River Assemblage, Southwest Yukon: New Insight into the Terminal Accretion of Insular terranes in the Northern Cordillera. *Lithosphere*, 2020, v.1: 2298288. <https://doi.org/10.2113/2020/2298288>
- Waldien, T.S., Roeske, S.M. & Benowitz, J.A., 2021b. Tectonic underplating and dismemberment of the Maclaren-Kluane schist records Late Cretaceous terrane accretion polarity and ~480 km of Post-52 Ma dextral displacement on the Denali fault. *Tectonics*, v.40, p.10, e2020TC006677. <https://doi.org/10.1029/2020TC006677>
- Waldien, T.S., Roeske, S.M., Benowitz, J.A., Twelker, E. & Miller, M.S., 2021a. Oligocene-Neogene lithospheric-scale reactivation of Mesozoic terrane accretionary structures in the Alaska Range suture zone, southern Alaska, USA. *Geological Society of America Bulletin*, v.133, n.3-4, p.691-716. <https://doi.org/10.1130/B35665.1>
- Wallace, W.K., Hanks, C.L. and Rogers, J.F., 1989. The southern Kahiltna terrane: Implications for the tectonic evolution of southwestern Alaska. *Geological Society of America Bulletin*, v.101, n.11, p.1389-1407. [https://doi.org/10.1130/0016-7606\(1989\)101<1389:TSKTIF>2.3.CO;2](https://doi.org/10.1130/0016-7606(1989)101<1389:TSKTIF>2.3.CO;2)
- Widmann, P., Davies, J.H.F.L. and Schaltegger, U., 2019. Calibrating chemical abrasion: Its effects on zircon crystal structure, chemical composition and U-Pb age. *Chemical Geology*, v.511, p.1-10. <https://doi.org/10.1016/j.chemgeo.2019.02.026>
- Wiedenbeck, M.A.P.C., Alle, P., Corfu, F.Y., Griffin, W.L., Meier, M., Oberli, F.V., Quadt, A.V., Roddick, J.C. and Spiegel, W., 1995. Three natural zircon standards for U-Th-Pb, Lu-Hf, trace element and REE analyses. *Geostandards Newsletter*, v.19, n.1, p.1-23. <https://doi.org/10.1111/j.1751-908X.1995.tb00147.x>

- Wilson, F.H., Hults, C.P., Mull, C.G, and Karl, S.M, comps., 2015, Geologic map of Alaska: U.S. Geological Survey Scientific Investigations Map 3340, pamphlet v.196, 2 sheets, scale 1:1,584,000, <http://dx.doi.org/10.3133/sim3340>.
<https://doi.org/10.3133/sim3340>
- Wilson, F.H., Hults, C.P., Schmoll, H.R., Haeussler, P.J., Schmidt, J.M., Yehle, L.A. and Labay, K.A., 2012. Geologic map of the Cook Inlet region, Alaska, including parts of the Talkeetna, Talkeetna Mountains, Tyonek, Anchorage, Lake Clark, Kenai, Seward, Iliamna, Seldovia, Mount Katmai, and Afognak 1: 250,000-scale quadrangles, n. 3153, p. i-71. US Geological Survey.
<https://doi.org/10.3133/sim3153>
- Woodhead, J., Hergt, J., Shelley, M., Eggins, S. and Kemp, R., 2004. Zircon Hf-isotope analysis with an excimer laser, depth profiling, ablation of complex geometries, and concomitant age estimation. *Chemical Geology*, v.209, n1-2, p.121-135.
<https://doi.org/10.1016/j.chemgeo.2004.04.026>
- Wotzlaw, J.F., Hüsing, S.K., Hilgen, F.J. and Schaltegger, U., 2014. High-precision zircon U–Pb geochronology of astronomically dated volcanic ash beds from the Mediterranean Miocene. *Earth and Planetary Science Letters*, v.407, p.19-34.
<https://doi.org/10.1016/j.epsl.2014.09.025>
- Yokelson, I., Gehrels, G.E., Pecha, M., Giesler, D., White, C. and McClelland, W.C., 2015. U-Pb and Hf isotope analysis of detrital zircons from Mesozoic strata of the Gravina belt, southeast Alaska. *Tectonics*, v.34, n.10, p.2052-2066.
<https://doi.org/10.1002/2015TC003955>

Chapter 6. Conclusions

The metamorphic, deformational, and geochronological information presented within this thesis provides a direct record of the timing and tectonic nature of Insular terrane accretion within the southwest Yukon region of the Northern Cordillera. These datasets highlight that the Kluane Schist experienced a complex polymetamorphic evolution involving regional and contact events along with variable episodes of fluid infiltration (Chapters 3–5). The complexity of the Kluane Schist's metamorphic history made the accurate interpretation and integration of these independent datasets challenging. This said, by using such a multi-method approach and combining these independently derived datasets within the framework of fundamental observations such as those provided by fieldwork and petrography, I was successfully able to mitigate these issues. Petrological modelling and the definition of the specific phase relationships across the Kluane Schist (Chapter 3), both integral to petrochronology and the accurate determination of its *P-T-t-D* history (Chapter 4), are ground-truthed with direct observations of natural mineral assemblages and microstructure (Chapters 3 & 4). Interpretations made regarding the timing and paleotectonic environment of Kluane Schist deposition are interrogated with surrounding geological relationships and compared with similar datasets from other Jura-Cretaceous basins of the Northern Cordillera (Chapter 5).

When combined, the results presented in this thesis can be used to derive a coherent model for the evolution of the Kluane Schist, from its initial deposition, through metamorphism and to final exhumation (Chapter 5). This provides a modern analysis analogue for the Kluane Schist within the context of both the new and long-standing debates that surround the timing and tectonic nature of Insular terrane accretion within the Northern Cordillera (e.g., Monger, 2014; Sigloch & Mihalynuk, 2013; 2017; Pavlis *et al.*, 2019). The following sections provide a synopsis of the main conclusions I draw from the datasets presented within this thesis and bear on the primary research goals set in Chapter 1.

6.1.1. Re-evaluating the metamorphic and deformational evolution of the Kluane Schist

A collective understanding of both the metamorphic and deformational evolution of the Kluane Schist is key to unravelling the information it possesses regarding the timing and tectonic style of Insular terrane accretion within southwest Yukon. Previous studies have produced disparate interpretations into the geological processes governing its metamorphic and deformational character with limited insight into the tectonic processes driving its evolution (Erdmer & Mortensen, 1993; Mezger, 1997; Mezger *et al.*, 2001b; Israel *et al.*, 2011a). As such, testing these hypotheses and completing a re-evaluation of the tectono-metamorphic evolution of the Kluane Schist was a primary goal during the early work completed as part of this thesis.

This initial work involved the integration of fieldwork, structural geology, detailed petrography, and petrological modelling to reveal that the metamorphic evolution of the Kluane Schist is intrinsically coupled with deformation (Chapter 3). This differs from previous interpretations that suggest the metamorphic-deformational character preserved by the Kluane Schist either represents the juxtaposition of two distinct metamorphic belts (Erdmer & Mortensen, 1993) or the overprinting of an initial Barrovian-style metamorphic event by an extensive, 5–6 km wide, contact aureole (Mezger, 1997; Mezger *et al.*, 2001b). Additionally, this work defines mineral isograds across the Kluane Schist which document both an inverted metamorphic sequence preserved within its northern and eastern regions, as well as a correct way up sequence towards its southwestern contact with Kluane Lake (Chapter 3). Petrological modelling of the distinct mineral assemblages preserved across these metamorphic sequences quantifies two phases of metamorphism preserved within the Kluane Schist; initial sub-greenschist-facies metamorphism (M_1) is followed by a more penetrative episode of Buchan-style metamorphism (M_2) during which the Kluane Schist experienced P - T conditions between 3.0–3.5 kbar at 375–400 °C and 4–4.5 kbar at 700–750 °C (Chapter 3). Collectively, these metamorphic events are interpreted to track the evolution of the Kluane Schist from its initial collapse against North America to its progressive override by the flanking components of the North American margin which included the Yukon-Tanana terrane (Chapter 3). It is likely the Ruby Range batholith facilitated with the final stages and highest grades of Kluane Schist metamorphism, however, it was unlikely to act as the principal heat source responsible for developing the inverted, hot-side-up

metamorphic sequence preserved across the Kluane Schist (c.f., Mezger, 1997). In the absence of stratigraphic markers, the definition of these metamorphic sequences and mineral isograds additionally provided a basis for conducting the sampling transects used for the subsequent projects carried out as part of this thesis.

6.1.2. Constructing a *P-T-t-D* path for the Kluane Schist using *in-situ* monazite petrochronology

Prior to this work, the age of metamorphism experienced by the Kluane Schist was poorly constrained and provided limited insight into the timing of Insular terrane accretion within the southwest Yukon (e.g., Erdmer & Mortensen, 1993; Mezger, 1997; Israel *et al.*, 2011a). Largely underpinning these poor constraints were the limited geochronological sample sizes and a lack of *in-situ* context of the analyses that were previously completed, along with the differences in interpretation as to the geologic processes responsible for the metamorphic character of the Kluane Schist (see above & Chapters 2 & 3). The new petrochronology completed within this thesis combines well-constrained phase relationships (e.g., Chapter 3) with monazite spot analyses (Chapter 4) to demonstrate that the metamorphic character of the Kluane Schist was largely the result of a single phase of metamorphism (M_2 above & in Chapter 3) between ca. 70 and ca. 55 Ma (Chapter 4). As opposed to the previous analysis of monazite separates across the Kluane Schist (Erdmer & Mortensen, 1993), the *in-situ* context to the monazite petrochronology presented within this thesis additionally showed that there was limited evidence for a relationship between the metamorphic character of the Kluane Schist and the intrusion of the Ruby Range batholith (Chapter 4). Instead, the progressive younging of monazite with structural depth is consistent with the preservation of a single inverted metamorphic sequence that developed in response to a single downward penetrating phase of metamorphism coeval with deformation (Chapters 3 & 4). This said, the coincidence between the age of the Ruby Range batholith (ca. 64–57 Ma; e.g., Israel *et al.*, 2011a) and the highest grades of Kluane Schist metamorphism (i.e., migmatite development, domain 4, ca. 61–55 Ma; Table F1; see Chapter 4) suggests the emplacement of the batholith may have facilitated during the final stages of Kluane Schist metamorphism.

Together these results are consistent with the Kluane Schist having experienced a clockwise P - T - t - D evolution defined by an initial burial event prior to ca. 70 Ma followed by a more protracted episode of metamorphism up until ca. 55 Ma (Chapters 3 & 4). A rapid and largely isothermal decompression of the Kluane Schist is associated with the development of migmatites between ca. 62 and ca. 56 Ma (Chapters 3 & 4). The final exhumation history of the Kluane Schist is best recorded by previous ^{40}Ar - ^{39}Ar mica dates, which return cooling ages between ca. 55–40 Ma (Mortensen and Erdmer, 1992; Mezger, 1997). The diachronous attainment of peak metamorphic conditions during the main phase of Kluane Schist metamorphism (M_2 ; Chapter 3) is consistent with its overthrusting by the Yukon-Tanana terrane and the Ruby Range batholith from the northeast (Israel *et al.*, 2011a). These results further imply that the terminal accretion of the Insular terranes was most likely driven by the southwesterly-directed override of the North American margin in an upper plate position (e.g., Monger & Gibson, 2019) rather than by slab-pull and west-dipping subduction along the inboard margin of the Insular terranes (e.g., Sigloch & Mihalynuk, 2013; 2017).

6.1.3. Unravelling the timing and original geodynamic setting of Kluane Schist deposition

Understanding the original tectonic position of the Kluane Schist, as with other Jura-Cretaceous basins, remains key to integrating their extensive post-depositional datasets with current models of Cordilleran orogenesis (e.g., Monger, 2014). However, a detailed basin-wide provenance analysis has not previously been completed across the Kluane Schist. Therefore, to better constrain its original geodynamic setting, provenance, and depositional age, U-Pb age and Hf-isotope compositions were determined for five detrital zircon samples from the Kluane Schist. These five samples encompass the entire metamorphic and structural range of the currently exposed Kluane Schist (e.g., Chapter 3). Additionally, interpretations of this dataset incorporate the recent restoration of ~480 km of dextral slip along the Denali fault from the Cenozoic (ca. 52 Ma, Waldien *et al.*, 2021b), which offers an abundance of potential new source areas for the Kluane Schist outboard of the Denali fault.

The new detrital zircon data presented in this thesis provides an updated Late Cretaceous maximum depositional age for the Kluane Schist (ca. 90–75 Ma; Chapter 5) and is used to infer strong provenance ties between the Kluane Schist and the inboard Intermontane terranes (Chapter 5). Together these results suggest the Kluane Schist was likely deposited in a continentally bound forearc-style basin of limited width during the very latest stages of Insular terrane accretion. Further, integration of these results with the structural, metamorphic, and geochronological constraints presented within Chapters 3 & 4 provides evidence that the Kluane Schist most likely represents the uppermost part of a contractional forearc to a Cretaceous arc build on the Yukon-Tanana terrane (Chapter 5).

6.1.4. Potential correlations between the Kluane Schist and other Jura-Cretaceous basins within the Northern Cordillera

Previous studies have suggested the Kluane Schist may be correlative with similar metapelitic rock packages within the Northern Cordillera, including the Blanchard River assemblage of southwest Yukon (Vice, 2017) and Maclaren Schist within south-central Alaska (e.g., Forbes *et al.*, 1973; Eisbacher, 1976; Nokleberg *et al.*, 1985; Erdmer & Mortensen, 1993; Waldien *et al.*, 2021b). Recent tectonic models of Insular terrane accretion also include a potential correlation between the Maclaren Schist and Kluane Schist and suggest their collective deposition between 100–90 Ma as a single, west-verging forearc to a Cretaceous arc built upon the Yukon-Tanana terrane (e.g., the Kluane–Maclaren Schist of Waldien *et al.*, 2021b). However, earlier studies have questioned this correlation, particularly with respect to potential differences in the tectono-metamorphic evolution of each unit (e.g., Mezger *et al.*, 2001b). Given that a re-evaluation of the tectono-metamorphic evolution of the Kluane Schist forms a central topic of this thesis, these correlations were tested in the context of these new datasets.

Comparison of the new structural, metamorphic, and geochronological datasets from the Kluane Schist with recent equivalents from both the Blanchard River assemblage (Vice, 2017; Vice *et al.*, 2020) and the Maclaren Schist (Davidson & McPhillips, 2007; Waldien *et al.*, 2021a, b) highlight important similarities and differences between these assemblages. Detrital zircon recovered from all three assemblages

provide strong provenance links to inboard (i.e., Intermontane bound) plutonic suites (Vice, 2017; Waldien *et al.*, 2021a, b; Chapter 5), and the southern Yukon-Tanana terrane, suggesting these as key sources for all three assemblages (Chapter 5). This data indicates that all three assemblages likely occupied a similar along-strike position relative to the paleo-western margin of North America during their deposition and in turn generally supports the recent restoration of ~480 km of post 52 Ma dextral slip along the Denali fault (Waldien *et al.*, 2021 b).

In contrast, the apparent abundance of Insular derived detritus supplied to each unit differs; the Maclaren Schist and Blanchard River assemblage both show potential provenance ties to the Insular terranes while the Kluane Schist only shows limited, if any, sourcing from the Insular terranes (Chapter 5; Vice, 2017; Waldien *et al.*, 2021a, b). This result suggests these units may have occupied different positions within the ocean or seaway separating the Insular and Intermontane terranes (Chapter 5). Potentially the Maclaren Schist and Blanchard River assemblage represent the more distal parts of a forearc (accretionary wedge?) to a Cretaceous arc build upon the Yukon-Tanana terrane with the Kluane Schist representing a continentally bound forearc-style basin deposited atop the Maclaren Schist and Blanchard River assemblage (Chapter 5). This model could be tested through a modern re-evaluation for the *P-T-t-D* evolution of the Maclaren Schist and re-analysis of zircon across the Blanchard River assemblage for Hafnium-isotopes.

Comparison of the metamorphic and structural character of these Jura-Cretaceous units also provides key insight into the nature of Insular terrane accretion within other parts of the Northern Cordillera. Initial Barrovian-style metamorphism is recorded by both the Blanchard River assemblage and Maclaren Schist and is associated with the development of kyanite-grade mineral assemblages. Both the Blanchard River and Maclaren Schist assemblages were subsequently overprinted by lower-pressure cordierite–andalusite/sillimanite +/- staurolite–spinel sequences, which are inferred to develop coeval with deformation (Stout, 1965; Smith & Turner, 1973; Davidson & McPhillips, 2007; Vice *et al.*, 2020; Waldien *et al.*, 2021a). In contrast, the Kluane Schist, along with parts of the Kahiltna Basin (e.g., Devil Creek area of Davidson & McPhillips, 2007), lack the high-pressure mineral assemblages observed across either the Blanchard River assemblage or Maclaren Schist (Mezger *et al.*, 2001b; Davidson & McPhillips, 2007; Chapter 3). Instead, these units only show the syn-deformational

cordierite–andalusite/sillimanite +/- staurolite–spinel grade assemblages that commonly overprint the Barrovian metamorphism recorded by the Blanchard River assemblage and Maclaren Schist (e.g., Davidson & McPhillips, 2007; Chapter 3). On the basis of their disparate metamorphic histories, it's unlikely that the Kluane Schist has a direct tectonic correlation with either the Blanchard River assemblage or Maclaren Schist (Chapters 3–5). This conclusion is further supported by the distinctly younger metamorphic age of the Kluane Schist (ca. 70–55 Ma; Chapter 4) compared with either the Blanchard River assemblage (ca. 83–61 Ma; Vice *et al.*, 2020) or the Maclaren Schist (ca. 84–55 Ma; Waldien *et al.*, 2021b). Moreover, the timing associated with the development of the distinct high- T , low- P assemblages preserved by all these Jura-Cretaceous units (i.e., cordierite–andalusite/sillimanite +/- staurolite–spinel) shows general alignment in both age and duration (Chapters 4 & 5). This alignment in the timing and conditions of metamorphism provides evidence for an extensive high- T , low- P metamorphic event within the southwest Yukon (present coordinates) between ca. 75–55 Ma (ca. 70–55 Ma, Kluane Schist; ca. 70–61 Ma, Blanchard River assemblage, ca. 75–55 Ma Maclaren Schist; ca. 68–63 Ma, Devil Creek; Chapter 4). Associated with this high- T , low- P event are the development of continentally dipping inverted metamorphic sequences, continentally dipping foliations, and consistent southwest- to south-oriented shear structures (Smith, 1981; Mezger *et al.*, 2001b; Davidson & McPhillips, 2007; Israel *et al.*, 2011a; Vice *et al.*, 2020; Waldien *et al.*, 2021a; Chapters 3 & 4), which together suggest the collective metamorphism of these Jura-Cretaceous assemblages during their progressive override from the north- to northwest (Chapters 3 & 4). It is therefore likely that the syn-deformational metamorphism of these Jura-Cretaceous basins, accompanied by the terminal accretion of the Insular terranes, was primarily driven by the override of the thermally mature North American margin between the latest Cretaceous to early Paleogene (Chapters 3, 4 & 5).

6.2. Summary of tectonic model and insight into the timing, style, and tectonic nature of Insular terrane accretion within the northern Cordillera

The new datasets derived from the Late Cretaceous Kluane Schist provide important insight into the tectonic processes operating during the final stages of Insular terrane accretion within the Northern Cordillera. Combined with equivalent datasets from other Jura-Cretaceous basins these new datasets may hold answers to key questions relating to Mesozoic tectonic architecture of the Cordillera including: 1) the width and geometry of the ocean separating the Insular and Intermontane terranes during the Mesozoic, 2) the timing and driving mechanism of Insular terrane accretion, and 3) the polarity of subduction during Insular terrane accretion. Below I summarize these new datasets in the context of a tectonic model accounting for the evolution of the paleo-western margin of North America centred on the Yukon-Alaska border (present coordinates) from Late Jurassic through to Eocene times. This model represents a summary of that presented in Chapter 5 and is aimed at addressing the key questions outlined above while also highlighting potential avenues for further work.

The initial deposition of Jurassic through Early Cretaceous basinal assemblages within the Northern Cordillera is defined by two distinct and terrane-specific lithofacies; one being primarily derived from and deposited upon the inboard margin of the Insular terranes and another being largely derived from and deposited upon the paleo-western margin of North America (e.g., Hults *et al.*, 2013; Yokelson *et al.*, 2015; Box *et al.*, 2019; Trop *et al.*, 2020). Correlation between these distinct lithofacies (e.g., the “northern flysch” and ‘southern flysch” units of Hults *et al.*, 2013) can be used to infer that the seaway separating the Insular and Intermontane terranes within the Northern Cordillera was likely characterized by at least 2,000 km of along-strike connectivity from the Jurassic through to Early Cretaceous times (e.g., Hults *et al.*, 2013; Box *et al.*, 2019; Trop *et al.*, 2020). However, these distinct flysch units only offer limited additional insight into the width of this inter-connected seaway. Evidence for mixed provenance signatures within Late Jurassic and younger terrane-intervening units suggests a tectonic linkage and proximity (< 1000 km?) between the Insular and Intermontane terrane groups from at least the latest Jurassic (e.g., Hampton *et al.*, 2010; Hults *et al.*, 2013; Yokelson *et al.*,

2015; Vice, 2017; Box *et al.*, 2019). However, the nature of this tectonic connection and the absolute width of the intervening seaway remains largely unconstrained. In contrast, tomographic imaging of deep mantle slabs provides a more precise 2,000–4,000 km approximation for the width of this ocean (e.g., Sigloch & Mihalynuk, 2017). This said, the presence of such an extensive ocean is inconsistent with evidence for Early-Middle Jurassic Insular terrane accretion within west central British Columbia and southeast Alaska (ca. 180–175 Ma; e.g., van der Heyden, 1992; Gehrels, 2001; Gehrels *et al.*, 2009) and the evidence for a shared tectonic history between Jura-Cretaceous basins of the Northern Cordillera from the latest Jurassic (e.g., Chapter 5; Pavlis *et al.*, 2019 and references therein). An understanding of the width and geometry of this terrane-intervening seaway therefore still forms a critical unknown in current models of Cordilleran orogenesis. As such, further work should focus on this problem. Potential untapped sources of data could include the Bear Creek assemblage of the southwest Yukon (Israel *et al.*, 2015) and the Taku terrane southeastern Alaska and British Columbia (e.g., Giesler *et al.*, 2016). These enigmatic belts of marine clastic strata and volcanic rock may represent fragments of the oceanic floor that once separated the Insular and Intermontane terranes.

Initial accretion of the Insular terranes to the western margin of North America within the Yukon and central Alaskan regions of the Cordillera is recorded by Early Cretaceous deformation and sub-greenschist metamorphism within the Nutzotin Mountains sequence and Dezadeash Formation (Lowey, 2000; Manuszak *et al.*, 2007; Lowey, 2021). This provides the first definitive insight into the tectonic nature and potential driving force for Insular terrane accretion within the Northern Cordillera; the south- and west-vergent deformation recorded by these units is consistent with them having been underthrust beneath the former continental margin along north- and east-dipping décollements (e.g., Lowey, 2000; Manuszak *et al.*, 2007). This serves as strong evidence for north- and east-dipping structures having characterized the Insular-Intermontane suture during the Mesozoic (e.g., Box *et al.*, 2019; Trop *et al.*, 2020) rather than west- or south-dipping ones (e.g., Sigloch & Mihalynuk, 2013; 2017). Nonetheless, the nature of these north- and east-dipping décollements remains unclear (e.g., Waldien *et al.*, 2021b). There is evidence that the Jura-Cretaceous basins of the southwest Yukon were floored by oceanic crust during their deposition (e.g., Bear Creek assemblage in Fig. 5.2; Israel *et al.*, 2015), with the possibility of a subduction zone

between the Insular and Intermontane terranes supported by the presence of potential ophiolitic fragments interleaved with Jura-Cretaceous metasedimentary units, including the Kluane Schist (Mezger, 2000), and the inferred presence of an interconnected seaway separating the Intermontane and Insular terranes during the Late Jurassic and Early Cretaceous (see above Fig. 5.12b; e.g., Hults *et al.*, 2013; Box *et al.*, 2019; Trop *et al.*, 2020). However, the lack of a paired magmatic belt to account for this subduction zone, in addition to the one magmatic belt that is interpreted to record paleo-east dipping subduction outboard of the Insular terranes, provides evidence against wholesale oceanic subduction beneath the paleo-western margin of North America during the mid-Cretaceous (e.g., Clift *et al.*, 2005; Gehrels *et al.*, 2009; Amato *et al.*, 2013). Therefore, furthering our understanding into the crustal architecture underlying the Jura-Cretaceous basins should form a key aspect of further work. This should additionally help unravel the tectonic nature of the north- and east-dipping décollements that once separated these terrane groups.

After the initial Early Cretaceous accretion of the Insular terranes within Yukon and central Alaska, the younger depositional ages recorded by the Maclaren Schist (ca. 86 Ma; Waldien *et al.*, 2021a), the Upper Koksetna River sequence (ca. 85 Ma; Hults *et al.*, 2013), the Tordrillo Mountains sequence (ca. 92 Ma; Hults *et al.*, 2013) and parts of both the Kahiltna Basin (ca. 81 Ma; Box *et al.*, 2019) and Gravina belt (ca. 105 Ma; Yokelson *et al.*, 2015) are consistent with a protracted and diachronous accretion of the Insular terranes throughout the Late Mesozoic (e.g., Box *et al.*, 2019). This inference is consistent with the increased contribution of Insular derived zircon to the younger units deposited along the paleo-western margin of North America (see Chapter 5; e.g., Hampton *et al.*, 2010; Hults *et al.*, 2013; Box *et al.*, 2019). Shortly after the mid-Late Cretaceous deposition of these continentally bound Jura-Cretaceous units (e.g., Maclaren Schist, Blanchard River assemblage, eastern Gravina Belt), they experienced Barrovian-style metamorphism between ca. 90–85 Ma ($P \sim 6.5\text{--}7$ kbar; McClelland *et al.*, 1991; Davidson & McPhillips, 2007; Vice *et al.*, 2020; Waldien *et al.*, 2021b). The development of continentally dipping foliations and shear zones within these units is consistent with this metamorphism having involved their collective underplating below North American margin along south- and west-verging structures (e.g., Davidson & McPhillips, 2007; Vice *et al.*, 2020; Waldien *et al.*, 2021b). As such the polarity of the subduction or megathrust system that characterized the Insular-Intermontane suture

zone at this time (e.g., Box *et al.*, 2019; Trop *et al.*, 2020; Waldien *et al.*, 2021b) was most likely north- and east-dipping (e.g., Pavlis *et al.*, 2019). A lack of equivalent grades of metamorphism within the Jura-Cretaceous basins deposited along the inboard margin of the Insular terranes (e.g., SE Kahiltna, Clearwater, Nutzotin, Dezadeash, western Gravina; Yokelson *et al.*, 2015; Hults *et al.*, 2013; Lowey, 2000; Manuszak *et al.*, 2007; Lowey, 2021; Waldien *et al.*, 2021b) is also consistent with this interpretation.

In contrast to the other continentally bound Jura-Cretaceous units, the Kluane Schist lacks a distinct high- P metamorphic event and only shows strong provenance ties inboard terranes (Chapters 3–5). This unique character indicates the deposition of the Kluane Schist likely occurred during the very final stages of Insular terrane accretion, within a continentally bound forearc-style basin atop the Maclaren Schist and Blanchard River assemblage (Chapter 5). This inference is supported by the contemporaneous nature of Kluane Schist deposition (ca. 90–75 Ma; Chapter 5) and the deeper-seated metamorphism experienced by both the Blanchard River assemblage and Maclaren Schist (ca. 90–85 Ma; Vice *et al.*, 2020; Waldien *et al.*, 2021b). Further, the tectono-metamorphic evolution of the Kluane Schist, which includes a distinct sub-greenschist facies burial event prior to override by the North American margin (Chapter 3), is in line with its deposition just prior the final docking of the Insular terranes and its limited underplating below the paleo-western margin of North America (Chapter 5).

Shortly following its Late Cretaceous deposition and sub-greenschist facies burial, the Kluane Schist was subject to an extensive high- T , low- P Buchan-style metamorphic event between ca. 70–55 Ma (Chapters 3 & 4). Coeval high- T , low- P metamorphism is also experienced by numerous continentally bound Jura-Cretaceous basinal assemblages within the Northern Cordillera (e.g., Maclaren Schist, Davidson *et al.*, 1992; Davidson & McPhillips, 2007; Waldien *et al.*, 2021b; Blanchard River assemblage, Vice *et al.*, 2020 & Kahiltna Basin, Davidson & McPhillips, 2007) while early Paleogene (ca. 65; Waldien *et al.*, 2021a) upper-greenschist facies metamorphism is recorded within Jura-Cretaceous strata along the inboard margin of the Insular terranes (e.g., Dezadeash-Clearwater; Lowey, 2000; 2021; Waldien *et al.*, 2021a). The development of continentally dipping inverted metamorphic sequences and southwest- to south-oriented shear structures within both Insular- and Intermontane-bound Jura-Cretaceous units (Smith, 1981; Davidson *et al.*, 1992; Mezger *et al.*, 2001b; Davidson & McPhillips, 2007; Israel *et al.*, 2011a; Vice, 2017; Vice *et al.*, 2020; Waldien *et al.*, 2021a, b) is consistent

with their collective metamorphism and juxtaposition during a period of southwesterly-directed override by the continental margin of North America (Chapters 3–5; e.g., Waldien *et al.*, 2021a, b). This coupled tectono-metamorphic relationship provides strong evidence that the westward migration of the North American continent and the overthrusting of its thermally mature flanking components (e.g., Yukon-Tanana terrane) was a primary driver of Jura-Cretaceous basin inversion and terminal Insular terrane accretion within the Northern Cordillera. Such a model is consistent with recent reconstructions of the Mesozoic-Cenozoic trajectory of the North American craton (e.g., Monger & Gibson, 2019) and is best reconciled by a model of Insular terrane accretion that involves eastward, continentally dipping subduction below a westward migrating North American continent.

6.3. Potential future research avenues

Considering the above discussion and the new data presented within this thesis, multiple new and exciting research avenues can be identified which could further our understanding into the nature of Insular terrane accretion within the Northern Cordillera. Equally, some insights and potential improvements into the methods used during data collection and processing are also provided. A list of these is provided below.

- Full investigation into the relationship between graphite-bearing metapelites and water activity (a_{H_2O} ; see Chapter 3) and the implication this has on mineral phase equilibria. My own thermodynamic models were greatly improved (as in they better replicated observations) when modified for a varied a_{H_2O} but what is the best way to constrain these values, especially during progressive dehydration and prograde metamorphism?
- Providing more precise constraint on the timing and conditions on the sub-greenschist facies metamorphism of the Kluane Schist (i.e., M_1 as defined in Chapter 3).

This event is likely a direct record of the final docking of the Insular terranes to the paleo-western margin of North America.

- Petrological, geochronological and provenance re-evaluation of the enigmatic units of the Kluane Basin including the ultramafic and carbonate bodies (see Chapter 2). This could place additional constraint on the original depositional and geodynamic environment of the Kluane Basin.
- Investigation of the basement (seafloor?) to the Kluane Schist and the other Jura-Cretaceous assemblages within the Intermontane-Insular suture (e.g., Bear Creek assemblage; Israel *et al.*, 2015; Chapters 2, 3, 5 & 6). This could potentially provide insight into the architecture of the crust that once separated the Insular and Intermontane terranes prior to their collision and further our understanding into key questions including: (1) what was the width and geometry of their terrane-intervening seaway during the Jurassic and Early Cretaceous? and (2) what was the nature of the east- and north- dipping structures that separated the Insular and Intermontane terranes within the northern Cordillera during their initial accretion?
- A full geochronological characterisation of the Ruby Range batholith. Current studies constrain the main phase of the Ruby Range batholith to ca. 64–57 Ma (e.g., Israel *et al.*, 2011a), however, there is also evidence for a potential Late Cretaceous phase to the batholith (ca. 71–68 Ma; Israel *et al.*, 2011a). Given the coincidence between these Late Cretaceous ages and the age of Kluane Schist metamorphism (ca. 70–55 Ma; Chapter 4), a full geochronological characterisation of the batholith would be beneficial to fully understanding its role (or lack of) during the metamorphism of the Kluane Schist (c.f., Chapters 3 & 4).
- A modern and updated *P-T-t-D* study of the Maclaren Schist and higher-grade portions of the Kahiltna Basin (e.g., Devil Creek rocks). These units, combined with the Kluane Schist and Blanchard River assemblage, potentially represent a forearc to a Cretaceous arc build upon the Yukon-Tanana terrane and thus may preserve a record of

the progressive encroachment of the Insular terranes with the paleo-western margin of North America; a direct comparison of their *P-T-t-D* evolutions would help refine models accounting for the progressive accretion of the Insular terranes (e.g., Chapters 5 & 6).

- Are there any potential correlative sequences to the Kluane Schist further south within the Cordillera? My investigation focused on Jura-Cretaceous basins within the southwest Yukon, Alaska, and northern British Columbia; however, examples of these Jura-Cretaceous units extend all the way down to Mexico (e.g., Sauer *et al.*, 2017). How do the metamorphic histories of these southern Jura-Cretaceous basins compare to those up north? What can this tell us about Insular terrane accretion across the Cordillera as a whole.
- Evaluate zircon derived from mid-Late Cretaceous plutons and volcanic units within the southern Yukon-Tanana terrane (Chapter 5; e.g., Casino, Rancheria, Prospector Mountain, Carmacks Group) for Hafnium-isotope and U-Pb age data; these could potentially provide a source for the abundant, Late Cretaceous zircon recovered from the Kluane Schist.
- Re-analyse zircon from the Blanchard River assemblage for Hafnium-isotopes; this will provide a direct comparison to the Kluane Schist and allow for a re-evaluation of its current ties to the outboard Insular terranes (e.g., its Early Cretaceous population; c.f., Vice, 2017).
- Evaluate the extent to which the youngest, concordant zircon recovered from the Kluane Schist are recrystallized (see Chapter 5). Could this potentially provide a more accurate estimate for the depositional age of the Kluane Schist and/or more information into its *P-T-t* history? Especially if the recrystallization and detrital age could be separated (e.g., by depth profiling of individual, unpolished grains using LA-ICP-MS). Equally, in the absence of additional information (e.g., high-resolution CL images, age of metamorphism, existing constraints from surrounding geology), could similar zircon recrystallisation have affected the estimated depositional age of other metasedimentary units within the Cordillera?

6.4. References

- Amato, J.M., Pavlis, T.L., Clift, P.D., Kochelek, E.J., Hecker, J.P., Worthman, C.M. and Day, E.M., 2013. Architecture of the Chugach accretionary complex as revealed by detrital zircon ages and lithologic variations: Evidence for Mesozoic subduction erosion in south-central Alaska. *Geological Society of America Bulletin*, v.125, n.11-12, p.1891-1911. <https://doi.org/10.1130/B30818.1>
- Box, S.E., Karl, S.M., Jones, J.V., Bradley, D.C., Haeussler, P.J. & O'Sullivan, P.B., (2019). Detrital zircon geochronology along a structural transect across the Kahiltna assemblage in the western Alaska Range: Implications for emplacement of the Alexander-Wrangellia-Peninsular terrane against North America. *Geosphere*, v.15, n.6, p.1774-1808. <https://doi.org/10.1130/GES02060.1>
- Clift, P.D., Draut, A.E., Kelemen, P.B., Blusztajn, J. and Greene, A., 2005. Stratigraphic and geochemical evolution of an oceanic arc upper crustal section: The Jurassic Talkeetna Volcanic Formation, south-central Alaska. *Geological Society of America Bulletin*, v.117, n.7-8, p.902-925. <https://doi.org/10.1130/B25638.1>
- Davidson, C., & McPhillips, D., 2007. Along strike variations in metamorphism and deformation of the strata of the Kahiltna basin, south-central Alaska. In K. D. Ridgway, J. M. Trop, J. M. G. Glen, & J. M. O'Neill (Eds.), *Special Paper 431: Tectonic growth of a collisional continental margin: Crustal evolution of Southern Alaska*, v. 431, p. 439– 453. Geological Society of America. [https://doi.org/10.1130/2007.2431\(17\)](https://doi.org/10.1130/2007.2431(17))
- Davidson, C., Hollister, L. S., & Schmid, S. M. (1992). Role of melt in the formation of a deep-crustal compressive shear zone: The Maclaren Glacier Metamorphic Belt, south central Alaska. *Tectonics*, v.11, n.2, p.348–359. <https://doi.org/10.1029/91TC02907>
- Eisbacher, G.H., (1976). Sedimentology of the Dezadeash flysch and its implications for strike-slip faulting along the Denali fault, Yukon Territory and Alaska. *Canadian Journal of Earth Sciences*, v.13, n.11, p.1495-1513. <https://doi.org/10.1139/e76-157>

- Erdmer, P. and Mortensen, J.K., 1993. A 1200-km-long Eocene metamorphic-plutonic belt in the northwestern Cordillera: Evidence from southwest Yukon. *Geology*, v.21, n.11, p.1039-1042. [https://doi.org/10.1130/0091-7613\(1993\)021<1039:AKLEMP>2.3.CO;2](https://doi.org/10.1130/0091-7613(1993)021<1039:AKLEMP>2.3.CO;2)
- Forbes, R. B., Smith, T. E., & Turner, D. L., 1974. Comparative petrology and structure of the Maclaren, Ruby Range, and Coast Range belts: Implications for offset along the Denali fault system. *Geological Society of America Abstracts with Programs*. V.6, n.177.
- Gehrels, G., Rusmore, M., Woodsworth, G., Crawford, M., Andronicos, C., Hollister, L., Patchett, J., Ducea, M., Butler, R., Klepeis, K. & Davidson, C., (2009). U-Th-Pb geochronology of the Coast Mountains batholith in north-coastal British Columbia: Constraints on age and tectonic evolution. *Geological Society of America Bulletin*, v.121, n.9-10, p.1341-1361. <https://doi.org/10.1130/B26404.1>
- Giesler, D., Gehrels, G., Pecha, M., White, C., Yokelson, I. and McClelland, W.C., 2016. U–Pb and Hf isotopic analyses of detrital zircons from the Taku terrane, southeast Alaska. *Canadian Journal of Earth Sciences*, v.53, n.10, p. 979-992. <https://doi.org/10.1139/cjes-2015-0240>
- Hampton, B.A., Ridgway, K.D. and Gehrels, G.E., 2010. A detrital record of Mesozoic island arc accretion and exhumation in the North American Cordillera: U-Pb geochronology of the Kahiltna basin, southern Alaska. *Tectonics*, v.29, n.4. <https://doi.org/10.1029/2009TC002544>
- Hults, C.P., Wilson, F.H., Donelick, R.A. and O’Sullivan, P.B., 2013. Two flysch belts having distinctly different provenance suggest no stratigraphic link between the Wrangellia composite terrane and the paleo-Alaskan margin. *Lithosphere*, v.5, n.6, p.575-594. doi: <https://doi.org/10.1130/L310.1>
- Israel, S., Cobbett, R., Westberg, E., Stanley, B. and Hayward, N., 2011b. Preliminary bedrock geology of the Ruby Ranges, southwestern Yukon, (Parts of NTS 115G, 115H, 115A and 115B) (1:150 000 scale). Yukon Geological Survey, Open File 2011-2.

- Israel, S., Colpron, M., Cubley, J., Moynihan, D., Murphy, D.C. & Relf, C., (2015). The Bear Creek assemblage: A latest Triassic volcano-sedimentary succession in southwest Yukon. In: Yukon Exploration and Geology 2014, K.E. MacFarlane, M.G. Nordling and P.J. Sack (eds.), Yukon Geological Survey, p. 99-112.
- Israel, S., Murphy, D., Bennett, V., Mortensen, J. and Crowley, J., 2011a. New insights into the geology and mineral potential of the Coast Belt in southwestern Yukon. In: Yukon Exploration and Geology 2010, MacFarlane, K.E., Weston, L.H., and Relf, C. (eds.), Yukon Geological Survey, p. 101-123.
- Lowey, G.W., 2000. The Tatshenshini shear zone (new) in southwestern Yukon, Canada: Comparison with the Coast shear zone in British Columbia and southeastern Alaska and implications regarding the Shakwak suture. *Tectonics*, v.19, n.3, p.512-528. <https://doi.org/10.1029/1999TC001119>
- Lowey, G.W., 2021. Very low-grade metamorphism of the Dezadeash Formation (Jurassic-Cretaceous): Constraints on the tectonometamorphic history of the Dezadeash flysch basin and implications regarding the tectonic evolution of the Northern Cordillera of Alaska and Yukon. *AIMS Geosciences*, v.7, n.3, p.355-389. doi: 10.3934/geosci.2021022
- Manuszak, J.D., Ridgway, K.D., Trop, J.M., and Gehrels, G.E., 2007, Sedimentary record of the tectonic growth of a collisional continental margin: Upper Jurassic–Lower Cretaceous Nut-zotin Mountains sequence, eastern Alaska Range, Alaska, in Ridgway, K.D., Trop, J.M., Glen, J.M.G., and O'Neill, J.M., eds., *Tectonic Growth of a Collisional Continental Margin: Crustal Evolution of Southern Alaska: Geological Society of America Special Paper 431*, p. 345–377, [https://doi.org/10.1130/2007.2431\(14\)](https://doi.org/10.1130/2007.2431(14)).
- McClelland, W.C., Anovitz, L.M. and Gehrels, G.E., 1991. Thermobarometric constraints on the structural evolution of the Coast Mountains batholith, central southeastern Alaska. *Canadian Journal of Earth Sciences*, v.28, n.6, p.912-928. <https://doi.org/10.1139/e91-083>

- Mezger, J.E., 1997. Tectonometamorphic evolution of the Kluane metamorphic assemblage, southwest Yukon: evidence for Late Cretaceous eastward subduction of oceanic crust underneath North America [unpublished PhD thesis]: University of Alberta, 306 p. <https://doi.org/10.7939/R3DJ58N76>
- Mezger, J.E., 2000. 'Alpine-type' ultramafic rocks of the Kluane metamorphic assemblage, southwest Yukon: Oceanic crust fragments of a late Mesozoic back-arc basin along the northern Coast Belt. In: Yukon Exploration and Geology 1999, D.S. Emond and L.H. Weston (eds.), Exploration and Geological Services Division, Yukon, Indian and Northern Affairs Canada, p.127-138.
- Mezger, J.E., Chacko, T. and Erdmer, P., 2001. Metamorphism at a late Mesozoic accretionary margin: a study from the Coast Belt of the North American Cordillera. *Journal of Metamorphic Geology*, v.19, n.2, p.121-137. <https://doi.org/10.1046/j.0263-4929.2000.00300.x>
- Monger, J.W. and Gibson, H.D., 2019. Mesozoic-Cenozoic deformation in the Canadian Cordillera: The record of a "Continental bulldozer"?. *Tectonophysics*, v.757, p.153-169. <https://doi.org/10.1016/j.tecto.2018.12.023>
- Monger, J.W., (2014). Logan Medallist 1. Seeking the suture: The Coast-Cascade conundrum. *Geoscience Canada*, v.41, n.4, p.379-398. <https://doi.org/10.12789/geocanj.2014.41.058>
- Mortensen, J.K., and Erdmer, P., 1992, U-Pb, ⁴⁰Ar-³⁹Ar, and K-Ar ages for metamorphism of the Kluane and Aishihik assemblages in southwestern Yukon Territory, in *Radiogenic Age and Isotopic Studies: Report 6*; by Geological Survey of Canada; Geological Survey of Canada, Paper n.92-2, p.135-140, <https://doi.org/10.4095/134174>
- Nokleberg, W. J., Jones, D. L., & Silberling, N. J. (1985). Origin and tectonic evolution of the Maclaren and Wrangellia terranes, eastern Alaska Range, Alaska. *The Geological Society of America Bulletin*, v.96, n.10, p.1251–1270. [https://doi.org/10.1130/0016-7606\(1985\)96<1251:oateot>2.0.co;2](https://doi.org/10.1130/0016-7606(1985)96<1251:oateot>2.0.co;2)

- Pavlis, T.L., Amato, J.M., Trop, J.M., Ridgway, K.D., Roeske, S.M. and Gehrels, G.E., 2019. Subduction polarity in ancient arcs: A call to integrate geology and geophysics to decipher the Mesozoic tectonic history of the Northern Cordillera of North America. *GSA Today*, v.29, n.11, p.4-10.
<https://doi.org/10.1130/GSATG465Y.1>
- Sigloch, K. and Mihalynuk, M.G., 2013. Intra-oceanic subduction shaped the assembly of Cordilleran North America. *Nature*, v.496, n.7443, p.50-56.
<https://doi.org/10.1038/nature12019>
- Sigloch, K. and Mihalynuk, M.G., 2017. Mantle and geological evidence for a Late Jurassic–Cretaceous suture spanning North America. *Geological Society of America Bulletin*, v.129, n.11-12, p.1489-1520. <https://doi.org/10.1130/B31529.1>
- Smith, T.E., 1981. *Geology of the Clearwater Mountains, south-central Alaska*, v.60. Division of Geological & Geophysical Surveys.
- Smith, T.E., and Turner, D.L., 1973, *Geochronology of the Maclaren metamorphic belt, south-central Alaska; A progress report: Isochron/West*, n.7, p.21-25.
- Stout, J. H., 1965. *Bedrock geology between Rainy Creek and the Denali fault, Eastern Alaska Range, Alaska*. (Unpublished master's thesis). Fairbanks, AK: University of Alaska.
- Trop, J.M., Benowitz, J.A., Koeppe, D.Q., Sunderlin, D., Brueseke, M.E., Layer, P.W. and Fitzgerald, P.G., 2020. Stitch in the ditch: Nutzotin Mountains (Alaska) fluvial strata and a dike record ca. 117–114 Ma accretion of Wrangellia with western North America and initiation of the Totschunda fault. *Geosphere*, v.16, n.1, p.82-110.
<https://doi.org/10.1130/GES02127.1>
- Vice, L., 2017. *Late Cretaceous to Paleocene evolution of the Blanchard River assemblage, southwest Yukon; implications for Mesozoic accretionary processes in the northwestern Cordillera [unpublished master's thesis]*: Simon Fraser University.

Vice, L., Gibson, H.D. and Israel, S. 2020. Late Cretaceous to Paleocene tectonometamorphic evolution of the Blanchard River Assemblage, Southwest Yukon: New insight into the terminal accretion of insular terranes in the Northern Cordillera. *Lithosphere*, v.2020, n.1, <https://doi.org/10.2113/2020/2298288>

Waldien, T.S., Roeske, S.M. and Benowitz, J.A., 2021b. Tectonic underplating and dismemberment of the Maclaren-Kluane schist records Late Cretaceous terrane accretion polarity and ~ 480 km of Post-52 Ma dextral displacement on the Denali fault. *Tectonics*, v.40, n.10, p.e2020TC006677. <https://doi.org/10.1029/2020TC006677>

Waldien, T.S., Roeske, S.M., Benowitz, J.A., Twelker, E. and Miller, M.S., 2021a. Oligocene-Neogene lithospheric-scale reactivation of Mesozoic terrane accretionary structures in the Alaska Range suture zone, southern Alaska, USA. *Geological Society of America Bulletin*, v.133, n.3-4, p.691-716. <https://doi.org/10.1130/B35665.1>

Yokelson, I., Gehrels, G.E., Pecha, M., Giesler, D., White, C. and McClelland, W.C., 2015. U-Pb and Hf isotope analysis of detrital zircons from Mesozoic strata of the Gravina belt, southeast Alaska. *Tectonics*, v.34, n.10, p.2052-2066. <https://doi.org/10.1002/2015TC003955>

Appendix A: Supporting information for Chapter 3.

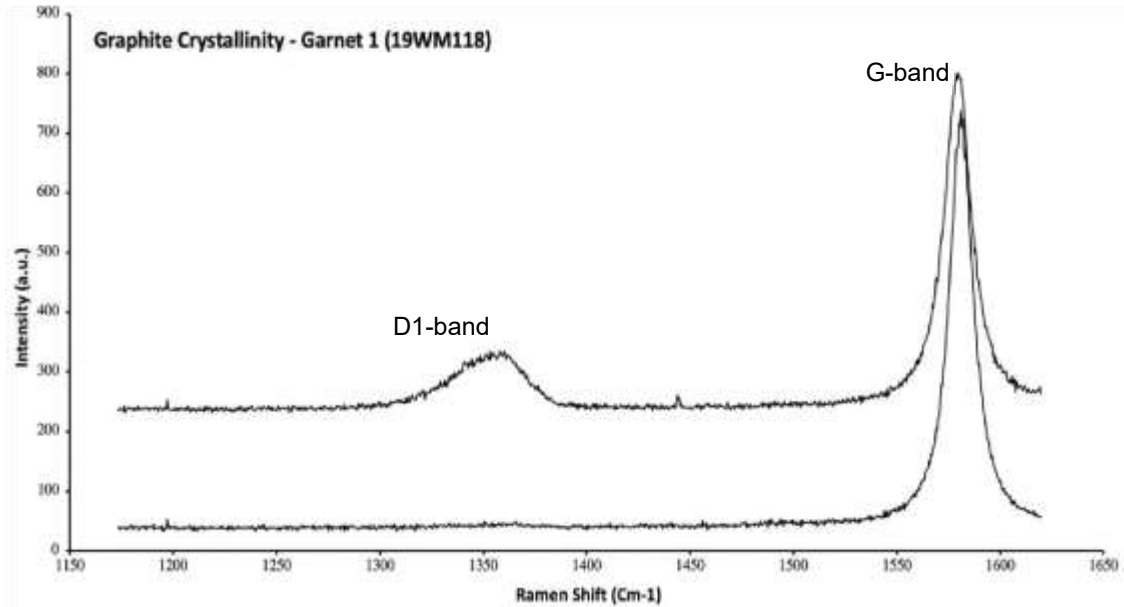


Figure A1: Raman spectrum of graphite inclusions within garnet in sample 19WM118 (zone 6). The D1-band and G-band are highlighted. Based on the relative integrated intensities of the two latter Raman bands and using the calibration equation provided by Beyssac et al. (2002), we obtain temperature estimates ranging from 500 to 630 °C.

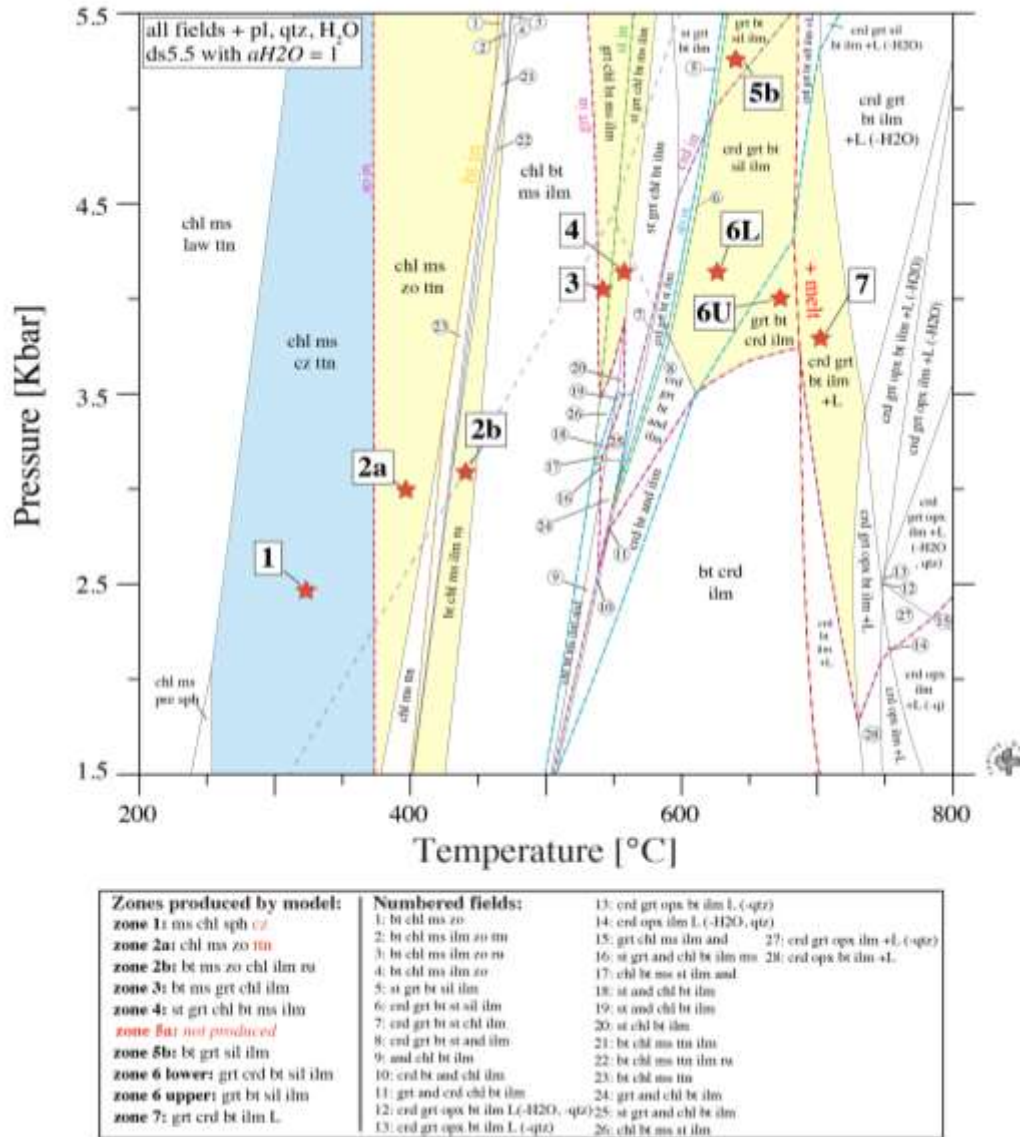


Figure A2: Result from petrological modelling with ds5.5 and aH₂O = 1 across the entire *P-T* range considered. Activity models used are described in main text. The resulting phase diagram is unable to produce the assemblage that characterizes zone 5a (bt-grt-pl-q-and). Individual reactions are not labelled as in the main publication, instead the first predicted appearance of individual index minerals is highlighted with coloured dashed lines. This result highlights that defining an inaccurate water activity predicts the appearance of cordierite prior to aluminium silicate, a relationship not observed across the Kluane Schist.

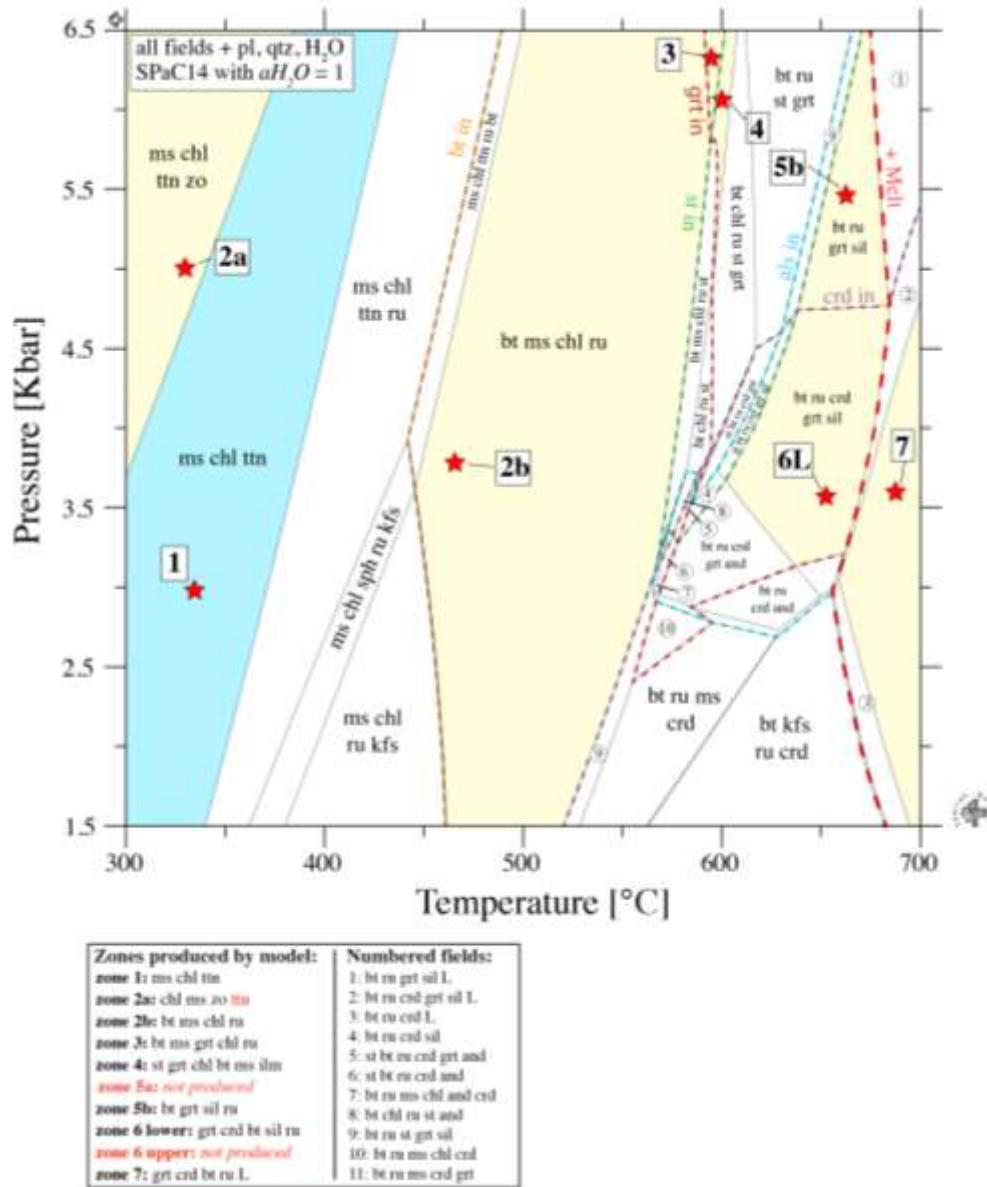


Figure A3: Result from petrological modelling when using the modified SPaC14 dataset of Spear & Cheney (1989) and activity models as described in Pattison & Debuhr (2015); $a_{H_2O} = 1$ across the entire P - T range considered. The resulting phase diagram is unable to produce the assemblages that characterize zones 5a/b (bt-grt-pl-q-and/sill) and structurally higher regions of zone 6 (crd-bt-grt-pl-q). Individual reactions are not labelled as in the main publication, instead the first predicted appearance of individual index minerals is highlighted with coloured dashed lines. Correctly predicted assemblages do not align with results from AvP , conventional barometry and Raman spectroscopy (e.g., zones 3 & 4 are predicted at much higher P). Further, the relationship, in terms of predicted P - T , between zones suggested by the phase diagram is not supported by petrographic analysis.

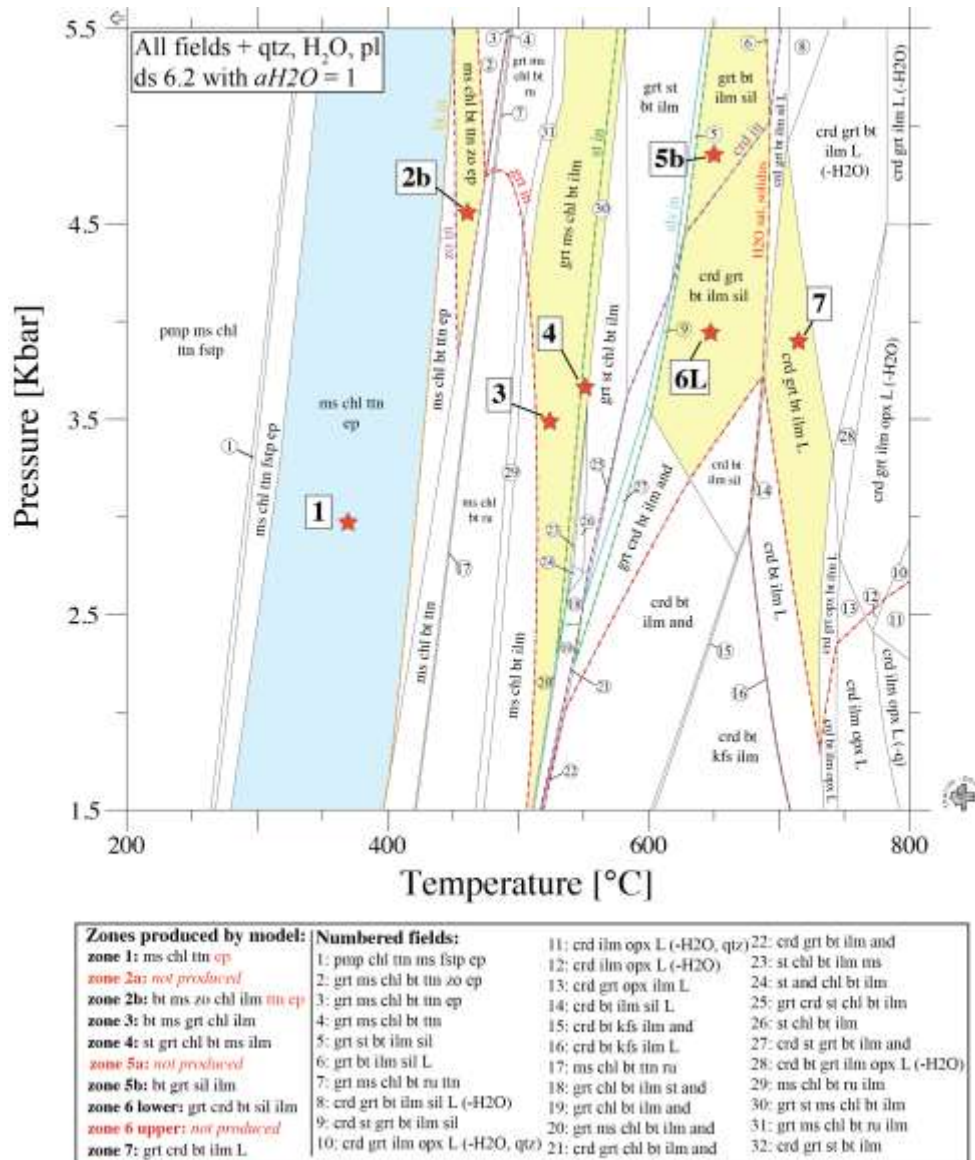


Figure A4: Result from petrological modelling with ds6.2 and aH₂O = 1 across the entire *P-T* range considered. Activity models used are described in main text. The resulting phase diagram is unable to produce the assemblages characteristic of zones 2b (zo-chl-ms-pl-q-ru), 5a (bt-grt-pl-q-and) and the structurally higher regions of zone 6 (crd-bt-grt-pl-q). Individual reactions are not labelled as in the main publication, instead the first predicted appearance of individual index minerals is highlighted with coloured dashed lines. Correctly predicted assemblages do not align with results from AvP, conventional barometry and Raman Spectroscopy (e.g., zones 2b & 6 are predicted at much higher *P*). Overall, the relationship between assemblage *P-T* predicted by this modelling combination is not supported by our petrographic analysis.

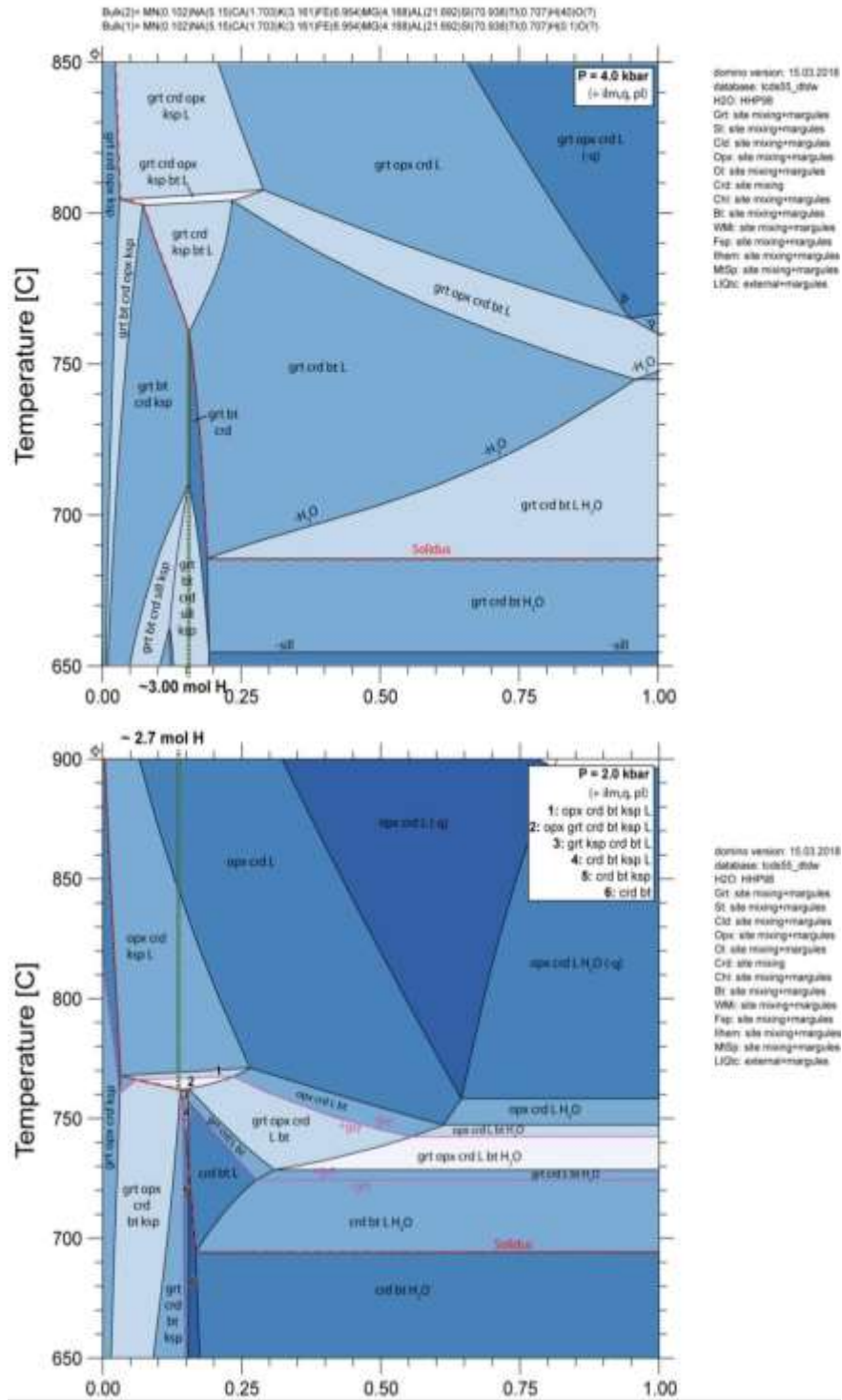


Figure A5: Isobaric T-XH₂O diagrams for the average bulk composition of the Kluane Schist. Green dashed lines show the minimum amount of H₂O required to saturate the system at the solidus (red dashed line) at (a) 4.0 kbar and (b) 2.0 kbar.

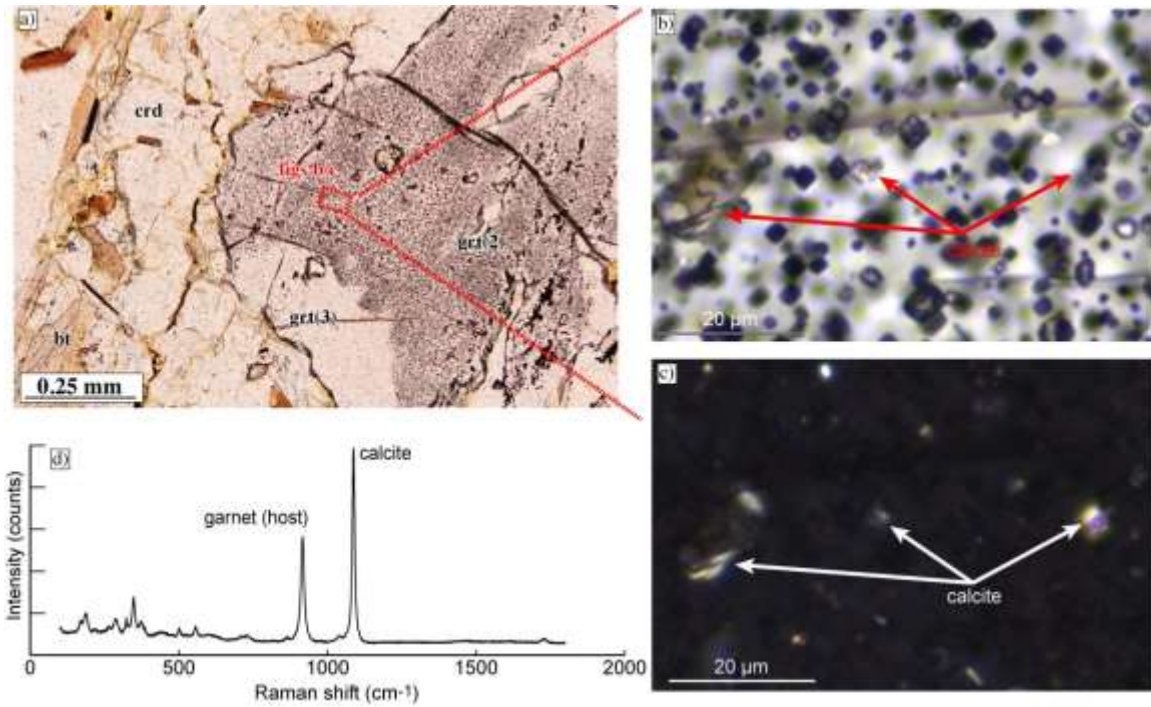


Figure A6: a) Thin section image highlighting the location of calcite inclusions within the core of the analysed garnet. b-c) PPL (b) and XPL (c) thin section images of calcite inclusions within the garnet core (red box in (a)). d) Raman spectrum identifying calcite inclusions within garnet (host) in sample 19WM118 (zone 6).

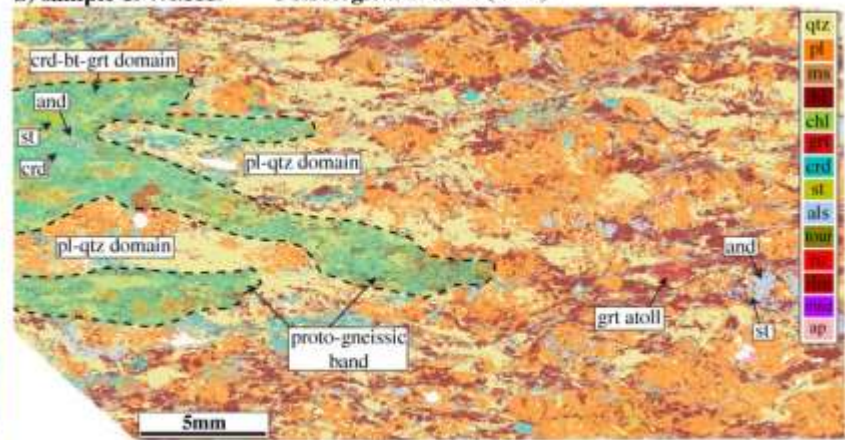
Appendix B. Supporting information for Chapter 4.

Figure B1 (overleaf): a) Phase map of sample 18WM07b, from petrological zone 1, consisting of an assemblage chlorite–muscovite–plagioclase–quartz +/- titanite– calcite. The dominant muscovitechlorite fabric is highlighted by the red dashed line and is overgrown by plagioclase. Blue dashed lines outline the crenulated fabric which wraps plagioclase. The lowest grade (zone 1) assemblage is devoid of monazite, instead allanite and apatite occur within both labelled fabrics. b) Sample 19WM119, base of zone 6. Assemblage consists of cordierite– plagioclase–biotite–staurolite– muscovite–garnet–andalusite/sillimanite. A protogneissic band shows development within more cordierite-rich domains of the thin section. Staurolite is typically seen included within andalusite while cordierite commonly overgrows andalusite. Weathered and atollated garnet is common. Monazite occurs locally and aligned with biotite-rich fabrics. Allanite is absent and apatite is rare. c) Phase map of sample 19WM229, zone 6. Assemblage consists of cordierite– plagioclase– biotite–garnet–andalusite/sillimanite. A penetrative gneissic band is seen with the segregation of quartzplagioclase and cordierite-biotite domains. Garnet is abundant, however, inclusion-rich and corroded. Cordierite is seen wrapping all other prograde phases including garnet, staurolite and andalusite. Andalusite in turn is seen to wrap relic staurolite. Monazite is rare, allanite is absent, and apatite is abundant; this likely relates to the high abundance of garnet within this sample. d) Sample 19WM116 which occurs towards the middle of zone 6. A thin and penetrative gneissic band is seen defined by cordierite-biotite-sillimanite. Staurolite and garnet are absent from the assemblage and andalusite/sillimanite show reduced abundance. e) sample 18WM10b from the top of zone 7 shows a cm-scale penetrative gneissic band defined by coarse cordierite and biotite. Aluminum silicate is now lost from the assemblage except for that included within cordierite. f) sample 19WM123 from the base of zone 7. A strong and penetrative, cm-scale gneissic band dominates. Cordierite shows coarsening and limited sillimanite inclusions. Garnet shows breakdown and atolls of cordierite, chlorite, and muscovite.

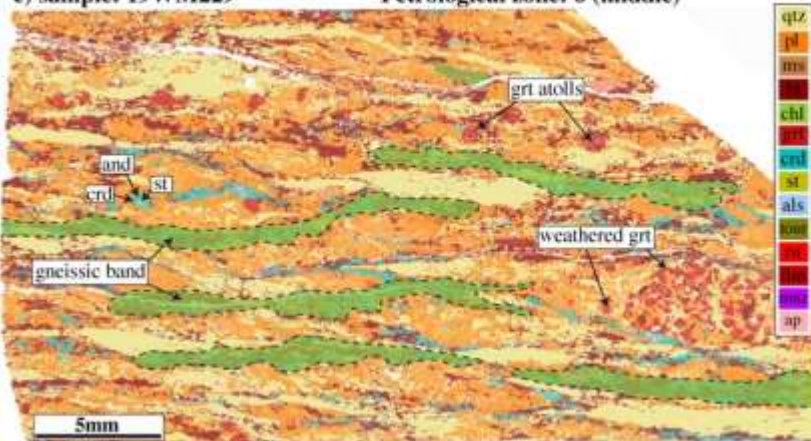
a) sample: 18WM07 Petrological zone: 1



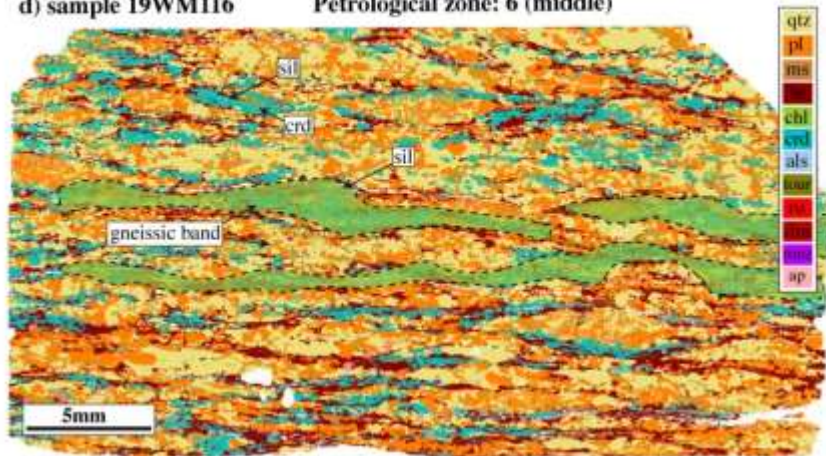
b) sample 19WM119 Petrological zone: 6 (base)

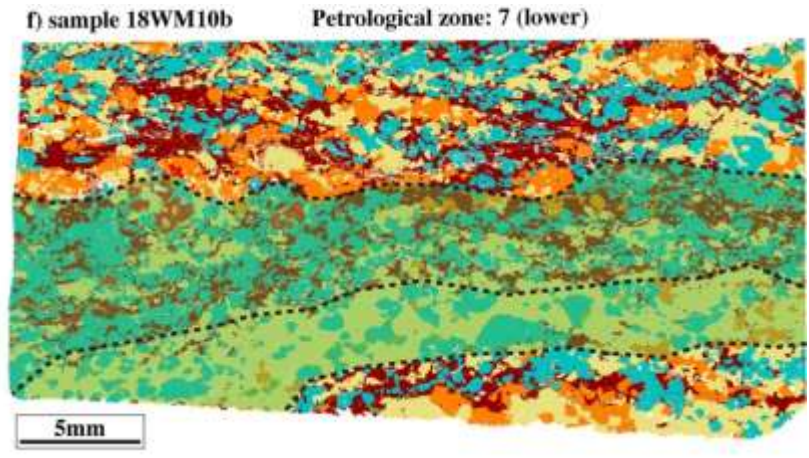
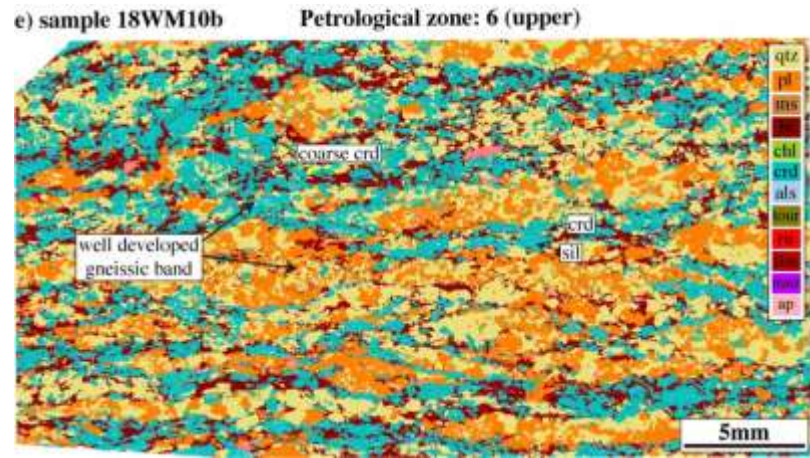


c) sample: 19WM229 Petrological zone: 6 (middle)



d) sample 19WM116 Petrological zone: 6 (middle)





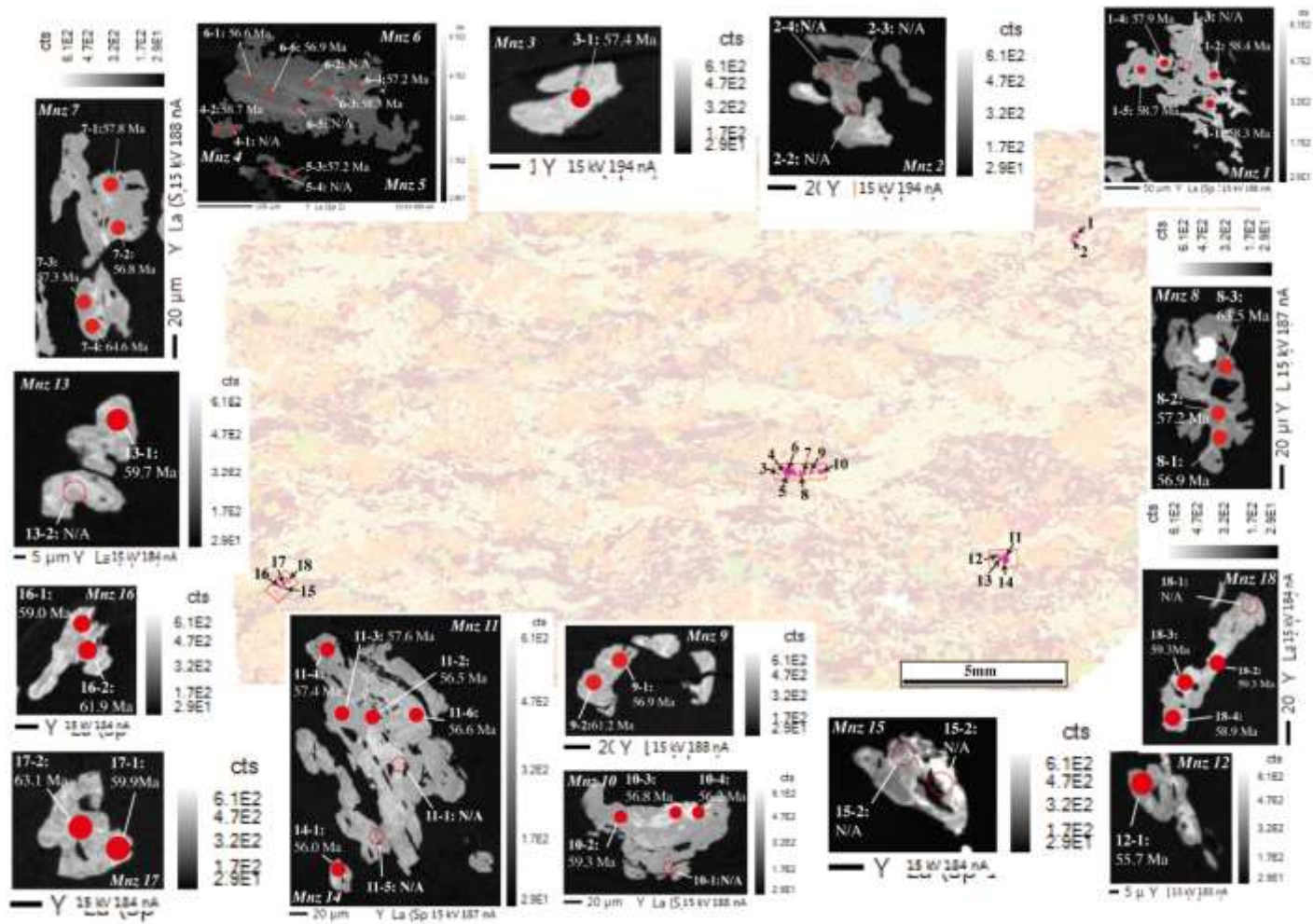


Figure B2: Analyzed monazite grains in sample 19WM120.

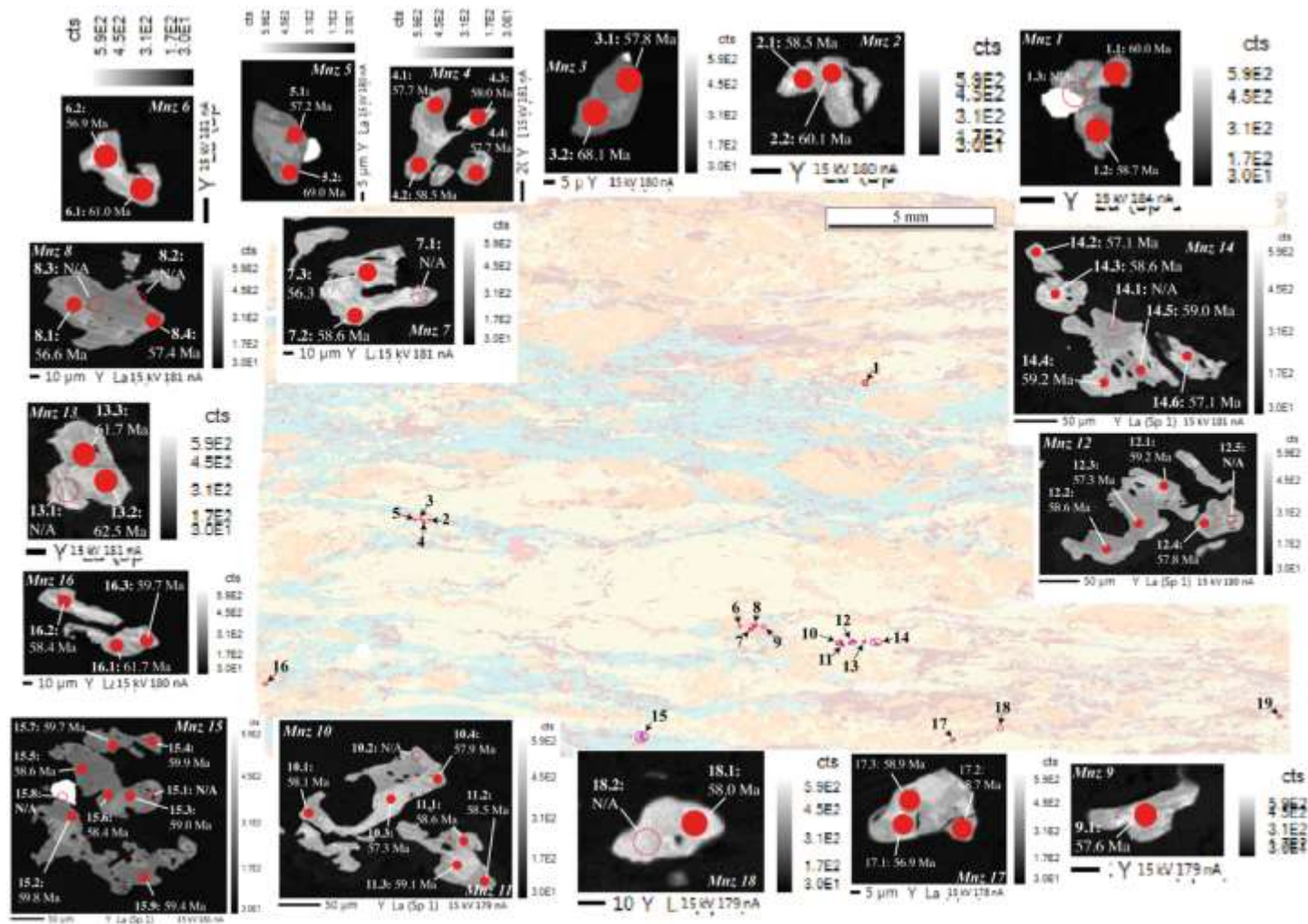


Figure B3: Analyzed monazite grains in sample 19WM118. Note grain 19 was not imaged.

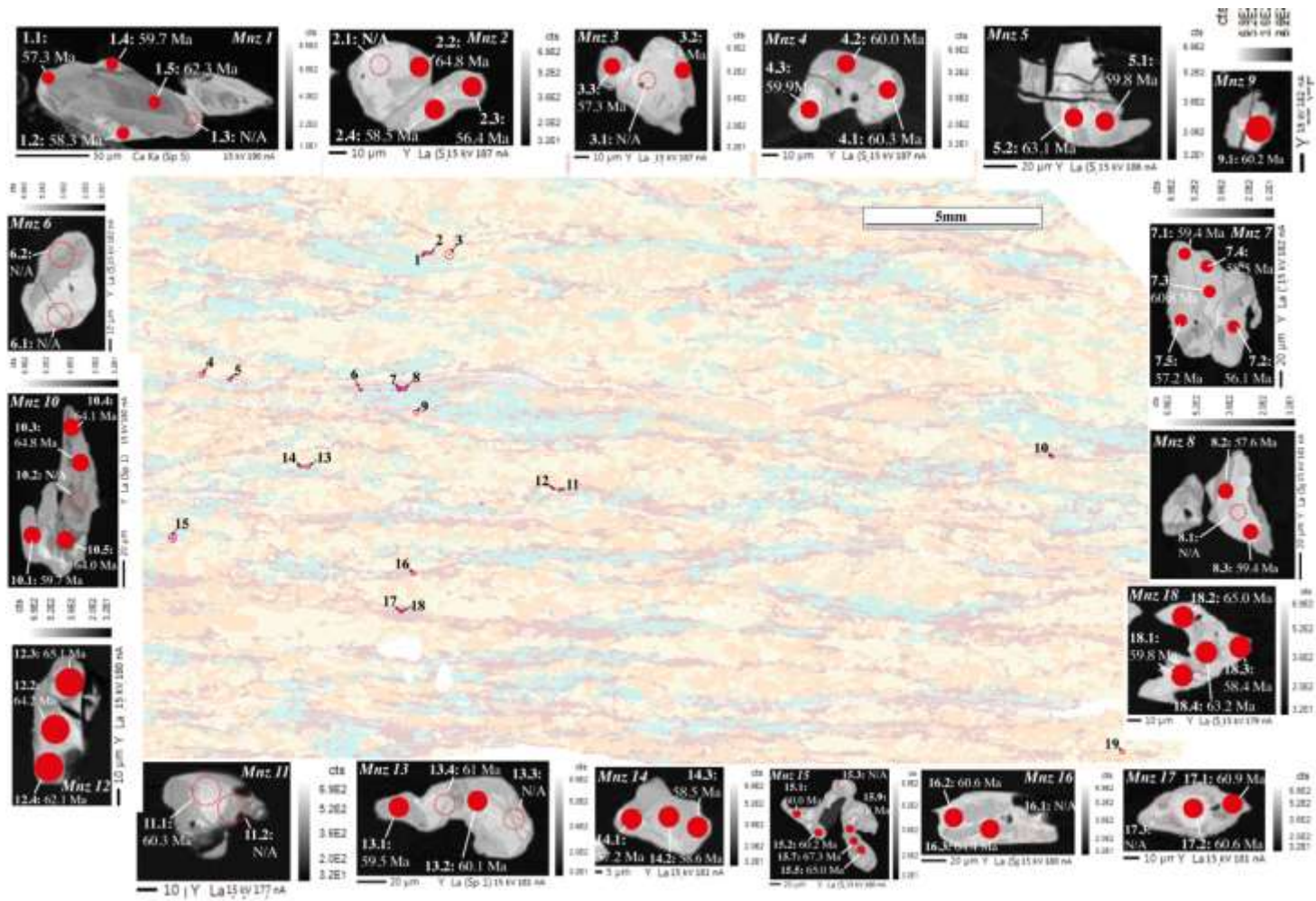


Figure B4: Analysed monazite grains in sample 19WM116.

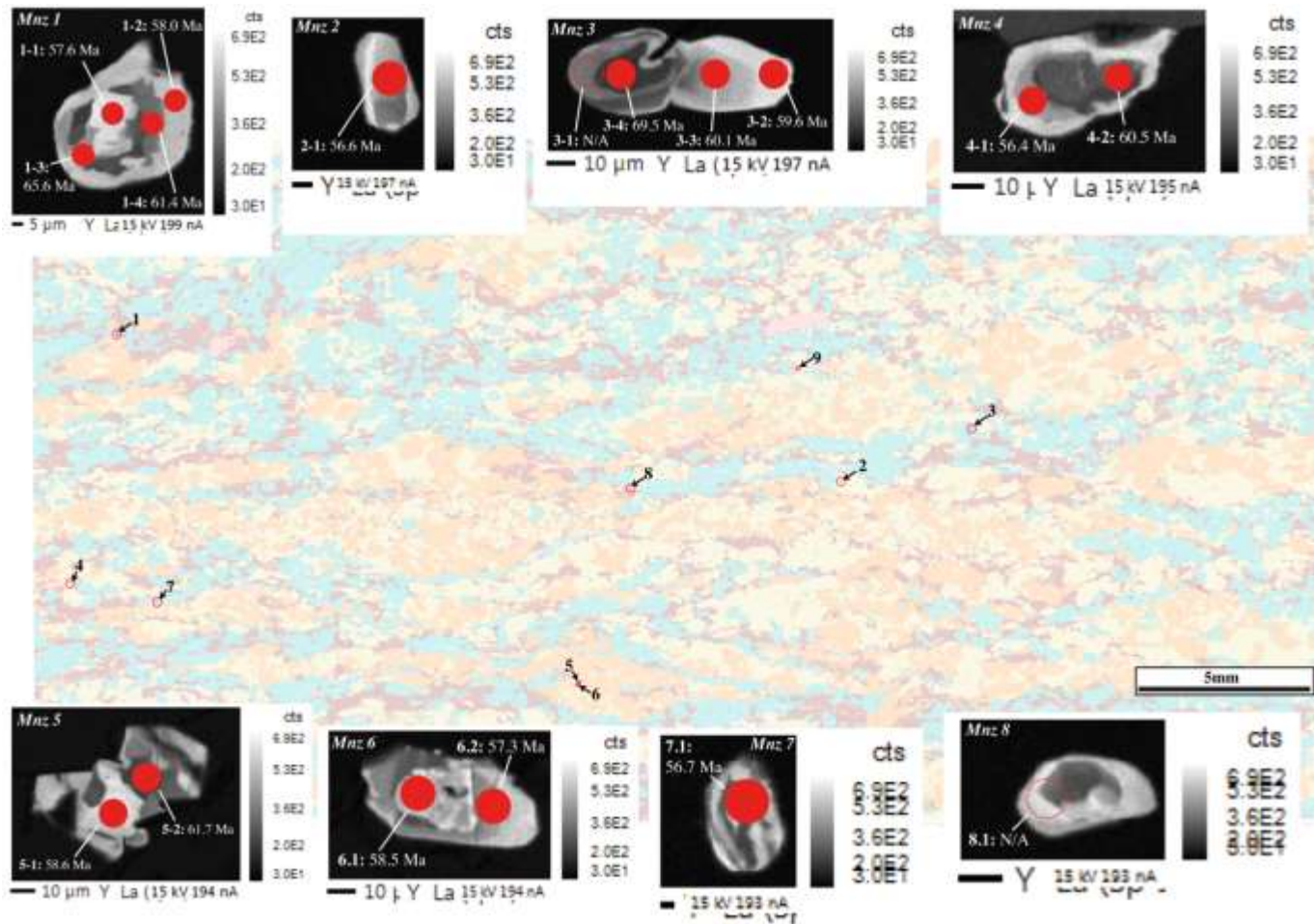


Figure B5: Analysed monazite grains in sample 18WM10b.

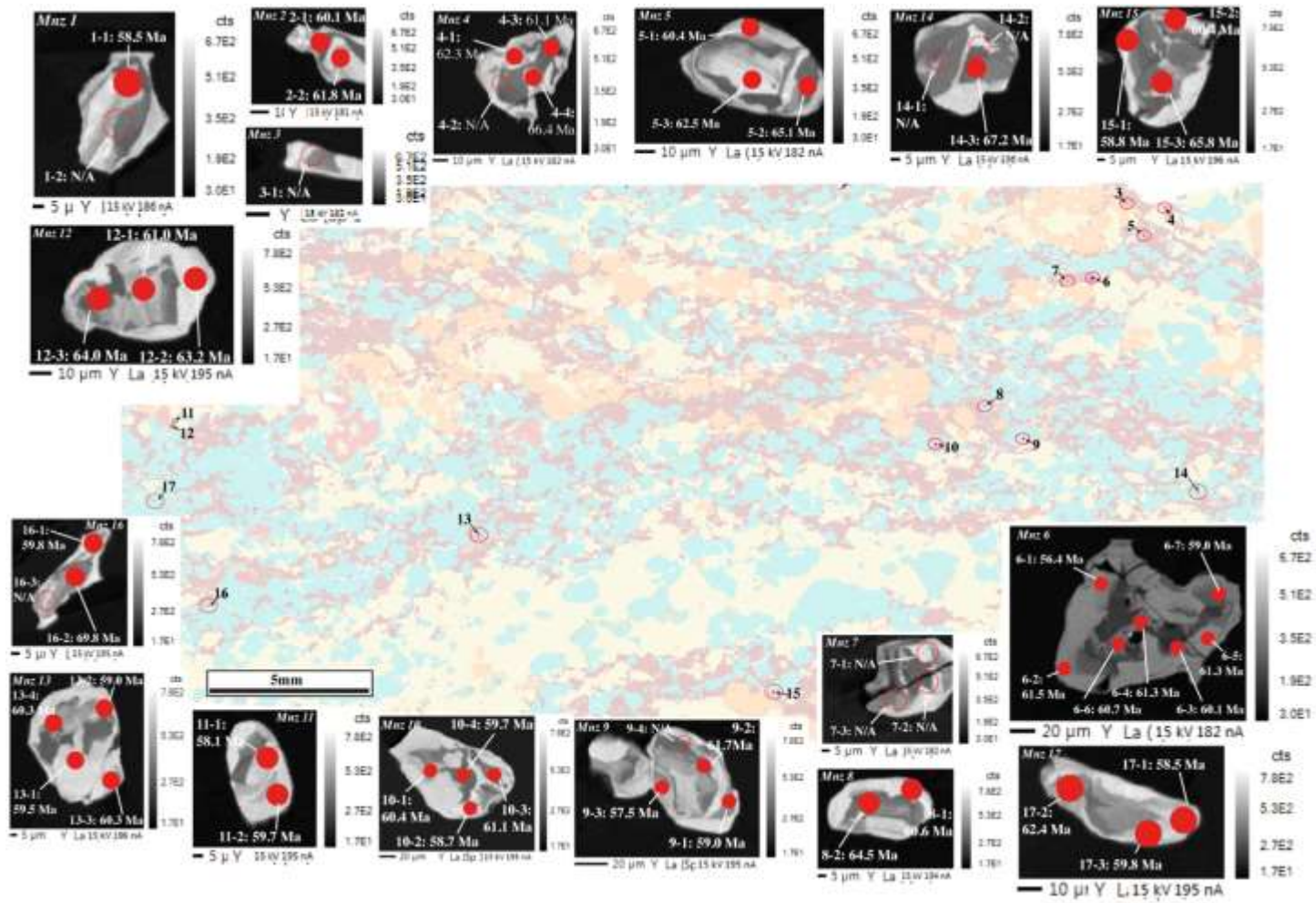


Figure B6: Analysed monazite grains in sample 19WM123.

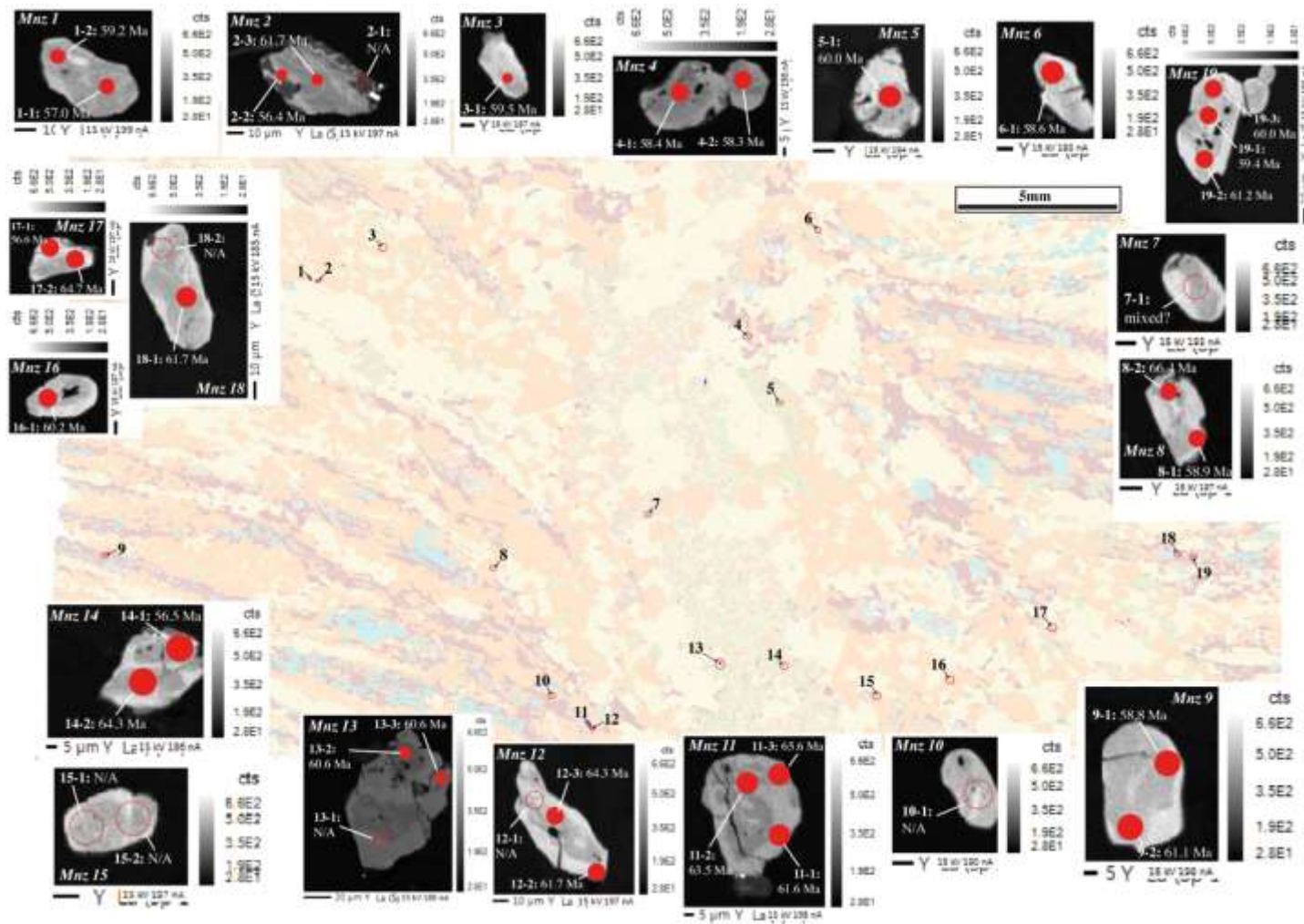


Figure B7: Analyzed monazite grains in sample 19WM230.

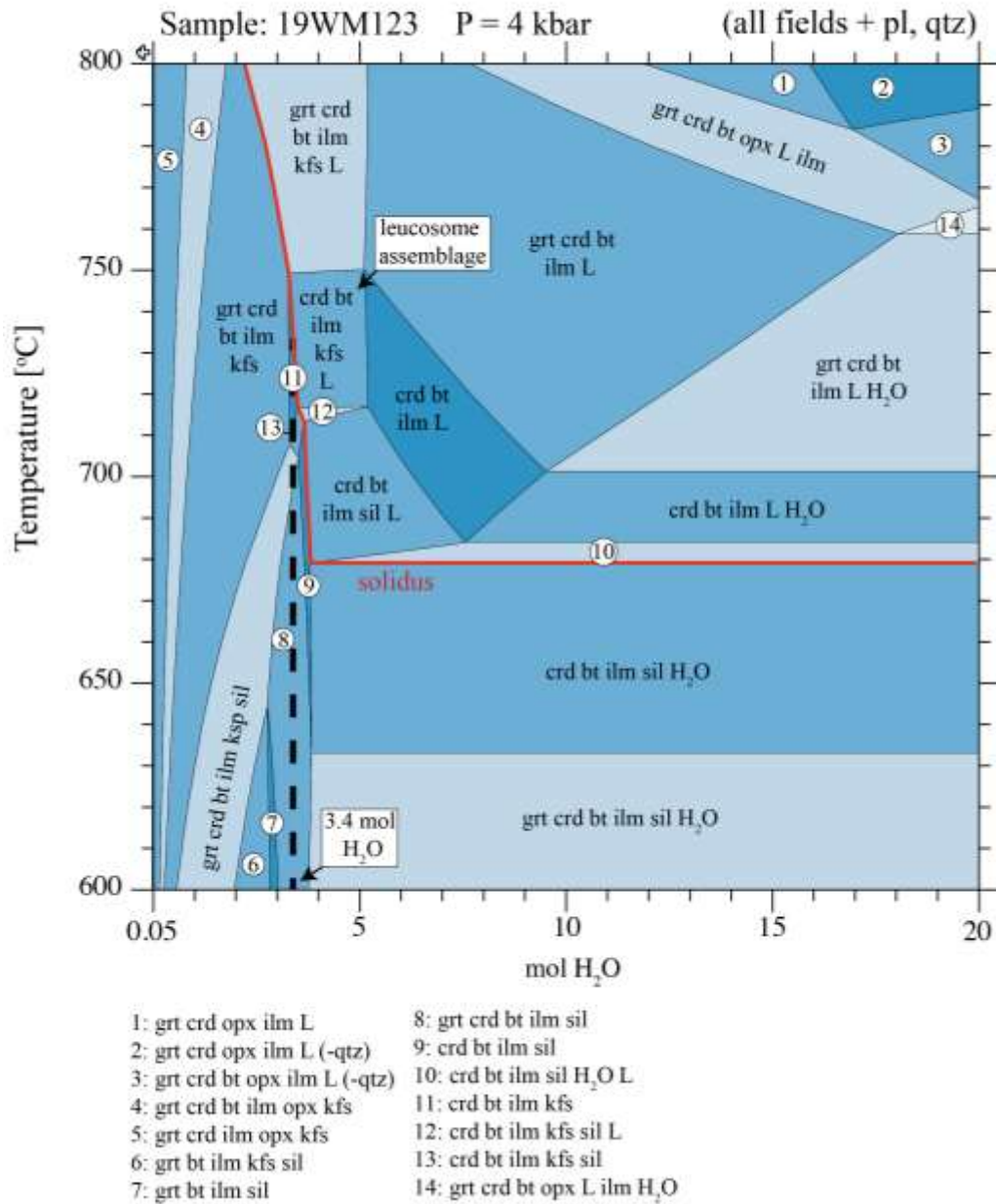


Figure B8: Isobaric T-X_{H₂O} phase diagram for sample 19WM123. Black dashed line shows minimum amount of H₂O required the system at the solidus.

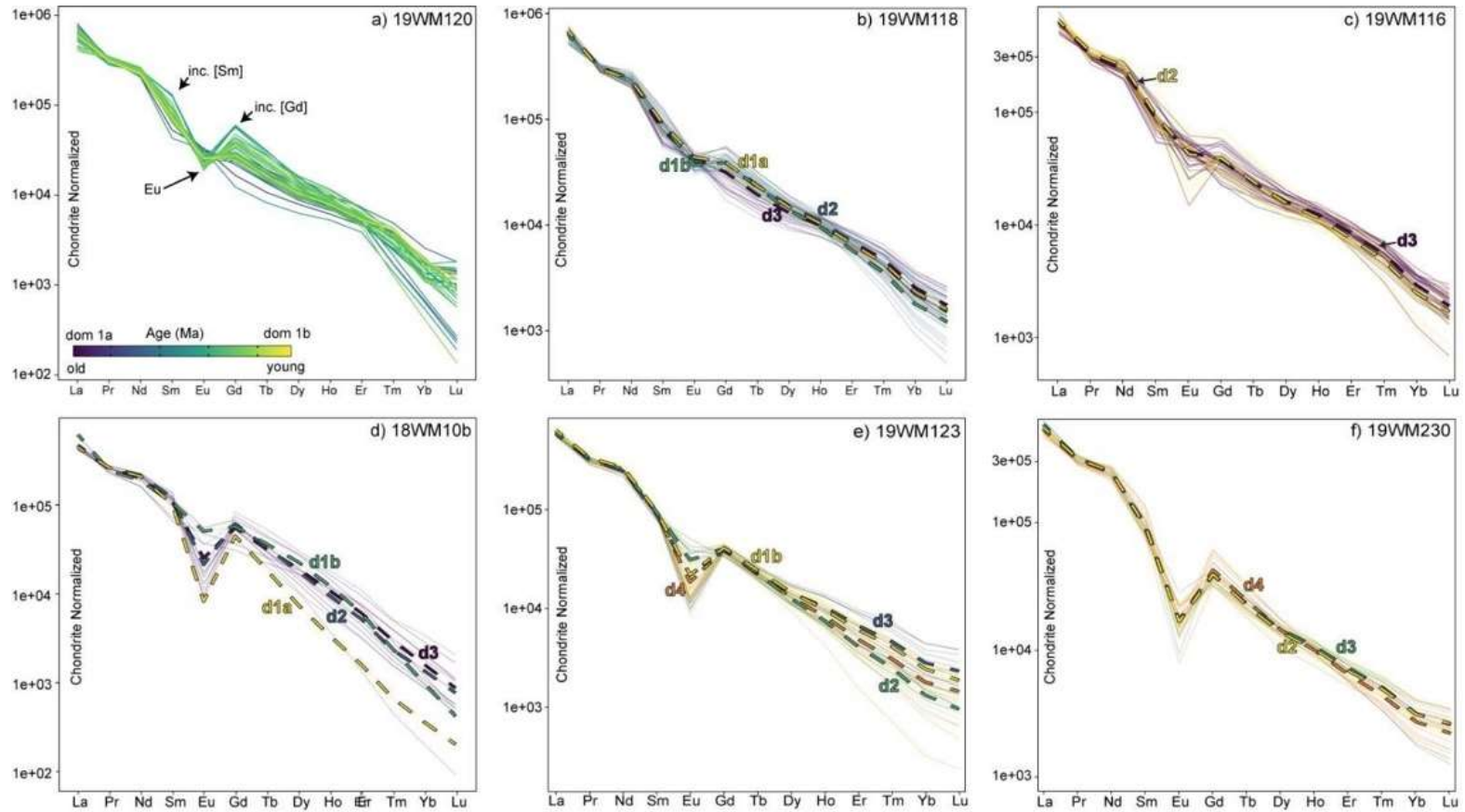


Figure B9: Spider diagrams highlighting the variation in REE chemistry between individual monazite domains within all samples across the Kluane Schist; a) 19WM120, b) 19WM118, c) 19WM116, d) 18WM10b, e) 19WM123, f) 19WM230. Full description and interpretations of these chemical trends, including their standing on the timing of Kluane Schist paragenesis can be found in the main text.

Appendix C: Supporting information for Chapter 5.

Note: Due to their size, Figures C1-C5 (imaged detrital zircon mounts & labelled grains) are provided as a separate PDF file ("Figures. C1-5.pdf").

Figure C1: Imaged grain mount for sample 19WM229.

Figure C2: Imaged grain mount for sample 19WM230d.

Figure C3: Imaged grain mount for sample 20WM25b.

Figure C4: Imaged grain mount for sample 20WM26.

Figure C5: Imaged grain mount for sample 20WM40.

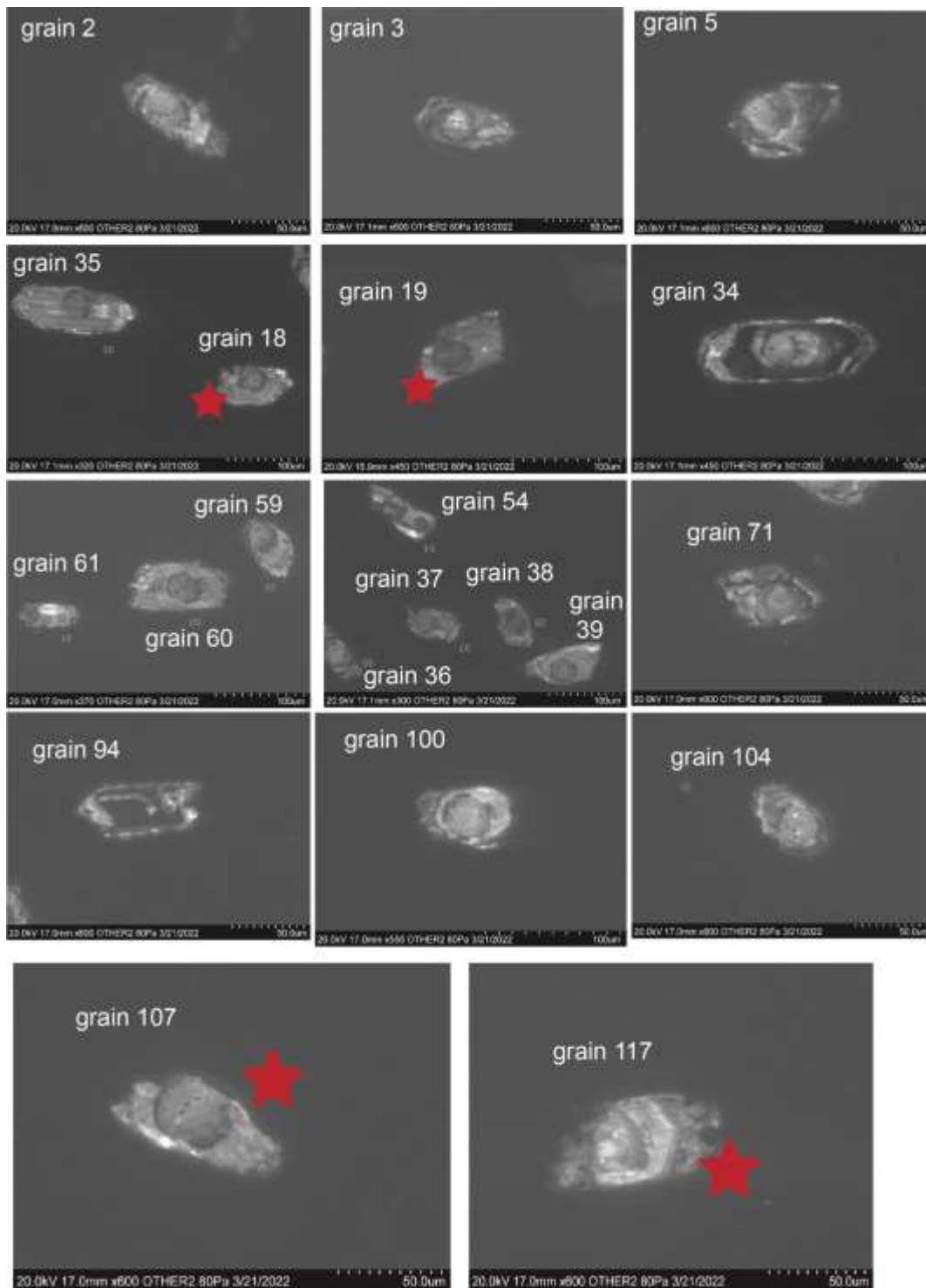


Figure C6: Post-ablation CL images of a subset of young zircon from sample 19WM229. Red stars highlight grains selected for TIMS analyses.

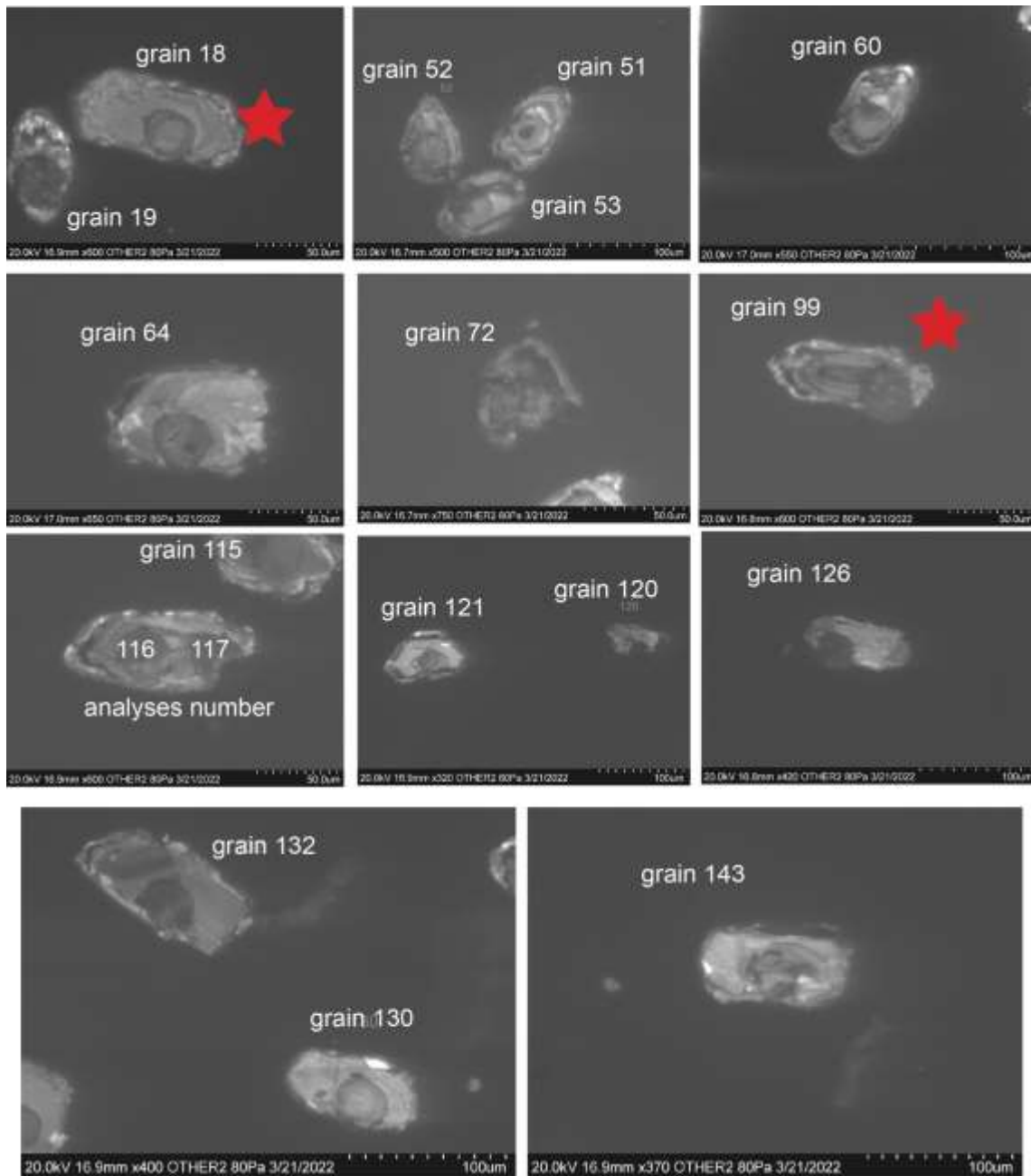


Figure C7: Post-ablation CL images of a subset of young zircon from sample 19WM230d. Red stars highlight grains selected for TIMS analyses.

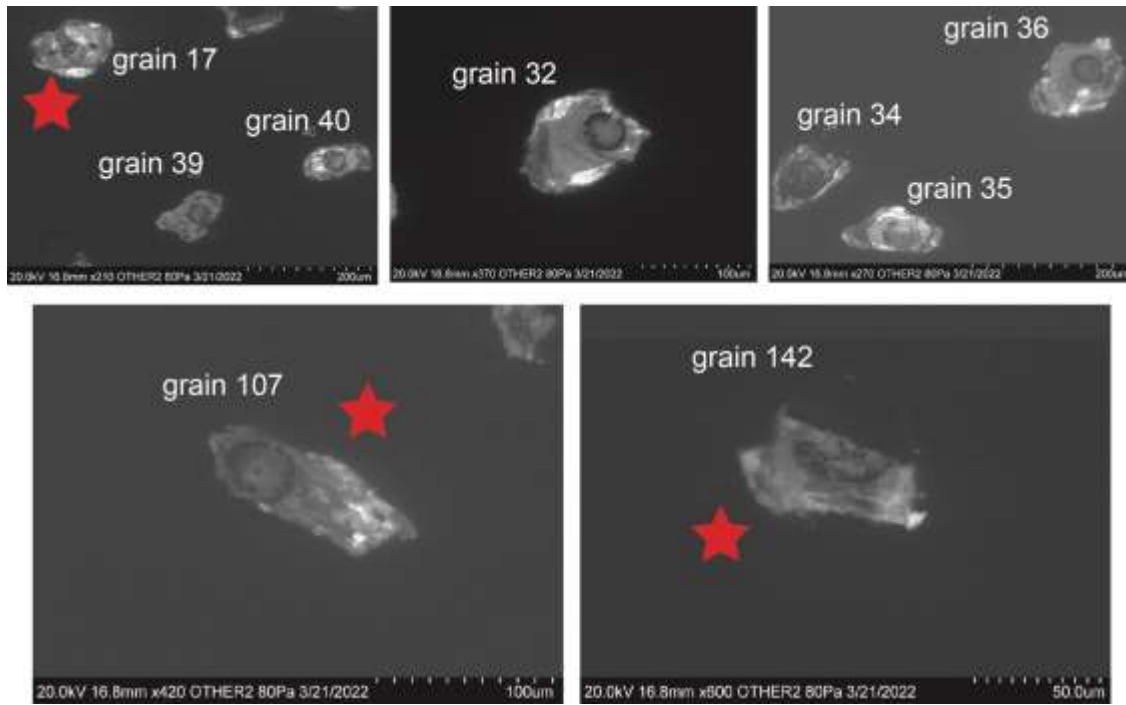


Figure C8: Post-ablation CL images of a subset of young zircon from sample 20WM25b. Red stars highlight grains selected for TIMS analyses.

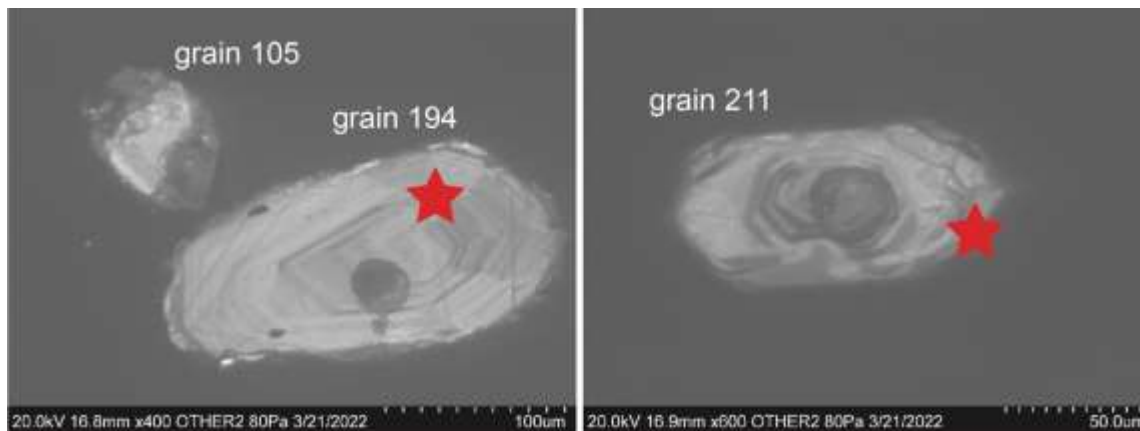


Figure C9: Post-ablation CL images of a subset of young zircon from sample 20WM26. Red stars highlight grains selected for TIMS analyses.

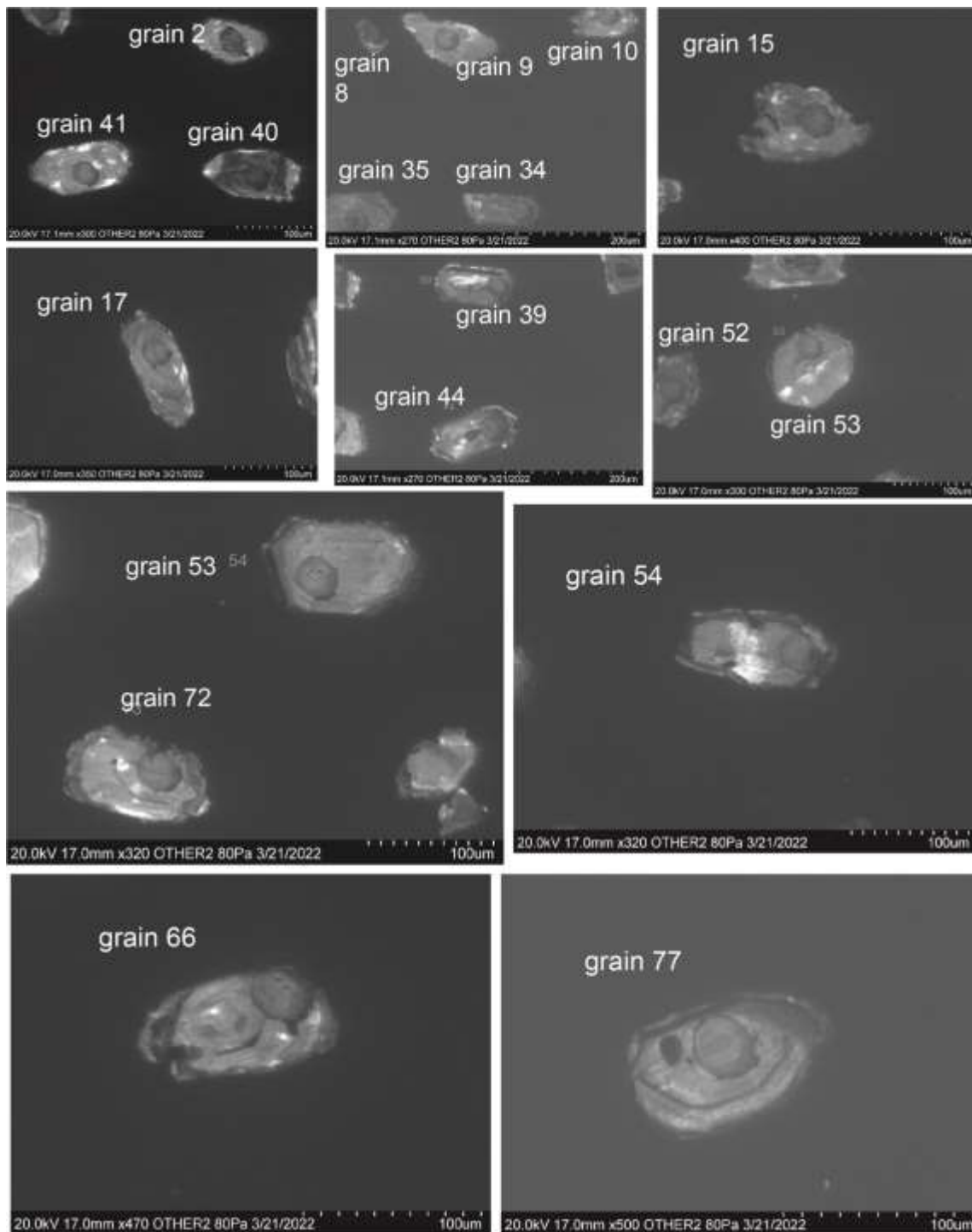


Figure C10: Post-ablation CL images of a subset of young zircon from sample 20WM40. Note: grains selected for TIMS were not imaged for this sample.

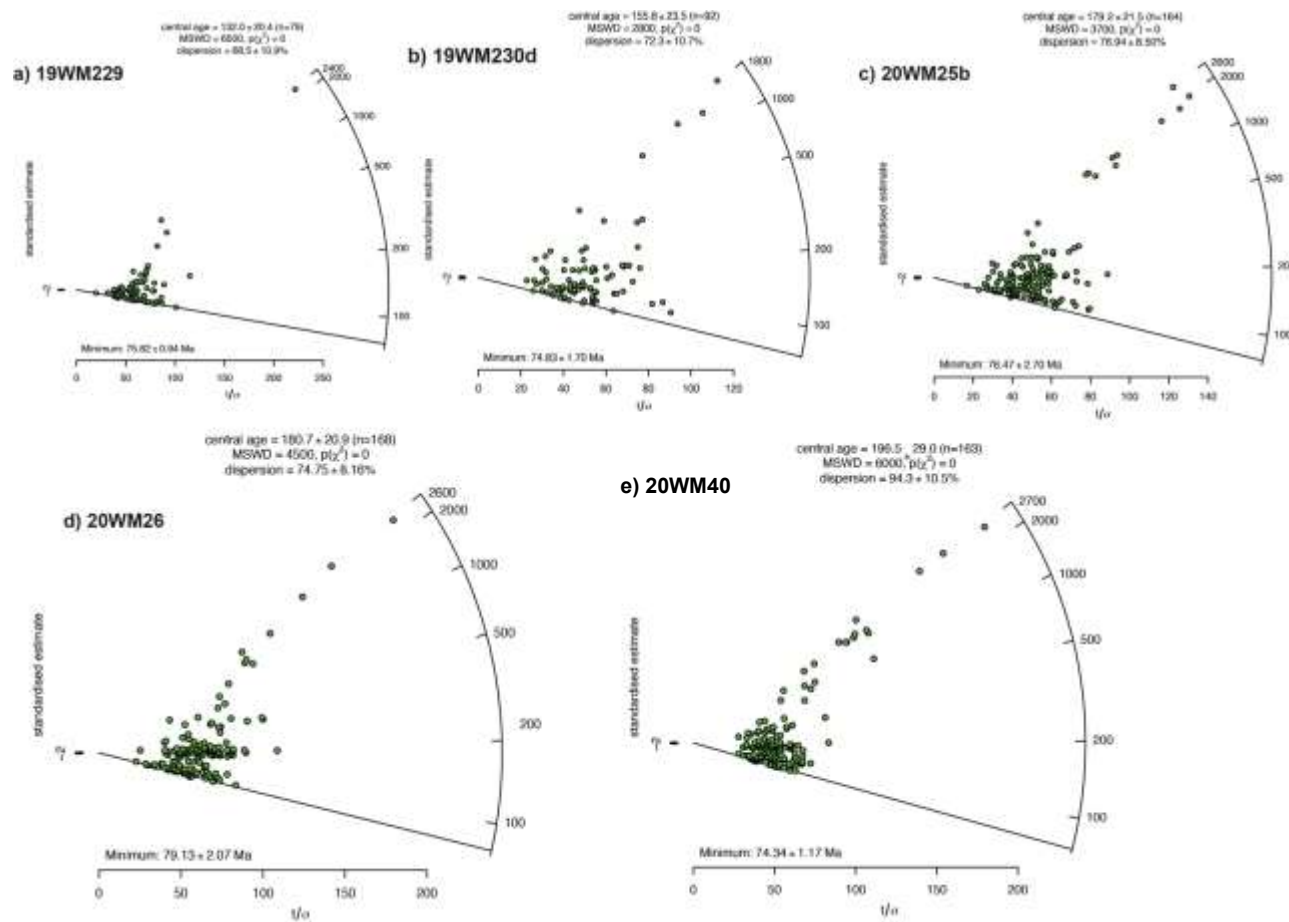


Figure C11: Radial plot outputs from IsoplotR (Vermeesch, 2018a) for a) 19WM229, b) 19WM230d, c) 20WM25b, d) 20WM26, e) 20WM40. These were used to estimate the maximum depositional age of the Kluane Schist (c.f., Vermeesch, 2021).

Appendix D: Supplementary data file.

Description: The accompanying excel spreadsheet contains the XRF data used for the petrological modelling presented within Chapter 3. This file consists of a single table:

- **Table D1:** Bulk rock chemistry determined by X-ray fluorescence.

File Name: Appendix_D XRF data for Kluane Schist.xlsx

Appendix E: Supplementary data file.

Description: The accompanying excel spreadsheet contains a compilation of the electron microprobe data used for the petrological modelling and thermobarometry presented within Chapters 3 and 4. This file consists of 8 separate tables arranged in the following format:

- **Table E1:** Garnet mineral compositions determined by electron microprobe.
- **Table E2:** Muscovite mineral compositions determined by electron microprobe.
- **Table E3:** Chlorite mineral compositions determined by electron microprobe.
- **Table E4:** Cordierite mineral compositions determined by electron microprobe.
- **Table E5:** Staurolite mineral compositions determined by electron microprobe.
- **Table E6:** Biotite mineral compositions determined by electron microprobe.
- **Table E7:** Plagioclase mineral compositions determined by electron microprobe.
- **Table E8:** Summary of garnet compositional profiles.

File Name: Appendix_E EPMA data and garnet profiles Kluane Schist.xlsx

Appendix F: Supplementary data file.

Description: The accompanying excel spreadsheet contains a compilation of the U-Th-Pb age and trace element data from Kluane Schist monazite presented within Chapter 4. This file consists of 2 separate tables arranged in the following format:

- **Table F1:** Unknown U-Th-Pb age & trace element data Kluane Schist monazite.
- **Table F2:** Standard U-Th-Pb age & trace element data Kluane Schist monazite.

File Name: Appendix_F U-Th-Pb age and trace element data for Kluane Schist monazite.xlsx

Appendix G: Supplementary data file.

Description: The accompanying excel spreadsheet provides the individual bulk rock compositions used for the petrological modelling presented in Chapter 4. The additional temperature estimates presented in chapter, provided by the titanium-in-biotite thermometer, are also included. This file consists of 2 separate tables arranged in the following format:

- **Table G1:** Bulk rock chemistry determined by X-ray maps and mineral data.
- **Table G2:** Ti-in-biotite calculations.

File Name: Appendix_G Bulk rock (individual) and Ti-in-Bt thermometry Kluane Schist.xlsx

Appendix H: Supplementary data file.

Description: The accompanying excel spreadsheet provides a compilation of the detrital zircon geochronological data and specific LA-MC-ICP-MS parameters for all 2021 and 2022 analyses conducted at Geotop labs in the Université du Québec à Montréal and presented in Chapter 5. This file consists of 7 separate tables arranged in the following format:

- **Table H1:** Detrital zircon geochronological data and specific LA-MC-ICP-MS parameters for all 2021 analyses conducted at Geotop labs in the Université du Québec à Montréal.
- **Table H2:** Reference material values for 2021 detrital zircon U-Pb analyses.
- **Table H3:** Detrital zircon geochronological data and specific LA-MC-ICP-MS parameters for all 2022 analyses conducted at Geotop labs in the Université du Québec à Montréal.
- **Table H4:** Reference material values for 2022 detrital zircon U-Pb analyses.
- **Table H5:** Single age KDE and MDA datasets for Kluane Schist.
- **Table H6:** Single age KDE distribution for Kluane Schist (all samples; detrital only).
- **Table H7:** Single age vs. U/Th dataset for Kluane Schist.

File Name: Appendix_H detrital zircon U-Pb Kluane Schist.xlsx

Appendix I: Supplementary data file.

- **Description:** The accompanying excel spreadsheet provides a compilation of the detrital zircon Hf-isotope determinations and specific LA-MC-ICP-MS parameters for all analyses conducted at Pacific Centre for Isotope and Geochemical Research, University of British Columbia and presented in Chapter 5. This file consists of 3 separate tables arranged in the following format:
- **Table I1:** Raw zircon Hf-isotope data collected at the Pacific Centre for Isotope and Geochemical Research, University of British Columbia.
- **Table I2:** Zircon Hf-isotope standard data.
- **Table I3:** Metadata and specific LA-MC-ICP-MS parameters for Hf-isotopic analyses.

File Name: Appendix_I detrital zircon Hf-isotope analysis Kluane Schist.xlsx

Appendix J: Supplementary data file.

Description: The accompanying excel spreadsheet provides the raw data and specific analytical parameters for the Thermal Ionisation Mass Spectrometry (TIMS) conducted at Geotop labs in the Université du Québec à Montréal and presented in Chapter 5. This file consists of a single table:

- **Table J1:** Detrital zircon TIMS geochronological data (unknown and standards 2022).

File Name: Appendix_J detrital zircon TIMS data Kluane Schist.xlsx

Appendix K: Supplementary data file.

Description: The accompanying excel spreadsheet contains a compilation of all the field data collected across the Kluane Schist and its surrounding lithologies during fieldwork in 2019 and 2020. This file consists of two tables:

- **Table K1:** Field data 2019
- **Table K1:** Field data 2020

File Name: Appendix_K field data 2019/2020 Kluane Schist.xlsx